Bonded Patch Repair Applications for Primary Aircraft Structures

Author:
Tanulia, Veldyanto

Publication Date:
2022

DOI:
https://doi.org/10.26190/unsworks/2062

THE UNIVERSITY OF NEW SOUTH WALES

Bonded Patch Repair Applications for Primary Aircraft Structures

Veldyanto Tanulia

A dissertation in fulfilment of the requirements for the degree of Doctor of Philosophy

School of Mechanical and Manufacturing Engineering
Faculty of Engineering

January 2022

Surname/Family Name	:	**Tanulia**
Given Name/s	:	**Veldyanto**
Abbreviation for degree as give in the University calendar	:	**PhD**
Faculty	:	**Faculty of Engineering**
School	:	**School of Mechanical and Manufacturing Engineerign**
Thesis Title	:	**Bonded Patch Repair Applications for Primary Aircraft Structures**

Abstract 350 words maximum: (PLEASE TYPE)

Adhesively bonded joints have been widely used to manufacture aircraft components. However, its application to single load-path airframe structure is costly to certify as extensive validation testing is required. Certification of bonded joints or patch repairs for primary aircraft structures requires demonstration of damage tolerance. In recent years, a damage slow growth management strategy has been considered acceptable by Federal Aviation Administration to reduce the maintenance cost. This thesis evaluates the applicability of a damage slow growth management strategy to bonded joints/patch repairs of primary aircraft structures through both experimental and computational study. The investigation was carried out first by 2-D strip specimen assessment and finally using 3-D analysis of wider panel specimen.

This research was a collaborative project between ARC Training Centre for Automated Manufacture of Advanced Composites (AMAC) at the University of New South Wales (UNSW) and Defence Science and Technology (DST) Group. Fatigue tests of 2-D strip specimen were conducted to investigate the entire process of disbond growth from initiation up to joint ultimate failure. The residual static strength of the joint as a function of disbond length was established using finite element modelling based on the characteristic distance approach. A virtual crack close technique (VCCT) approach was utilised to assess the strain energy release rates (SERRs) as a function of disbond crack length.

The measured disbond growth rates were correlated with the SERRs using a modified Paris law that enabled prediction of joint fatigue life. The fatigue test results indicated that for a joint having a sufficient static strength safety margin under a typical fatigue loading that would propagate disbond, the disbond growth would remain stable within a particular length range. Thus, the slow growth approach would be feasible for bonded joints/patch repairs if the patch is designed to be sufficiently large to allow extended damage propagation.

Cohesive zone element (CZE) technique was utilised to assess the SERRs and estimate the disbond growth of 3-D wider panel specimen analysis. The impact of local or partial width disbond (load shedding effect) was investigated in detail. The results indicate that for a local or part width disbond, some load was redistributed to the adjacent regions that causes a slower disbond growth compared to the full width disbond.

ORIGINALITY STATEMENT

'I hereby declare that this submission is my own work and to the best of my knowledge it contains no materials previously published or written by another person, or substantial proportions of material which have been accepted for the award of any other degree or diploma at UNSW or any other educational institution, except where due acknowledgement is made in the thesis. Any contribution made to the research by others, with whom I have worked at UNSW or elsewhere, is explicitly acknowledged in the thesis. I also declare that the intellectual content of this thesis is the product of my own work, except to the extent that assistance from others in the project's design and conception or in style, presentation and linguistic expression is acknowledged.'

Signed ……………………………………………………........

Date 15 January 2022

COPYRIGHT STATEMENT

AUTHENTICITY STATEMENT

UNSW is supportive of candidates publishing their research results during their candidature as detailed in the UNSW Thesis Examination Procedure.

Publications can be used in their thesis in lieu of a Chapter if:

- The candidate contributed greater than 50% of the content in the publication and is the "primary author", ie. the candidate was responsible primarily for the planning, execution and preparation of the work for publication
- The candidate has approval to include the publication in their thesis in lieu of a Chapter from their supervisor and Postgraduate Coordinator.
- The publication is not subject to any obligations or contractual agreements with a third party that would constrain its inclusion in the thesis

Please indicate whether this thesis contains published material or not:

☐ This thesis contains no publications, either published or submitted for publication
(if this box is checked, you may delete all the material on page 2)

☒ Some of the work described in this thesis has been published and it has been documented in the relevant Chapters with acknowledgement
(if this box is checked, you may delete all the material on page 2)

☐ This thesis has publications (either published or submitted for publication) incorporated into it in lieu of a chapter and the details are presented below

CANDIDATE'S DECLARATION

I declare that:

- I have complied with the UNSW Thesis Examination Procedure
- where I have used a publication in lieu of a Chapter, the listed publication(s) below meet(s) the requirements to be included in the thesis.

Candidate's Name	**Signature**	**Date (dd/mm/yy)**
Veldyanto Tanulia		**15 January 2022**

Abstract

Adhesively bonded joints have been widely used to manufacture aircraft components. However, its application to single load-path airframe structure is costly to certify as extensive validation testing is required. Certification of bonded joints or patch repairs for primary aircraft structures requires demonstration of damage tolerance. In recent years, a damage slow growth management strategy has been considered acceptable by Federal Aviation Administration to reduce the maintenance cost. This thesis evaluates the applicability of a damage slow growth management strategy to bonded joints/patch repairs of primary aircraft structures through both experimental and computational study. The investigation was carried out first by 2-D strip specimen assessment and finally using 3-D analysis of wide bonded metal joint.

This research was a collaborative project between ARC Training Centre for Automated Manufacture of Advanced Composites (AMAC) at the University of New South Wales (UNSW) and Defence Science and Technology (DST) Group. The double overlap tapered end specimen (DOTES) specimen which represents both disbond tolerant zone and safe-life zone in bonded patch repair was investigated first through a detailed computational and experimental investigation. The residual static strength of the joint as a function of disbond length was established using finite element modelling based on the characteristic distance approach. The virtual crack close technique (VCCT) approach was utilised to assess the strain energy release rates (SERRs) as a function of disbond crack length.

Fatigue tests of the DOTES coupon specimen were conducted to investigate the entire process of disbond growth from initiation up to ultimate failure of the joint. The measured disbond growth rates were correlated with the SERRs using a modified Paris

law that enabled prediction of joint fatigue life. The fatigue test results indicated that for a joint having a sufficient static strength safety margin under a typical fatigue loading that would propagate disbond, the disbond growth would remain stable within a particular length range. Thus, the slow growth approach would be feasible for bonded joints/patch repairs if the patch is designed to be sufficiently large to allow extended damage propagation.

Cohesive zone element (CZE) technique was utilised to assess the SERRs and estimate the disbond growth of 3-D wide bonded metal joint analysis. The impact of local or partial width disbond (load shedding effect) was investigated in detail. The results indicate that for a local or part width disbond, some load was redistributed to the adjacent regions (load shedding effect) that causes a slower disbond growth and accordingly longer fatigue life compared to the full width disbond.

The key outcomes from this research are: (a) accurate prediction of the disbond growth behaviour in bonded patch repairs through the developed generic patch repair specimen i.e DOTES, (b) fatigue life prediction of the joints has been established through modified Paris law, by conducting numerical integration and (c) the effect of initial disbond size in 3-D wide bonded metal joint specimen was investigated through computational assessment using a cohesive fatigue model.

Acknowledgements

- To my supervisor Prof. Gangadhara Prusty and joint supervisor Associate Professor. Garth Pearce from University of New South Wales (UNSW) for guiding, monitoring and giving constant encouragement throughout my PhD study.
- To my co-supervisors Dr. John Wang and Dr. Alan Baker from Defence Science and Technology Group (DSTG) for their continuous support, guidance, and critical advice on the thesis research project.
- To my ex-co-supervisor Dr. Matthew David for his invaluable support during my first two years of candidature.
- To ARC Training Centre for Automated Manufacture of Advanced Composites (AMAC) for their scholarship program.
- To DSTG for their financial and in-kind (materials/facilities) supports.
- To University of New South Wales (UNSW) especially School of Mechanical and Manufacturing Engineering for providing the facilities.
- To AMAC staff, Dr. Md Shamsuddoha and Dr. Matthew Donough for their valuable suggestions.
- To Dr. Paul Chang and Mr. John Van Den Berg from DSTG for their guidance in surface preparation technique and their supports throughout my 12 months industrial placement at DSTG.
- To DSTG Aerospace Division for the facilities and the staff, particularly Dr. Andrew Rider, Kelvin Nicholson, Thomas, Gram Smith, Eudora Yeo, Vu Dao and Andrew Charles for the invaluable support at DSTG Melbourne.

- To Seetharam Mahadevan for the guidance in the use of various testing equipment in the UNSW Solids laboratory.
- To my colleagues, Nikhil Garg, Prashanth Nagulapally, Xie Li, and Yiwen Gu for supporting me in various aspects.
- To Michelle Gracia Onggo for her support in writing this thesis.
- Finally, to my parents (Andrian Tjhin and Asiati Dharma) for their patient, promptness, constant support, and care. This thesis indeed a realisation of their dream.

Table of Contents

List of Figures

List of Tables

Abbreviations

AL	Aluminium Alloy
BVID	Barely Visible Impact Damage
BWT	Boeing Wedge Test
CDM	Continuum Damage Modelling
CZE	Cohesive Zone Element
CZM	Cohesive Zone Modelling
DCB	Double Cantilever Beam
DLL	Design Limit Load
DOFS	Double Overlap Fatigue Specimen
DOTES	Double Overlap Tapered End Specimen
DOTES-ST	Double Overlap Tapered End Specimen – Short Tapered
DOTES-LT	Double Overlap Tapered End Specimen – Long Tapered
DUL	Design Ultimate Load
ERR	Energy Release Rate
FAA	Federal Aviation Administration
FDC	Fatigue Damage Criteria
FE	Finite Element
FEA	Finite Element Analysis
FEM	Finite Element Method
GR	Gap Region
HW	Hot Wet
MEK	Methyl Ethyl Ketone
NDI	Non-Destructive Inspection
RD	Room Temperature and Dry
RH	Relative Humidity
RT	Room Temperature
RW	Room Temperature and Wet

SCL	Simplified Cyclic Loading
SDS	Skin Doubler Specimen
SERR	Strain Energy Release Rate
SHM	Structural Health Monitoring
SIF	Stress Intensity Factor
TE	Tapered End
TIA	Thicker Inner Adherend
TOA	Thicker Outer Adherend
VCCT	Virtual Crack Closure Technique
VID	Visible Impact Damage

Notations

Tg	Glass transition temperature
GIc	Critical Energy Release Rate Mode I (G_{Ic})
GIIc	Critical Energy Release Rate Mode II (G_{IIc})
G	Strain energy release rate
η	Bond-line thickness
E	Elastic Modulus
G	Shear modulus
γ_{max}	Maximum shear strain
γ_{p}	Adhesive plastic shear strain limit
γ_{e}	Adhesive elastic shear strain limit
τ_{max}	Max. Shear Stress
t_a	Adhesive layer thickness
T_i	Inner adherend thickness
T_o	Outer adherend thickness
ν	Poisson's Ratio
W	Width of the adherend
L	Overlap length
σ_y	Yield stress
N	Number of cycles
K	Stress intensity factor
R	Load ratio
S	Tapered length
μ	Mean

σ	Standard deviation
k_B	One sided B-basis tolerance limit factor
T_c	Maximum traction
δ_c, Δ_c	Critical opening displacement
δ_m, Δ_f	Maximum opening displacement
C_1, C_2	Parameters in Paris law
m_1, m_2	Exponents in Paris law
n_{cz}	Number of cohesive elements in the process zone
A_{cz}	Cohesive element area
σ_{max}	Maximum stress
λ	Displacement jump
a	Crack length
F	Force
d	Damage
D	Damage norm
D^{fat}	Fatigue damage
λ_*	Reference displacement
β, γ	Coefficients of heuristic fatigue damage accumulation model
D^T	Tearing damage
K	Stiffness

Chapter 1

Introduction

1.1 Background

Back in the fifteenth century, Leonardo DaVinci designed a brilliant helicopter concept (see Figure 1.1) [1]. This design concept still exists until the twenty-first century for the next generation composite aircraft. Indeed, adhesive bonding is required for this concept to reduce weight and minimise stress concentrations. Thus, this concept was unable to be realised until adhesive bonding technology has been developed to the point where it is considered as reliable as mechanical fastener joining method [2].

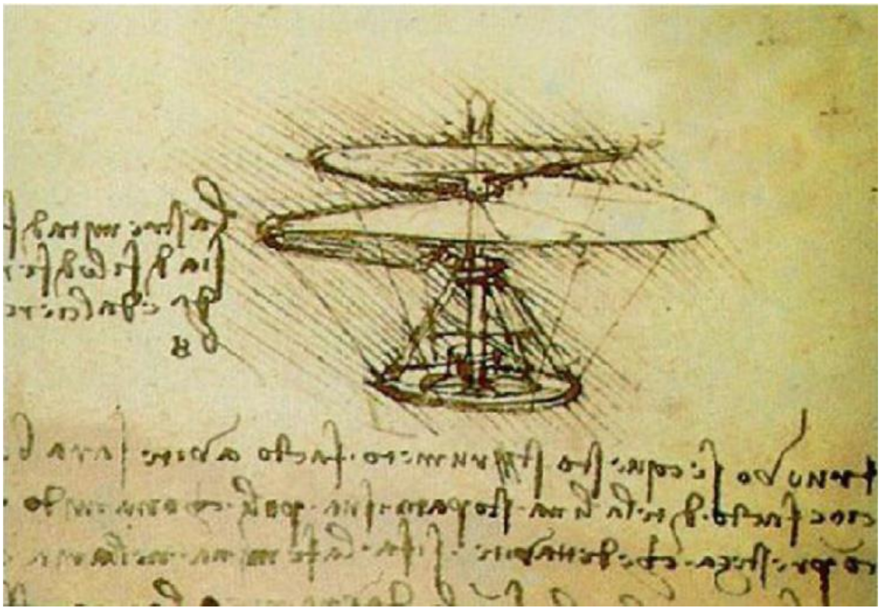

Figure 1.1: Leonardo DaVinci's helicopter design concept [1].

The existence of bonding technology has been established since World War II. It was firstly applied for bonded wood aircraft, namely de Havilland Mosquito. Later, bonded metallic structures were established, called the Havilland Dove commuter aircraft, the Fokker F-27 Friendship turbo-prop, and the de Havilland Comet jetliner [2]. Sailplanes were the first large scale bonded composite aircraft developed by Germany in 1950s. Since then, composite bonding technology has been utilised for various type of aircraft, such as small-powered aircraft, general transport and military and transport aircraft. Recently, composite bonding technology was widely applied in large commercial aircraft company such as Boeing and Airbus [1].

Nowadays, fleet operators are willing to use aircraft longer than their original design life due to economic reasons. Fatigue became the most important issue while maintaining these aircrafts or normally called as "aging aircraft". Repairs are generally needed to be safe, damage tolerant, and cost-effective. The Aloha Airlines Flight 243 (Boeing 737-200) accident was one example of repairs needed to be safe. An explosive decompression was occurred in the upper cabin area as shown in Figure 1.2. Number of researchers have identified the key issue, that is, there has been multiple fatigue cracks existed in the riveted joints of the aircraft aluminium skin. Thus, a technique was required to restore the desired service life of these aging aircrafts [3].

Figure 1.2: The Aloha Airlines flight 23 incident [3].

Qantas found a structural cracking in one of its Boeing 737 aircraft as stated in the news found in Figure 1.3. Consequently, a total of 33 Boeing 737 aircraft required immediate inspection and needed to be grounded which resulted in a loss of billions of dollars [4]. Damage in aircraft structures which might have appeared from manufacturing defect, or caused during the service by blunt body impacts, operating loads or tool drops was unavoidable. Thus, structural modifications of aircraft structures were required either to extend the fatigue life or to repair damaged regions by reducing the stresses in potential areas of cracking [1].

Figure 1.3: Crack found in Qantas plane Boeing 737 [4].

A study conducted by Vogelesang and Schijve [2] showed that fuselage repairs on 71 Boeing 747 aircraft could extend the aircraft life with an average of 29,500 flying hours. The adequate performance of an aircraft required proper maintenance technique from the scheduled inspection to restore its structural integrity. The reliability of an aircraft relied upon the repair design quality, repair technique, as well as the workmanship applied in performing those repairs. Although there were numerous techniques to repair primary aircraft structures as illustrated in Figure 1.4, this thesis will only focus on adhesively bonded joint or repair mechanism.

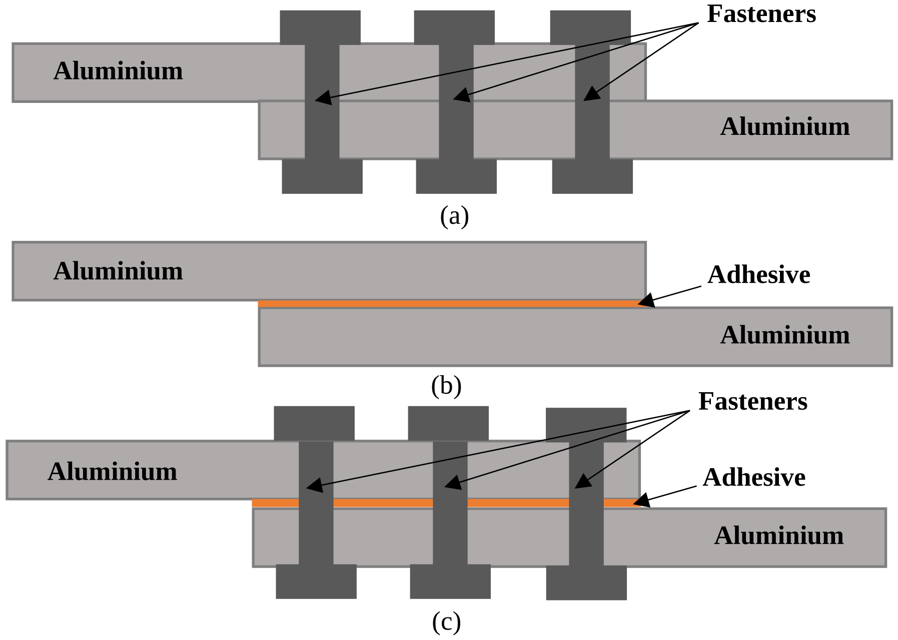

Figure 1.4: Repairing techniques a) mechanical fasteners b) adhesive bonding c) hybrid joints.

Bonded patches are one of the reliable solutions to extend the service life of aircraft structures [3]. Bonded patching provides many advantages over the conventional mechanical fastened patches including improvement in damaged tolerance and reduction of stress intensity factor [4]. In early 1970s, this bonded patch repair has been applied to RAAF fighter aircraft by the Australian Defence Science and Technology Group (DSTG). Later in 1997, bonded composite doubler patch has been installed to the first commercial aircraft, namely Delta Airlines L-1011. The right mid-section access door of the plane has been reinforced by this composite doubler. The typical applications of bonded composite doubler patch to commercial aircraft structures are shown in Figure 1.5. The bonded repair technique has been approved by the Federal Aviation Administration (FAA) to extend the service life of commercial aging aircraft [5].

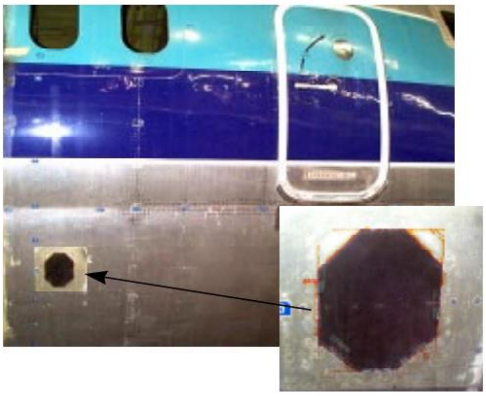

(a)

(b)

Figure 1.5: Bonded repair applications on commercial aircraft structures a) fuselage skin repair b) door corner repair [6].

1.2 Motivation

A brief history on the application of bonded joints or patch repairs for aircraft structures has been provided in Section 1.1. In general, a reinforcing patch is required to repair a significant structural damage either in metallic or composite airframe structures. Traditionally, mechanical fasteners were used to attach the reinforcing patch. However, the implementation of adhesive bonding to attach the reinforcing patch provides several advantages, namely:

- Enhance the repair efficiency;
- Minimise variation in surface contour;
- Prevent further damage in both parent structure and sub-structure;
- Provide smoother stress transition than mechanical fasteners due to large contact surfaces; and
- Lighter than other repairing technique, which resulted in less consumption of fuel.

Besides its advantages, the applications of adhesive bonding are limited to multiple load-path primary or to secondary structures [7]. Defence Science and

Technology Group (DSTG) has identified the key issues of bonded repairs application on primary aircraft structures which is to satisfy the certification requirements. Certification of bonded joints or patch repairs of primary aircraft structures requires demonstration of damage tolerance. Traditionally, a demonstration of damage "no-growth" criteria under a structural fatigue loading is required as per guidance from FAA AC20-107A (1984) [8], due to the lack of understanding about fatigue damage in bonded joints or patch repairs. In the most recent version of the guidance from FAA AC20-107B [9], a damage slow growth management strategy is considered acceptable, provided that the slow growth is predictable, and without reducing the strength of the bonded structures.

For the above requirements, "test" or "analysis supported by test" were required to identify the compliance. For a typically one-off repair, design by analysis methods that have been validated on generic, representative repairs, using material properties that have been approved by representative coupon and element tests for the repair materials and parent materials are highly desired [10]. This further motivates to develop a generic patch repair design to satisfy the certification requirements.

The main requirements of bonded repair certification for primary aircraft structure are listed as below [10]:

- The strength and durability of adhesive bond-line must be assured within the operating environment.
- The requirements of all structural performance must be fulfilled.

In early 2000s, Chalkley et al. [11] proposed an approach to facilitate airworthiness certification in relation to fatigue issues by means of generic patch repair joint called the Double Overlap Fatigue Specimen (DOFS) and the Skin Double Specimen (SDS). These two specimens have been successfully used to assess the behaviour of bonded joints under fatigue loading [10-20]. However, assessment of a long disbond up to ultimate failure of the joint was unachievable just based on testing these specimens. To implement the damage slow growth management strategy, disbond stable growth range and allowable fatigue life of a joint need to be determined. To achieve these, the entire process of disbond growth from disbond initiation up to the ultimate failure of the joint needs to be assessed. Therefore, development on generic patch repair design that can be used to assess disbond growth up to ultimate failure of adhesively bonded joints is required.

1.3 Research Aim and Objectives

The aim of this research is to implement adhesively bonded joints or patch repairs on primary aircraft structures. To achieve the overall aim of this research, the following objectives were identified as follow:

i. Design and development of defect or damage-tolerant for bonded joints and patch repairs in primary aircraft structures;
ii. Assess the suitability along with the support to damage growth management approach for standard taper geometries; and
iii. Satisfy the certification requirement of bonded joints or patch repairs on primary aircraft structures together with damage tolerance in the tapered region.

Several works were attempted to accomplish these objectives, such as:

- A detailed literature review on the certification requirements of bonded joints or patch repairs for primary aircraft structures. Other factors that contributed to the certification process such as damage assessment, repairing method, and damage tolerance regions were reviewed, and the research gaps identified.
- Development of generic patch repair specimen design represents both disbond tolerant zone and safe-life zone in bonded patch repair was established.

- Robust simulation methods to assess the disbond growth of bonded joints or patch repairs were established. The configured material model representing the FM300-2K adhesive was tested using the single element analysis.
- Parametric studies to investigate the influence of adherend thickness variations to adhesive bond strength and disbond growth rate were carried out.
- Experimental assessments (static and fatigue testing) of the designated bonded joints were carried out to calibrate and validate the finite element (FE) model and to measure the disbond growth rate.
- A modified Paris law to predict the fatigue life of the joints has been established by correlating the computational and measured results.
- A cohesive fatigue damage model was established to investigate the effect of initial disbond size on the disbond growth behaviour using 3D wide bonded metal joint specimen.

1.4 Thesis Outline

This thesis is documented in seven chapters including the Introduction Chapter. A brief overview of each chapter is defined as follow:

Chapter 2 Literature review

Initially, the classification of aircraft structures including the damage assessment and repair requirements are reviewed. Furthermore, the certification requirements and damage tolerance of repairs are discussed. Finally, the last part of the review focused on the numerical analysis and fatigue crack growth for adhesively bonded structures.

Chapter 3 Material Properties, Modelling Approach and Design of the DOTES Specimens

The material properties of the Aluminium and FM300-2K adhesive film used in this study are thoroughly described. The configured material properties in MSC Marc were assessed using the single element analysis. The specimen configurations and modelling approach used to assess the disbond growth in adhesive bonded joints or patch repairs were discussed.

Chapter 4 Numerical Assessment of Disbond Growth and Fatigue Life of The DOTES Specimens

Preliminary works focused on the simulation model to assess the disbond growth behaviour, predict the structure residual strength and fatigue life of the double overlap tapered end specimen (DOTES) were carried out in this chapter. The effect of joint stiffness imbalance was performed to support the experimental design. Also, the fatigue life prediction, slow growth approach and joint failure mode are discussed.

Chapter 5 Fatigue Disbond Growth Rate Correlation of the DOTES specimen

Experimental assessment to determine the residual strength of the joint as a function of disbond length was carried out by conducting static residual strength tests under room-temperature and hot-wet conditions. The process to establish the modified Paris law correlation was defined in this chapter by correlating the computational and measure results. As a result, the disbond length as a function of number of fatigue of cycles was predicted using the modified Paris law through an integration calculation. Finally, the fatigue life of the joint, that is, when the disbond length reached the critical value in which the residual strength was equivalent to the fatigue peak load was also determined.

Chapter 6 Onset and Propagation of Disbonds in 3D Wide Bonded Metal Joint Under Cyclic Loading using CZE Method

The effect of initial disbond size to disbond growth behaviour was investigated computationally through 3D wide bonded metal joint specimen in this chapter. Cohesive fatigue damage model was developed to determine the strain energy release rates (SERRs) as a function of disbond length and predict the disbond growth rate of the wide bonded metal joint specimen. The focus was to investigate the effect of local or partial width disbond (load shedding effect) to the behaviour of disbond growth.

Chapter 7 Conclusions and Future Work

The final chapter summarised the findings of this research and recommendations for future work is discussed.

1.5 List of Publications

Several publications were produced during this research, which are listed as follow:

1.5.1 Journal Publication

V. Tanulia, J. Wang, G. M. Pearce, A. Baker, M. David, and B. G. Prusty, "A Procedure to Assess Disbond Growth and Determine Fatigue Life of Bonded Joints and Patch Repairs for Primary Airframe Structures," *International Journal of Fatigue,* p. 105664, 2020.

V. Tanulia, J. Wang, G. M. Pearce, A. Baker, P. Chang, and B. G. Prusty, "Experimental and Computational Assessment of Disbond Growth and Fatigue Life of Bonded Joints and Patch Repairs for Primary Airframe Structures," *International Journal of Fatigue,* p. 106776, 2022.

V. Tanulia, J. Wang, G. M. Pearce, A. Baker, and B. G. Prusty, "Computational Assessment of Disbond Size Effect on Disbond Growth Behaviour in Adhesively Bonded Wide Joints/Patch Repairs of Aircraft Primary Structures," *Theoretical and Applied Fracture Mechanics*, 2022 (submitted).

1.5.2 Peer-Reviewed Conference Publications

V. Tanulia, J. Wang, G. M. Pearce, A. Baker, M. David, and B. G. Prusty, "Disbond Growth Assessment for Bonded Joints and Patch Repairs of Primary Airframe Structures," in International Conference on Composite Materials (ICCM-22), Melbourne, Australia, 2019.

V. Tanulia, J. Wang, G. M. Pearce, A. Baker, P. Chang, and B. G. Prusty, "Static Strength and Fatigue Life Prediction of Bonded Joints/Patch Repairs Used in Primary Aircraft Structures," in the 5th Australasian Conference on Computational Mechanics (ACCM 2021), Sydney, Australia, 2021.

1.5.3 Poster Presentation

V. Tanulia, J. Wang, G. M. Pearce, A. Baker, M. David, and B. G. Prusty, "Damage Tolerance of Bonded Patch Repairs for Primary Aircraft Structures," 4th UNSW Engineering Postgraduate Research Symposium, Sydney, 26-27 September 2018.

Chapter 2

Literature Review

A graphical abstract to describe the literature review of this investigated topic is illustrated in Figure 2.1.

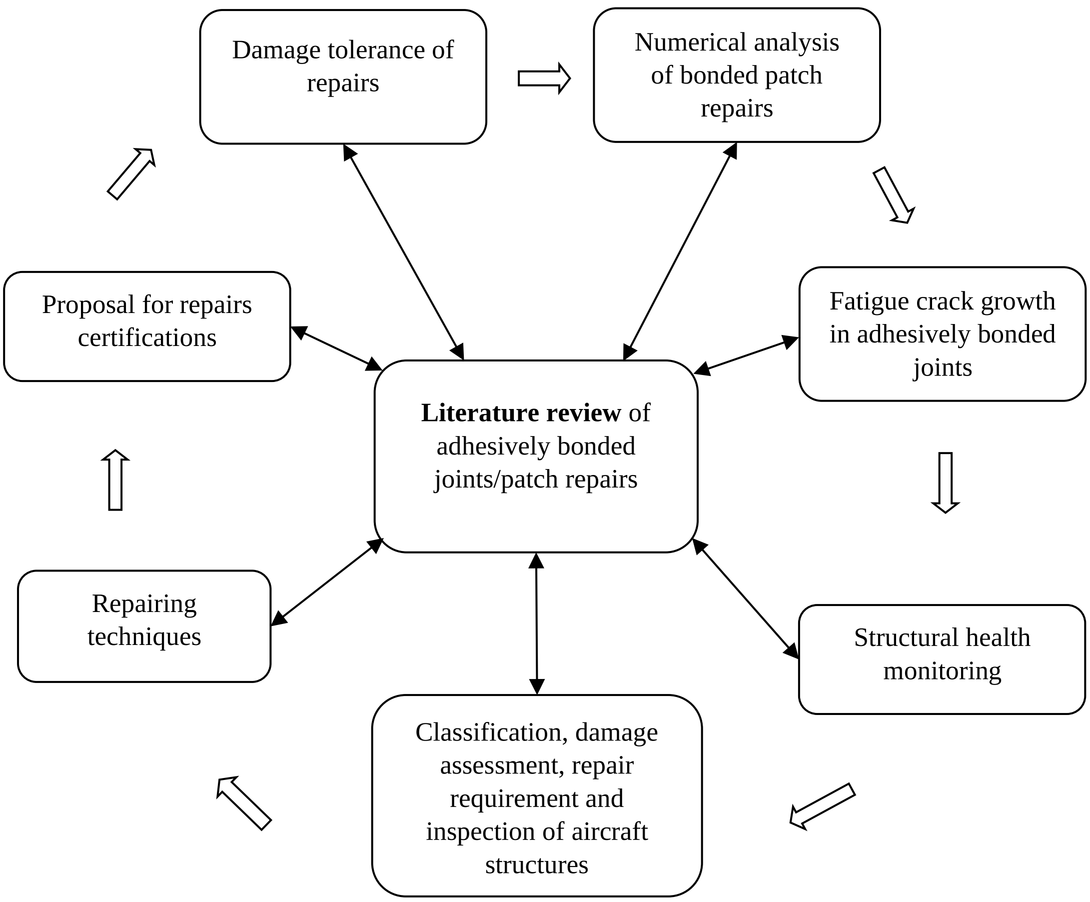

Figure 2.1: Graphical abstract.

2.1 Introduction

Adhesively bonded joints have been used in various engineering applications including aeronautical, automotive and space structures. It is considered as an easy technique to join the components together with the assurance of design requirements [21] as illustrated in Figure 2.2. Single or double-sided doubler patches [22-24] along with scarf or stepped patch repairs are mostly applied for bonded repair assessment of damage structure specifically for aerospace applications [25-28]. The primary purpose of repairing a structure is to restore both the stiffness and strength of the damage component [29].

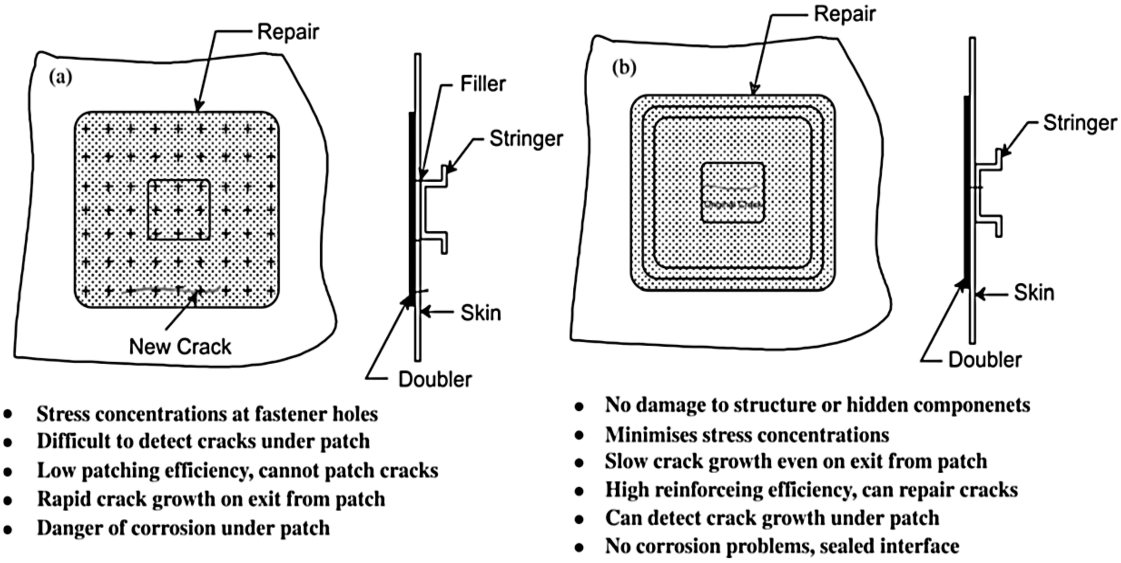

Figure 2.2: Comparison of standard mechanical fastened repair and adhesively bonded repair [30].

Defence Science and Technology Group (DSTG) has identified the key issues of bonded repairs application on primary aircraft structures which is to satisfy the certification requirements. The approaches to meet the key certification requirements are described as follows:

- Optimisation of damage removal to enhance the residual strength [31-33]

- Design improvement and quality assurance assessment of bonded repair.
- Ensure the initial and enduring integrity of the adhesive bond-line.
- Satisfy all structural performance requirements [10].

Therefore, a proper repair design including the defect and damage tolerance, and fatigue life assessment is required for certification of bonded repair. Accordingly, design and development of defect or damage tolerant for bonded repairs in primary aircraft structures together with the improvement of design and configuration of the overlap bonded patch repair are the aims of this study.

2.2 Classification, Damage Assessment, Repair Requirements and Inspection of Aircraft Structures

According to Baker [34], aircraft structures are divided into three categories for inspection and repair purposes, namely primary, secondary and tertiary structure. Primary aircraft structure can be defined as the critical part of an aircraft to ensure safe operation. These parts include wings, empennage and fuselage of an aircraft. It is relatively thick compared to other parts of the structure and generally highly loaded. The thickness of primary aircraft structures ranging from 3 mm to over 25 mm [10].

Secondary structure is defined as a structure that will not lead to a loss when it fails, but it would affect the aircraft operation. When failure of the structure would not significantly impact the aircraft operation, it was classified as tertiary structure [35].

The damage assessment, repair requirements, and inspection technique for all the classified structures mentioned above are significantly different. Details about the certification and design of aircraft structures are defined as follows:

i. **Static Strength**

There are two categories in determining deformation due to static loading called Design Limit Load (DLL) and Design Ultimate Load (DUL). DLL is when no failure or unacceptable deformations occurred and generally considered as the maximum load of the structure in its lifetime. On the other hand, DUL is when an acceptable permanent deformation acquired, but no failure existed. Generally, DUL is equal to 1.5 times DLL [36].

ii. Fatigue Strength

There are three requirements used in designing aircraft structures, namely safe life approach, fail-safe approach, and slow crack growth approach.

- Safe-Life Approach

Safe-life approach is categorised in the situation where cracking does not appear in the airframe life. This approach mostly used in designing older fighter aircraft and United States Navy fighter aircraft such as F-18 and helicopters.

- Fail-Safe Approach
  - Alternate Load Path: in this approach, the structure is in damage tolerance where cracking is possible to appear; however, it will not weaken the structural strength less than the acceptable level. This condition is generally satisfied by multi-load path design where the remaining load paths are still able to provide the requisite residual strength level when one of the load paths is failed. This approach mostly used in large transport aircraft structure.
  - Slow Crack Growth Approach: in this procedure, the damage tolerance condition is similar to the alternate load path, but cracks will propagate slowly and not lead to failure. This approach is suitable to apply for a

structure with a single load path where the failure condition is catastrophic. Additionally, this approach is adopted for USAF fighter aircraft.

iii. **Damage tolerance general requirement:**

The structural strength should not drop below 1.2 x DLL when the structure representative damage such as fatigue cracking, corrosion, and accidental mechanical contact appeared. The size of critical damage must be able to be detected by a high degree of probability.

iv. **Durability and financial requirement:**

For the airframe life, costly repairs for damage due to fatigue or corrosion will not occur [30].

2.3 Repairing Techniques

There are three common techniques of combining composite laminates namely mechanical fastening, adhesively bonded and the combination of these two joints which is called the hybrid joint [37]. Details of these repairing technique are defined in the following sections.

2.3.1 Mechanical Fastener

Mechanical repair is also known as a traditional repair. The patch material is attached to the parent structure through bolts, pins or rivets after removing the cracked region. The purpose of this repairing method is to restore the mechanical properties (residual strength, damage tolerance, fatigue resistance, and stiffness) to an acceptable level [38]. When subjected to tensile loading, this repairing method commonly failed in one or more of the three modes namely tension, shear-out and bearing failures [39]. Moreover, this repairing method creates a stress concentration issue that resulted from drilling the additional fastener hole [40]. During the fabrication process, the local damages are generated into the composite laminate due to the implementation of mechanical fastener. Consequently, strength degradation occurred in the structures. Moreover, the mechanical fastener itself causes an increase in structural weight [41]. The potential failure modes of mechanical fastener joints are illustrated in Figure 2.3.

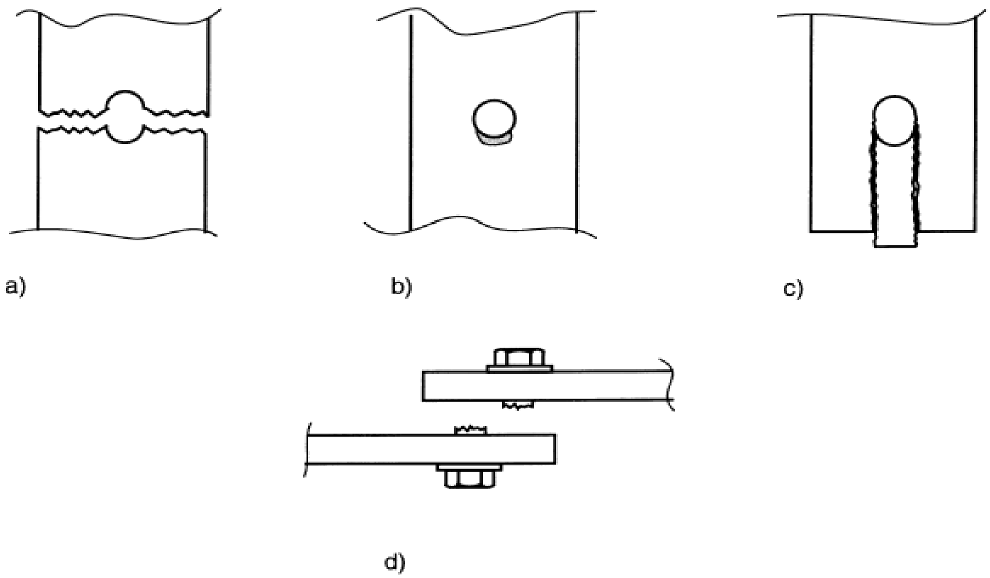

Figure 2.3: Failure modes in bolted repair applications to aircraft structures a) net section failure b) bearing failure c) shear out failure and d) fastener failure [42].

2.3.2 Adhesive Bonding

Adhesive bonding is widely used to manufacture aircraft components. However, its application to single load-path airframe structure is costly to certify as extensive validation testing is required. Consequently most applications of bonded joints are limited to multiple load-path primary or to secondary structures [43]. More recently, adhesive bonding has been used to modify aircraft structures either to extend the fatigue life by reducing the stresses in potential areas of cracking or to repair fatigue-cracks by stress reduction and crack bridging. Because of the high reinforcing efficiency of bonded repairs [43], residual cracks may be left in situ in many cases.

Nowadays, bonded repair technology is commonly accepted as the alternative method of mechanically fastened repairs for primary, secondary and tertiary aircraft structures [44]. This method intends to reinstate the load path removed by the impact damage or fatigue cracking [45]. Moreover, bonded joints perform better in disseminating the load that causes the elimination of high-stress concentration issues occurred in bolted joints. Consequently, this joint technique is more effective in structural cases than mechanically fastened joints [37].

The use of adhesive patch bonding in repairing significant structural damage can assist for increment in reinforcing efficiency, minimising the transition in surface contour, and avoiding further damage penetration of the main structure and substructure. Metal or composite materials can be used for the patch material of bonded repairs application. Composite patch material offers many advantages compared to metal such as the ability to match the stiffness, strength and thermal expansion coefficient of the parent structure, and capability to fit into complex shapes [10]. The joining method and adhesive properties influence the efficiency and structural property of adhesively bonded composite structures [46].

In general, adhesively bonded joints provide numerous advantages over the mechanically fastened joints which listed as follow [47]:

1. Large bond area for load transfer
2. Smooth external surfaces at the joint
3. Low-Stress Concentration
4. Less sensitivity to cyclic loading compared to mechanical fastened joint
5. High Strength to weight ratio
6. Crack retardation

7. Electrical and thermal insulation
8. Time and cost saving

However, the application of this technique requires stringent cleaning and processing steps to produce very efficient joints which can share the load over a large area [30]. Also, ensuring the quality of bonds is a challenging task due to difficulty in confirming joint integrity by inspection [47]. The primary issue of the adhesively bonded joint is the structures must be destroyed when disassembling the bonded joint [41]. Also, the analysis and design of this joint are complicated because of the non-linear properties of the structure [48]. There are several types of adhesively bonded joints namely stepped, single, double lap joints and scarf joints as demonstrated in Figure 2.4 [49].

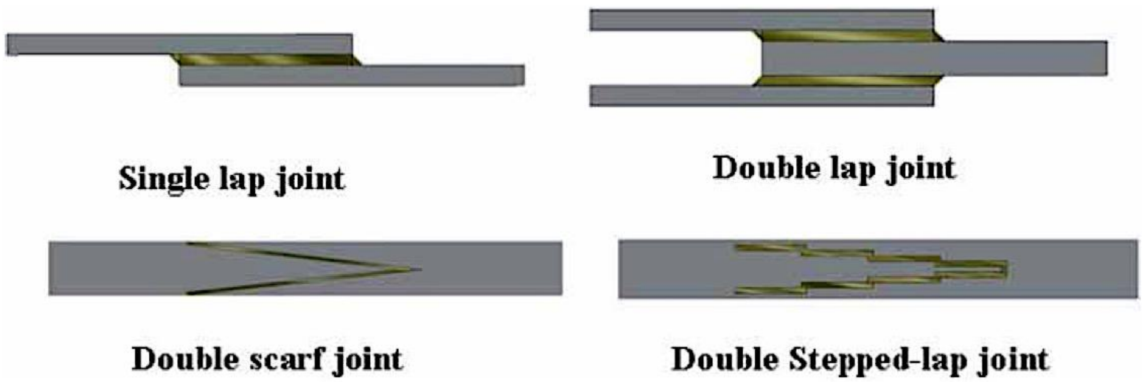

Figure 2.4: Type of adhesively bonded joints [50].

Adhesively bonded joints have been widely used to repair cracks in aircraft structures. A repair design tool has been developed by Ricio et al. [51] to obtain the optimal repair geometry that can minimise the adhesive shear stress and the overlap length. This tool is applicable for several joint configurations including single lap, double lap and multi-stepped joints. Recently, Riccio et al. [52] performed a numerical investigation of several bonded joints configuration through the simulation of elastic-plastic and failure behaviour of ductile adhesive material. Experimental work has been performed by Okafor et al. [53] to verify the durability of cracked aluminium panel repaired with single sided composite patch. They reported that the single sided composite patch effectively increases the load carrying capacity by 42%.

2.3.3 Hybrid Joints

A hybrid joint is the combination of adhesive bonding and mechanical fastening. This repairing method has been adopted to avoid catastrophic failure in the adhesive layer [54]. Wang et al. [55] mentioned that the adhesive bond in hybrid joints was beneficial to improve the fatigue and static strength resistance. Consequently, the stress concentrations in the fastener holes region are much lower than in mechanically fastened joint. This situation arises because of the existence of adhesive layer that causes the load is distributed evenly in the bond region. Moreover, the fasteners in the hybrid joint are useful to carry the remaining load [37]. A number of researchers [41, 56-62] have investigated that initial failure of hybrid joints is mostly caused by debonding.

Hart-Smith [58] performed a non-linear analysis of bolted and bonded joints to identify the strength of hybrid joint arrangements. The results indicated that hybrid joint methods did not provide any significant benefit when compared to well-design adhesive bonding. On the other hand, Hart-Smith [58] mentioned hybrid joint configurations were beneficial to prevent defect or damage propagation. The illustration of hybrid joint arrangements is depicted in Figure 2.5. The yellow line represents the adhesive layer in the hybrid stepped lap joint configuration [55].

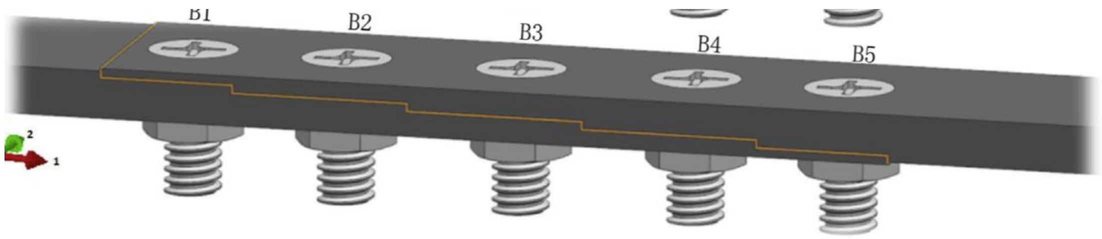

Figure 2.5: Hybrid Joint with bolt as the mechanical fastener and adhesive layer indicated by the yellow line [55].

2.4 Proposal for Repairs Certification

Airworthiness certification is the primary concern of repairing the critical damage of primary structure, particularly in highly loaded condition [12]. Certification of bonded joints or patch repairs of primary aircraft structures requires demonstration of damage tolerance. Traditionally, a demonstration of damage no-growth under structural fatigue loading is required. If disbond growth is detected in the critical region of a joint, even if it is in a small, localised region, an aircraft would be grounded for repair or component replacement. In recent years, in order to reduce maintenance cost, a damage slow growth management strategy has been considered acceptable by Federal Aviation Administration, provided the slow growth is predictable, and without reducing the strength of the bonded structures below a required safety margin prior to scheduled inspection [9].

A minor modification of the load path or stress elevation in the damaged region does not affect much the certification base. It may be caused by the presence of an original crack in the case of repairs to the metallic structure. Therefore, testing at the representative joint level is required to achieve the design strength and fatigue durability allowable. It can be done by investigating the representative joint design allowable that is valid to the specific local repair region in the range of environmental situations and similar geometries [36].

There are two types of generic bonded joints used for the validation process of bonded patch repair certification which is known as the double overlap-joint fatigue specimen (DOFS) and the skin doubler specimen (SDS). These two types of joint are selected to demonstrate the bonded repair area with various damage-tolerance conditions. Chalkley et al. [11] mentioned that these two generic joints are appropriate for illustrating the necessary materials allowable on the fatigue resistance of a bonded patch system. More details about the DOFS and SDS are described in detail in section 2.5.2 and 2.5.3 respectively.

2.5 Damage Tolerance of Repairs

In general, damage tolerance can be defined as the capability of a structure to sustain from the representative weakening defects that occur inside the structure under typical loading conditions [63]. The damage tolerant conditions in primary aircraft structures are becoming very significant because of the aircraft requirements for longer design life and longer inspection intervals [64]. The primary target of damage tolerance is the effect of damage that leads to failure in the patch material or patch disbonding from the parent structure. The representative joint specimens described in section 2.5.2 and 2.5.3 could be used to determine the knockdown factors resulted from the presence of disbonds [36]. Furthermore, knockdown factors can be defined as applied elements to permit the corrupting influences such as voids, spectrum loading and undercure [11]. Moreover, significantly larger representative specimens are required for more realistic evaluations of impact damage [36].

2.5.1 Damage-Tolerance Regions in a Bonded Repair

The schematic of a bonded patch repair in a cracked plate is illustrated in Figure 2.6. An area where disbond between the adherend and patch can be tolerated is called disbond-tolerant zone. In this region, the disbond slightly reduce the repair effectiveness that resulted in slow and stable of disbond growth under repeated loading.

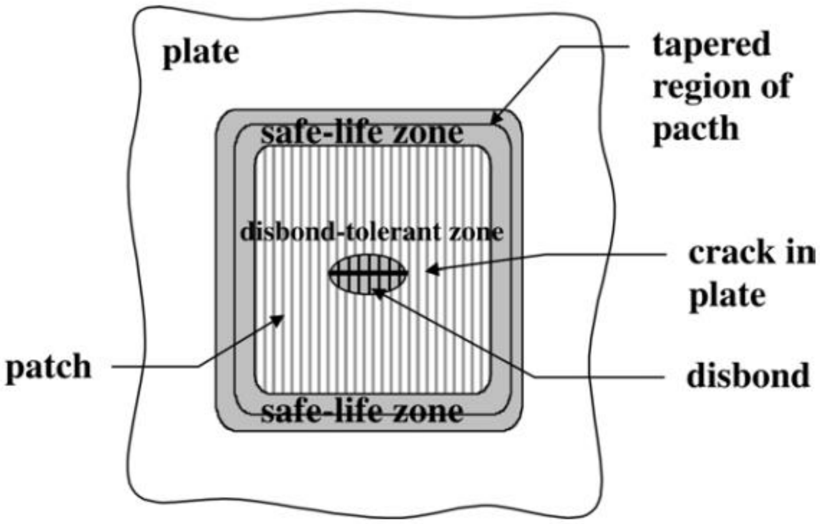

Figure 2.6: Schematic of Bonded Patch Repair representing the damage tolerant and safe-life zone [11].

Another region where disbond cannot be tolerated is called safe-life zone. The patch ends are generally stepped and thinning down to the certain thickness [12]. A greater driving force of disbond growth will occur in this region where shear and peel are the damaging strains in the adhesive system [22].

Therefore, DOFS and SDS specimens are proposed to represent the disbond tolerant zone and safe life zone. The DOFS represents the disbond tolerant zone in the situation where the patch spans the crack. On the other hand, the SDS demonstrates safe life zone at the patch termination [12].

2.5.2 Double Overlap Fatigue Specimen (DOFS)

The DOFS demonstrates the disbond tolerant zone in a bonded patch system of a cracked plate [12]. Some information is required to identify the static and fatigue joints strain allowable along with confirming the accuracy of the failure criteria based on the coupon test data. It can be obtained from two approaches that are listed in Table 2.1. Moreover, identifying the knockdown factors also required for various situations such as hot/wet conditions, non-optimum manufacture, typical damage, and more representative loading conditions [36].

Table 2.1: The scheme of generic specimen joint to achieve system allowable [36].

Approach	Aims
Attempt the static strength tests	Check the strength against prediction based on the coupon data.
Attempt fatigue tests	• Obtain the B-basis threshold for the fatigue disbond growth. • Use constant amplitude and spectrum loading rate for the disbond growth.

The geometry of the DOFS specimen is illustrated in Figure 2.7. Based on this specimen design, Baker [36] stated that high shear stress is expected to occur at the middle area of the joint that represents the fatigue crack region whereas the peel stress is supposed to be negative at the middle of the joint that indicates peel damages will not arise in this region.

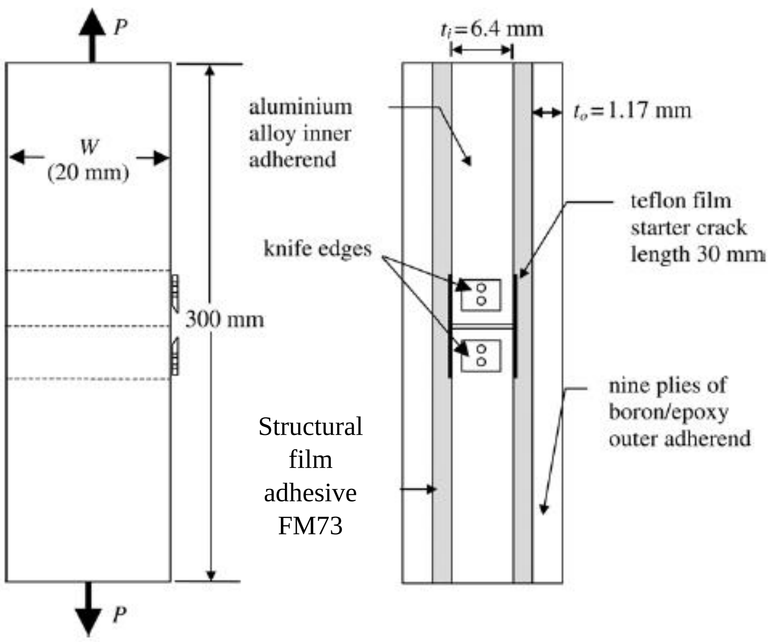

Figure 2.7: Schematic geometry of the DOFS [11].

Chalkley and Baker [12, 13] conducted fatigue tests of the DOFS and demonstrated that the adhesive shear strain range was a promising fatigue damage parameter. In accordance, Baker [14] proposed the allowable adhesive shear strain range for acceptable damage growth. Madelpech et al. [15] reported good correlation between the disbond damage growth rate and disbond crack energy release rate from their fatigue test results with DOFS specimens made of aluminium central adherend and Carbon Fibre Reinforced Polymer (CFRP) doublers. They also conducted generic specimen testing and tried to use the correlation established from the DOFS tests to predict disbond growth behaviour in the generic specimens. The prediction accuracy was poor; however, the authors stated that it was due to inaccurate assumption of disbond growth pattern and some experimental errors. Thus, the poor prediction accuracy did not necessarily cast doubts on their general procedure.

There are some critical points to transfer the disbond growth rate data from the DOFS to the generic structural design specimen which are specified as follow:

- Using the driving force of disbond growth under fatigue loading condition to validate the adhesive shear strain range
- The analytical prediction and measurement of the adhesive shear strain in the DOFS are demonstrated in good correlation.
- Validation of the DOFS is performed through FE analysis based on the analytical estimation of the adhesive shear strain obtained from the generic structural specimen design [36].

According to Chalkley et al. [11], the strain range criterion of the DOFS is convenient to use for designing the patch system; however, further validation is required. The issue related to the damage parameter of the actual interface failure mode in composites is required to be figure out. Furthermore, the effects of environment and temperature on disbond growth rate needs to be considered as failure modes in the adhesive tend to change to cohesive at elevated temperatures especially in hot/wet conditions.

2.5.3 Skin Doubler Specimen (SDS)

The Skin Doubler Specimen describes the ends of the repair patch system as depicted in Figure 2.8 [11]. It consists of inner and outer adherends which are bonded with epoxy adhesive film [65]. Matta et al. [66] mentioned that this specimen is also able to perform as a case representative where restoration is needed to improve the strength and stiffness of the flange at the flexural section. Furthermore, the configuration of this specimen can represent the disbond initiation data; hence, it does not require Teflon film as the starter crack length [11].

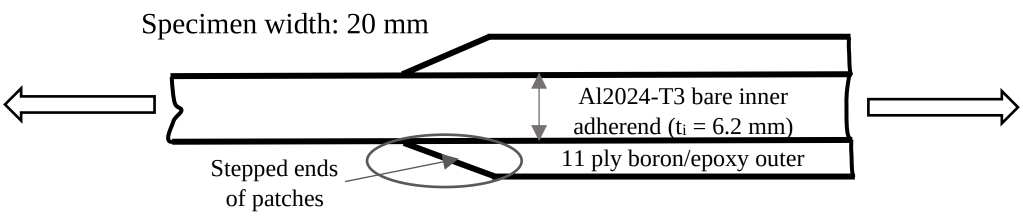

Figure 2.8: The Skin Doubler Specimen (SDS) [10, 11].

As mentioned earlier, the SDS is tested to analyse the safe-life zone of a bonded patch repair. Hence, the emphasis of this test is to acquire disbond initiation data. This disbond initiation can be identified using strain gauges. When one of the strain gauges amplitude was dropped by 10%, the disbond initiation was indicated [11]. Regarding the shear and peel stresses expectation, Baker [36] mentioned that the SDS had different behaviour with the DOFS. When subjected to tensile loading, the main differentiation between these two joints is that the adhesive peel stress at the ends of SDS is positive, whilst for the DOFS is negative.

The fatigue tests with SDS specimens conducted by Chalkley et al. [11] showed that the disbond crack growth could be detected by measuring the reduction of strains at the patch edge measured using a strain gauge. They stated that insufficient work had been performed to establish any suitable Fatigue Damage Criteria (FDC). Several problems including fundamental and contradictory related to negative peel stress and residual stresses are required to be resolved. Consequently, Chalkley et al. [11] suggested that further testing on all metal specimens are needed to differentiate the residual stress problem. Therefore, design improvement of the SDS is essential to overcome the fundamental and contradictory obstacles.

With the SDS specimens, Wang et al. [16] measured disbond crack growth rates under fatigue loadings and assessed the effect of optimum outer adherend end taper geometry on fatigue resistance. The authors reported that the predicted crack initiation loads, based on the threshold value of mode I strain energy release rate (SERR) calculated by means of the Virtual Crack Close Technique (VCCT), correlate well with the experimental results. Cheuk et al. [17] assessed disbond growth behaviour of single and multi, symmetrical and unsymmetrical disbond cracks under fatigue loadings. Pascoe et al. [18] used a specimen similar to a SDS specimen but with the double ends to assess the behaviour of disbonds at both ends (Figure 2.9). They also used an asymmetric specimen with only single lap. They predicted disbond growth due to constant amplitude fatigue loading by correlating the disbond growth rate with SERR calculated using VCCT. The best correlation between the SERR and the growth rate was found when using the mode II component of the SERR.

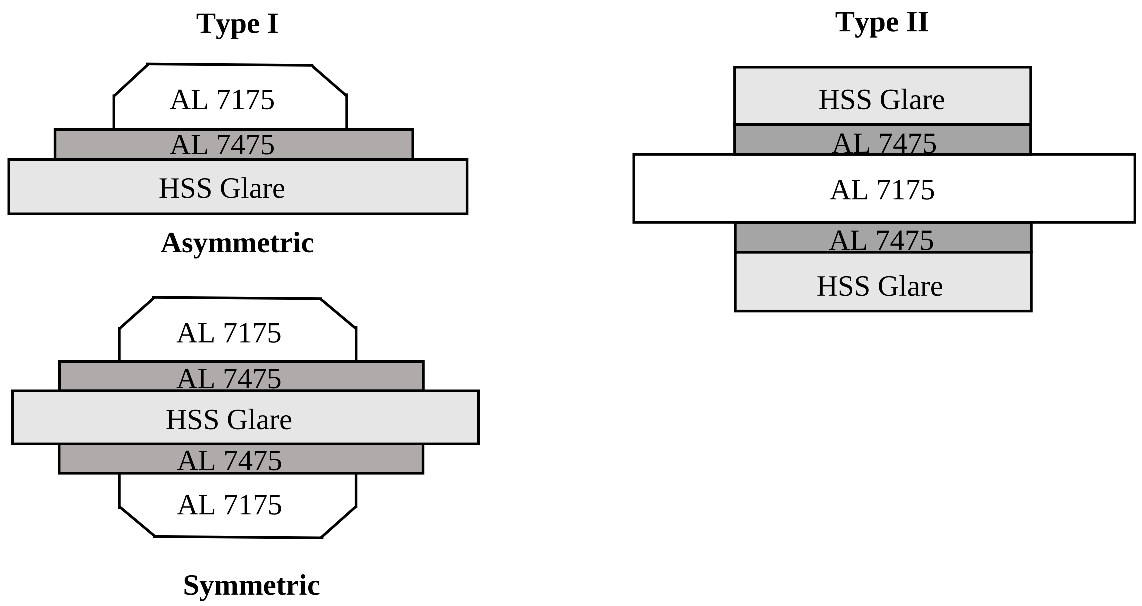

Figure 2.9: Schematic diagram of the configuration of the test coupons used by Pascoe et al. [18].

2.6 Structural Health Monitoring

Structural Health Monitoring (SHM) is one of the possible approaches to detect any load transfer reduction in the patch system. It is also possible to recognise the damage propagation in the parent structure. Furthermore, SHM can monitor the patch integrity autonomously and on a continuous basis [67]. The primary goal of the SHM system is to monitor the high-stress zones in the patch where failure is expected to result in total patch failure or massive reduction in patching efficiency. Strain transfer is one of the patches disbonding options to measure the patch efficiency and integrity at the tapered ends of a patch system. It requires a fatigue durable strain gauges that embedded into the parent structure [10]. Consequently, strain gauges are the most common strain measuring options used in SHM systems as it offers several advantages such as easy to install, cost-effective and good sensitivity of detection [68]. It indicates disbonding of the patch through the reduction in strain transfer [30]. The application of strain gauges to detect patch disbanding is demonstrated in Figure 2.10.

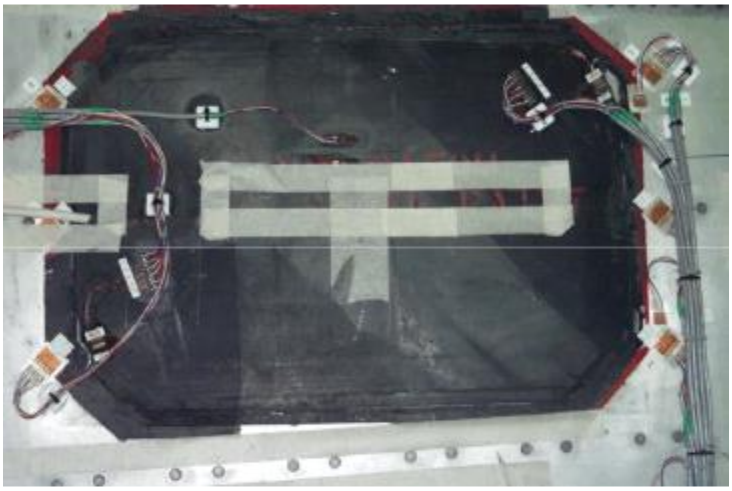

Figure 2.10: Application of strain gauge for SHM during fatigue test of bonded patch repair to F-111 wing [67].

2.7 Numerical Analysis of Bonded Patch Repairs

Number researchers have been analysed the disbond growth of bonded patch repairs using Finite Element Analysis (FEA) technique [11, 12, 69-71]. Chalkley and Baker [12] performed a three-dimensional FEA to investigate the adhesive shear strain results. The FEA results for adhesive elasticity case indicated a good agreement with the analytical results. However, for the adhesive plasticity case, the results showed that the adhesive shear strain values obtained from the FEA under-estimate the theoretical value. Hence, further research on modelling the adhesive material properties in FEA is required to be executed.

Previous work on modelling of structural adhesives has been done by several researchers [72-77]. There are several approaches to model the structural adhesives, namely: tied nodes, continuum damage modelling, linear elastic fracture mechanics (LEFM) and cohesive zone modelling (CZM). Details of these approaches are defined in the section below.

2.7.1 Tied Nodes

In the tied node's model, the nodes on the adherends are bond together, and failure is predicted using a stress-based criterion [72, 78, 79]. Van Hoof [80] employed the model of the tied node to illustrate the adhesive joints for delamination analysis in composite materials. Trimino and Cronin [81] affirmed that the tied nodes method was useful to identify the general behaviour of joints under specified loading conditions. However, there is some constrained in the case of prediction capabilities as this model only require limited information (i.e., stresses to failure). Moreover, it requires very refined meshes for the element formulations that lead to computationally expensive and the calculation times can be impractical and prohibitive [82].

2.7.2 Continuum Damage Modelling (CDM)

CDM approach has been used to identify the stress gradient in a joint and possible to assist design engineer to characterise the adhesive performance in the specific joint configuration [77, 83]. However, CDM leads to the increment in solution time for a particular model due to the requirement of multiple elements through the adhesive thickness. Consequently, this approach is rarely implemented for large structures due to high computational cost. Also, a constitutive model is needed to define the material response. This material sensitivity response such as damage, deformation rate and mode of loading will be used to determine the use of a material model. Hence, determination of the material classes such as elastic, viscoelastic, metal plasticity, viscoplastic and polymer specific models are required as the aforementioned [81].

2.7.3 Linear Elastic Fracture Mechanics (LEFM)

Linear elastic fracture mechanics (LEFM) have been widely used to simulate the fatigue crack growth behaviour [84]. The crack will propagate when the strain energy release rate (SERR) at the crack tip is equal to its critical value [85]. The virtual crack closure technique (VCCT) is an effective method in LEFM to determine the SERR and compute the crack growth by utilising the moving mesh technique. Further to its application, a slight crack extension does not significantly modify the state of the crack tip, and thus the separation can be estimated from the displacements of the nodes behind the crack tip [86]. The VCCT was initially proposed by Rybicki and Kanninen [87] for 2D four node elements based on the Irwin's crack closure integral, and later an eight-noded and quarter-point element was developed by Raju [88].

Jokinen et al. [89] used the VCCT method to analyse the crack growth of adhesively bonded joints. The analyses were performed using double cantilever beam (DCB) specimen bonded with epoxy adhesive. The authors concluded that linear VCCT analysis is a suitable technique to analyse crack growth in a yielding adhesive particularly when the crack growth is self-similar. Senthil et al. [90] performed a comprehensive numerical study on the debond growth initiation of adhesively bonded composite joints subjected to uni-axial compressive loading. The authors used the VCCT with mixed-mode failure criteria to investigate the effect of laminate sequence and debond's location, shapes (square and circular) and sizes.

Quaresimin and Ricotta [91] developed a model based on the sequence of the crack initiation and propagation phase to predict the fatigue life of bonded joints. The life span of debond propagation in composite single lap joints (SLJ) was predicted using integration of a Paris-like power law which relates the SERR to the crack growth rate. The results have shown good agreement with the experimental fatigue data. Pirondi et al. developed a VCCT fatigue model in Abaqus FE code based on the direct cyclic procedure. The model was implemented to the DCB, ENF, and SLJ specimens. The authors compared the VCCT fatigue model with the cohesive zone modelling (CZM) fatigue model. They concluded that generally the two models are in a good agreement with each other. Moreover, they reported that CZM is easier to implement although requiring more modelling effort.

Based on the literature, the VCCT method is considered as an efficient method to model debond growth in bonded joints subjected to both static and fatigue loadings. Although it has its own pros and cons, its application on FE method is continually improving.

2.7.4 Cohesive Zone Modelling (CZM)

In the last decade, CZM has been widely used for strength prediction of the adhesive joints. In FE analyses, CZM allows damage growth simulation inside the interfaces between different materials or bulk regions of continuous materials [74, 92]. Shape variations in the feature of CZM can be integrated into the cohesive laws which allow for a more accurate strength prediction. According to the results obtained by Campilho et al. [93], bonded joints with ductile adhesives are profoundly affected by the shape of CZM. Numerous researchers [92, 94, 95] mentioned that trapezoidal shape provides the best correlation to the experimental data.

Although CZM is insufficient for determining the non-toughened epoxy response, it is computationally effective and can reproduce the rate effects [81]. Also, cohesive elements are useful to precisely determine the response of joint load and identify the crack growth of bonded joints in Mode I loading condition [96-98] and Mixed Mode loading conditions [99]. Campilho et al. [24] used zero thickness cohesive elements to evaluate the stress distribution and residual strength of single and double lap of carbon epoxy composite joints loaded under tensile loading. Fernández-Cañadas et al. [100]

investigated the effect of the cohesive law shape and its parameters on the performance of adhesively single lap CFRP joint under tensile loading. The analysis was conducted in a 3D numerical model using cohesive elements. The authors reported that the difference between linear, exponential, and trapezoidal cohesive laws was below ±7%.

Ridha et al. [101] investigated the residual strength, ultimate failure and damage progression of a bonded composite scarf repairs using cohesive zone method (CZM) with various cohesive law shapes. They concluded that the exponential cohesive law was insensitive to the input parameters of cohesive elements, whilst the bi-linear and trapezoidal cohesive laws were sensitive to the input parameters of cohesive elements. Recently, Bayaramoglu et al. [102] conducted experimental tests of single step lap joint (SSL) and compared the results with the FE analysis using CZM as the material model. They reported that a good correlation was observed between the experimental results and FE analysis.

In the past decade, Cohesive Zone Model (CZM) has been widely accepted as a simulation tool for predicting the onset and propagation of debonding in bonded joints subjected fatigue loading [103]. Linking the damage variable (d) with the crack growth rate (da/dN) is the primary challenge in developing a cohesive fatigue model [104]. Turon et al. [105] proposed a function to link the damage variable with crack propagation rate. The fatigue model is developed based on the results generated from the loading history that is quasi-static overload and cyclic loads. The correlation is defined as follows:

$$\frac{\mathrm{d}d}{\mathrm{d}N} = \frac{1}{l_{pz}} \frac{(\Delta_f(1-d)+\Delta_c d\,)^2}{\Delta_f \Delta_c} \frac{\mathrm{d}a}{\mathrm{d}N} \tag{2.1}$$

Where dd/dN is the rate of change of the damage variable, l_{pz} is the length of process zone, d is damage variable, da/dN is the rate of crack propagation described in Paris law, Δ_c and Δ_f are the critical and maximum displacement jump in cohesive law, respectively.

However, the l_{pz} was calculated based on the analytical expression which is then implemented to constitutive model as a material property. This l_{pz} would be subjected to change with different adherend thicknesses and mix modes.

Moroni and Pirondi [106] developed a model based on Turon et al. [105] to predict fatigue crack propagation in 2D geometries. They translated the crack growth rate into the variation of damage distribution. The SERR was calculated based on a contour integral covering a path around the cohesive zone. Later, Moroni et al. [107] extended the model into 3D planar cracks. The authors used double cantilever beam (DCB), end loaded split (ELS) and mixed mode end loaded split (MMELS) to verify the accuracy of the model. The estimated SERR was compared with that determined using the VCCT method and good agreement was achieved.

Recently, Davila [108] developed a cohesive fatigue model based on the S-N diagram to predict the propagation rates of delamination in composites. The capability of the developed fatigue model was assessed by comparing the predicted crack propagation rates in DCB and mixed-mode bending (MMB) specimens with experimental data. The specimens were manufactured from IM7/8552 graphite/epoxy material. The author concluded that the proposed cohesive fatigue model is capable to predict the crack propagation rate.

Compared to tied nodes model, cohesive elements permit the ductile adhesive material to fail progressively [81]. Needleman [109] identified the limitations in cohesive formulations including material parameters dependency on deformation rate and the size effect. Accordingly, mechanical properties describing the adhesive material response is essential for analysis using numerical methods [81]. Therefore, selection of material models is critical which defined in the following section.

2.8 Material Models for the Adhesive

For integration into the design process, the ability to model the adhesive joints are very crucial. The small thickness of the adhesive layer is the first challenge in modelling the adhesive joints which resulted in relatively small elements. Another problem is the detail level in the material model that defines the mechanical properties which measured as the inputs to the model. Therefore, selection on the adhesive material models is very critical to improve the accuracy of design calculations as it determines the deformation behaviour of the adhesive material. Details of literature reviews on material models for the adhesive are described in the section below.

2.8.1 Deformation Behaviour of Toughened Adhesive

There are two types of deformation behaviours of toughened adhesive, one is called linear elastic behaviour, and the other is non-linear behaviour. Initial yield stress (σ_y) indicates the situation where plastic deformation in the elastic-plastic model is started. A region in non-linear behaviour where the deformation leads to a plateau in stress is called strain hardening. Moreover, an area where the minuscule change in stress with the increment in strain prior to failure is called flow region. Details of the elastic-plastic models are illustrated through the measurement of stress/strain curve loaded under uniaxial tension as depicted in Figure 2.11.

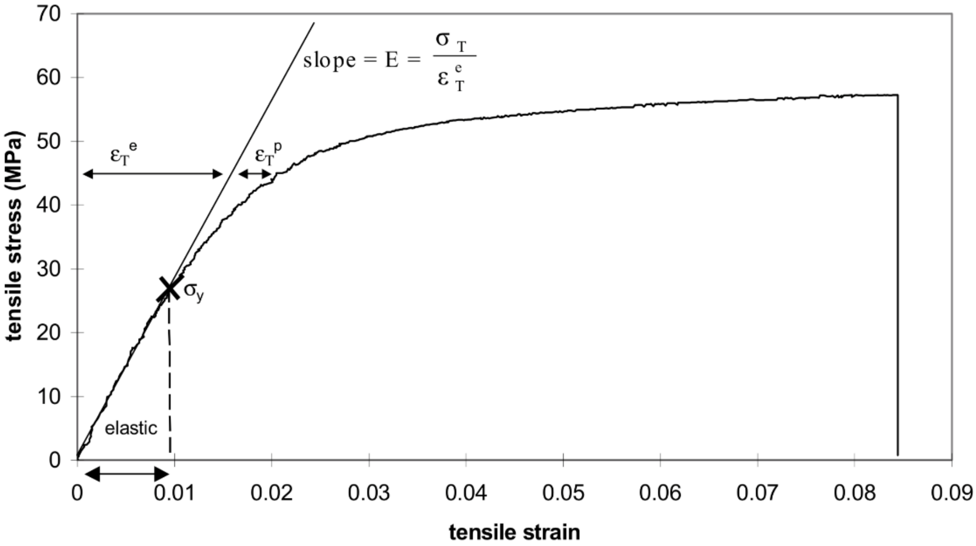

Figure 2.11: Tensile stress/strain curve of toughened epoxy adhesive [110].

2.8.2 Elastic Behaviour

The elastic behaviour is defined through stress and strain positions up to the initial yield stress. Dean and Crocker [110] affirmed that adhesives are linear viscoelastic materials where the properties are depending on the timescale measurements. However, the changes in timescale are relatively small in most of the experiment for glassy adhesives (temperature below the glass to rubber transition temperature) [111]. Hence, the effect of viscoelasticity can be ignored.

2.8.3 Non-Linear Behaviour

The relationships between stress and strain above the linear behaviour limit are non-linear. In FE packages, the material non-linearity in rigid materials typically considered as elastic-plastic models. Hence, stress analysis calculations in plastic deformation region generally involve the use of a flow law and multiaxial yield criteria. Accordingly, the Von Mises yield criterion and the Drucker-Prager yield criterion are utilised to define the yield criteria of adhesives [112]. Raghava et al. [113] developed an adhesive yield criterion that has been used by several researchers [114-118] to define the yield criterion in the deformation region. The two critical equations of the general stress state are:

$$J_1 = (\sigma_x + \sigma_y + \sigma_z) \tag{2.2}$$

$$J_2' = \frac{(\sigma_x - \frac{J_1}{3})^2 + (\sigma_y - \frac{J_1}{3})^2 + (\sigma_z - \frac{J_1}{3})^2}{2} + \tau_{xy}^2 + \tau_{xz}^2 + \tau_{yz}^2 \tag{2.3}$$

Where J_1 is the first stress invariant which measures the hydrostatic level and J_2 is the second stress invariant that measures the deviatoric stress level difference. The complete equation of Raghava et al. adhesive yield criterion is:

$$\sigma_y = \frac{J_1(S-1) + \sqrt{J_1^2(S-1)^2 + 12J_2S}}{2S} \tag{2.4}$$

Whereas the Von Mises Criterion is:

$$\sigma_y = \sqrt{3J_2} \tag{2.5}$$

The Drucker-Prager criterion is the alternative of adhesive yield criterion. Many researchers [115], [119], [120] used this criterion as it considers a higher level of hydrostatic stress. The complete equation of the Drucker-Prager criterion is:

$$\sigma_y = \frac{J_1(S-1) + [(S+1)\sqrt{3J_2}]}{2S} \tag{2.6}$$

Where S = $\frac{Compressive\ yield\ stress}{Tensile\ yield\ stress} = \frac{Y_c}{Y_t}$ and σ_y is the yield strength in the specific loading direction. Figure 2.12 demonstrates the Rhagava et al. adhesive yield criterion and Von Mises yield criterion whereas Figure 2.13 illustrates the yield envelopes comparison of the Drucker-Prager yield criterion and Von Mises yield criterion.

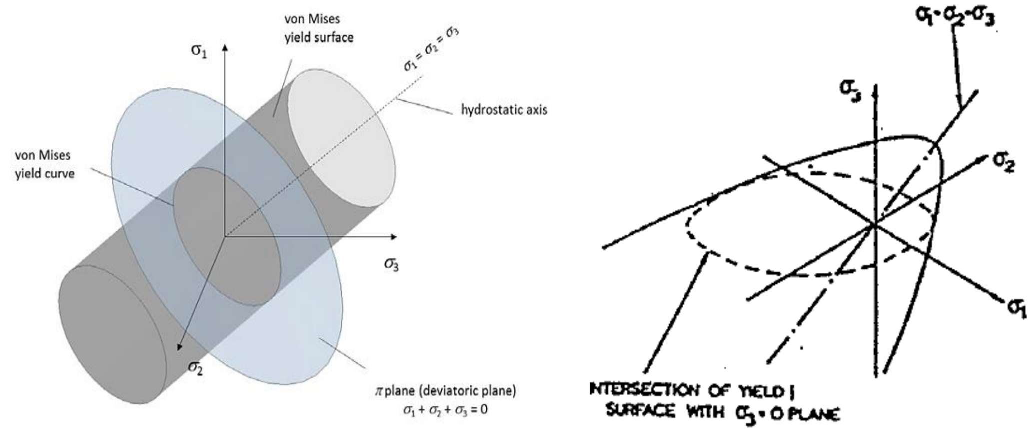

(a) (b)

Figure 2.12: Yield Envelopes a) von Mises [121] b) Rhagava et al. [112].

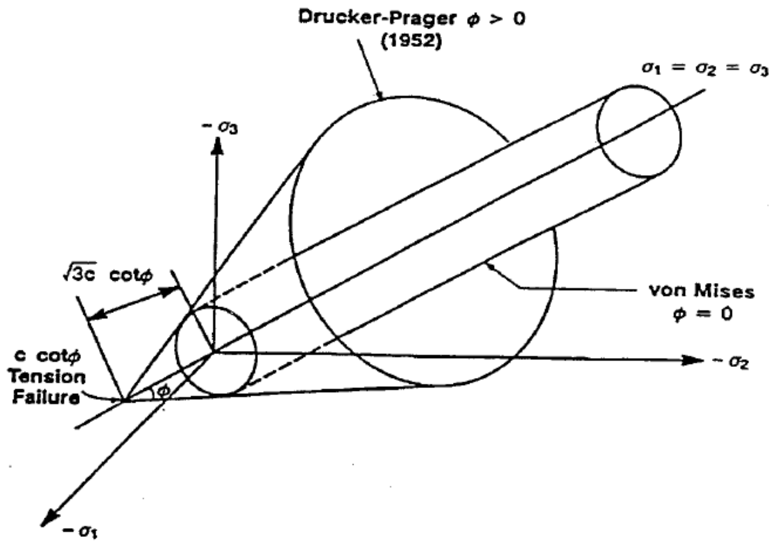

Figure 2.13: Yield envelopes comparison between Von Mises and Drucker-Prager yield criterion [112].

2.9 Fatigue Crack Growth

In late 1950s, number of researchers [122-125] used the Strain Energy Release Rate (SERR) to characterise fatigue crack propagation. Later, Paris and Endorgan [126] developed a crack propagation law based on the power law relationship between the SIF range (ΔK) and crack growth rate (da/dN).

$$\frac{da}{dN} = C\Delta K^n \tag{2.7}$$

Where C and n are material constants and ΔK refers to the stress intensity factor (SIF) range caused by the cyclic fatigue loading ($K_{max} – K_{min}$). This equation is widely known as the Paris crack growth equation. As conveyed by Hartman and Schijve [127], the fatigue crack growth rate is comparable to the amount, in which ΔK exceeds its threshold value ΔKth., i.e. to ΔK – ΔKth. Furthermore, Lindley et al. [128] stated that due to the Paris equation underestimating the crack growth rate as Kmax approaches 70% Kc (fracture toughness of the material), the fatigue crack growth behaviour is divided into three regions as shown in Figure 2.14. The first region is the threshold region where cracks do not propagate. In Region II, the curve is generally linear on logarithmic scales which reflect to Equation 2.7. The third Region is the rapid crack growth, in which the SIF approaches the material fracture toughness.

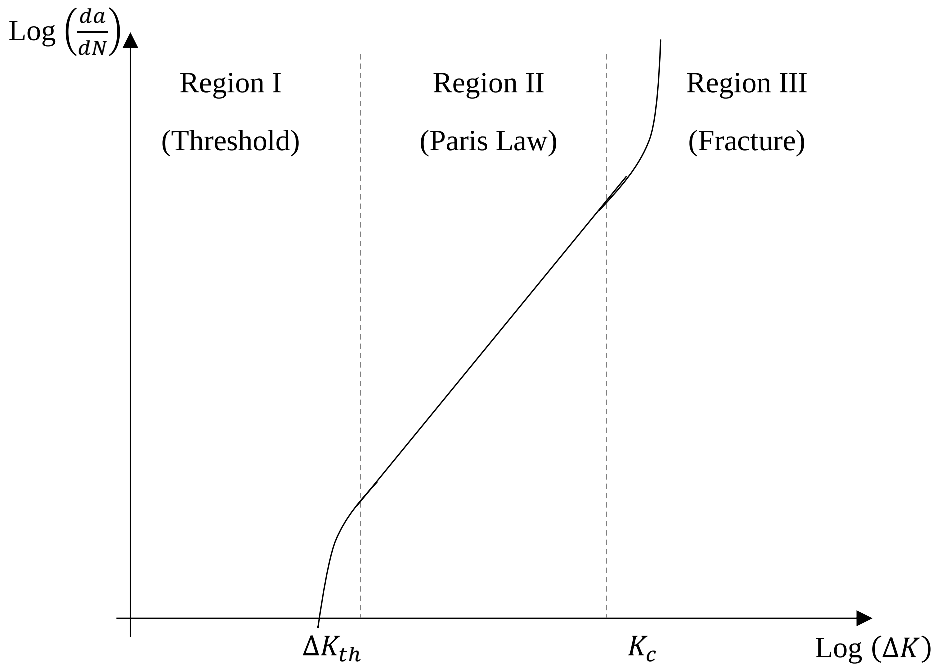

Figure 2.14: Typical fatigue crack growth behaviour.

2.9.1 Fatigue in Adhesively Bonded Joint

In late 1970s, Wang et al. [129] performed an analysis based on finite element method to investigate the stress distribution in a DCB specimen bonded with adhesive.

The authors reported that for the crack embedded in the adhesive, the stresses field close to the crack tip are singular and may be defined by the conventional strain energy release rate and stress intensity factor. The stress field in the adhesive layer essentially becomes uniform after a distance of less than one layer of adhesive thickness from the crack tip [129]. As a result, when applying fracture mechanics approach to analyse the failure of anisotropic bodies such as structural adhesive and fibre reinforced composite, G is generally used rather than K as the adhesive material properties are governed by G [130, 131]. Thus, the Paris law is plotted in da/dN versus ΔG when analysing the fatigue crack growth rate of structural adhesives.

$$\frac{da}{dN} = \mathrm{D}\Delta G^{m} \tag{2.8}$$

Where D and m are material constants determined from the experimental test.

2.9.2 Mixed-Mode Fatigue Crack Growth

Table 2.2 listed several modified Paris law equations which have been commonly used to characterise the Mode I (G_I) and Mode II (G_{II}) crack propagation. Until now, there is no universal equation for describing the mixed mode propagation in anisotropic materials. It is worth considering that square root of G which is directly correlated with K, or other forms of G are generally used rather than K as the variable [130, 131].

Table 2.2: Various equations used to characterise the mixed mode crack propagation.

Reference	Equation
Mall et al. [132, 133]	$\frac{da}{dN} = D[\Delta(G_I + G_{II})^m$
Gustafson and Hojo [134]	$\frac{da}{dN} = D_I(\Delta G_I)^{m_I} + D_{II}(\Delta G_{II})^{m_{II}}$
Quaresimin and Ricotta [91, 135]	$\frac{da}{dN} = D[\Delta(G_I + \frac{G_{II}}{G_I+G_{II}} G_{II})]^m$
Brussat et al. [136]	$\frac{da}{dN} = D[(1 + \frac{2G_{II}}{G_I+G_{II}})\Delta G_I)]^m$
Cheuk et al. [20]	$\frac{da}{dN} = D[\Delta(G_I + \frac{G_{Ic}}{G_{IIc}} G_{II})]^m$
Rans et al. [137]	$\frac{da}{dN} = D_I\left[\left(\Delta\sqrt{G_I}\right)^2\right]^{m_I} + D_{II}\left[\left(\Delta\sqrt{G_{II}}\right)^2\right]^{m_{II}}$
Benzeggagh and Kenane [138]	$\frac{da}{dN} = D[\Delta(G_I + (G_{II} - G_I)\left(\frac{G_{II}}{G_I+G_{II}}\right)^\gamma)]^m$

Disbond growth of adhesively bonded joints under fatigue loading has been investigated by several researchers [10-20, 139-141]. Curley et al. [139] conducted fatigue tests with short (12.7 mm long overlap) single lap joint specimens made of mild steel adherends and AV119 epoxy adhesive. They reported that the experimentally measured disbond growth rate and fatigue life could be predicted using a modified Paris law as a function of strain energy release rates (SERR). Jones et al. [141] recently discussed the requirements for implementing the slow damage growth management approach for adhesively bonded joints. Based on review and assessment of the available data in literature, they suggested the disbond growth could be accurately predicted using a modified Paris law equation, namely the Hartman–Schijve crack growth equation.

2.10 Specimen Preparation

Specimen preparation is the most crucial part for the bonded repair application process. This includes material selections of the adherend and method to assess the bond integrity. The two sub-sections below discuss the effect of clad layer on fatigue resistance in adhesively bonded joints and test method to determine the quality of surface preparation technique.

2.10.1 Effect of Clad Layer on Fatigue Strength

Fatigue cracking on aircraft components that are subjected to fatigue loading often are followed by corrosion damage [142-144]. To address this issue, the substrate alloy is cladded with a more anodic aluminium alloy. The thickness of the Clad layer is generally below 5% of the sheet thickness. Although the existence of the clad layer is usually neglected in the strength calculations, it has been observed that fatigue crack initiated in the cladding layer is sooner than the bare alloys [143, 145].

Duquesnay et al. [146] performed an experimental test on central drilled hole substrate to simulate the damage on aircraft skin, that was then repaired using adhesively bonded patch over the top of the hole. The specimens were manufactured using Al2024-T3 bare and Al7075-T6 clad material bonded with FM73 epoxy adhesive. The specimens then tested under axial fatigue loading at R = 0 to represent aircraft cabin re-pressurisation cycles. The authors observed that specimen with clad layer failed by fatigue crack initiation at a stress levels lower by factor of two or greater than the unpatched substrates. The cracks were observed to initiate and propagate at the cladding layer. Whilst for the bare alloy patched specimen, no fatigue failure observed after 25 million cycles. The results show that by applying an adhesively bonded patch repair to the clad aluminium substrate, it will significantly reduce the fatigue strength as well as the life of the structure being repaired. Thus, it is strongly suggested to remove the clad layer prior to applying the adhesively bonded patches.

2.10.2 Boeing Wedge Test (BWT)

BWT (ASTM D3762) has been widely used to assess the integrity and long-term bond strength of an adhesively bonded joints in aircraft structure. This test method is proven as the reliable method to determine the environmental durability and quality of the surface preparation technique [147]. In addition, the environmental and moisture effects of metal bonded structures have become the research interest over the years [148]. Davis and Bond [149] reported that insufficient surface preparation treatment will result in poor environmental durability of the adhesive. Cognard [150] performed the BWT with 5 different adhesive types namely plastified epoxy, commercial adhesive (AV 118), epoxy-nitrile, epoxy-nylon and fille nitrile epoxy in tropical environment (40℃ and 90% RH) condition. The results have shown that the increase in fracture length is positively corrected to the time of exposure. He concluded that the property of adhesive-bonded joints decreases in strength under humid conditions. Sargent [151] conducted a durability testing with small peel test specimens immersed in distilled and tap water. They concluded that water has little effect on the bond integrity for a least seven years if the adherends did not corrode. The author reported that pre-treatment of the adherends is the main concern of bond integrity.

2.11 Summary

This chapter discussed the relevant literature about the disbond growth assessment of bonded joints or patch repairs for primary aircraft structures. The associated certification requirements for primary aircraft structures have been examined. Other factors that contribute to the certification process such as damage assessment, repairing method, and damage tolerance regions were also reviewed. From the literature, it can be summarised that:

- Adhesively bonded joints offer many advantages among other repairing techniques, such as minimising the transition in surface contour, avoiding further damage in bonded parts, and distributing a more uniform stress. However, certification of bonded joints or patch repairs for primary aircraft structures is still a significant issue.

  Research Gap 1: Opportunities to establish a novel solution to address the certification issue of bonded joints or patch repairs of primary aircraft structures were identified. Improved solutions should consider the demonstration of damage tolerance.

- The application of adhesively bonded joint technique requires stringent cleaning and processing steps to produce very efficient joints which can share the load over a large area. Also, ensuring the quality of bonds is a challenging task due to difficulty in confirming joint integrity by inspection

  Research Gap 2: The surface preparation technique prior to adhesive bonding is the most crucial part for bonded repair application process. Thus, to perform experimental tests, the skills of the technicians must be prior assessed to ensure the adhesive bond quality.

- A damage slow growth management strategy has been considered acceptable to reduce the maintenance cost, provided the slow growth is predictable and without reducing the strength of the bonded structures below a required safety margin prior to scheduled inspection [9].

  Research Gap 3: Simulation models for understanding and computing the disbond growth behaviour of bonded structures are required to help satisfy the certification requirement and implement the damaged slow growth management strategy.

- The generic patch repair joint called the Double-Overlap Fatigue Specimen (DOFS) and the Skin Doubler Specimen (SDS) have been effective to facilitate airworthiness certification in relation to fatigue issues. However, assessment of a long disbond up to ultimate failure of the joint cannot be achieved just based on tests with these specimens.

  Research Gap 4: The key focus is on the development of the generic patch repair design which accounts for a long disbond assessment up to the ultimate failure of the joint.

- Finite Element Method (FEM) has been widely used for the analysis of adhesively bonded joints. It provides a great advantage in determining the mechanical properties of an adhesively bonded joints under different loading conditions and any geometrical shape. Furthermore, it could be used in conjunction with fracture mechanics (i.e. VCCT) and cohesive zone method (CZM) to stimulate the crack growth.

Research Gap 5: Finite Element Method (FEM) is required for the analysis of disbond growths behaviour in adhesively bonded joints due to its versatility in modelling with various approaches.

- Strain energy release rate (G) is generally used rather than stress intensity factor (K) when applying fracture mechanics approach to analyse the failure of structural adhesive. However, there is no common equation to define the mixed mode propagation in structural adhesive.

Research Gap 6: Relationship between the disbond growth rates and disbond strain energy release rates (modified Paris Law) should be established. This is achieved by (i) computationally determining strain energy release rates as a function of disbond lengths and loads, (ii) conducting fatigue tests and measuring the disbond growth rates at different disbond lengths and fatigue loads, and (iii) correlating the computational and measured results.

Chapter 3

Material Properties, Modelling Approach and Design of the DOTES Specimens

Preface

The accuracy of an FE simulation is highly dependent on its capability to precisely capture the material's behaviour. This chapter discussed about the materials used, the modelling approaches, and specimen designs of the double overlap tapered end specimen (DOTES). Two specimen designs were considered in this study. One was considered as a preliminary specimen design and the other was the refinement of the first specimen design. The process of configuring a material model within MSC Marc is presented. The equivalent von Mises stress/strain relationship was used to model the linear response of FM300-2K adhesive material properties. Moreover, the plastic response was determined using the von Mises yield criterion. The configured material model was tested using a single element simulation. The residual strength of the designated bonded joints was predicted using the analytical and FE approach. The analytical prediction implemented in this work was developed by Hart-Smith [19], whereas the FE approaches used were the total strain energy density of the adhesive material and the virtual crack closure technique (VCCT). These approaches were used to predict the generic bonded joints that were modelled in two dimensional. Later, in Chapter 6, the cohesive zone element (CZE) method will be utilised to simulate the 3-D wide bonded metal joint specimen.

3.1 Introduction

A good understanding of the material properties present in the adhesive epoxy is required especially regarding their behaviour in strength and failure strain. It is also important to understand the mapping process of material properties into the implementation of material model in finite element analysis. Thus, the FEM will behave similarly with the material being investigated.

This chapter aims to describe the coupon specimen design configuration, material properties, and modelling approaches that were used in this research project. The effort included:

- to specify the coupon specimen design including the trial and refinement specimen designs;
- to define the material properties along with their behaviour in Hot-Wet (HW) environment;
- to describe the analytical (Hart-Smith) and FEM (adhesive element failure criteria, the VCCT method and the CZE method) modelling approaches; and finally
- to calibrate the material properties of FM300-2K using single element analysis to ensure that it was correctly implemented in the FE software.

In Chapter 4, the modelling approaches such as the Hart-Smith analytical formula, adhesive element failure criteria and VCCT approach were used for computational assessment of the disbond growth behaviour and fatigue life prediction of the designated coupon specimen. As follows, experimental assessments were carried out in Chapter 5 to calibrate and validate the FEM prediction model developed in Chapter 4. Later in Chapter

6, the adhesive element failure criteria along with the CZE approach were used to assess the disbond growth behaviour of the 3-D wide bonded metal joint specimen.

The accuracy of the numerical modelling discussed in the Chapters 4 -6 is strongly linked to the three components specified in this chapter.

3.2 Specimen Design

The adhesively bonded patch repair configuration that is commonly used to repair cracks in aircraft structures is illustrated in Figure 3.1. The outer edges of the patch were tapered to minimise peel and shear stresses. The DOTES specimen illustrated in Figure 3.1 represented the area over the crack in the parent structure (previously analysed by the DOFS specimen) and the area at the outer end of the patch (previously analysed by the SDS specimen).

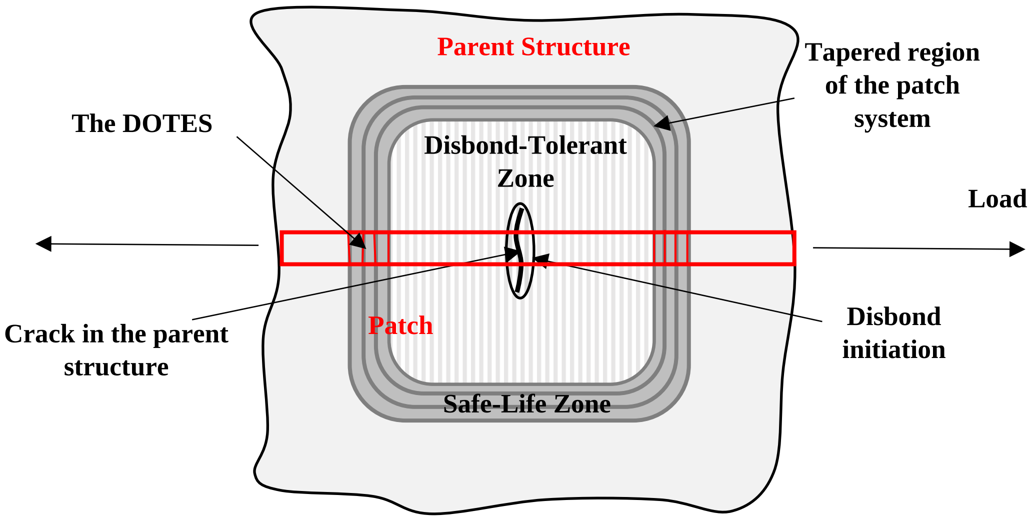

Figure 3.1: Schematic of bonded patch repair representing the disbond tolerant and safe-life zones.

The geometry of the DOTES specimen shown in Figure 3.2 consists of three different parts, namely inner adherend (thickness T_i), adhesive layer, and outer adherend (thickness T_o). A gap of 2 mm between the inner adherends was created to simulate a crack in the parent structure. For the baseline configuration, the thickness ratio between inner adherend and outer adherend was 2:1, while the selected value of T_o was 3 mm. The aspect ratio between the inner adherend thickness and overlap length (L) was 1:30. The thickness of the adhesive layer (t_a) was 0.15 mm and the width of the specimen considered was 20 mm.

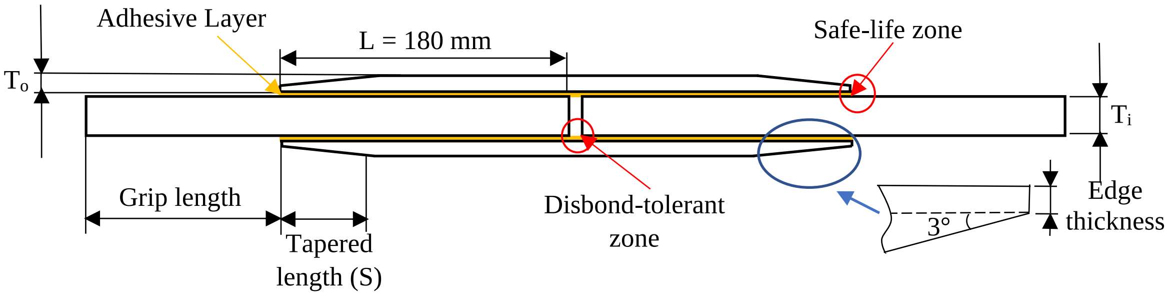

Figure 3.2: The geometry of Double Overlap Tapered End Specimen (DOTES).

3.2.1 Specimen Overall Description

Two different configurations of the DOTES specimen design were considered which mainly focused on the chamfer design at the tapered end and gripping length. The first specimen design was depicted in Figure 3.3a which has a shorter tapered end and thicker edge thickness. This specimen was called the DOTES-ST (short tapered). Whilst the second specimen design was set to minimise the edge thickness which resulted in a longer tapered end as shown in Figure 3.3b. This specimen was called the DOTES-LT (long tapered).

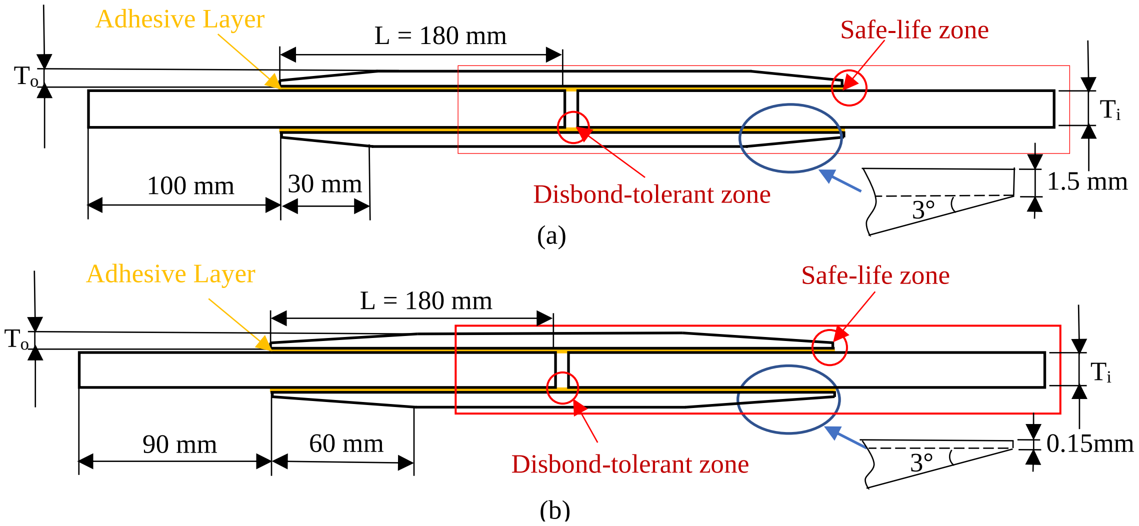

Figure 3.3: The DOTES configurations a) the DOTES-ST b) the DOTES-LT.

The specimens used in this study are shown in Figures 3.4 and 3.5, which are experimental versions of the DOTES specimen (Figure 3.3). Due to symmetry, only the right half of the DOTES specimen was considered. The adhesively bonded metal to metal includes three different parts, namely inner adherend (thickness T_i), adhesive layer, and outer adherend (thickness T_o). A gap of 2 mm between the inner adherend was created to simulate the crack in the parent structure. The width of the specimen was 20 mm.

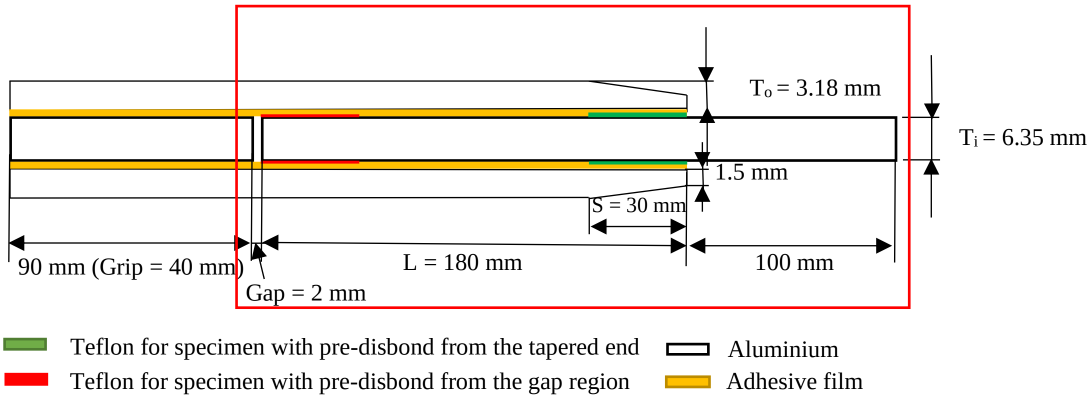

Figure 3.4: Schematic overview of the DOTES-ST coupon specimen configuration.

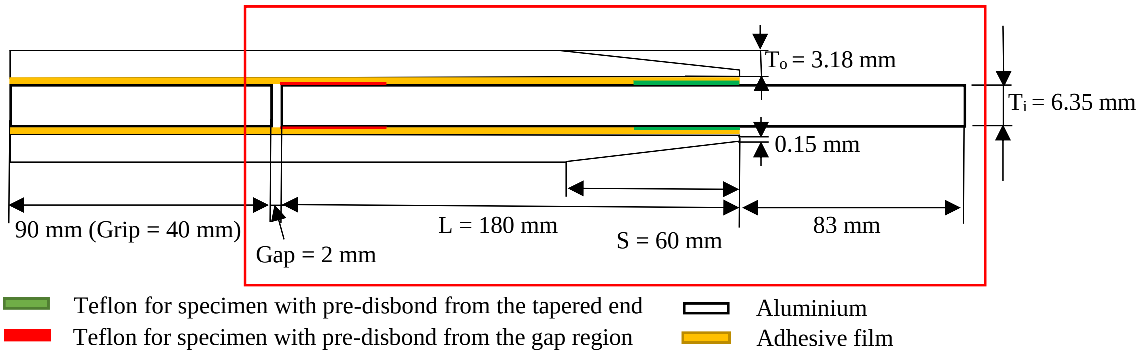

Figure 3.5: Schematic overview of the DOTES-LT specimen configuration.

3.2.2 The DOTES-ST Specimen Design

The geometry of the DOTES-ST coupon specimen configuration as marked by the red rectangular box in Figure 3.3a is shown in Figure 3.4. This specimen design was considered as the trial specimen for tests subjected to static and fatigue loading. The edge thickness was set to 1.5 mm. For the baseline configuration (Balance joint configuration), the tapered length was set to 30 mm to achieve 3° tapered angle at the chamfer. The gap region was extended by 90 mm for machine gripping and to avoid the end shoulder effect on the test region. Teflon film was inserted between the adhesive film and inner adherend to represent the pre-disbond. As shown in Figure 3.4, the Teflon illustrated in red represents the Teflon position for specimen with pre-disbond from gap region, whilst the green represents the Teflon position for specimen with pre-disbond from Tapered end.

3.2.3 The DOTES-LT Specimen Design

Assessment on the shear and peel stresses distribution along the tapered end of 1.5 mm edge thickness (The DOTES-ST specimen design) and 0.15 mm edge thickness (maximum machine can reach) was conducted as demonstrated in Figure 3.6. The blue curve showed the stresses of 1.5 mm edge thickness whereas the red curve showed the stresses of 0.15 mm edge thickness. The FE results indicated that the shear and peel stresses of 0.15 mm edge thickness were reduced by 51% and 47% respectively, compared to the 1.5 mm edge thickness. Thus, another coupon specimen design was considered to reduce the shear and peel stresses at the tapered region.

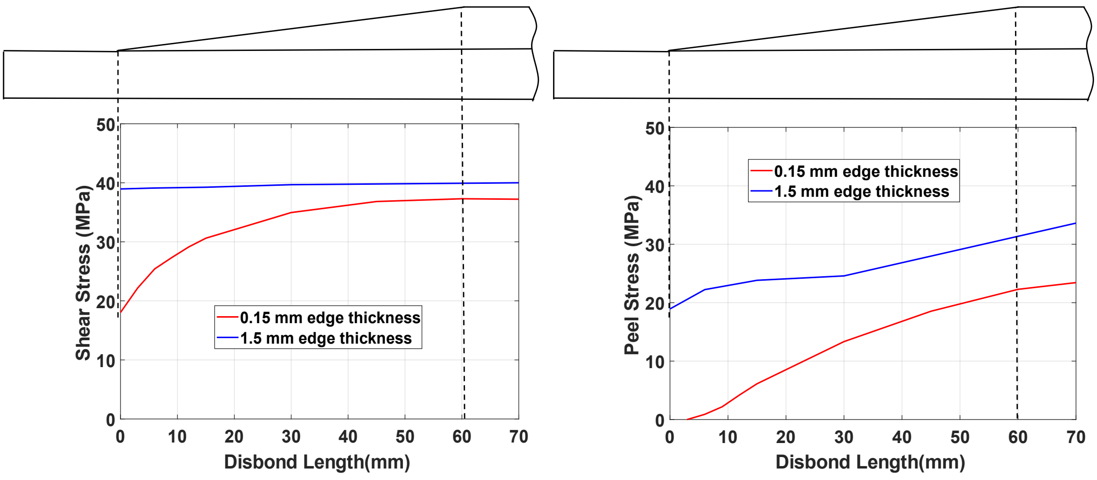

(a) (b)

Figure 3.6: Stresses distribution along the tapered end of the joint with 0.15 mm and 1.5 mm edge thickness a) shear Stress b) peel stress.

The new design of coupon specimen is shown in Figure 3.5 which was called the DOTES-LT specimen. The edge thickness was reduced to 0.15 mm to minimise the peel and shear stresses at the tapered end. Moreover, the tapered length was extended to 60 mm for maintaining the 3° tapered angle. Also, for the purpose of HW testing condition, the gripping section was shortened from the DOTES-ST specimen. Apart from these three changes, all specimen design was the same with the DOTES-ST specimen design.

3.2.4 Stress State in the DOTES

A distributed load of 1.4 kN/mm was applied to the inner adherend, which was equivalent to 28 kN load on the full model. The peel and shear stresses distribution of the DOTES-ST and the DOTES-LT specimens are presented in Figure 3.7. Since a linear elastic model was implemented here, the plots for any other load would be similar and thus can be obtained using a scale factor.

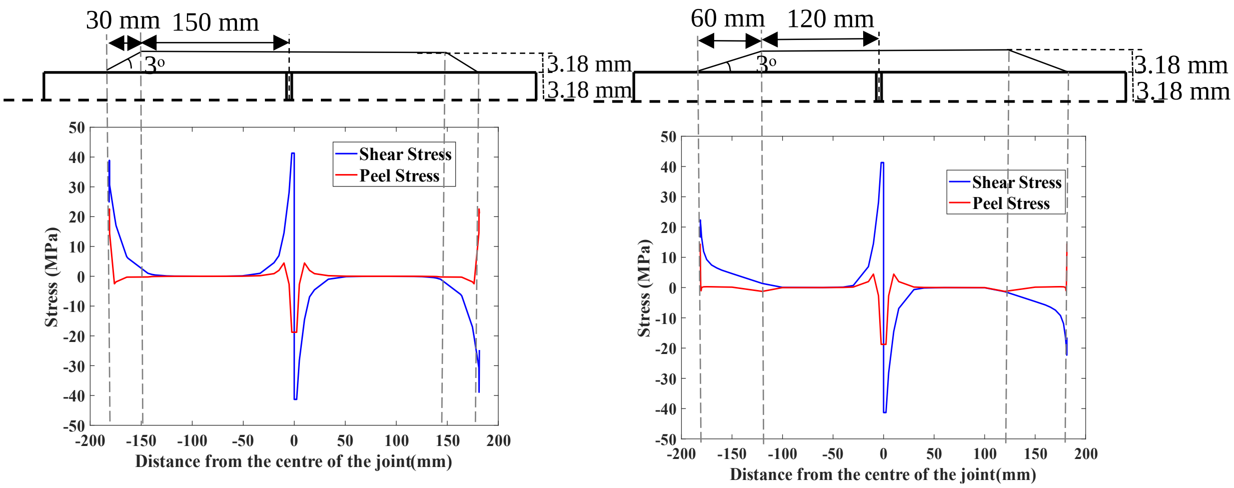

(a) (b)

Figure 3.7: Shear and peel stresses along the mid-plane of the adhesive layer of the DOTES, load/unit width = 1.4 kN/mm a) the DOTES-ST b) the DOTES-LT.

As shown in Figure 3.7a, at the end of the joints (gap region and tapered end), the shear stress was high and gradually decreased to zero as it approached the middle of the joint. Whilst for the peel stress, it was initially high at the tapered end of the joint and decreased to zero as it was further from the tapered end; it was then decreased to negative as it approached the middle gap of the joint. This stress state in the middle gap region was in good agreement with the double overlap fatigue specimen (DOFS) analysis done by [11]; that is, a state of shear plus compressive peel stress.

Higher positive shear and peel stresses were observed at the tapered end for the DOTES-ST specimen design (Figure 3.7a, 1.5 mm edge thickness). As compared to Figure 3.7b, 0.15 mm edge thickness, the stress state at the tip of the tapered end was reduced. Thus, high positive peel and shear stresses at the tapered end could be minimised by reducing the edge thickness. The effect of edge thickness as a function of disbond length is further discussed in Section 4.6.

3.2.5 Specimen Configuration

The baseline configuration shown in Figures 3.4 and 3.5 were used for testing under fatigue loading in RD condition and static loading in HW condition. The thickness ratio between inner adherend (t_i) and outer adherend (t_o) was 2:1 with a T_i selected value of 6.35 mm. The aspect ratio between the inner adherend thickness and overlap length (L) was 1:30.

Based on the work demonstrated by Hart-Smith [19], the loading capacity of an adhesive bonded joint would reduce when the thickness ratio between the inner and outer adherend was unbalanced ($T_i \neq 2T_o$). The condition where the stiffness at one end of a joint differs from the other end is represented in Figure 3.8. This phenomenon caused the adhesive shear strain distribution to be rendered unsymmetric. The maximum strength of the joints was reached when the stiffness ratio of the inner adherend (t_i) was equivalent to two times the outer adherend thickness ($2t_o$) (stiffness ratio = 1).

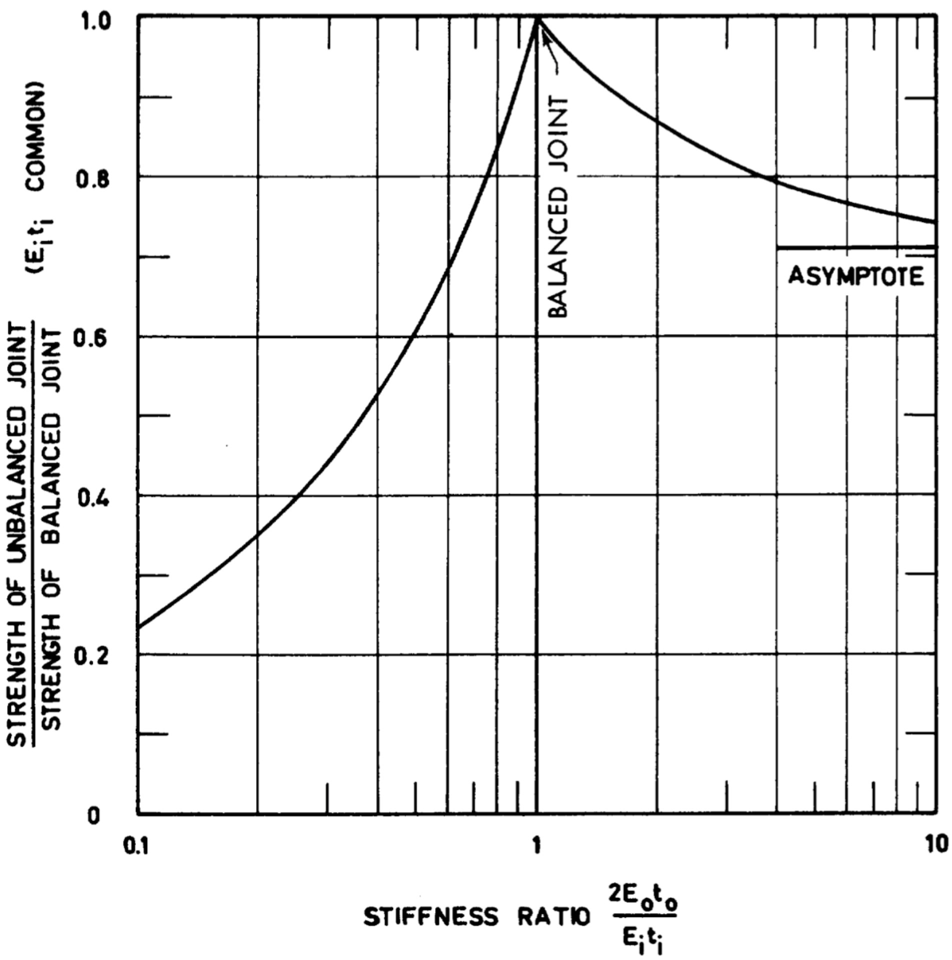

Figure 3.8: Effect of adherend stiffness imbalance to the strength reduction of bonded joints [19].

From this finding, it suggested that failure of the joint could be forced to be in the adhesive. Thus, to force adhesive cohesive failure in the adhesive, thicker inner adherend could be used for specimen with pre-disbond from the gap region, whilst thicker outer adherend could be used for specimen with pre-disbond from the tapered end. The results of tests where failure occurred cohesively in the adhesive were used for calibration of material properties and mesh size used in numerical analysis.

The adherend thickness variations used for the static test are summarised in Table 3.1. The tapered length was adjusted in accordance with 3° tapered angle whereas the overlap length was maintained at 180 mm.

Table 3.1: Variation of specimen configuration of Batches 1 and 2 coupon design.

Variation	Thickness ratio (Inner to Outer)	Inner adherend thickness (mm) (T_i)	Outer adherend thickness (mm) (To)	Tapered Length (mm) (S)	Overlap Length (mm) (L)
			DOTES-ST		
1 – Thicker outer adherend (TOA)	1:1	6.35	6.35	60	180
2 – Thicker inner adherend (TIA)	3:1	9.53	3.18	30	180
			DOTES-LT		
1 – Thicker outer adherend (TOA)	1:1	6.35	6.35	120	180
2 – Thicker inner adherend (TIA)	3:1	9.53	3.18	60	180

3.3 Material

3.3.1 Aluminium

Aerospace-grade aluminium (AL 7050-T7451) was used for the inner and outer adherend. The inner and outer adherend components of the DOTES-ST specimen were manufactured from various thicknesses of aluminium plates as specified in Table 3.2. The material properties of AL 7050-T7451 are presented in Table 3.3.

Table 3.2: Adherend thickness variations.

Variation	Aluminium thickness
1	3.18 mm (0.13 inch)
2	6.35 mm (0.25 inch)
3	9.53 mm (0.38 inch)

Table 3.3: Material properties of AL 7050-T7451 [152].

Aluminium
Young's Modulus (E) = 71.7 GPa
Poisson's ratio (v) = 0.33
Yield Strength (S_y) = 469 MPa
Ultimate Strength (S_{UT}) = 524 MPa

In contrast with the DOTES-ST specimen, the DOTES-LT specimens were manufactured using 6.35- and 9.53-mm aluminium plates due to the existence of clad layer in the 3.18 mm aluminium sheet. Two researchers [146, 153] observed that patching over the clad material would result in substrate failures at the tip of bonded patches. Thus, 3.18 mm adherend thickness was prepared from the 6.35 mm aluminium plates.

3.3.2 Adhesive

The adhesive used in this project was FM300-2K film, manufactured by Cytec with a nominal uncured thickness of 0.41 mm. The adhesive was used to bond the inner and outer adherend with the bond region of 180 mm x 20 mm (length x width). The specimen was cured at 121 °C for 90 min in an autoclave at a pressure of 40 psi (275 kPa) [154]. The curing process implemented in this experiment is demonstrated in Figure 3.9. The blue curve represented the curing pressure whereas the red curve showed the curing temperature.

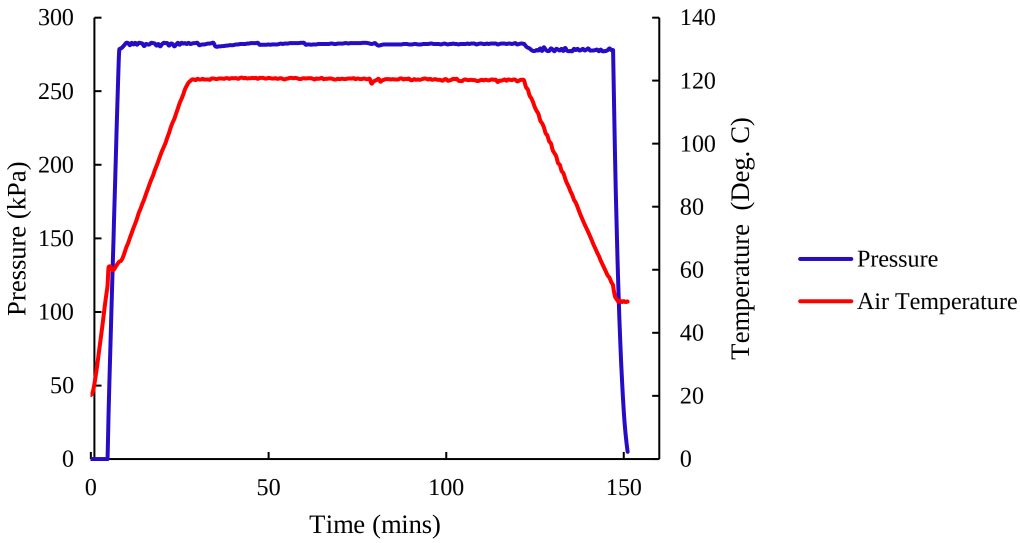

Figure 3.9: Curing procedure of FM300-2K.

Two different material properties adopted in this study are defined in Table 3.4. One was measured from AAP 7021.016-1 [155] and the other from the Cytec [154] manufacturer datasheet. The material properties measured from AAP 7021.016-1 was used as the framework to implement the slow growth approach, predict allowable fatigue life and determine inspection interval, in accordance with the guidance provided in FAA AC 20-107B [9]. Also, assessment on the effect of rigidity imbalance between inner adherend and outer adherend showed how varying the adherend thickness could affect the adhesive bond strength and disbond growth rate. This information would be useful in the design of validation experiment. The material properties provided by Cytec was used to verify the FEA results with the experimental assessment.

Table 3.4: FM300-2K material properties under RD and HW (80℃) conditions [37, 154, 155].

FM 300-2K (AAP 7021.016-1)	**FM 300-2K (RD, 25℃)**	**FM 300-2K (HW, 80℃)**
Shear Modulus (G) = 483 MPa	Elastic Modulus (E) = 2400 MPa	Elastic Modulus (E) = 1062 MPa
Max. Shear Strain ($\boldsymbol{\gamma_{max}}$) = 0.19	Max. Shear Strain (γ_{max}) = 0.82	Max. Shear Strain (γ_{max}) = 1.08
Max. Shear Stress ($\boldsymbol{\tau_{max}}$) = 46.2 MPa	Max. Shear Stress (τ_{max}) = 54.4 MPa	Max. Shear Stress (τ_{max}) = 35.2 MPa
	Poisson's Ratio (v) = 0.4	
	Bond-line thickness ($\boldsymbol{\eta}$) = 0.15 mm	
	Critical Energy Release Rate Mode I (G_{Ic}) = 1.3 kJ/m^2	
	Critical Energy Release Rate Mode II (G_{IIc}) = 5 kJ/m^2	

The specimens were tested in two different conditions, one was tested in room temperature dry (RD) condition, and another was tested in hot wet (HW) condition. For the hot-wet condition, the specimen was pre-conditioned at 80℃ in a humidity chamber. Details of the pre-conditioning procedure are described in Section 5.2.4.

3.4 Modelling Approach

Two approaches were used in the modelling. The first was a closed-form analytical model developed by Hart-Smith [11] which was used to predict the joint strength of pristine specimens (without disbond). The second was finite element (FE) method used to predict the residual strength and SERR of the joint with the existence of disbonds. Details of these two approaches are described in Sections 3.4.1 and 3.4.2, respectively.

3.4.1 Analytical Approach

Hart-Smith developed an approach to predict the load carrying capacity of a bonded joint based on the total strain energy density of the adhesive material [19]. For a pristine specimen, Hart-Smith approach has been widely used and was reasonably accurate to predict joint strength. For a balanced (T_i = $2T_o$) joint with a long overlap length, such as the DOTES design described above, the loading capacity can be estimated using the following equation [19]:

$$P = 4\sqrt{ET_o}\sqrt{\tau_p\eta(\frac{\gamma_e}{2} + \gamma_p)} \tag{3.1}$$

where the elastic strain (γ_e) =τ_p /G and the plastic strain (γ_p) = γ_{max} - γ_e . The geometry parameters (T_o and η) and material properties (E, τ_p, G, and γ_{max}) are provided in Figure 3.3 and Table 3.4.

3.4.2 FE Approach

Finite element (FE) technique was developed using the commercial software MSC Marc to predict the propagation behaviour of the disbond in the bonded patch repair configuration. Twofold symmetry (red marked zone in Figures 3.4 and 3.5) was considered; and thus, only a quarter of the specimen was modelled. This model also represented a single lap joint with full bending constraint.

In this FE investigations, 2D four-node linear plane-strain quadrilateral elements were used. The element size in the adhesive bond-line was set to 0.075 mm in most areas. There were two elements through the adhesive bond-line thickness corresponding to the patch configuration. The mesh was redefined as disbond length increased as illustrated in Figures 3.10 and 3.11.

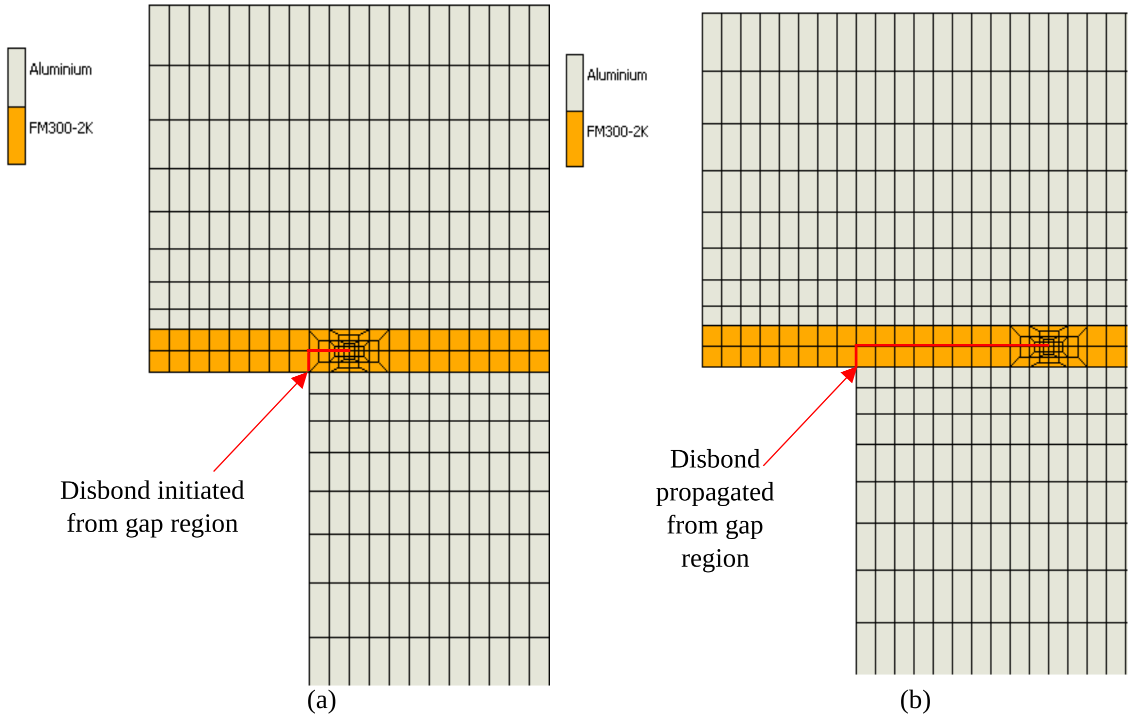

Figure 3.10: Implementation of meshing strategy for disbond initiated from the gap region a) disbond initiation (disbond length 0.15 mm) b) disbond propagation (disbond length 1.2 mm).

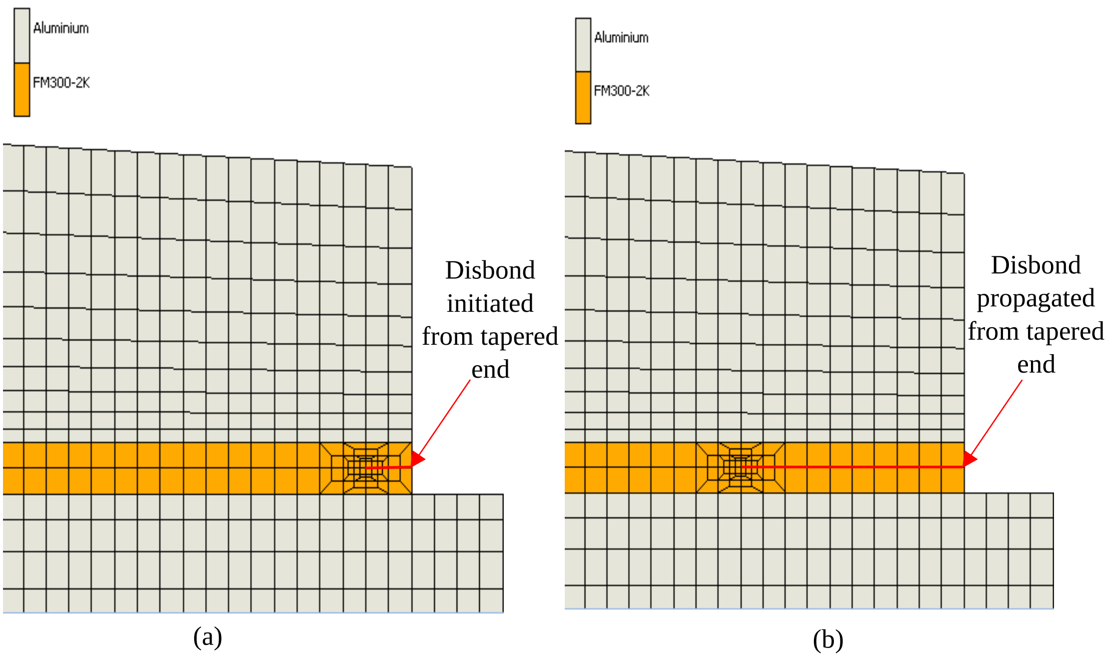

Figure 3.11: Implementation of meshing strategy for disbond initiated from tapered end a) disbond initiation (disbond length 0.15 mm) b) disbond propagation (disbond length 1.2 mm).

For a disbond initiated from the gap region of the joint, the disbond was assumed to initiate in the vertical direction through the adhesive thickness and propagate in the horizontal direction through the middle of the adhesive layer (Figure 3.10). Whilst for a disbond initiated from the tapered end of the joint, the disbond was assumed to initiate and propagate in the middle of the adhesive layer as shown in Figure 3.11.

Fine element size was considered in the adhesive bond line at the disbond crack tip region. Accordingly, a patch mesh configuration (see Figure 3.12a) was developed to reduce the computational cost. As the element size was reduced, eight elements marked in the red rectangular section of Figure 3.12a were replaced by another patch configuration. Hence, the element size was reduced by half ratio as illustrated in Figure 3.12b. The material properties used in this model are listed in Tables 3.3 and 3.4.

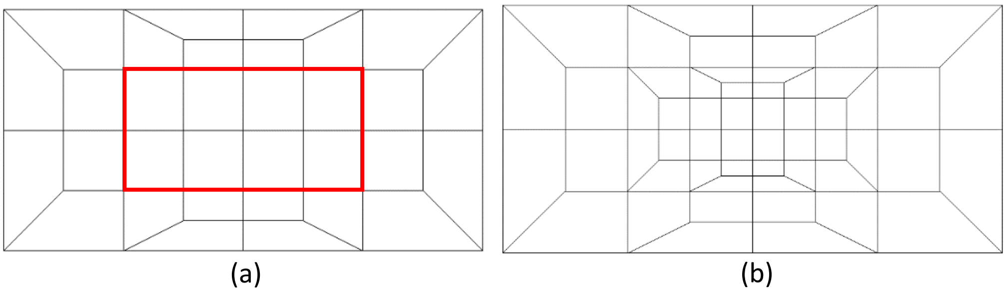

Figure 3.12: Adhesive mesh refinement strategy a) patch configuration b) mesh refinement.

3.4.2.1 Modelling of Adhesive Material

An elastic-perfectly plastic material model was considered for the adhesive material. The linear response of FM300-2K material properties was defined through elastic modulus and Poisson’s ratio (Table 3.4). In MSC Marc, the non-linear behaviour was determined through the equivalent von Mises stress/strain relationship. The von Mises yield criterion was used to determine the plastic response of the adhesive material properties.

To ensure the material property was correctly implemented, single element analyses subjected to tension, compression and shear loadings as presented in Figure 3.13 were performed to examine the stress/strain relationship response. The shear stress/strain curve obtained from the analysis was compared with the shear stress/strain curve from the manufacturer datasheet.

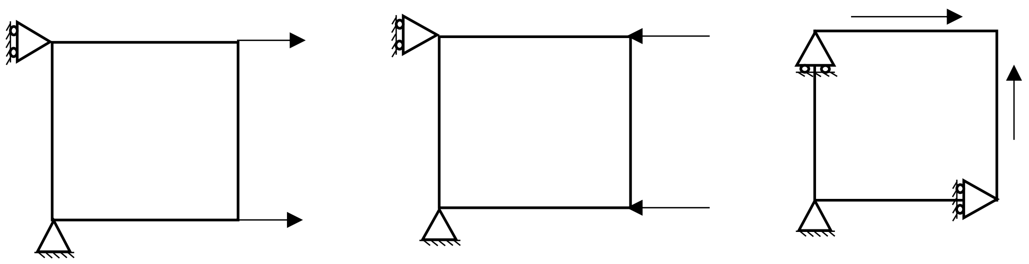

Figure 3.13: Single element analysis using MSC. Marc a) tensile loading b) compression loading c) shear loading.

The shear stress/strain curve obtained from the simulation was compared with the defined shear stress/strain curve as depicted in Figure 3.14. It was concluded that the equivalent stress/strain data defined in the material properties were acceptable.

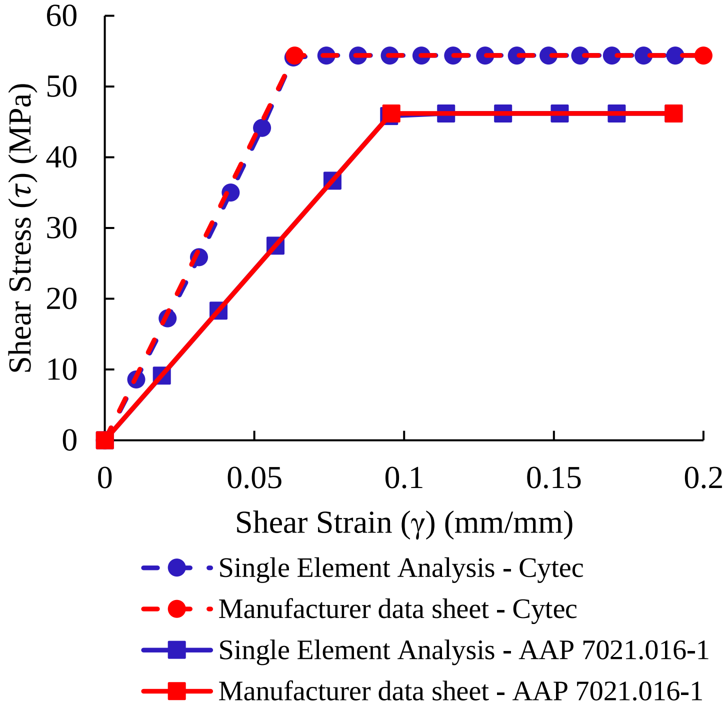

Figure 3.14: Elastic-perfectly plastic adhesive material (FM300-2K).

3.4.2.2 Strength Prediction using adhesive element failure criteria.

The adhesive element failure criteria (total strain energy density of the adhesive material) were used to predict the load carrying capacity. Failure of an adhesive element was predicted when the strain in the element reached the maximum strain defined in Table 3.4 and Figure 3.14.

With the finer mesh around the stress concentration area, a lower strength of the joint would be predicted. This issue of mesh dependence could be handled by using the characteristic distance method proposed by Whitney and Nuismer [156]. The characteristic distance generally was determined by calibration with the experimental test result [157] or if available, with a known accurate analytical result.

A stepwise linear prediction concept was considered in this analysis to predict the adhesive joint strength as a function of disbond length, through a series of static analyses with a pre-defined disbond length.

The stability of disbond crack under static loading was determined by the increment of failure load as disbond length increasd. Increasing failure load predicted a stable crack, whereas a decreasing failure load predicted unstable crack propagation under a static load.

3.4.2.3 Fracture Mechanics Approach

The virtual crack closure technique (VCCT) method is a well-established fracture mechanics approach in predicting failure analysis of composite structures. In this study, two-dimensional plane strain analysis was selected to examine the strain energy release rate (SERR) along with considerations of joint geometry, loading conditions and the assumption of uniform crack propagation. In order to numerically determine SERR components, G_I, G_{II}, and G_{III}, several techniques can be applied. The technique and its applications are extensively covered in [87, 158, 159]. The implementations were based on the nodal displacements (δ_x and δ_y) behind the crack tip, nodal forces (F_x and F_y) at the crack tip, and virtual crack jump (Δa) ahead of the crack tip as illustrated in Figure 3.15 and stated in Equations (3.2), (3.3). The crack would propagate under a static load when the energy release rate (G) reached the critical energy release rate required to propagate a crack (G_c). Under fatigue loading, a crack would grow in a stable manner when the energy release rate (G) decreased as the crack propagates; conversely, an unstable crack propagation would occur.

Mode I:

$$G_I = -\frac{1}{2\Delta a} F_y(\delta_{y2} - \delta_{y1}) \tag{3.2}$$

Mode II:

$$G_{II} = -\frac{1}{2\Delta a} F_x(\delta_{x2} - \delta_{x1}) \tag{3.3}$$

Total (G_T):

$$G_T = G_I + G_{II} \tag{3.4}$$

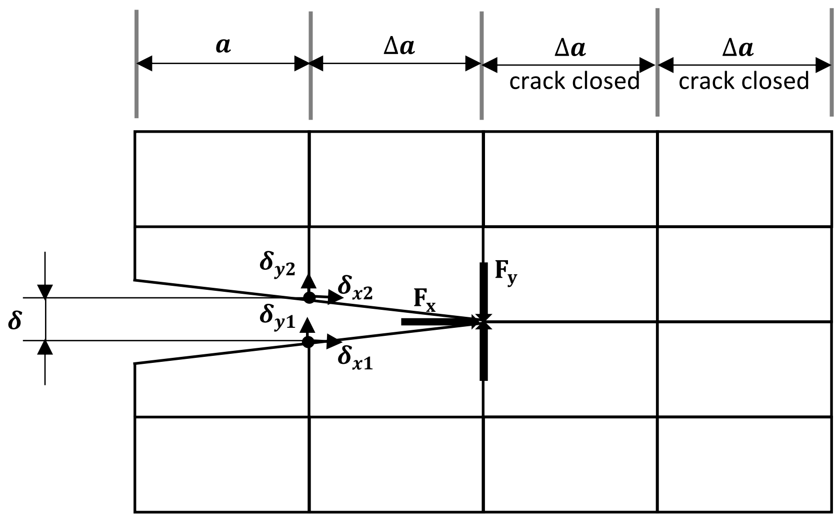

Figure 3.15: Virtual Crack Closure Technique for four nodes element (Adapted from [160]).

The SERR was calculated through MSC Marc post-processing VCCT results. The mesh-sensitivity results presented in Figure 3.16 demonstrate that the total strain energy release rate tend to converge with a smaller element size. According to Rybicki and Kanninen [87], a good estimation of SERR was obtained when the element size around the crack tip is small compared to the pre-defined crack length (less than 10% of the crack length). In addition to the sensitivity analysis, the MSC Marc VCCT approach was also benchmarked against previously published results [87, 158] to validate its accuracy.

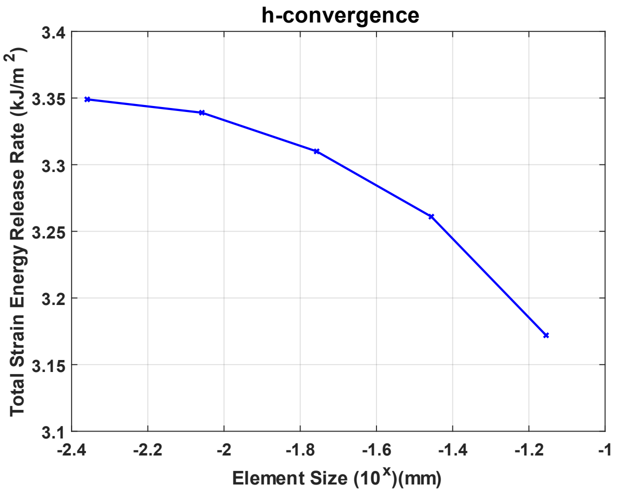

Figure 3.16: H-convergence study for VCCT approach (Crack length = 0.15 mm).

3.4.2.4 Cohesive Zone Element (CZE) Approach

The Cohesive Zone Element (CZE) has been widely used to predict the strength of adhesively bonded joints [74, 92]. When compared to the previous two methods defined in Sections 3.4.2.2 and 3.4.2.3 (Adhesive element failure criteria and Virtual Crack Closure Technique), the CZE method allows simulation of damage onset and growth without requirements to define the initial crack. Therefore, the CZE method could predict the residual strength up to the failure of the joint (propagation of cracks until failure of the joint). The CZE method was also able to model the evolution of a 3-D crack automatically, whilst the VCCT method has difficulty in propagating cracks in 3-D conditions [161]. In Chapter 6, the cohesive fatigue model was developed to model the

3-D wide bonded metal joint specimen. One of the major drawbacks of the CZE method was the requirement to identify the regions where damage was prone to occur, especially when modelling a relatively complex structure [162].

The implementation of the CZE method was based on the establishment of the traction-separation laws (known as CZE laws) to model the interfaces [74]. Various shapes of cohesive laws could be developed which depends on the nature of the materials to be simulated [163]. In MSC Marc (2018 version), two standard functions were available called the exponential and bi-linear functions. These two standard functions were considered in this study to simulate the onset and propagation in the adhesive. Also, these two standard functions were benchmarked against previously published results [164] to validate their accuracy.

The schematic damage process zone of the cohesive zone model under Mode I loading condition is presented in Figure 3.17. Also, the response of typical interface element formulation, governed by bi-linear traction separation law to predict damage initiation and propagation are shown in Figure 3.17. The key parameters such as fracture energy (G_c), maximum traction (σ,τ) and Young's modulus (E) defined in Table 3.4 were required to generate the cohesive laws.

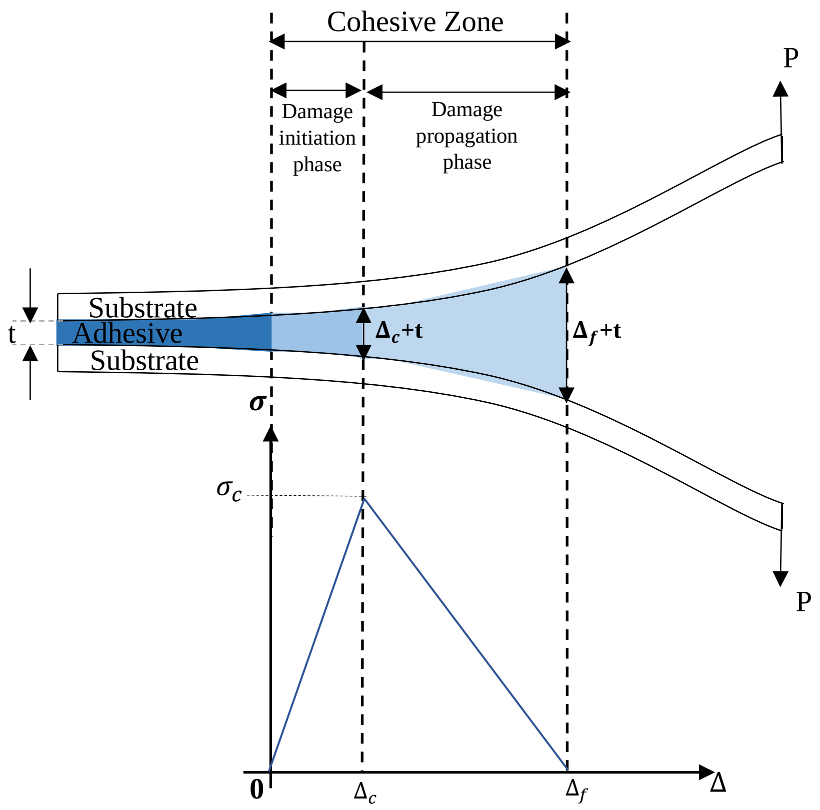

Figure 3.17: Illustration of damage process zone along with corresponding bi-linear traction–separation law in an adhesively bonded joint (Adapted from [165]).

The exponential traction-separation law of FM300-2K is shown in Figure 3.18. Alfano [166] has shown that this exponential law was optimal in FE approximation. According to the MSC Marc handbook [160], the key parameters to define the exponential cohesive law are cohesive energy (G_c), maximum traction (T_c) and the critical opening displacement (δ_c). Where G_c and T_c are defined in Table 3.4 and the critical opening displacement was defined as [160]:

$$\delta_c = \frac{G_c}{eT_c} \tag{3.5}$$

With coefficient of maximum shear to normal stress (β_1) = τ/σ and coefficient of cohesive energy (β_2) = G_{IIC}/G_{Ic}.

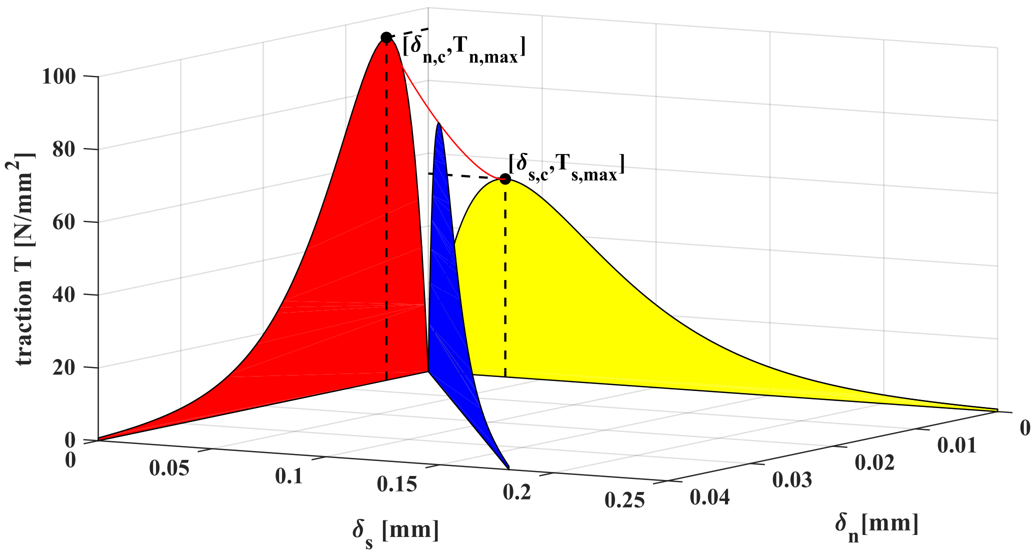

Figure 3.18: Exponential cohesive law of FM300-2K in Mode I, Mode II and Mixed-Mode.

According to Wahab [167], bi-linear traction separation law is commonly used in adhesively bonded joints and to model the cohesive fatigue damage. Also, Alfano [166] reported that this bi-linear cohesive law showed a good balance between the accuracy of simulation process and computational cost. Thus, the bi-linear cohesive law presented in Figure 3.19 would be implemented to develop the fatigue damage model defined in Chapter 6, Section 6.2. The key parameters required to define the bi-linear cohesive law are cohesive energy (G_c), maximum traction (T_c) and elastic stiffness (K). By definition, the normal elastic stiffness (K_n) is defined by dividing Young's modulus (E) with the cohesive element thickness. Similarly, the second and third shear elastic stiffnesses (K_s and K_t) are determined by dividing the shear modulus (G) with cohesive element thickness [168]. However, in this study, the elastic stiffnesses were adjusted with the static test. The critical (δ_c) and maximum displacement (δ_m) can be defined as:

$$\delta_c = \frac{T_C}{K} \tag{3.6}$$

$$\delta_m = \frac{2G_C}{T_C} \tag{3.7}$$

Where G_c and T_c are defined in Table 3.2 and coefficient of maximum shear to normal stress (β_1) and coefficient of cohesive energy (β_2) are identical with exponential law.

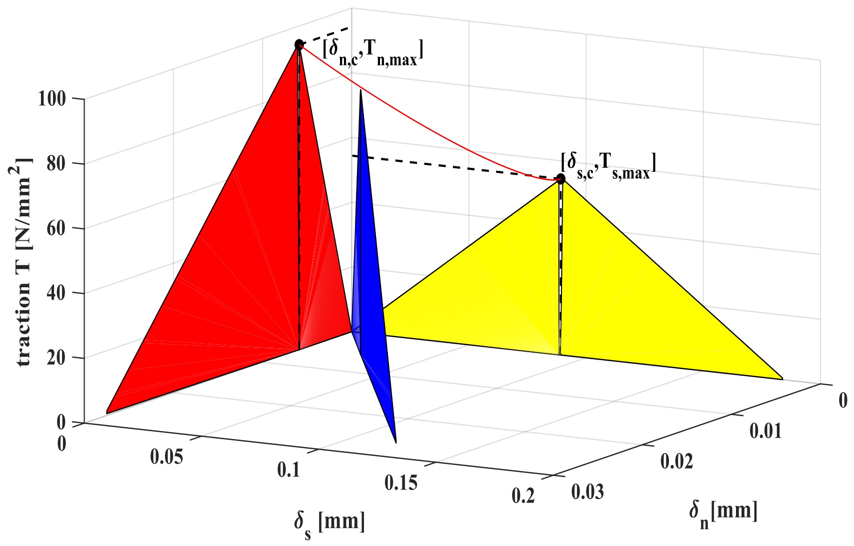

Figure 3.19: Bi-linear cohesive law of FM300-2K in Mode I, Mode II and Mixed-Mode.

3.5 Summary

- Two different constitutive material properties of FM300-2K were used. These properties were successfully used in the MSC Marc material model to represent the numerical model of the adhesive layer. The failure behaviour was studied through single element simulations subjected to various loading conditions.
- The DOTES specimen was developed in this study for assessing a long disbond up to the ultimate failure of the joint. Two coupon specimens design that represent the DOTES were used. Also, the shear and peel stresses distribution of each coupon specimen design was identified. The numerical results showed that by reducing the edge thickness to 0.15 mm, the shear and peel stresses were also reduced by 51% and 47%, respectively.
- Three variations of specimen configuration were utilised to obtain adhesive cohesive failure from the static test. The balance joint specimen was considered as the baseline configuration. Under static loading, thicker inner adherend was required to achieve adhesive cohesive failure of specimen with artificial disbond from the gap region, which was defined as Variation 2, whilst thicker outer adherend was required to achieve adhesive cohesive failure of the specimen with artificial disbond from the tapered end.
- The Hart-Smith analytical model was used to predict the joint strength of pristine specimen. This approach has been widely used to predict the joint strength of double lap joint.
- The adhesive element failure criteria were used to predict the residual strength of the joint with the existence of disbond. The characteristic distance was determined when the predicted joint strength (disbond crack length approaches zero) using

FEM analysis was equivalent to that predicted using the Hart-Smith analytical formula. Once the experimental work was carried out, the characteristic distance was determined by calibration with the experimental test result.

- The VCCT technique was utilised to calculate the SERR of the joint with various disbond lengths.
- The CZE approach was used to determine the SERR and assess the disbond growth behaviour of the 3-D wide bonded metal joint specimen.

The modelling approaches such as the Hart-Smith analytical formula, adhesive element failure criteria and VCCT approach defined in this chapter were used to develop a procedure to assess the disbond growth rate and fatigue life prediction of the DOTES specimen in Chapter 4. Furthermore, experimental assessments were conducted in Chapter 5 to calibrate and validate the FEM prediction model developed in Chapter 4. Finally, the cohesive fatigue model was developed based on the CZE approach to assess the disbond growth behaviour of the 3-D wide bonded metal joint specimen in Chapter 6.

Chapter 4

Numerical Assessment of Disbond Growth and Fatigue Life of the DOTES Specimens

Preface

This chapter presents the development of a numerical procedure for disbond growth assessment of bonded joints or patch repairs used in primary aircraft structures. The numerical investigation was carried out based on the 2-D strip specimen assessment. The configured material properties and modelling approaches presented in Chapter 3, were used to assess the residual strength, and analyse the SERR of the designated coupon specimen. This chapter provides an analysis on the effect of stiffness imbalance and the edge thickness variations of the DOTES specimen. The key highlights of the assessments presented in this Chapter are: fatigue life prediction, slow growth approach and joint failure mode. The numerical procedure performed was further expanded in Chapter 5 by conducting the experimental assessment.

The research works presented in this chapter are part of a paper entitled "A procedure to assess disbond growth and determine fatigue life of bonded joints and patch repairs for primary airframe structures", published in *"International Journal of Fatigue"* (DOI: https://doi.org/10.1016/j.ijfatigue.2020.105664).

4.1 Introduction

Certification of bonded joints or patch repairs of primary aircraft structures requires a demonstration of damage tolerance. Traditionally, a demonstration of damage no-growth under structural fatigue loading is required. In recent years, a damage slow growth management strategy was being considered acceptable to reduce the maintenance cost, provided the slow growth was predictable and without reducing the strength of the bonded structures below a required safety margin prior to scheduled inspection [9]. To help satisfy the certification requirement and implement the damaged slow growth management strategy, a numerical simulation model for assessing the disbond growth behaviour of bonded structures is presented in this chapter.

By using MSC Marc, implicit finite element (FE) models were developed to assess the residual strength and determine the SERR of a bonded joint with various disbond lengths. The modelling approach, specimen configuration, and material properties implemented have been discussed earlier in Chapter 3. Assessment of a long disbond length, the effects of joint stiffness imbalance, and edge thickness variations were performed to support the experimental design, presented in the next chapter. The work conducted in this chapter mainly focuses on the procedure to assess the disbond tolerance of metallic parent materials subjected to tension-tension fatigue loading. Although the current analysis applies to both adhesively bonded joints and patch repairs, the discussion below will primarily focus on bonded patch repairs.

4.2 Loading and Boundary Conditions

The geometry of the DOTES specimen used in this chapter was presented earlier in Figure 3.4, section 3.2. The boundary conditions shown in Figure 4.1 were used to predict the load carrying capacity and determine the SERR components of the joint. Later in

Chapter 5, the full specimen model (Figure 4.1d) will be used to analyse the asymmetry disbond propagation. All specimens were modelled using two-dimensional four-node linear plane-strain quadrilateral elements.

For the double overlap fatigue specimen (DOFS) presented in Figure 4.1a, the total overlap length was 90 mm. Similarly, the overlap length of the skin doubler specimen (SDS) shown in Figure 4.1b, was 90 mm with an extended grip region of 50 mm. The total overlap length of the double overlap tapered end specimen (DOTES) was equivalent to the summation overlap length of the DOFS and the SDS specimen.

Ideally, the boundary condition of the DOFS specimen was equivalent to the left half of the DOTES specimen (symmetry condition), whilst the boundary condition of the SDS specimen was equivalent to the right half of the DOTES specimen (symmetry condition). For the DOFS specimens, disbond was initiated and propagated from the gap region whereas disbond was initiated and propagated from the tapered end for the SDS specimens. Whereas for the DOTES specimens, disbond was initiated from either the gap end or tapered region up to the ultimate failure of the joint.

Details of disbond initiation and propagation from the gap region and tapered end were presented in Figures 3.10 and 3.11 in Section 3.4.2.

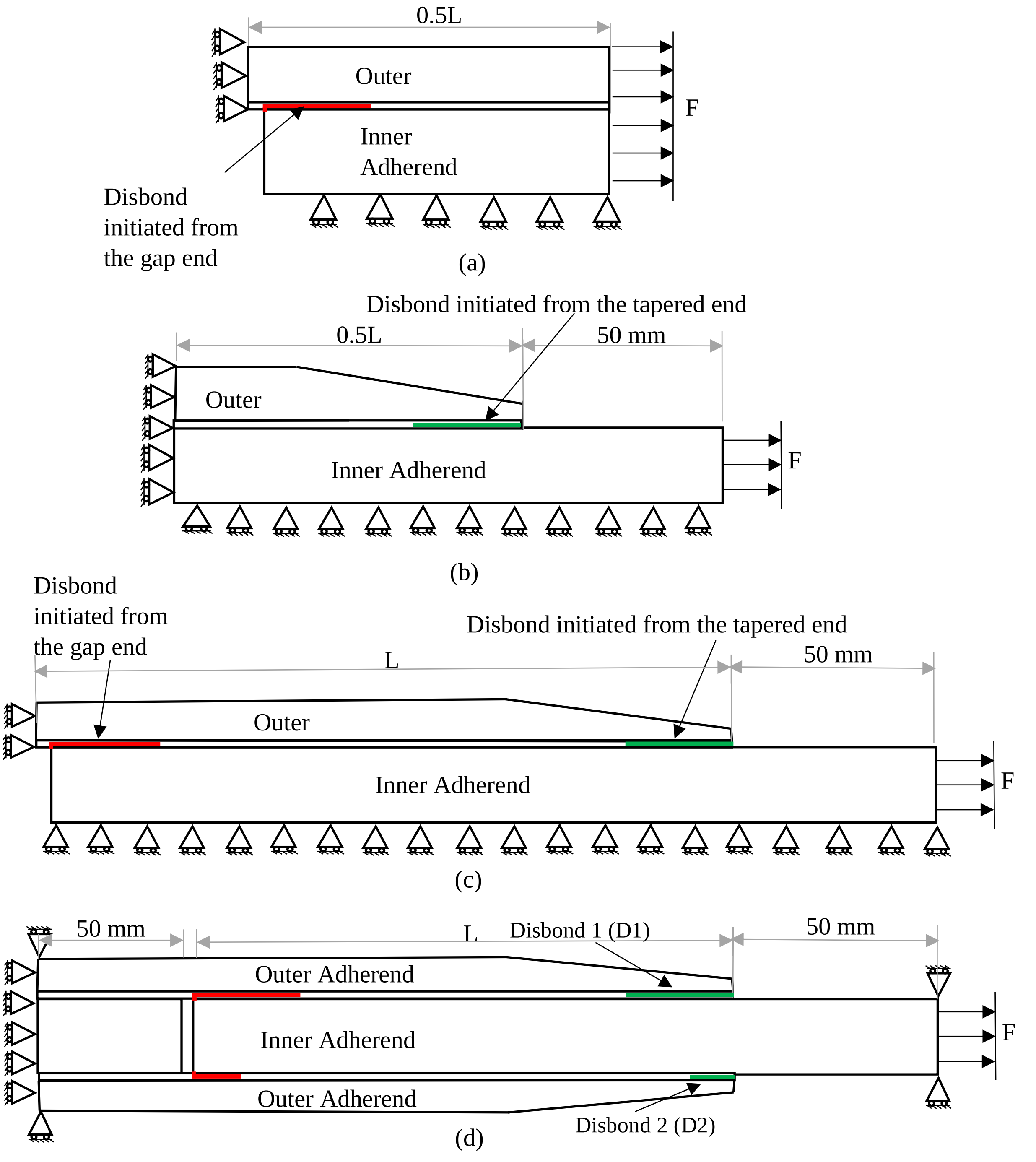

Figure 4.1: Loading and boundary conditions for: a) the DOFS, b) the SDS and c) quarter model of the DOTES (symmetry disbond propagation) d) full model of the DOTES (asymmetry disbond propagation).

4.3 Assessment of Residual Static Strength of a Joint with Various Disbond Crack Length

The failure load of a balanced joint configuration predicted using the analytical approach were defined in Section 3.4.1. With the values of E, t_o, τ_p, η, γ_e and γ_p defined in Tables 3.3 and 3.4, the failure load of a pristine specimen was predicted. to be 36.8 kN. As mentioned in Section 3.4.2.2, the issue of mesh dependence was handled by using the characteristic distance approach. The characteristic distance was so determined that the predicted strength of a pristine specimen (disbond crack length equals zero) using FE analysis was equivalent to the failure load predicted using the analytical approach.

The load carrying capacity of the DOFS, SDS, and DOTES were predicted using the adhesive element failure criteria defined in Section 3.4.2.2 and the results are presented in Figure 4.2 for comparison. The results were consistent between these three specimens. As described earlier, the major difference between these three analyses was that with DOTES analysis, the disbond could propagate up to the ultimate failure of the joint. This is an essential part of the procedure to determine the fatigue life of the joint.

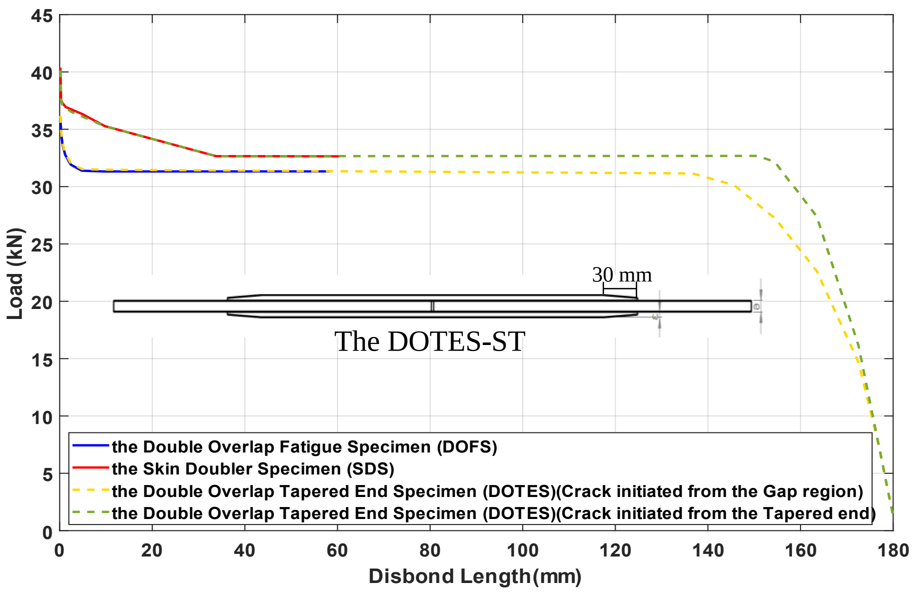

Figure 4.2: The load carrying capacity of the DOFS, the SDS, and the DOTES-ST.

For disbond initiated from the gap region of the specimen (damage-tolerant zone), the residual strength would reduce as the disbond length increases from zero (initiation) to 6 mm; then subsequently became steady up to 150 mm. On the other hand, for disbond initiated from the tapered end (safe-life zone), the residual strength would reduce as disbond length increased up to 30 mm (where the outer adherend end taper terminates). The curve then became flat as the disbond length further increased. It is mindful to note that this analysis was done for specimen design with a tapered length of 30 mm (Batch 1 specimen design). It was observed that the residual strength rapidly decreased as the disbond length approached the total overlap length of the specimen. In both cases, the data showed a significant reduction of the residual strength as disbond length increased from the initial point on the curve (0 mm disbond length).

In terms of progressive failure assessment for joint under a static load, the DOTES curves in Figure 4.2 suggested that the disbond growth in both cases (disbond initiates from the gap region or tapered end) was unstable. Particularly with a static load that could initiate the disbond or propagate a short disbond crack would rapidly rapture the joint. Thus, the fatigue peak load must be below the residual strength to avoid any instant static failure while loaded under fatigue loading.

When disbond propagated to the length for which the residual strength was equivalent to the fatigue peak stress, it would result in occurrence of a fatigue failure. Nevertheless, it is possible to have slow disbond growth under fatigue loading that is dependent on the ratio between the fatigue peak load and the residual strength. A good indication of the growth rate could be determined by the SERR assessment which was described in Section 4.4.

The load-displacement curves of the DOTES-ST for disbonds initiated both from the gap region and tapered end are plotted in Figure 4.3. Each curve represents a case where the DOTES-ST has a particular existing disbond length and the load was applied to the specimen (in the way as shown in Figure 4.1c) from zero up to the load that would propagate the existing disbond crack (residual strength). Three disbond lengths, namely 6 mm, 120 mm and 165 mm were selected based on the load carrying capacity prediction of the DOTES-ST in Figure 4.2 (one in initial higher load range, one in constant load range, and one in final load drop range).

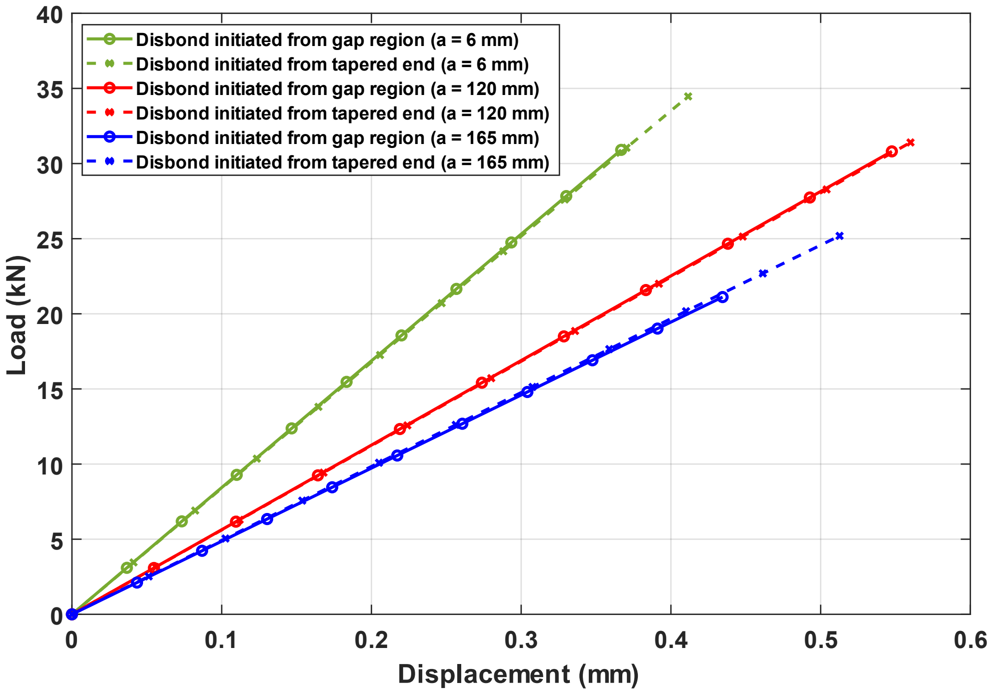

Figure 4.3: Load vs displacement curves of the DOTES-ST with various disbond lengths (a) in both cases of disbond initiated from gap region and tapered end.

In addition, Figure 4.3 showed that the compliance of the joint (inverse of the slope of the curves) was decreasing as the disbond crack length increased, and the maximum displacement before the disbond was propagated increased initially and eventually decreased as the disbond crack length increased.

4.4 Determination of SERR

The strain energy release rate (SERR) was determined using two different constant amplitude fatigue test conditions, called constant amplitude load (load control) and constant amplitude joint end displacement (displacement control) methods. A generic fatigue loading was considered to simulate the fatigue loading analysis by taking into account the fatigue peak load and R-ratio. Moreover, the maximum fatigue peak load was determined by the correlation of the static residual strength and the static strength safety factor. A detailed description of the fatigue life approach is discussed in Section 4.7.

4.4.1 Load Control

A load of 20 kN (slightly lower than the predicted load in Figure 4.2 divided by a safety factor of 1.5 in the range of disbond length up to 140 mm) was applied through the entire disbond length variations. Note that for a different load applied, the SERR plots would have a similar trend as with the 20 kN. Furthermore, Wang et al. *[16]* performed the fatigue test using SDS specimens with the same configuration as described in Section 4.2. The authors observed that a fatigue peak load of 17 kN could propagate the disbond crack.

The SERR results of the DOTES for both cases with disbond initiated from the gap region and disbond initiated from the tapered end are presented in Figure 4.4. In Figure 4.4a, the analysis results of disbond initiated from the gap region indicated that Mode I was insignificant compared to Mode II. Thus, only SERR of Mode II was considered.

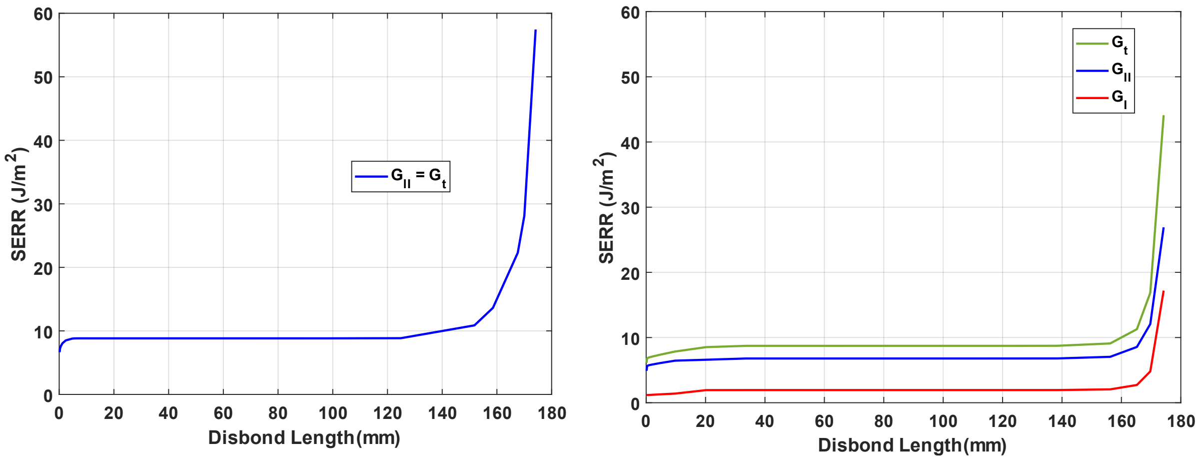

(a) (b)

Figure 4.4: Strain Energy Release Rate a) disbond initiated from the gap region b) disbond initiated from the tapered end.

Different phenomenon was observed for disbond initiated from the tapered end. As presented in Figure 4.4b, the results for disbond initiated from the tapered end signify that Mode I provided 22% contribution to the total SERR. Also, from Reference [37], the ratio between G_{Ic} and G_{IIc} is 0.26:1 (1.3 kJ/m^2 : 5 kJ/m^2). Thus, in terms of the ratio to the critical values of the SERR, for disbond initiated from the tapered end, Mode I and Mode II have nearly equal contributions (1.08:1).

As illustrated in Figures 4.4 a and b, the SERR curves initially increased as the disbond propagated. They then became steady when the disbond lengths reached a few millimetres. The curves continue to be flat or rise slowly up to 120 mm disbond crack length, followed by the rapid rise of SERRs.

Since the SERR was considered as the dominating factor to determine the fatigue disbond growth rate, the analysis presented in Figure 4.4 indicated that the disbond growth rate would initially increase as disbond propagates. Stable disbond propagation could then be expected with a large range of disbond length before the disbond rapidly propagated. Thus, the results indeed suggested that the slow growth approach was possible even when a disbond crack was significantly long.

4.4.2 Displacement Control

A fixed displacement which corresponded to an applied load of 20 kN where a small disbond length of 0.15 mm existed in the specimen was applied through the entire SERR calculations. As shown in Figure 4.5, the SERR predictions based on displacement control have different trends from those with load control. This phenomenon was caused due to the decreasing load with the displacement control as the disbond length increased, since the disbond would reduce the specimen rigidity along the loading direction. In contrast, with the load control technique, the displacement would increase as the disbond propagated.

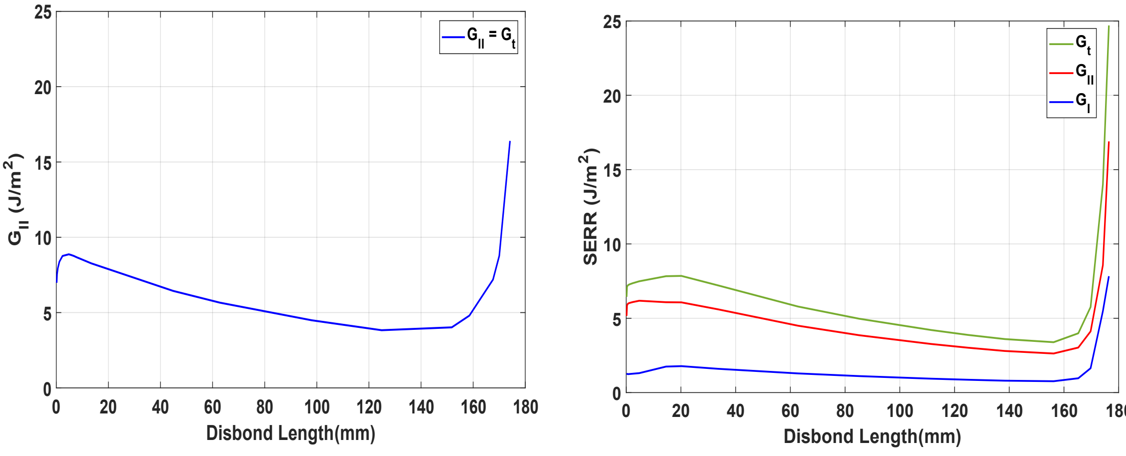

(a) (b)

Figure 4.5: SERR assessment using displacement control a) disbond initiated from the gap region and b) disbond initiated from the tapered end.

For disbond initiated from the gap region with a disbond length of 0 to 3.5 mm, the SERR value increased which subsequently indicated that the disbond growth rate would increase as the disbond length increased. However, with the disbond length of 3.5 mm up to at least 120 mm, the SERR value decreased. The analysis suggested that the disbond growth rate would decrease as the disbond length increased. Consequently, within this range, the disbond crack would propagate in a stable manner under fatigue loading [169].

With the implementation of displacement control technique, this could provide a significant implication to the case of local or partial width disbond (load shedding effect). From the results plotted in Figure 4.5, this technique was an additional factor to suggest that stable disbond propagation was possible with a local disbond in the "safe life zone" as illustrated in Figure 4.6, where the effect of load sharing or redistribution to the adjacent region played an important role.

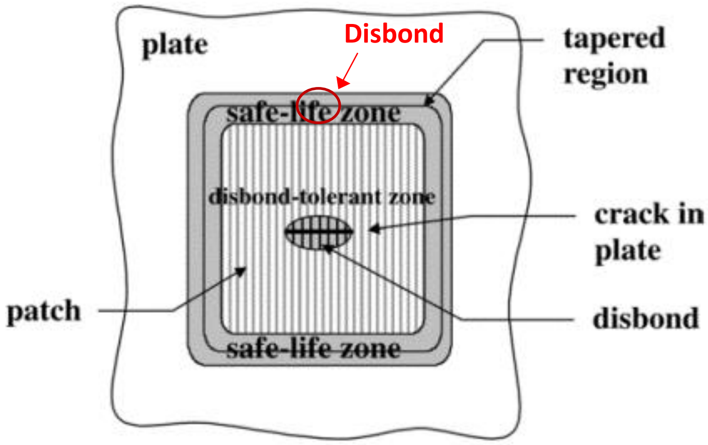

Figure 4.6: Illustration of local disbond [11].

This displacement control technique was meaningful only when applied to the full specimen (not the DOFS and the SDS specimens) that would reveal the effect of disbond crack growth on specimen rigidity reduction; and consequently, load or SERR reduction. Therefore, the DOTES specimen was valuable to be used in this analysis.

4.5 Effect of Stiffness Imbalance of Adherends

As described in Section 3.2.5, a study on adherend thickness variation was conducted. Three variations, including the baseline configuration were considered in this study. In Variation 1, the outer adherend thickness was increased from 3 mm to 6 mm.

Whilst in Variation 2, the inner adherend thickness was increased from 6 mm to 9 mm as specified in Table 3.1. The third variation was considered as the baseline configuration ($T_i = 2T_o$).

4.5.1 Load Carrying Capacity Assessment

The load carrying capacity analyses with various disbond lengths estimated using the element failure criteria as described in Section 3.4.2.2 are represented in Figure 4.7. The element sizes used were identical for all adherend thickness variations.

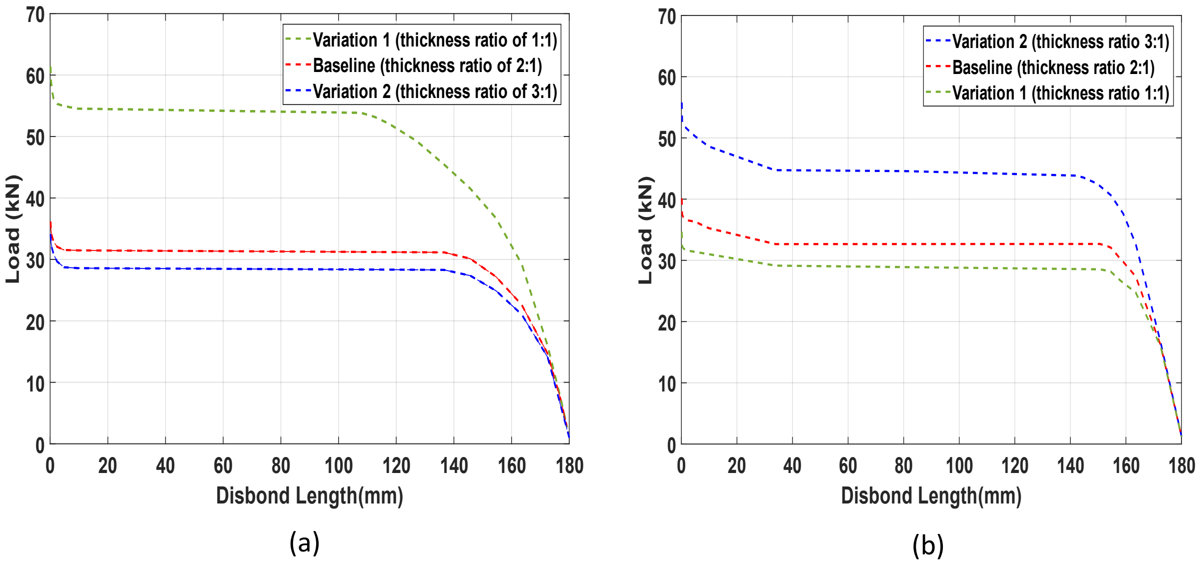

Figure 4.7: Variation of load carrying capacity with disbond initiation location: a) from the gap region b) from the tapered end.

The results plotted in Figure 4.7a (disbond initiated from the gap region) suggested that for disbond initiated from the gap region, the load carrying capacity of the adhesive bonding would reduce when increasing the inner adherend thickness. In contrast, the results presented in Figure 4.7b (disbond initiated from the tapered end) showed that the load carrying capacity of adhesive bonding would reduce when increasing the outer adherend thickness. Therefore, increasing the thicknesses of central adherend and outer adherend indeed provided a way to reduce the strength of the joint with disbond cracks initiated from the gap region and tapered end, respectively.

4.5.2 *Strain Energy Release Rate Assessment*

The results of SERR calculation with adherend thickness variation are presented in Figures. 4.8 and 4.9. A constant load of 20 kN was applied through all the inner adherend thickness variations. Since Mode I SERR value (G_I) was insignificant compared to that of Mode II (G_{II}) for disbond initiated from the gap region, only calculation of G_t ($G_I + G_{II}$) is presented as plotted in Figure 4.10a. In this case $G_t = G_{II}$.

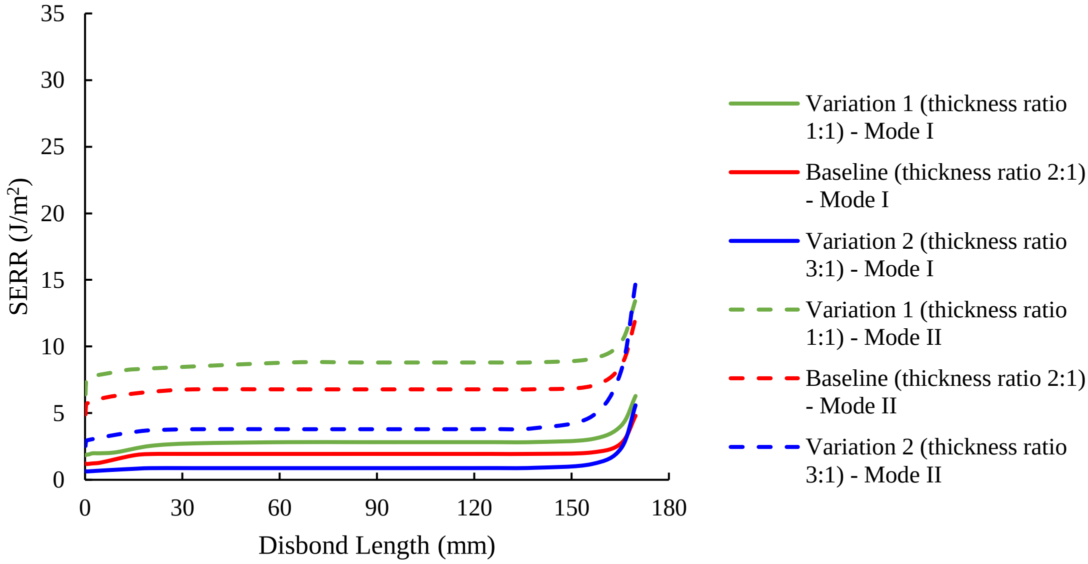

Figure 4.8: Variation of Mode I and Mode II of the SERRs for disbond initiated from the tapered end.

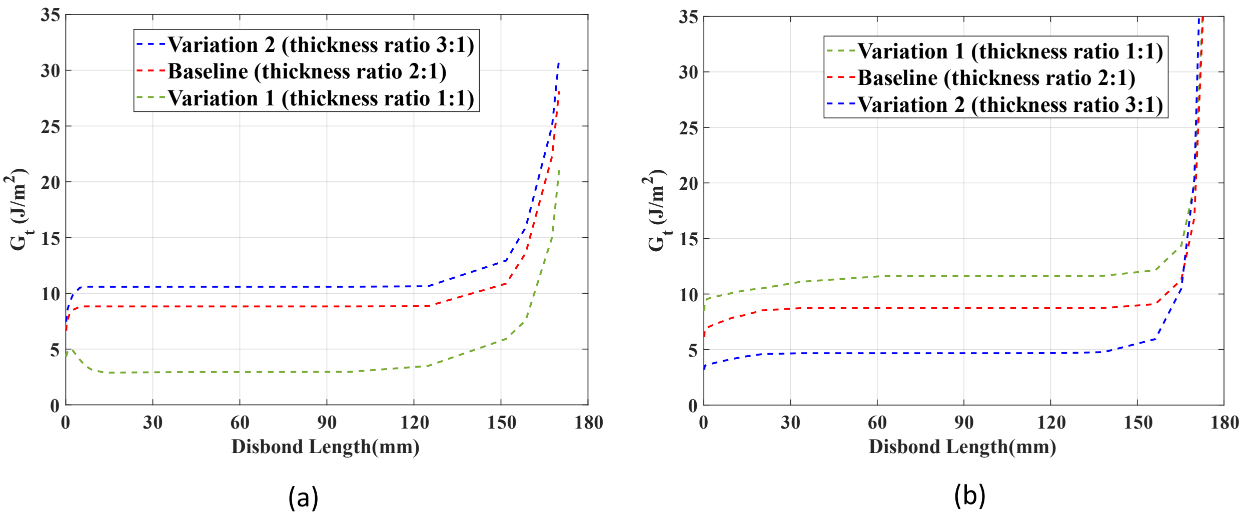

Figure 4.9: Variation of total SERR a) disbond initiated from the gap region (Note that $G_{II} = G_t$) b) disbond initiated from the tapered end.

For the case of disbond initiated from the tapered end, Mode I contributes about 22% of the total SERR for all the three adherend thickness variations (see Figure 4.8). That is, the ratio between Mode I and Mode II components remained unchanged even with varying adherend thicknesses.

The results of total SERR for both cases of disbonds initiated from the gap region and tapered end are plotted in Figure 4.9. As shown in Figure 4.9a, for disbond initiated from the gap region, when the central adherend thickness was increased from 6 mm to 9 mm (thickness ratio 3:1), the total SERR was increased by about 20% in the range where the disbond crack length was over 6 mm; whilst for the disbond initiated from the tapered end (Figure 4.9b), when the outer adherend thickness was increased from 3 mm to 6 mm (thickness ratio 1:1), the total SERR was increased by about 33%. Thus, increasing the thicknesses of central adherend and outer adherend also provided a way to increase disbond growth rates of disbond cracks initiated from the gap region and tapered end, respectively.

4.6 Effect of Edge Thickness on Peel and Shear Stresses

A distributed load of 1.4 kN/mm was applied to the end of the inner adherend, which corresponds to a 28 kN load on the full model. The shear and peel stresses in the middle line of adhesive layer for pristine specimen (specimen without disbond) are presented in Figure 4.10. The peel and shear stresses were analysed at 0.225 mm from the edge. The analyses were done with edge thickness ranging from 0 to 3 mm. 0.1 – 0.15 mm edge thickness was considered to be the maximum fabrication feasibility.

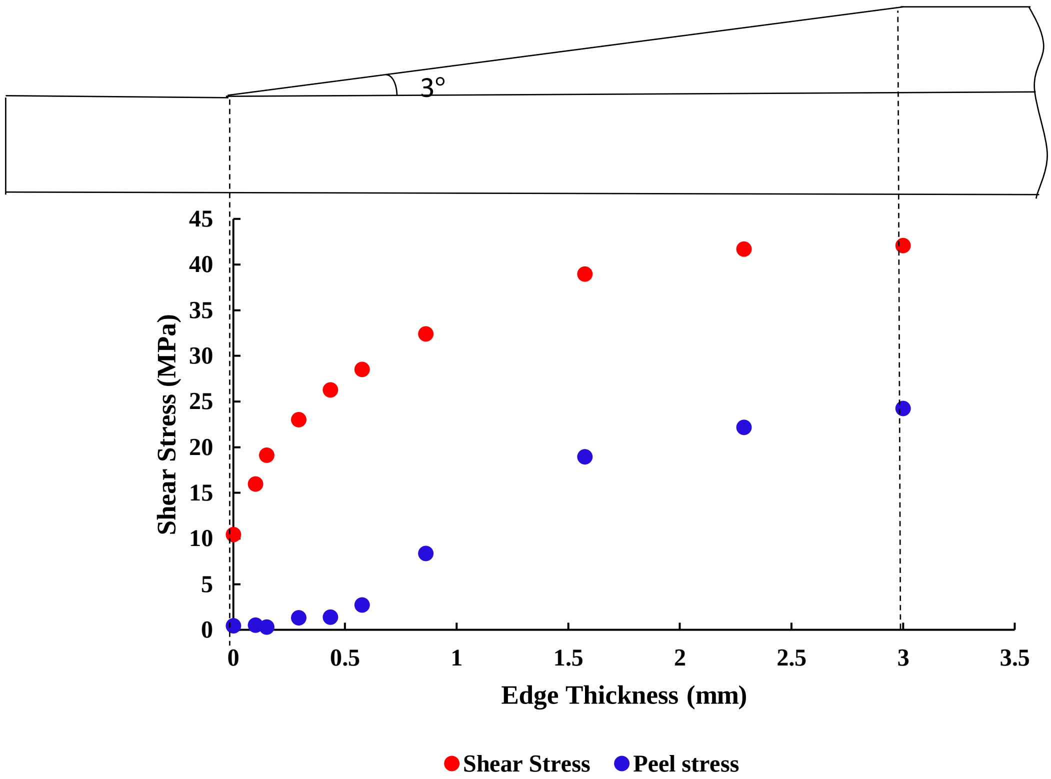

Figure 4.10: Peel and shear stress plot with various edge thicknesses ranging from 0 to 3 mm, force per unit width 1.4 kN/mm.

It is shown in Figure 4.10 that the peel stress was negligible for the edge thickness ranging from 0 to 0.15 mm. It then increased at an edge thickness of 0.3 mm up to 3 mm. As discussed in Section 3.2.2, the edge thickness used for the preliminary design of the DOTES-ST was 1.5 mm. High positive peel stress was observed with this designated edge thickness. This high positive peel stress could be more detrimental than high shear stress, which would assist disbond propagation at this region [170]. Therefore, with the designated edge thickness for the DOTES-ST, disbond might tend to initiate and propagate from the tapered end.

The shear and peel stress distribution with various disbond lengths initiated from the tapered end and gap region are plotted in Figure 4.11 (the arrow sign illustrates the direction of disbond initiation and propagation). In Figure 4.11a, the stresses distribution of the DOTES-ST with an edge thickness of 1.5 mm were presented, which was used in this chapter's discussion. On the other hand, Figure 4.11b illustrates the stresses distribution when the edge thickness reaches the maximum fabrication feasibility (0.15 mm edge thickness).

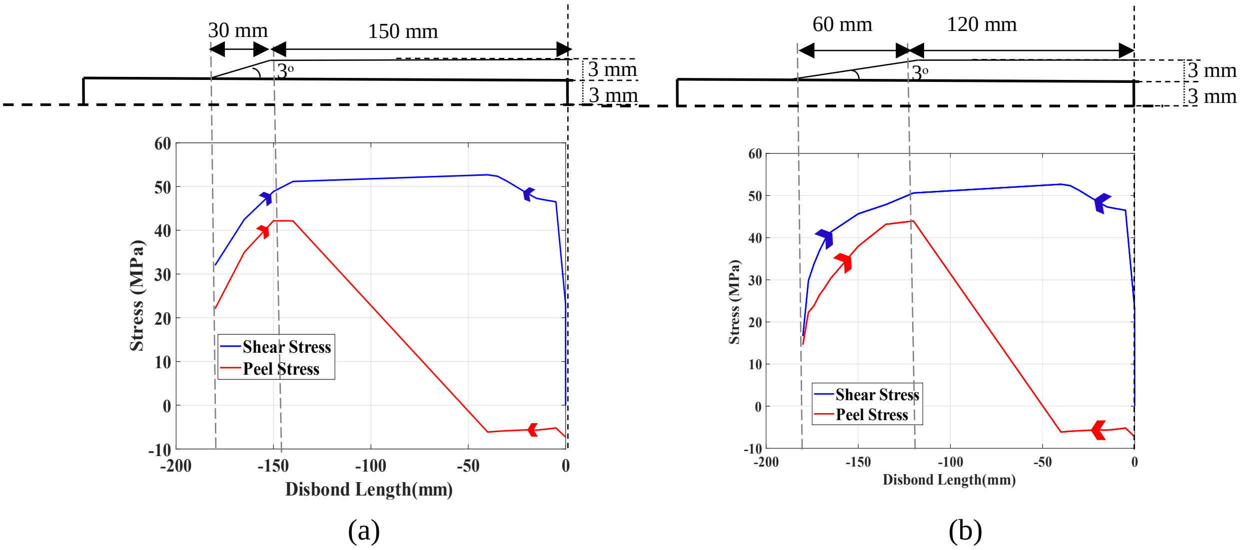

Figure 4.11: Shear and Peel stresses distribution with various disbond lengths along the mid-plane of the adhesive layer a) 1.5 mm edge thickness (The DOTES-ST) b) 0.15 mm edge thickness (The DOTES-LT); load/unit width = 1.4 kN/mm.

The results indicated that reducing the edge thickness would consequently reduce the shear and peel stresses by about 40% for disbond initiated and propagated from the tapered end. Furthermore, the peel and shear stresses increased with disbond propagation in the tapered region. After passing the tapered region, the shear stress has reached its steady state. The peel stress behaved similarly with the shear stress in the tapered region. However, it decreased towards the middle gap of the joints since the middle region was dominated by Mode II (shear only).

In the case of disbond initiated and propagated from the gap region, the results remained constant despite changing the edge thickness. Furthermore, within this gap region, resembling the crack, the shear stress increased to a constant level having that the peel stress was initially negative.

4.7 Discussion

4.7.1 Fatigue Life Prediction Approach

The fatigue life of adhesive bonded joint could be predicted through three components. The first component was to determine the SERR value as a function of disbond length (using the approach described in Section 3.4.2.3 above). The second component was to establish a relationship (modify Paris Law) between the fatigue disbond growth rate and SERR value through fatigue experiment, which will be discussed in Chapter 5. Achieving these two components would allow the disbond length to be estimated as a function of number of fatigue cycles through an integration calculation.

The last component was to determine the residual strength of the joint as a function of disbond crack length (using the approach described in Section 3.4.2.2). With the addition of the third component, the fatigue life can be determined, that is, when the disbond length reached its critical value with which the residual strength was equivalent to the fatigue peak load. Note that the analyses performed in this chapter to calculate the residual strength of the joint should be considered as preliminary. The issue of mesh dependence in strength prediction using adhesive element failure criteria (refer to Section 3.4.2.2) could be further assessed and calibrated against experimental results.

4.7.2 Slow Growth Approach

The fatigue life of a bonded joint can be predicted using the procedure described above. The applicability of slow growth management approach was further complicated by the factors of static strength safety margin requirement (including various knockdown factors) and defect tolerance requirement. The static strength safety margin requirement means the residual strength in the presence of a disbond must be at least 1.5 times[1] the fatigue peak load (otherwise a repair to, or replacement of, the joint would be required). The defect tolerance requirement means an NDI detectable disbond size should be assumed when the pristine specimen strength was estimated. These factors need to be considered for a practical application to a slow growth approach. Only within these constraints and if the fatigue loading was still able to propagate the disbond crack, could the slow growth approach be utilised.

The above description regarding the implementation of slow growth approach can be illustrated in Figure 4.12. This figure helped explain an important aspect of this study, that is, traditionally people focused on the early stages of damage (disbond) growth, whilst the damage considered in this research was far beyond that. For example, if we have a typical fatigue peak load level as the dashed line in Figure 4.12, Category 2 damage as defined in FAA AC 20-107B [1] (refer to Figure 4.13) was within Points c and d. The region near Point c within Points a and c range and the region between Points c and d were critically important for determining allowable fatigue life and inspection interval.

1 Residual strength needs to 1.5 times design limit load, or below this but above design limit load only for a short while which can be confidently picked up by scheduled inspection.

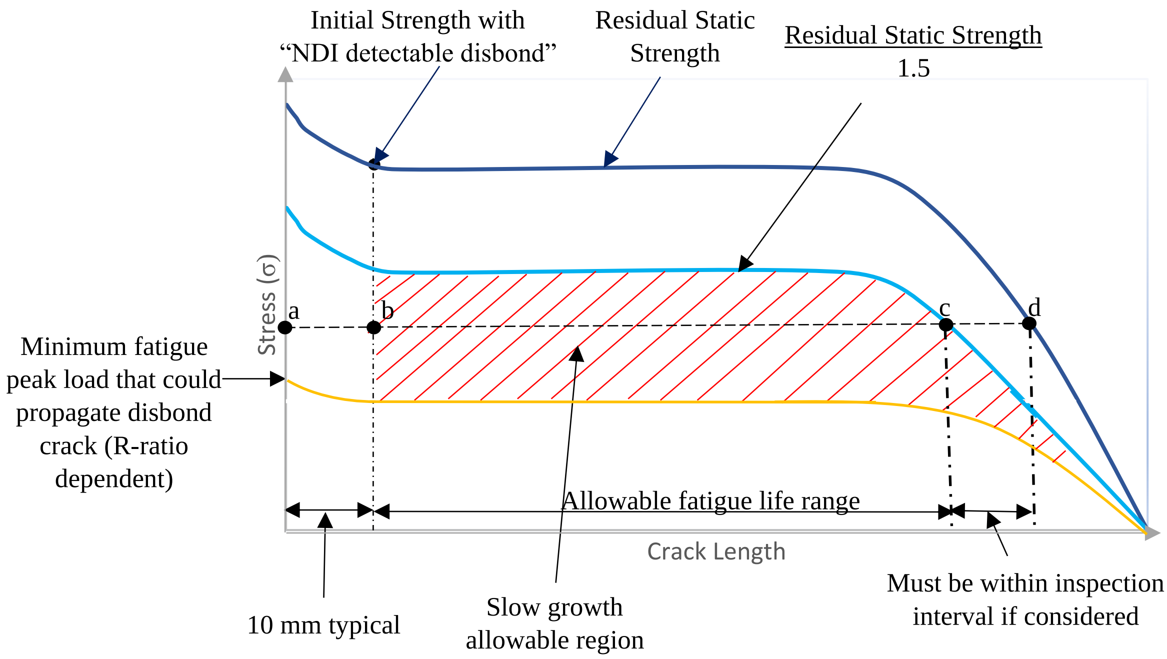

Figure 4.12: Illustration of Slow Growth Approach.

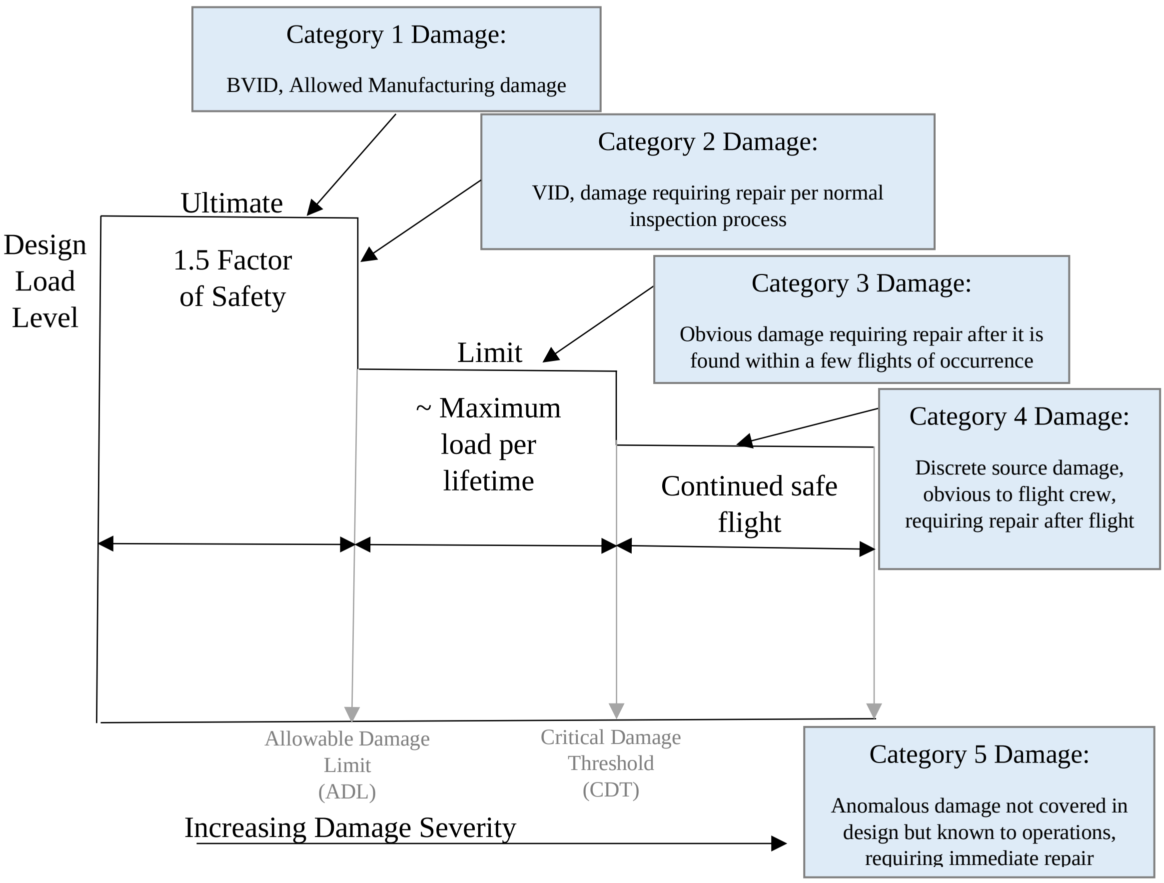

Figure 4.13: Schematic diagram of design load levels versus category of damage severity (Adapted from [9]).

4.7.3 Joint Failure Mode

The work conducted in this chapter focused on the investigation of adhesive failure with an aim to design a specimen which has a disbond fatigue growth without fatigue failure of the inner adherend or outer adherend. The approach described in Section 4.5 can be used to control the failure mode.

The study in this chapter was conducted to provide an approach that accurately estimate adhesive failure behaviour, which will then contribute to the proper design of a desirable adhesive joint in Chapter 5.

4.8 Summary

- The residual static strength of the joint as a function of disbond crack length was established using the finite element method with adhesive element failure criteria and progressive failure analysis. The results indicated that under the static load, the disbond growth in both cases (disbond initiates from the gap region or tapered end) was unstable. This happened particularly with a static load that can initiate the disbond or propagate a short disbond crack that would rapidly rapture the joint.
- A fatigue failure would occur when the disbond grows to the length in which the residual strength was equivalent the fatigue peak stress. In addition, when a fatigue loading with the peak load below the residual strength curves was considered, it would result in a no instant static failure.
- The SERR as a function of disbond length was assessed using the VCCT method. The analysis indicated that for a joint having sufficient static strength to propagate disbond with a safety margin under a typical fatigue loading, the disbond growth would be stable within the significant length range, which was initiated from either "disbond tolerant zone" or "safe-life zone".
- For a joint with a 180 mm overlap length and a tapered length of 30 mm, as considered in discussions of this chapter, the stable disbond length range was over 130 mm.
- The SERR results under constant amplitude end-displacement loading showed a significant decrease in SERR value within the specified disbond length range as the disbond length increased. The results suggested that for a local or part width disbond ("safe life zone"), the load shedding effect (load sharing or redistribution to the adjacent region) would further slow the damage growth.

- The study on the effect of rigidity imbalance between inner adherend and outer adherend showed that varying the adherend thickness could affect the adhesive bond strength and disbond growth rate.
- The study on the effect of edge thickness indicated that by reducing the edge thickness to 0.15 mm (maximum fabrication feasibility), the shear and peel stresses would reduce by 40% as compared to the specimen design used in this chapter (1.5 mm edge thickness).

The last two points will provide meaningful information in designing the experimental validation. In Chapter 5, the numerical approach established in this chapter are implemented and further assessed.

Chapter 5

Fatigue Disbond Growth Rate Correlation of the DOTES Specimens

Preface

This chapter details the process to establish the modified Paris law correlation which is used to determine the fatigue life of the joint. The material properties and specimen designs implemented were previously discussed in Chapter 3. The numerical assessment of disbond slow growth management strategy for metallic joints performed in Chapter 4 was further expanded for implementation and assessment in this chapter. Static tests of the designated bonded joint were carried out first to calibrate the mesh size used in finite element (FE) modelling. As follow, fatigue tests were carried out to measure the disbond growth rate of the double overlap tapered end specimen (DOTES). By correlating the measured disbond growth rate and computationally determined strain energy release rates (SERRs) of the joint, the modified Paris law relationship was established. Fatigue life predictions based on the design allowable was considered. Later in Chapter 6, the applicability of slow growth management strategy is further expanded using an active CZE technique to predict the disbond propagation (in an un-predefined manner) in the 3-D analysis of wide bonded metal joint specimen.

The research works presented in this chapter are part of a paper entitled "Experimental and Computational Assessment of Disbond Growth and Fatigue Life of Bonded Joints and Patch Repairs for Primary Airframe Structures", published in *"International Journal of Fatigue"* (DOI: https://doi.org/10.1016/j.ijfatigue.2022.106776).

5.1 Introduction

This chapter presents the implementation and assessment of a framework for the disbond slow growth management strategy for metallic joints which has been carried out earlier in Chapter 4. The specimen preparation including the surface treatment technique and specimen pre-conditioning procedure was discussed in Section 5.2.

The residual strength of the joint as a function of disbond length was further assessed by conducting the static residual strength tests under room temperature-dry (RD) and hot-wet (HW) conditions. These tests were performed to calibrate and validate the FEM prediction model. Subsequently, the allowable fatigue load range, particularly the upper limit of the fatigue peak load could be determined.

The relationship between the disbond growth rates and disbond strain energy release rates (modified Paris Law) was established by (i) computationally determining strain energy release rates as a function of disbond lengths and loads, (ii) conducting fatigue tests and measuring the disbond growth rates at different disbond lengths and fatigue loads, and (iii) correlating the computational and measured results.

Using the established modified Paris law formulation, the disbond length as a function of cycle count was estimated through an integration calculation. As for this reason, the fatigue life of the joint could be determined by considering the instant static failure of the joint, that is, when the disbond length reached the critical value in which the residual strength was equivalent to the fatigue peak load.

5.2 Specimen Preparation

All specimens were prepared by trained staff at Defence Science and Technology Group (DSTG), Melbourne. The samples from each batch were required to pass a Boeing Wedge Test (BWT). Detailed explanations about the surface treatment procedures implemented and post-surface treatment process will be discussed in Sections 5.2.1 and 5.2.3, respectively.

The designated coupon specimen was tested in hot-wet environment to identify the adhesive material behaviour in the aircraft service environment. Details of the test matrix for the DOTES-ST (double overlap tapered end specimen – short tapered) and the DOTES-LT (double overlap tapered end specimen – long tapered) specimen design are explained in Section 5.2.5. The last sub-section discussed the static and fatigue testing procedures applied for the experimental program.

5.2.1 Surface Treatment

The surface preparation technique prior to adhesive bonding was the most crucial part of bonded repair application process. The aim was to remove the weak boundary surface layer and create an oxidised layer which made the surface compatible for adhesive bonding [171]. The lack of any available Non Destructive Inspection (NDI) methods to determine the adhesive bond quality conveyed that skills of the technicians were considered as the primary source to control the bond quality [172].

Defence Science and Technology Group (DSTG) has done numerous investigations on bonding procedures to determine if there was a deterioration effect on the wedge test results [172]. These were done according to the Royal Australian Air Force (RAAF) engineering standard recommendation to provide a more robust system in maintaining the quality of bonded patch repairs. To obtain good quality of bonding, specialised training on the surface treatment was performed at DSTG along with support from the experienced technical staff. The standard surface treatment [37] used by the Australian Defence Science and Technology Group (DST Group) was:

1. The material was cleaned using cleanroom wipes (Boeing distribution services, Australia) wetted with Methyl-Ethyl-Ketone (MEK) by wiping unidirectionally, first in 0^{o} direction, then 90^{o} direction.
2. The surface was abraded using 'Scotch Brite' (Scotch-Brite 3M No. 447, 3M, Australia) pads soaked in MEK in unidirectional direction (0^{o} direction then 90^{o} direction).
3. The surface was cleaned using MEK soaked lanoline and lint-free tissues.
4. The surface was abraded using 'Scotch Brite' pad soaked in deionised/distilled water.
5. The surface was cleaned with distilled/deionized water-wetted cleanroom wipes.
6. The surface was water break tested by means of wetting the surface prepared with deionised/distilled water and observed that no areas were free of water.
7. The specimen was dried using a hot air gun or in an oven at $120^{o}C$ for 15 minutes.
8. The surface was grit-blasted (AccuBRADE-50, Coltronics, Australia) using 50 μm aluminium oxide and dry nitrogen propellant with a pressure of 450 kPa.
9. The grit-blasted surface was immersed in the silane solution for 15 minutes. (1% aqueous solution of γ-glycidoxypropyl-trimethoxysilane (γ-GPS) in distilled/deionized water was stirred for at least 1 hour).
10. The specimen was dried in an oven at $110^{o}C$ for 1 hour.
11. The specimen was cooled down, then proceed with adhesive bonding process straight away.

The above process was verified in this study using the Boeing Wedge Test (BWT) ASTM D3762 [147], which has been widely used as a quality control test to validate the manufacturing process for bonded joints in aircraft structures.

5.2.2 *Boeing Wedge Test (BWT)*

The wedge tests were manufactured from AL2024-T3 using FM300 adhesive film in a configuration as shown in Figure 5.1. The aluminium surface was prepared using the method defined in Section 5.2.1. In addition, the specimen was prepared and tested at 24 °C with 44.3% relative humidity, as measured by the equipment mounted on a wall in the room.

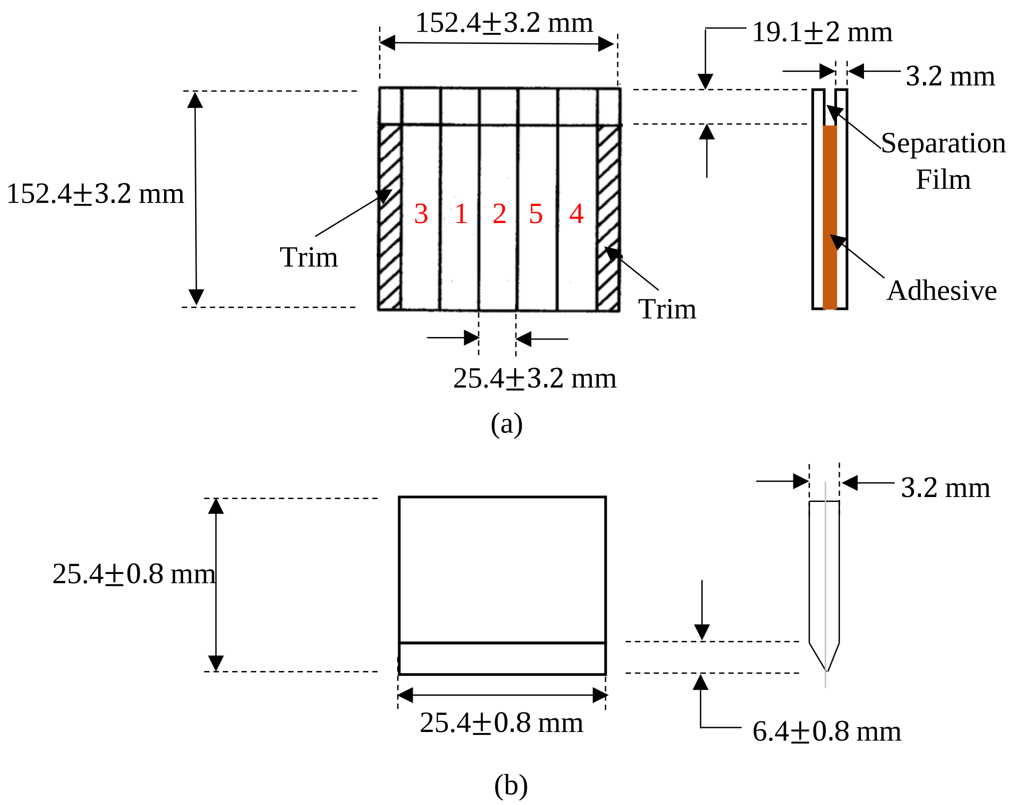

Figure 5.1: Wedge test specimen assembly a) specimen configuration b) wedge configuration (Adapted from [147]).

As per Cytec manufacturer's recommendation for FM300 adhesive [173], the panel was cured at 177 °C for 60 minutes in an autoclave at a pressure of 40 psi (275 kPa). To further the process, the panel was marked before it was trimmed into five specimens as illustrated in Figure 5.1a. It is worth considering the similarity between the surface preparation technique and the behaviours of FM300 and FM300-2k.

Based on RAAF engineering standard DEFAUST 9005-A and the associated document AAP 7021.016-2 [172], the acceptance criteria of a pristine wedge test was defined as follow:

i. The permissible crack growth in dry and humid conditions over 24 and 48 hours was 5.08 mm and 6.35 mm, respectively [174].

ii. The region of crack growth should exhibit more than 90% of cohesion failure for a technician to be qualified.

In this case, the cohesion failure indicated the failure where the crack propagated within the adhesive layer. Whilst adhesion failure was referred to failure where the crack propagates at the interface of the adhesive layer and aluminium.

The BWT results presented in Table 5.1 indicated that the quality of surface treatment has met the criteria defined above. The results indicated that the crack propagation was within the allowable crack growth range, as defined in the RAAF standard. After the crack propagation was monitored, the specimens were separated to identify the failure mode. A tiny area with voids was observed on specimens numbered 3 and 4 as shown by the red rectangular section in Figure 5.2. Nevertheless, after a detailed inspection of the two surfaces, both specimens exhibited equal composition with no silicon or aluminium detected, which suggested that the metallic side was covered by the epoxy adhesive. As for this reason, the voided regions did not result from the inadequate surface treatment.

Table 5.1: Results of Boeing Wedge Test manufactured at DSTG.

Specimen Number	Crack at 0 hours		Crack at 24 hours		Crack at 48 hours		Cohesive failure region
	Side 1 (mm)	Side 2 (mm)	Side 1 (mm)	Side 2 (mm)	Side 1 (mm)	Side 2 (mm)	
1	31.66	30.84	33.04	32.2	34.34	33.64	100%
2	31.47	30.2	31.68	31.05	31.95	32.27	100%
3	31.95	29.86	33.7	31.58	35.36	34.08	100%
4	31.84	30.72	32.45	32.75	33.92	34.22	100%
5	28.85	28.73	29.02	29.12	29.41	29.51	100%

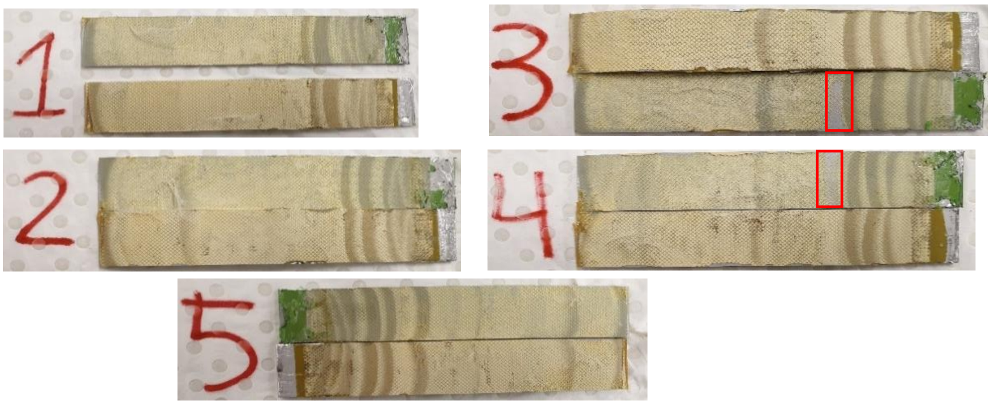

Figure 5.2: Images of BWT results after testing and separation (the specimens were marked following the configuration shown in Figure 5.1).

A factor that might cause the voided region was the peel angle generated during the separation of post failure process. A high peel angle might arise following the separation process, since there was difficulty in controlling the separation process using a hammer. This phenomenon was observed by Rider et al. [172] which showed that samples failed at high peel angles would show apparent adhesion failure. However, with a more comprehensive failure analysis, it generally indicates that the crack propagates in proximity to the adhesive metal interface, but still within the adhesive layer. Hence, it can be a proven example that the technician has been qualified for the surface treatment process.

5.2.3 Post Surface Treatment Process

The post surface treatment process of the DOTES specimen was slightly different as compared to the BWT specimen. With BWT, the specimen was trimmed from a panel where surface cleaning was not required, and as for the DOTES specimen, surface cleaning of the specimen was necessary. Figure 5.3 shows an example of the DOTES-ST specimen curing process. As shown in Figure 5.3b, the adhesive was squeezed out to the side of the specimen and the gap region (red rectangle section). This resulted in an uneven bond-line thickness through the overlap length of the joint as presented in Figure 5.3c.

(a)

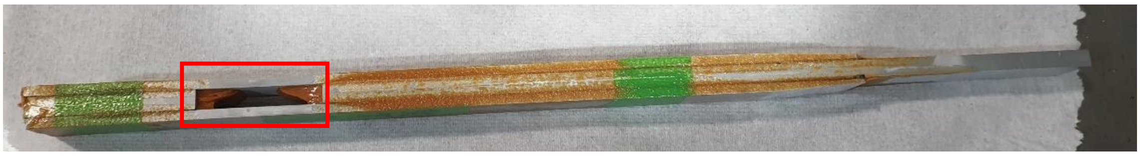

(b)

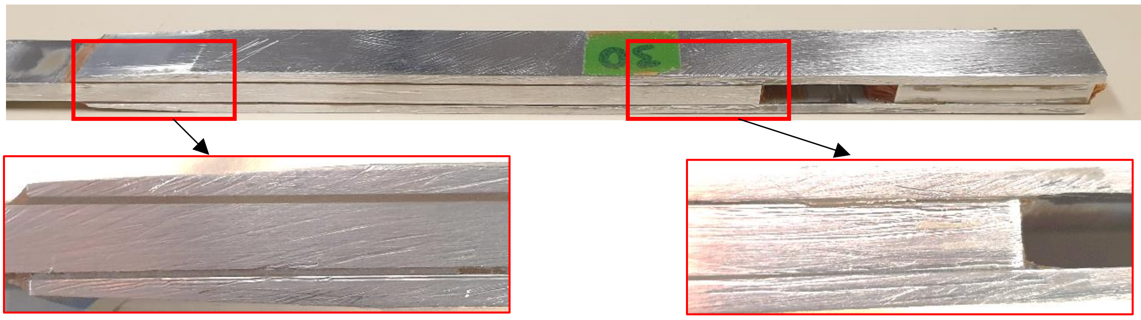

(c)

Figure 5.3: Post surface treatment process a) before curing b) after curing c) after surface cleaning process.

The uneven bond-line thickness during the curing process could be minimised by covering the specimen with Teflon tape as presented in Figure 5.4. With this technique, the adhesive was prevented to squeeze out during the curing process and helped minimise the process of sanding the side surface of the specimen. During the cleaning process, the adhesive spew fillet at the tapered region was carefully trimmed off using a file in a consistent manner. The fillet was left about 2 mm in length with a radius of 2 mm. The existence of spew fillet might reduce the stress concentration. However, the shape and size of the spew fillet among the specimens tested were inconsistent due to the handmade limitation.

Figure 5.4: Specimen covered with Teflon tape.

5.2.4 Specimen Pre-conditioning

According to CMH-17 [175], a relative humidity level of 85% was recommended as the upper-bound value for an aircraft service environment. The behaviour of adhesive material in the hot-wet environment (aircraft service environment) tend to be weaker and demonstrates stronger viscous behaviour [176]. Hence, the static loading capacity of an adhesively bonded joint was limited by its strength in such an environment.

The specimens were required to be pre-conditioned prior to testing. Theoretically, humidity conditioning was processed until tested specimens reach the equilibrium moisture content. However, special considerations apply for adhesively bonded specimens with metallic adherends. Since it might be impractical to wait for the entire adhesive bond line to fully reach equilibrium, a fixed time conditioning could be applied to ensure the critical regions of the joint (near the end tips) reached the moisture equilibrium state [177].

Higher humidity level (95% RH) could be used to accelerate the diffusion of moisture into the sample to reduce the conditioning time required [178]. Also, CMH-17 recommended conditioning at a level of below 82℃ for materials cured lower than 177℃. Thus, the specimens were conditioned at 71℃ with 95% relative humidity.

Based on DeIasi and Schultes calculations [179], the specimens would achieve the equilibrium moisture level within 30 days at 77 ℃ with 90% RH. Thus, a total of 7 specimens were pre-conditioned for 33 days to achieve the equilibrium moisture level. These specimens were used for both static and fatigue testing. Four specimens were used for static testing and the rest were used for fatigue test.

The inner and outer adherends including the grip region were weighed using a 0.001 g digital precision scale before bonding (before addition of the adhesive). The specimens were then weighed again after adding the adhesive and curing, to determine the actual weight of the adhesive layer. During the pre-conditioning process, the specimens were weighed every 3 days to assess the moisture content.

The percentage of moisture absorption in adhesive material was determined by the weight differences of specimens before and after pre-conditioning. It was calculated using Equation (5.1):

$$M_{\text{absorption}}\,(\%) = \frac{M_{final} - M_{initial}}{M_{initial}} \text{ x } 100 \tag{5.1}$$

The moisture absorption results of the pre-conditioned specimens are summarised in Table 5.2. It showed that the average moisture absorption was about 3%. This was consistent with the study conducted by DeIasi and Schulte [179], who reported that moisture absorption by FM300 adhesive at 77 ℃ with 90% RH was about 3%.

Table 5.2: Summary results for moisture absorption.

Specimen	$M_{absorption}$ (%)
120 mm pre-crack from Tapered End (TE) S-1	3.22
120 mm pre-crack from Tapered End (TE) S-2	3.69
120 mm pre-crack from Tapered End (TE) S-3	3.37
120 mm pre-crack from Gap Region (GR) S-1	3.05
120 mm pre-crack from Gap Region (GR) S-2	3.24
120 mm pre-crack from Gap Region (GR) S-3	3.6
150 mm pre-crack from Tapered End (TE) S-5	3.3

5.2.5 Specimen Design Matrix

Based on the analyses performed in Chapter 4, the following test matrixes were developed for static and fatigue testing. As the starting point, static tests of the DOTES-ST were carried out which was considered as the trial specimens. Subsequently, another set of static tests was conducted using the DOTES-LT specimen followed by the fatigue testing.

5.2.5.1 The DOTES-ST

A set of six specimens of baseline ($T_i = 2T_o$) configuration were manufactured and tested under static loading conditions. The specimen configuration used was based on the DOTES-ST specimen design with a shorter central adherend at the gripping area, as shown in Figure 5.5. However, this specimen design resulted in an uneven bond-line thickness at the gap region due to the adhesive that was squeezed out during the curing process, as shown in Figure 5.3c. The specimen was then re-designed by extending the central adherend at the gripping area, which was known as the DOTES-ST specimen (see Figure 3.4, Section 3.2.2).

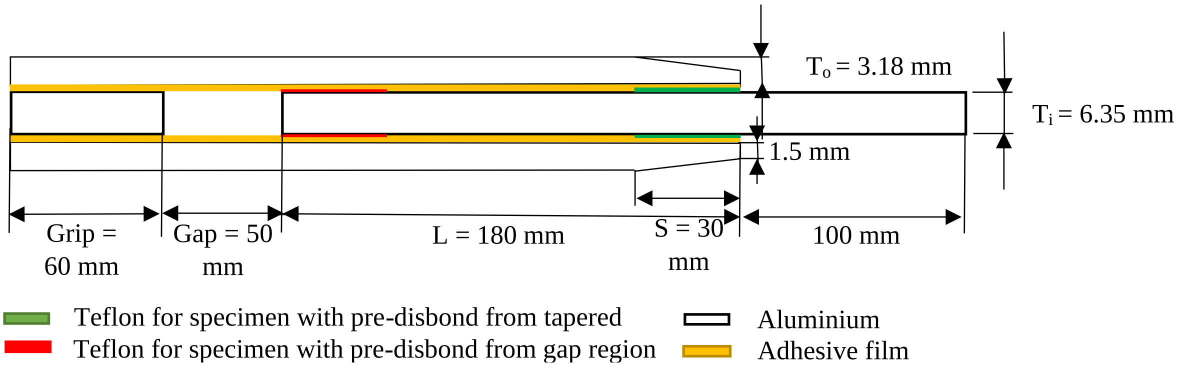

Figure 5.5: The DOTES-ST specimen configuration with shorter central adherend at the gripping area.

Another set of the DOTES-ST specimens was manufactured and tested under static loading conditions. As defined earlier in Section 3.2.5, the un-balanced ($T_i \neq 2T_o$) joint configuration was used for static testing at RD condition. Details of the DOTES-ST specimen configuration used for the un-balanced joint configuration was described in Section 3.2.2, Figure 3.4.

For specimens tested under static loading, cohesive failure of the adhesive was required. This failure pattern could only be achieved with a long artificial disbond length. Specimens with no disbond (pristine) or small artificial disbond length would fail in the inner or outer adherends. The selection of artificial disbond length was based on the residual strength analysis defined in Section 4.5.1 (load carrying capacity assessment on the effect of stiffness imbalance of adherends).

The test matrix that has been constructed for the baseline and un-balanced joint configuration are presented in Table 5.3.

Table 5.3: Test matrix of the DOTES-ST specimen.

Configuration	Description
Variation 1 – Thicker outer adherend (TOA)	30 mm pre-disbond from the Tapered end (TE)
	150 mm pre-disbond from the Tapered end (TE)
Variation 2 – Thicker inner adherend (TIA)	No pre-disbond (Pristine specimen)
	30 mm pre-disbond from the Gap region (GR)
	150 mm pre-disbond from the Gap region (GR)
Baseline	6 mm pre-disbond from the Tapered end (TE)
	6 mm pre-disbond from the Gap region (GR)
	30 mm pre-disbond from the Tapered end (TE)
	30 mm pre-disbond from the Gap region (GR)
	100 mm pre-disbond from the Tapered end (TE)
	100 mm pre-disbond from the Gap region (GR)

5.2.5.2 The DOTES-LT

A test matrix was developed for the static and fatigue loading conditions, presented in Table 5.4. As described earlier in Section 3.2.5, the un-balanced ($T_i \neq 2T_o$) joint configurations were used for static testing at room temperature and dry (RD) condition. For the baseline configuration (balanced joint), most of the specimens were used for fatigue testing in RD condition, and some other were used for static testing in Hot-Wet (HW) condition. For specimens tested under static loading condition, cohesive failure could only develop in those specimens with long pre-disbond length (shorter effective overlap length). Specimens with no disbond or small disbond length would fail in the inner or outer adherends. As the aforementioned, the pre-disbond length of static specimen was selected based on the residual strength plot performed in Section 4.3 (which showed the joint strength dropped when disbond length was 150 mm).

Table 5.4: Specimen matrix for static and fatigue tests.

Configuration	**Description**	**Number of specimens tested**			
		Static	**Fatigue**		
		RD[1]	**HW[2]**	**RD[1]**	**RW[3]**
Variation 1-TOA	150 mm pre-disbond from the Tapered end (TE)	2			
Variation 2-TIA	150 mm pre-disbond from the Gap region (GR)	2			
Baseline	6 mm pre-disbond from the Tapered end (TE)			2	
	6 mm pre-disbond from the Gap region (GR)			4	
	30 mm pre-disbond from the Tapered end (TE)			1	
	30 mm pre-disbond from the Gap region (GR)			5	
	60 mm pre-disbond from the Tapered end (TE)			2	
	60 mm pre-disbond from the Gap region (GR)			1	
	80 mm pre-disbond from the Tapered end (TE)			2	
	80 mm pre-disbond from the Gap region (GR)			2	
	120 mm pre-disbond from the Tapered end (TE)		1	3	2
	120 mm pre-disbond from the Gap region (GR)		2	3	1
	150 mm pre-disbond from the Tapered end (TE)		1		

Notes:
1. RD = Room temperature and dry
2. HW = Hot and wet
3. RW = Room temperature and wet

All the fatigue tests were conducted at room temperature, and most of those specimens used in the tests were dry specimens (not preconditioned in humidity environment). However, 7 specimens were pre-conditioned to see the effect of the moisture on the joint fatigue performance.

5.2.6 Testing Procedure

The static and fatigue tests were carried out using several servo-hydraulic testing machines. A detailed procedure of the static and fatigue tests is discussed in two-sub sections below.

5.2.6.1 Static testing

The quasi-static tests at RD and hot-wet (HW) conditions were carried out using INSTRON 8804 servo-hydraulic machine with 500 kN capacity. The machine was controlled by a computer using Bluehill software.

A crosshead displacement rate of 0.5 mm/min was applied. The displacement and load measurements were then recorded for each test. In regard to the hot-wet test specimen, a heater was used to obtain the test temperature of 80℃. A thermocouple was attached to the specimen surface during the test to control the test temperature within 80°C ±2°C.

5.2.6.2 Fatigue testing

The fatigue tests were carried out using the DOTES-LT specimen with INSTRON 8852 biaxial (100 kN capacity), servo-hydraulic testing machine. The system was controlled by a computer using Bluehill software.

The fatigue tests were performed in load control mode at a frequency of 5 Hz with a sinusoidal waveform. The load spectrum was maintained with constant amplitude tension-tension fatigue loading at a stress ratio ($R = \sigma_{min}/\sigma_{max}$) of 0.1. The peak stresses considered were in the practical load range for a joint i.e. not exceeding the nominal design limit load. The maximum stress was calculated based on the ultimate failure load obtained from the results of the static tests in Section 5.3.2. Further details of the applied cyclic load will be described in the fatigue test results section (Section 5.4).

The experimental setup for the fatigue test is depicted in Figure 5.6. The specimens were white painted and highlighted with a 1 mm interval along the side to facilitate measurement of the disbond propagation. The fatigue tests were carried out in two different conditions: a) with an anti-bending fixture and b) without the anti-bending fixture. Details of the test conditions are provided in Section 5.4. The tests without the anti-bending fixture resulted in severe asymmetry in disbond propagation. When the anti-bending fixture was used, a) Teflon films were inserted in between the anti-bending fixture and the specimen, and the hex screws were only finger tightened to minimise the friction during the test, and b) thread-locker (Loctite 222) was applied to prevent any thread loosening during the fatigue loading. The dimensions of the anti-bending fixture used are shown in Figure 5.7.

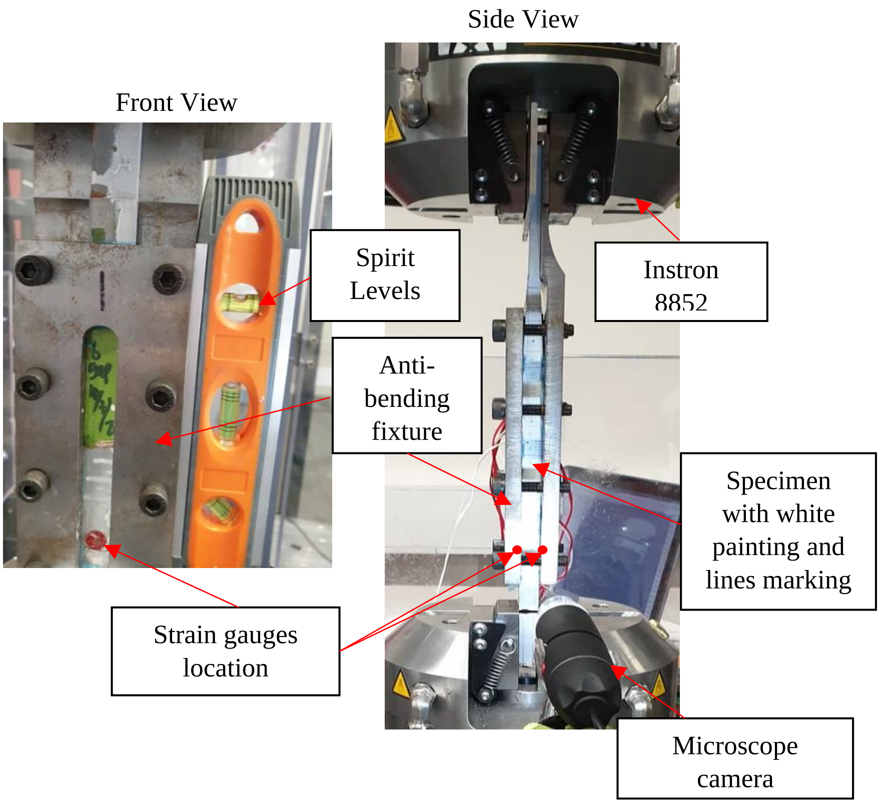

Figure 5.6: Experimental set up for fatigue testing.

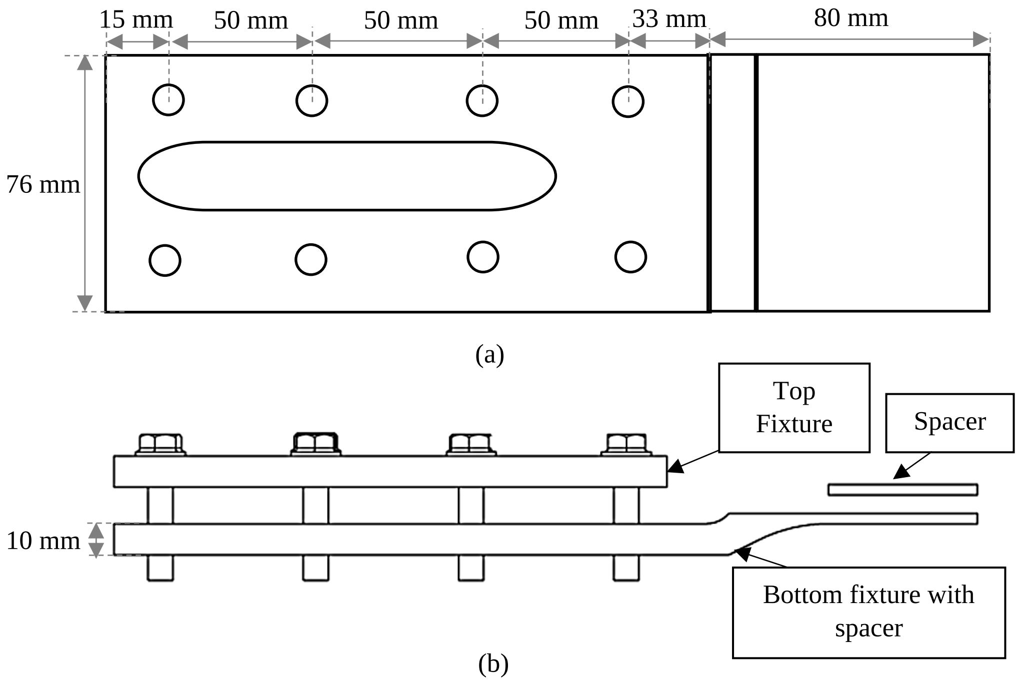

Figure 5.7: Anti-bending fixture a) top view b) side view.

A strain gauge was bonded to both sides of the outer adherend to monitor the bending and the actual transmitted load. When there was no bending occurred, the strain amplitude was constant from the beginning till the end of test as illustrated in Figure 5.8. The disbond propagation was tracked by a microscope camera.

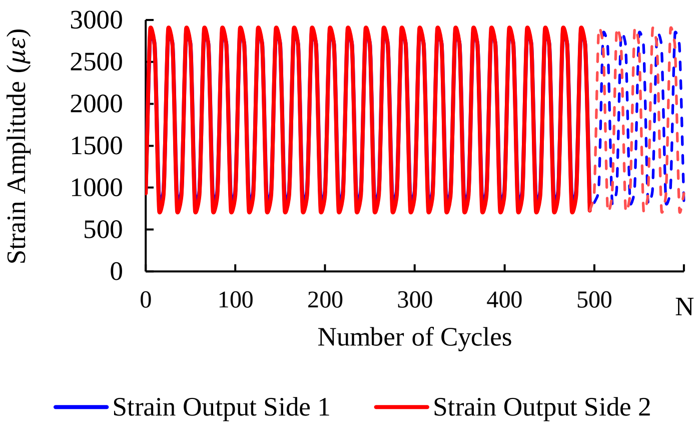

Figure 5.8: Illustration of strain gauges output (fatigue peak load of 33.3 kN, R = 0.1).

5.3 Static Test Results

The static tests carried out for the DOTES-ST and the DOTES-LT specimen were subjected to tension static loading. The static test results with cohesive failure in the adhesive were used to calibrate the mesh size and material properties applied in the numerical analysis. As an initiation, six specimens with baseline configuration were tested under static loading conditions. The results showed significant adherend yielding prior to the peak loads.

From the residual strength predictions in Chapter 4, modifying the adherend thickness could reduce the load carrying capacity of adhesive bonding. Thus, the static test carried out for another set of the DOTES-ST specimen was performed using the modified adherend thickness at RD condition. In addition, the static test carried out for the DOTES-LT specimen was performed using the un-balance configuration for the test at RD condition and balance configuration for the test at HW condition.

5.3.1 The DOTES-ST

As stated above, the static tests of the DOTES-ST specimen were carried out in RD condition. Three different adherend thickness variations (inner to outer adherend thickness ratio) were used for the static test of the DOTES-ST including variation 1 - thicker outer adherend (TOA), variation 2 – thicker inner adherend (TIA), and balanced configuration. The static test results with various pre-disbond lengths for the balanced and un-balanced joint configuration are discussed in the sub-sections below.

5.3.1.1 Balanced Joint Configuration

The static test results of baseline ($T_i = 2T_o$) configuration are presented in Figure 5.9. Most of the specimens showed significant adherend yielding prior to reaching the peak loads with an average peak of about 65.7 kN (3.28 kN/mm). Among the 6 specimens tested, one specimen failed adhesively with a peak load of 37.3 kN (1.86 kN/mm). This might be caused by the inadequate bond-line thickness at the gap region as the adhesive was squeezed out during the curing process (see Figure 5.3). In addition, the prediction of residual strength assessment defined in Section 4.3 suggested that the residual strength of the baseline specimen (balance joint configuration) should be steady up to 150 mm disbond length. Thus, the static test results from specimen with pre-disbond length of 100 mm from the tapered end was unacceptable. To achieve cohesive failure in the adhesive, specimens with un-balanced joint configuration defined in section 3.3.5 were required for static testing at RD condition.

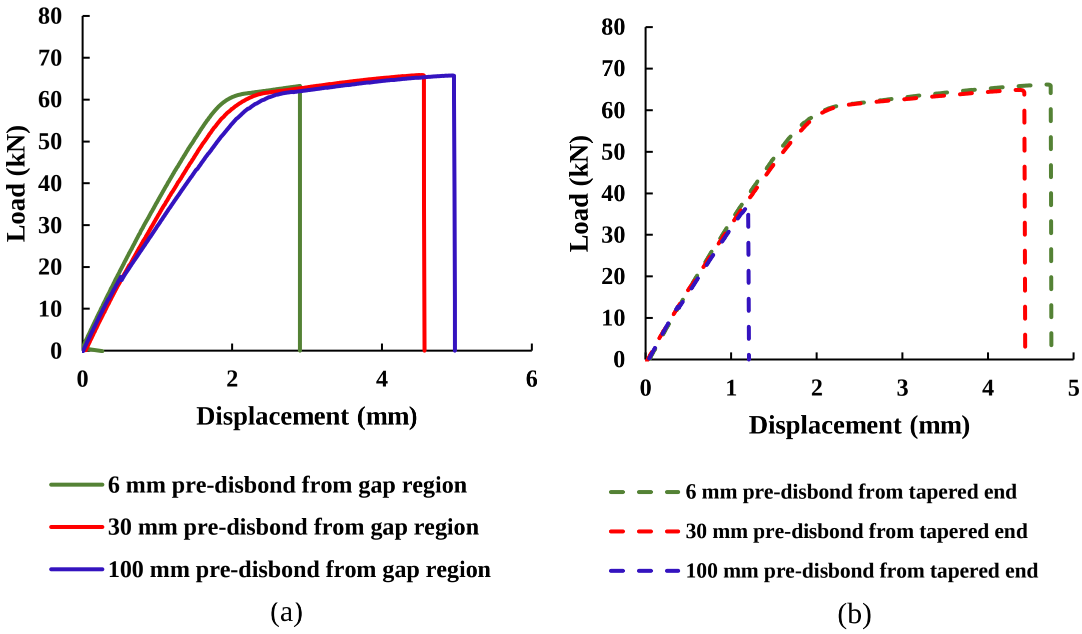

Figure 5.9: Static test results of the DOTES-ST with balance joint configuration a) artificial disbond from gap region b) artificial disbond from tapered end.

5.3.1.2 Unbalanced Joint Configuration

Three specimens with un-balanced joint configuration were tested against various artificial pre-disbond lengths initiated from the gap region. Among these 3 specimens, one specimen was manufactured and tested without pre-disbond length (Pristine specimen). The static test result of pristine specimen showed a significant adherend yielding prior to reaching the failure load. A similar phenomenon was observed for specimen with pre-disbond length of 30 mm from the gap region. Therefore, the loading capacity of these two specimens was limited by the yield strength of the outer adherend.

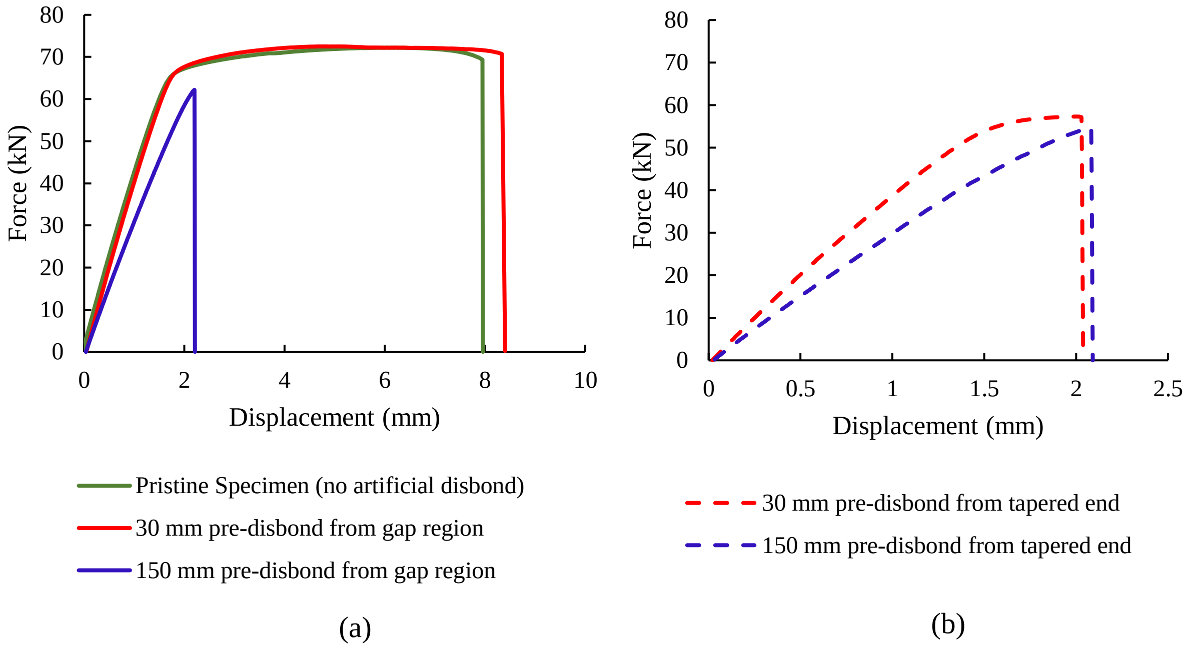

Figure 5.10*:* Static test results of the DOTES - ST specimen design a) variation 2-TIA b) variation 1-TOA.

A specimen with a longer artificial disbond length of 150 mm (only the tapered region was bonded) from the gap region was tested. The static test results plotted in Figure 5.10a showed that the specimen fails at a peak load of 62.2 kN (3.11 kN/mm). Post testing observation confirmed that no yielding at the outer adherend occurred. Thus, this failure load was considered to determine the maximum applied cyclic loading in the next section.

The static test results of specimen with various artificial disbond lengths initiated from the tapered end are shown in Figure 5.10b. The specimen with an artificial disbond length of 30 mm from the tapered end experienced a significant inner adherend yielding before reaching the peak load of 57.3 kN (2.86 kN/mm). However, the specimen with a longer artificial disbond length of 150 mm from the tapered end showed a peak failure load below the inner adherend yield strength that was 55.5 kN (2.73 kN/mm). Post testing observation also showed that cohesive failure of the adhesive failure mode existed.

5.3.2 The DOTES–LT

Based on the static test results from the DOTES-ST specimen, un-balanced specimen configurations were required to obtain cohesive failure mode in the adhesive for test at RD condition. Hence, the static test of the DOTES-LT specimen was carried out with three different adherend thickness variations.

Like the DOTES-ST, the static tests of the un-balanced joint (variation 1 – TOA, variation 2 – TIA) were conducted at room temperature (25℃) condition. Whilst the static test of balanced joint configuration was performed at an elevated temperature of 80℃ in which the specimens have been pre-conditioned for 33 days as discussed previously in Section 5.2.4.

5.3.2.1 Balanced Joint Configuration

Tests conducted at 80°C using pre-conditioned specimens with artificial disbond lengths up to 120 mm initiated from both gap and tapered ends still showed significant adherend yield failure mode.

Since the total overlap length was 180 mm and length of the tapered region was 60 mm, creating an artificial disbond longer than 120 mm from the gap region was not recommended. Thus, a specimen with a longer pre-disbond length (150 mm artificial disbond) was created with initiation from the tapered region.

The test result for a specimen that has an artificial disbond length of 150 mm from the tapered end is presented in Figure 5.11. A peak strength of 44.7 kN with a displacement of 1.82 mm was recorded with cohesive failure mode in the adhesive.

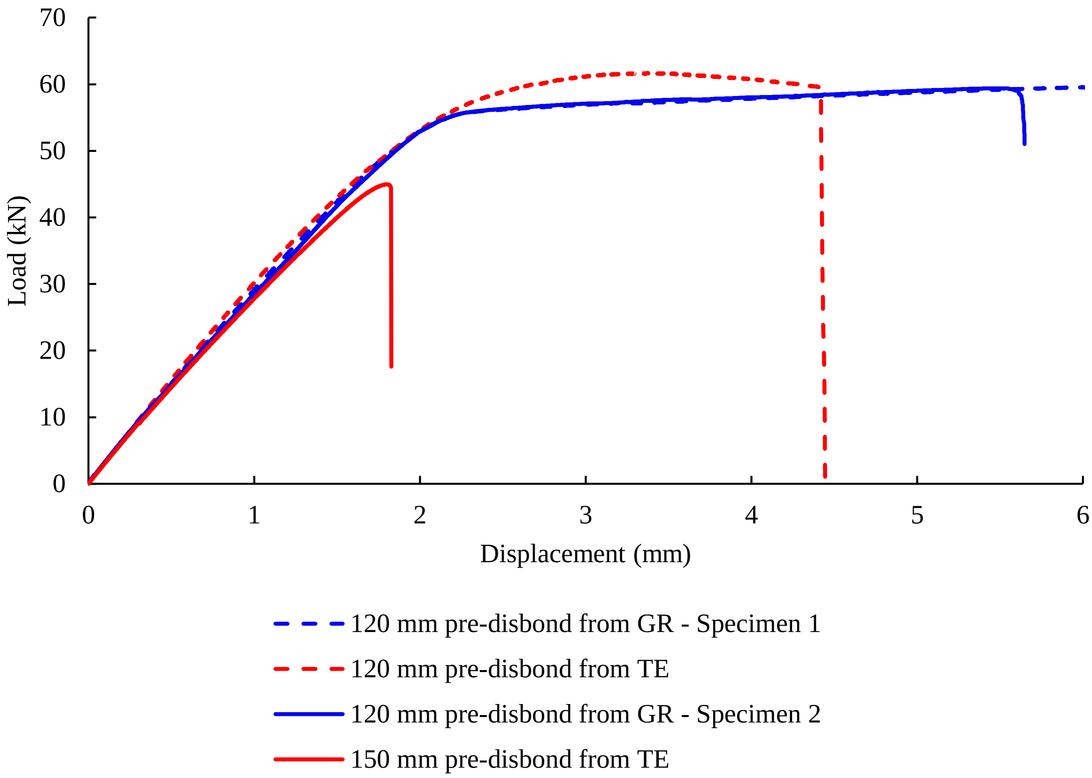

Figure 5.11: Static test results of the DOTES-LT specimen with baseline configuration tested in Hot-Wet (HW) condition.

5.3.2.2 Unbalanced Joint Configuration

Four unbalanced specimens ($T_i \neq 2\ T_o$) with two different inner to outer adherend ratios as specified in Table 3.1, Section 3.2.5 were tested in RD condition. The measured load-displacement curves are presented in Figure 5.12. The unbalanced specimens with thicker outer adherend (TOA) and pre-disbond from the tapered end (Variation 1) showed a typical adhesive bonding failure pattern with an average failure load of 52.4 kN. Whilst the unbalanced specimens with thicker inner adherend (TIA) and pre-disbond from the gap region (Variation 2) showed significant non-linear response prior to reaching the peak loads with an average peak load of 38 kN. Post testing observation confirmed the yield of aluminium outer adherend has occurred inside the tapered region. Thus, the loading capacity limited by the adhesive bonding of this joint would be higher than 38 kN. This information was also used in the calibration of mesh size for the computational modelling, that is, the calibration using Variation 1 (TOA) specimen test results must yield a loading capacity equal to or higher than 38 kN for Variation 2 (TIA) specimens (details in section 5.5.1).

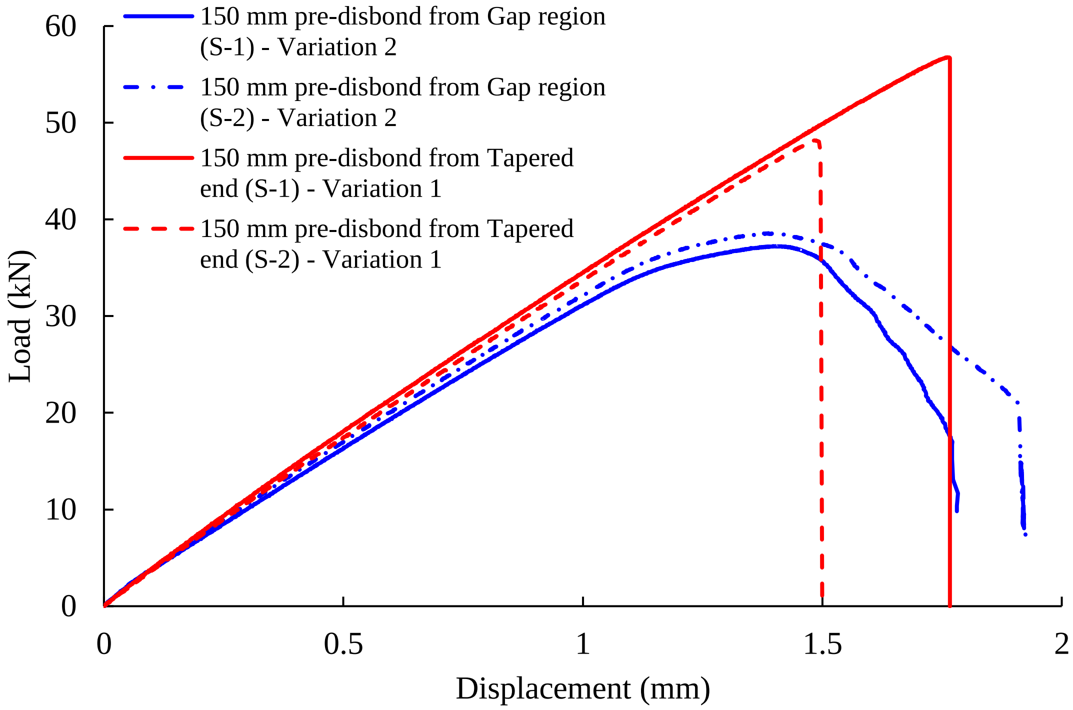

Figure 5.12: Static test results of the DOTES – LT specimen with un-balanced configuration tested in RD condition.

5.4 Fatigue Tests on DOTES-LT

The fatigue tests were performed for the DOTES-LT specimens. Two peak loads were considered in the fatigue tests. The first was 33.3 kN, which was approximately the upper limit value of the design limit load of this joint (determination of design limit load is discussed in Section 5.5.1). The second was 27 kN, being 80% of the first load. As defined in Table 5.4, most specimens tested were not pre-conditioned in a high humidity environment, whilst a small number of specimens were preconditioned in such an environment. The test conditions for the fatigue test are summarised in Table 5.5, with results of each condition are discussed separately in subsequent sections.

Table 5.5: Summary of fatigue test conditions.

Test condition	Humidity Condition	Peak load
Without anti-bending fixture	RD	27 kN
Without anti-bending fixture	RD	33.3 kN
With anti-bending fixture	RD	33.3 kN
With anti-bending fixture	RW	33.3 kN

5.4.1 Results from Tests without Anti-bending Fixture under Peak load of 27 kN

The results of specimens tested are presented in Table 5.6, excluding one specimen that has a short pre-disbond length of 6 mm from the tapered end. For this specimen, no disbond growth was observed until the outer aluminium adherend failed under fatigue loading.

Table 5.6: Summary of fatigue test results tested without anti-bending fixture (Fatigue peak load 27 kN).

Specimen Type	No of cycles during disbond pre-growth stage	Initial Disbond Length (mm)	Measured Fatigue Life (No of cycles)[1]	Measured No of cycles when disbond length last measured	Conservatively predicted No of cycles up to last measured disbond length[2]	Predicted fatigue life limited by joint residual strength[2] (No of cycles)	Failure Mode
Specimen with pre-disbond from Tapered End							
30 mm (TE)	12,072	31	28,793	23,295	6,318	81,829	P[3]
120 mm (TE)	10,108	121	44,453	23,377	17,987	19,356	O[4]
Specimen with pre-disbond from Gap Region							
6 mm (GR)	10,000	7	45,272	12,000	7,358	177,325	P
30 mm (GR)	22,000	31	39,518	16,008	11,736	139,801	P
120 mm (GR)	20,830	121	106,753	106,523	32,527	35,503	O

Notes:

1. Measured fatigue life = Total number of cycles prior to failure – Number of cycles during disbond pre-growth stage
2. Refer to Section 5.7 for the prediction
3. P = Failure of the outer adherend at gap region
4. O = Disbond propagated at one side until outer adherend peeled out

Since the pre-existing disbond in the specimens was created by artificially embedding Teflon films, to consider the "naturally grown disbond", a disbond pre-growth stage was considered. In Table 5.6 the initial length listed in the third column was the first measured disbond length of each specimen after disbond growth occurred. The numbers of cycles during the disbond pre-growth stage were included in the table which was correlated to the fatigue life of the aluminium adherends (though the life assessment of the aluminium adherends was not the scope of this study). Table 5.6 also listed the fatigue life and failure mode of each specimen which will be discussed in Section 5.4.5.

Since the anti-bending fixture was not used in these tests, significant uneven disbond growth along the two bond-line of the double lap joint specimens was observed. With the specimens having long pre-disbond (120 mm), disbond propagated nearly only at one side of the joint until failure.

From Table 5.6, it was shown that the fatigue life of the specimens with 121 mm initial disbond length was longer than that of the specimens with shorter initial disbond lengths. A question would be why did the adherend failure not occur earlier in the specimens with 121 mm initial disbond length? This phenomenon could be explained by considering specimen bending compliance. The unsymmetrical disbond growth would cause uneven loading in the two outer adherends at the gap region, whilst specimens with longer initial disbond length would have larger bending compliance. This would result in a lower uneven loading in the outer adherends when unsymmetrical disbond growth occurred, and thus causing the adherend to have longer fatigue life. This hypothesis was confirmed using FE analysis, as discussed in Section 5.5.

The fatigue life of specimens with disbond from the gap region was longer than those with disbond from the tapered end, as observed using specimens with 121 mm initial disbond length shown in Table 5.6. Also, a similar phenomenon was detected in other tests which will be presented below (Tables 5.7 – 5.9). This would suggest that the disbond growth was more significantly influenced by Mode I than Mode II crack opening mechanism. As predicted earlier in Chapter 4 and Section 5.5.2 (determination of SERR) of this chapter, specimens with pre-disbond from the tapered end have significant Mode I component, whilst specimens with pre-disbond from the gap region were dominated by Mode II component.

5.4.2 Results from Tests without Anti-bending Fixture under Peak load of 33.3 kN

The fatigue test results tested without an anti-bending fixture are presented in Table 5.7. As shown in this table, all the specimens failed in the form of disbond propagation fast at one side until the outer adherend peeled off. As expected, the specimens with longer initial disbond lengths had shorter fatigue life. Comparing the fatigue test results in Tables 5.6 and 5.7, it was evident that the fatigue life of the specimens loaded under higher peak loading had a much shorter fatigue life.

Table 5.7: Summary of fatigue test results tested without anti-bending fixture (fatigue peak load 33.3 kN).

Specimen Type	No of cycles during disbond pre-growth stage	Initial Disbond Length (mm)	Measured Fatigue Life (No of cycles)[1]	Measured No of cycles when disbond length last measured	Conservatively predicted No of cycles up to last measured disbond length[2]	Predicted fatigue life limited by joint residual strength[2] (No of cycles)	Failure Mode
Specimen with pre-disbond from Tapered End							
60 mm (TE)	2,356	62	24,981	24,930	17,697	35,903	O[3]
80 mm (TE)	3,026	84	22,484	22,255	13,853	27,236	O
80 mm (TE)	3,401	81	23,696	23,242	15,271	27,800	O
120 mm (TE)	55	122	18,318	18,167	12,166	12,256	O
Specimen with pre-disbond from Gap Region							
60 mm (GR)	1,400	61	29,449	28,709	23,381	64,436	O

Notes:

1. Measured fatigue life = Total number of cycles prior to failure – Number of cycles during disbond pre-growth stage
2. Refer to Section 5.7 for the prediction
3. O = Disbond propagated at one side until outer adherend peeled out

5.4.3 Results from Tests with Anti-bending Fixture under Peak load of 33.3 kN

In fatigue tests without using the anti-bending fixture, any asymmetrical disbond growth would result in a bending load on the specimen, causing uneven loading on the outer adherends, which in turn would result in a more significant uneven disbond growth, as discussed in sections above.

Adhesively bonded joints on aircraft structures were generally supported (bending constrained) and thus, their fatigue performance would be more representative when the anti-bending fixture (Figure 5.7) was used in the tests. The results of specimens tested with the anti-bending fixture under a peak load of 33.3 kN are presented in Table 5.8. As shown in this table, the specimens with shorter initial disbond lengths (or in other words, longer effective overlap lengths) failed in the form of outer adherend fatigue failure, and specimens with a long initial disbond length of 121 mm failed with adhesive bond line fatigue failure.

Table 5.8: Summary of fatigue test results of specimen tested with anti-bending fixture (fatigue peak load 33.3 kN).

Specimen Type	**No of cycles during disbond pre-growth stage**	**Initial Disbond Length (mm)**	**Measured Fatigue Life (No of cycles)[1]**	**Measured No of cycles when disbond length last measured**	**Conservatively predicted No of cycles up to last measured disbond length[2]**	**Predicted fatigue life limited by joint residual strength[2] (No of cycles)**	**Failure Mode**
Specimen with pre-disbond from Tapered End							
6 mm (TE)	2,852	8	26,726	26,045	22,648	77,700	P[3]
6 mm (TE)	3,897	9	20,866	20,540	19,388	75,827	P
60 mm (TE)	5,234	64	21,086	20,231	12,769	34,903	P
120 mm (TE)	750	121	22,390	22,250	16,519	16,519	C[4]
Specimen with pre-disbond from Gap Region							
6 mm (GR)	2,790	7	29,775	29,230	21,079		P
6 mm (GR)	1,200	7	24,645	23,800	13,701	130,491	P
6 mm (GR)	1,370	7	29,003	28,711	23,188		P
30 mm (GR)	1,350	32	31,150	30,518	26,321		P
30 mm (GR)	1,350	32	45,650	45,292	35,853	104,140	P
30 mm (GR)	1,650	32	37,196	37,150	31,633		P
30 mm (GR)	1,950	32	17,683	17,606	14,761		P
80 mm (GR)	2,760	82	23,425	23,298	21,090	51,409	P
80 mm (GR)	1,350	82	28,430	28,320	24,226		P
120 mm (GR)	4,650	121	34,297	34,252	17,050	17,501	C
120 mm (GR)	2,960	122	26,728	25,740	15,247	15,659	C

Notes:

1. Measured fatigue life = Total number of cycles prior to failure – Number of cycles during disbond pre-growth stage
2. Refer to Section 5.7 for the prediction
3. P = Failure of the outer adherend at gap region
4. C = Cohesive failure

For specimens with shorter pre-disbond lengths, the fatigue life of the outer adherend was shorter than the fatigue life of the adhesive bonding. Thus, manufacturing specimens with various pre-disbond lengths (as defined in Table 5.4) was important, to allow the assessment of disbond growth rates (refer to Section 5.4.6) within the full disbond length range of the DOTES specimens.

5.4.4 Results from Tests with Anti-bending Fixture under Peak load of 33.3 kN – Pre-conditioned Specimens

The results of specimens that were pre-conditioned in a high humidity environment are presented in Table 5.9. The failure mode of all the specimens was symmetrical disbond propagation until the final failure. Compared to the fatigue life of those specimens with similar initial disbond length shown in Table 5.8, the results indicated a significant fatigue life reduction due to the high moisture content in adhesive bond line.

Table 5.9: Summary of fatigue test results of pre-conditioned specimen tested with anti-bending fixture (fatigue peak load 33.3 kN).

Specimen Type	No of cycles during disbond pre-growth stage	Initial Disbond Length (mm)	Measured Fatigue Life (No of cycles)[1]	Measured No of cycles when disbond length last measured	Conservatively predicted No of cycles up to last measured disbond length[2]	Predicted fatigue life limited by joint residual strength[2] (No of cycles)	Failure Mode
Specimen with pre-disbond from Tapered End							
120 mm (TE)	30	124	8,193	8,153	6,384	7,671	C[3]
120 mm (TE)	41	122	11,478	11,430	7,538	8,130	C
Specimen with pre-disbond from Gap Region							
120 mm (GR)	183	122	19,531	18,831	14,125	14,568	C

Notes:

1. Measured fatigue life = Total number of cycles prior to failure -– Number of cycles during disbond pre-growth stage
2. Refer to Section 5.7 for the prediction
3. C = Cohesive failure

5.4.5 Failure Modes

Among the 28 specimens tested, three different failure patterns were observed, as shown in Figure 5.13. The first failure was when the specimens failed in the form of outer adherend fatigue failure at the gap region marked by (P). This failure pattern occurred when tested without and with an anti-bending fixture. When the specimens were tested without an anti-bending fixture, the specimens initially failed at one side of the outer adherend then followed by the other side. Whilst for specimens tested with anti-bending fixture, the specimens failed simultaneously at both sides of the outer adherend.

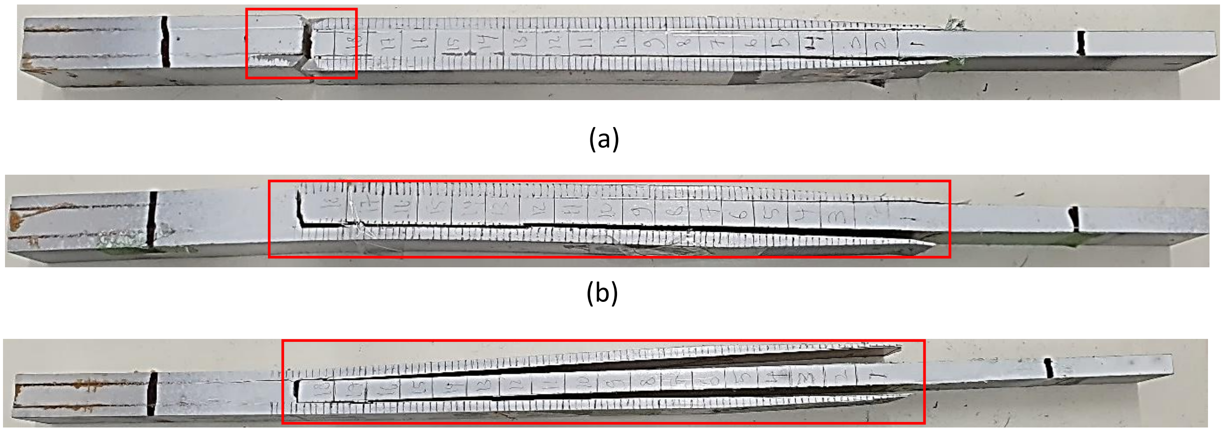

(a)

(b)

(c)

Figure 5.13: Failure modes a) failure of the outer adherend at gap region (P) b) disbond propagated at one side until outer adherend peeled out (O) c) cohesive failure (C).

The second failure mode marked by (O), which occurred when the specimens tested without an anti-bending fixture. While performing the fatigue tests without an anti-bending fixture, uneven disbond propagation was observed on all the specimens despite having it failed cohesively (one side disbond propagation) or at the outer adherend. Disbond was propagated faster at one side until the outer adherend peeled off. Uneven disbond growth along the two bond-line of the double lap joint specimens was observed, with one side of the joint propagated faster until it reached failure.

The last failure mode was cohesive failure (C) which was considered as the desired failure pattern. This failure pattern was only achieved when the specimens were tested with an anti-bending fixture.

5.4.6 Disbond Growth Rates

The measured disbond growth rates for all specimens with artificial disbond from the gap region (GR) which have not been previously humidity pre-conditioned are plotted in Figure 5.14. Since Mode II disbond growth dominated in these tests, the disbond growth rates could be accurately described as a function of the G_{II} strain energy release rate of adhesive in a Paris typed form, although there was significant scatter which was commonly associated with composites fatigue performance.

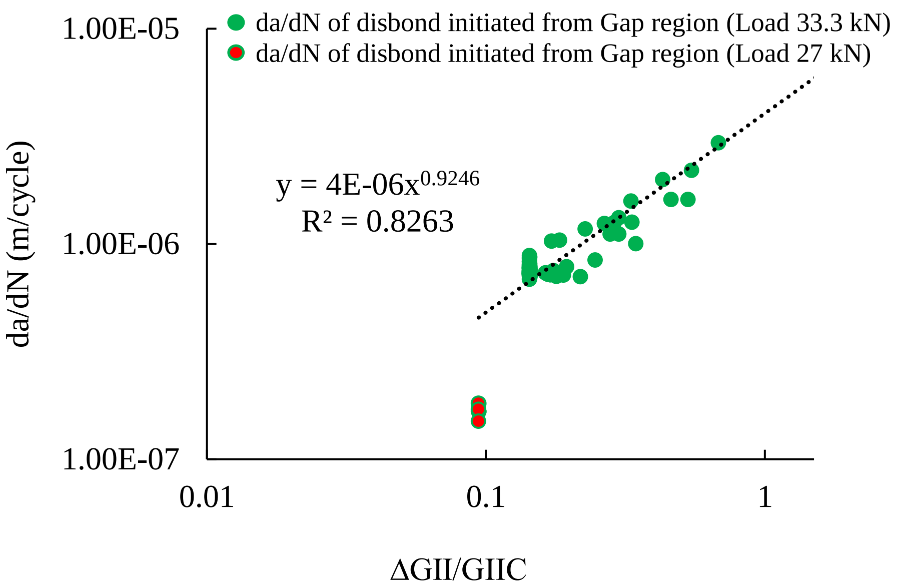

Figure 5.14: Disbond growth correlation for normal specimen with pre-disbond from gap region (27 and 33.3 kN fatigue peak load).

The measured disbond growth rates from all the tests using specimens without humidity pre-conditioning, including specimens with initial disbond from the tapered end (TE), are presented in Figure 5.15. Since both Mode I and Mode II disbond growths were present, the disbond growth rates were needed to be described as functions of G_I and G_{II}

strain energy release rates of adhesive in a more complicated Paris typed form. The detailed process to build the Paris typed disbond growth rates prediction formulae will be described in Section 5.6 below.

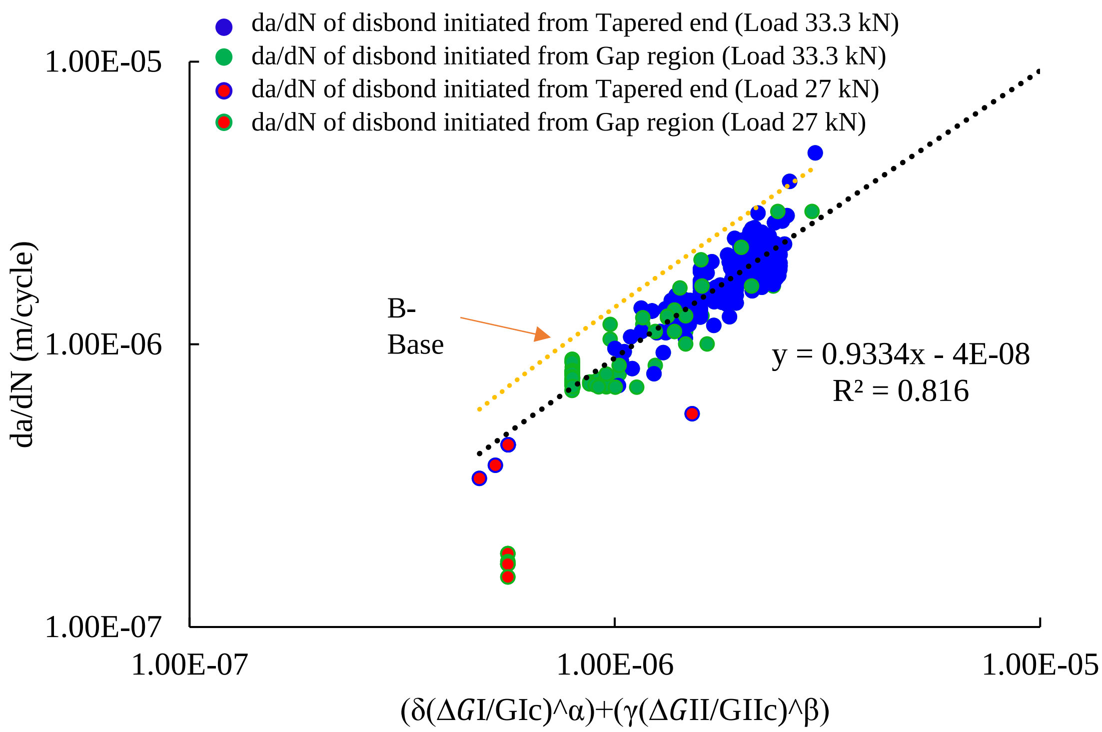

Figure 5.15: Disbond growth correlation for normal specimen with pre-disbond from gap region and tapered end (27 and 33.3 kN fatigue peak load).

Similar to Figures 5.14 and 5.15, the measured disbond growth rates from all tests using specimens with humidity pre-conditioning are presented in Figures 5.16 and 5.17.

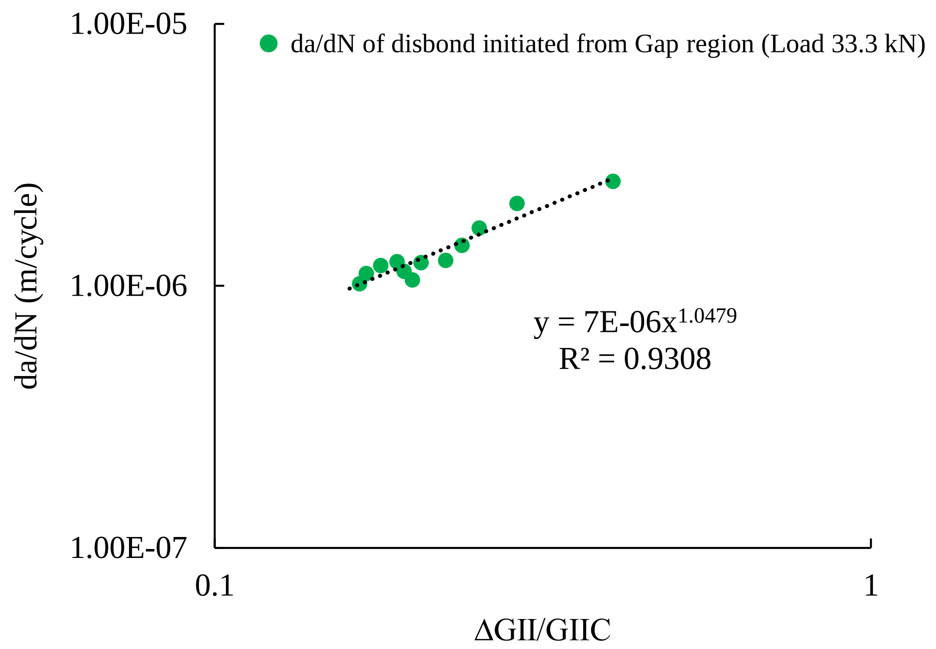

Figure 5.16: Disbond growth correlation for specimens that have been pre-conditioned with pre-disbond from gap region (33.3 kN fatigue peak load).

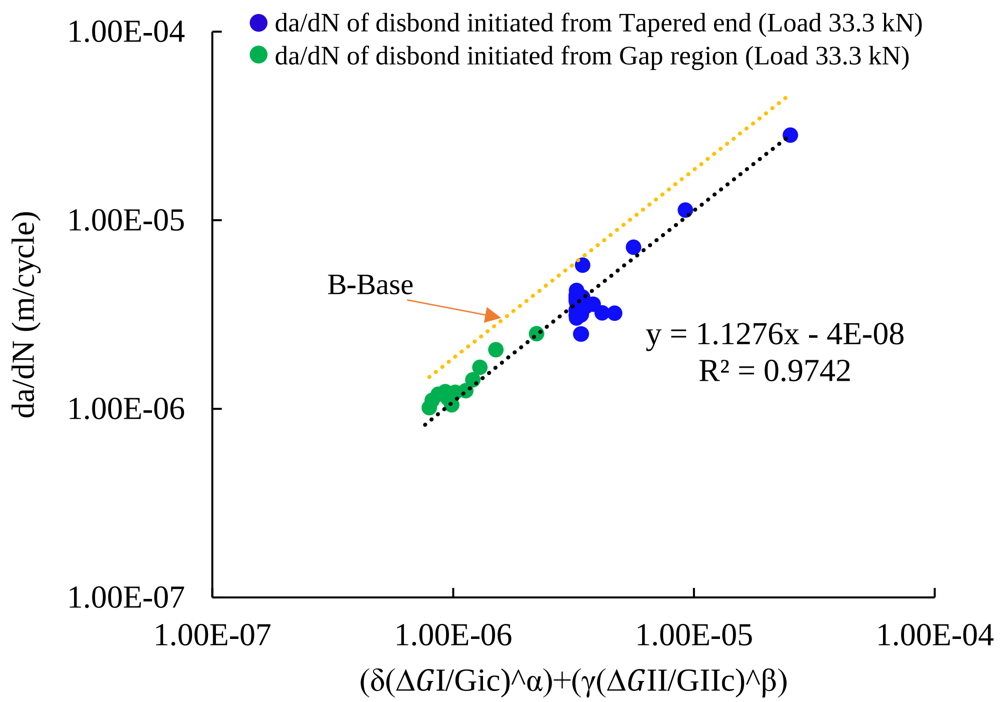

Figure 5.17: Disbond growth correlation for the specimens that have been pre-conditioned with pre-disbond from gap region and tapered end (33.3 kN fatigue peak load).

5.5 Modelling Results

Assessment of the residual strength of a joint was conducted to determine the disbond length where the instant static failure of the joint will occur. The VCCT method was utilised to determine the SERR value of the joint with symmetry and asymmetry disbond propagation. Using the modified Paris law (see Equation 5.3), a correlation between the calculated SERR value and experimentally measured disbond growth rate was established. Later, this correlation was used to predict the fatigue life of the joint.

5.5.1 Residual Static Strength Assessment of a Joint with Various Disbond Length

With the static failure loads obtained from the static test results of the DOTES-LT specimen (section 5.3.2), the mesh size at the disbond tip of the FEM model was calibrated. Using the failure load in Figure 5.12 for Variation 1 (TOA) specimen, the mesh size was calibrated to 1.25E-2 mm. The predicted results using the FEM model with this mesh size matched well with the measured failure loads of Variation 2 (TIA) specimen (Figure 5.12) and hot-wet test specimen (Figure 5.11) and thus, this mesh size was used in the following calculation.

The curves plotted in Figures 5.18 showed the load carrying capacity of the baseline configuration with pre-disbond both from the gap region and tapered end of the DOTES-LT specimen configuration. It is important to note that the joint static loading capacity in terms of adhesive bonding, is limited by its hot-wet strength. With a typical NDI detectable initial disbond length of 10 mm from the gap region assumed (damage tolerance requirement), the joint ultimate load would be around 62.5 kN. The B-basis was assumed to be typically 20% less than the joint ultimate load which resulted in 50 kN as an ultimate for the joint. With a safety factor of 1.5, the design limit was calculated to be 33.3 kN. This load was also lower than the aluminium adherend strength (56.7 kN) divided by 1.5. Thus, 33.3 kN load was considered as the upper limit of the fatigue peak load for this joint.

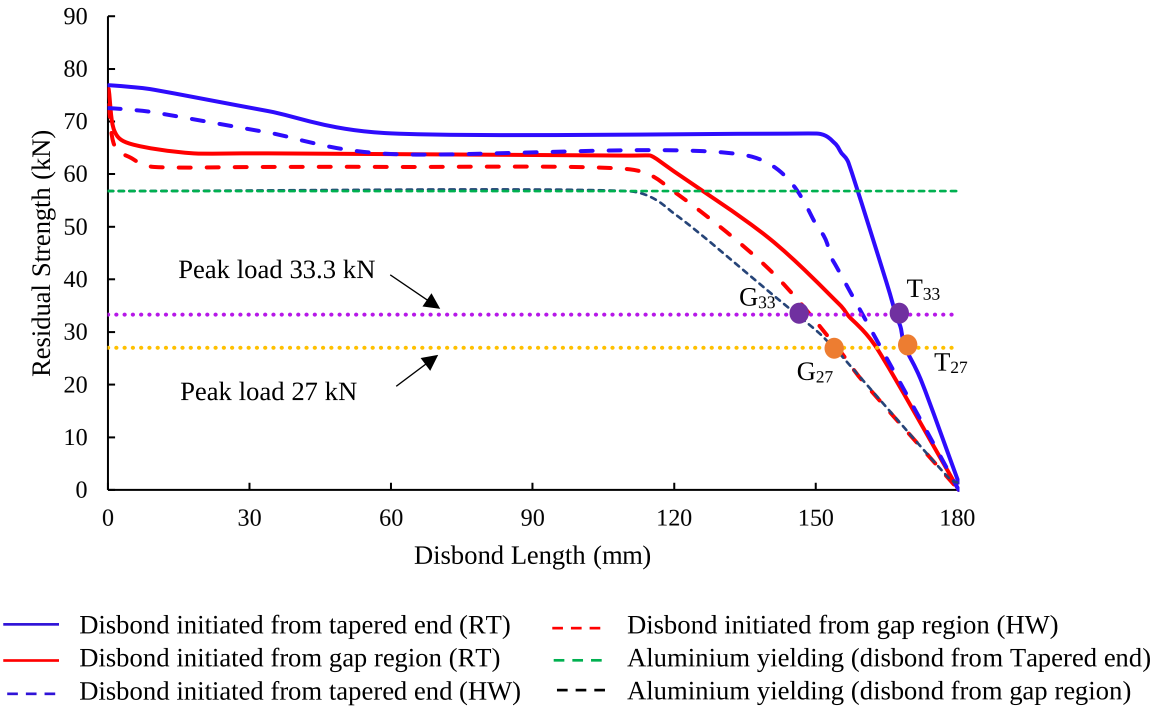

Figure 5.18: Residual strength of the DOTES - LT specimen configuration (balanced joint) for disbond initiated from gap region and tapered end (RD and HW).

The joint would rapture under static loads when the disbond reached the length where the peak fatigue load was equivalent to the joint residual strength (points T_{33}, G_{33}, T_{27} and G_{27} for the two load levels and disbond from two ends) as shown in Figure 5.18. Thus, in the fatigue life prediction (section 5.4), the life of the joint with symmetry disbond propagation should only be predicted up to:

i. Points G_{33} (146 mm) and T_{33} (164 mm) for disbond initiated from the gap region and tapered end, respectively, in the case of fatigue peak load equals to 33.3 kN.

ii. Points G_{27} (155 mm) and T_{27} (169 mm) for disbond initiated from the gap region and tapered end, respectively, in the case of fatigue peak load equals to 27 kN.

For the joint with asymmetry disbond propagation, the residual strength of the joint was predicted using the full model shown in Figure 4.1d (Section 4.2). The static failure point prediction was dependent on the disbond length on both sides. For instance, when the shorter disbond length from the tapered end (D2 in Figure 4.1d) was 80 mm, the instant static failure of the joint was predicted at 168 mm of the longer disbond under fatigue peak loading of 33.3 kN. Whilst, when the shorter disbond length increased to 120 mm, the instant static failure of the joint was predicted at 166 mm of the longer disbond.

5.5.2 Determination of Strain Energy Release Rates (SERRs)

The SERR values of the DOTES-LT specimen under peak loads of 33.3 kN and 27 kN were determined using the VCCT approach discussed in Section 3.4.2.3.

Since the fatigue test of the DOTES-LT specimen was typically conducted “with and without” anti-bending fixture, “symmetry and asymmetry” disbond propagation was observed. The procedure to account for symmetry and asymmetry disbond propagation was discussed in two sub-sections below.

5.5.2.1 Symmetry Disbond Propagation

For specimens with symmetry disbond propagation, the SERR results of the DOTES under 33.3 kN peak load for both cases with disbond initiated from the gap region and tapered end are presented in Figures 5.19 a and b, respectively. A similar trend for SERR vs disbond length could also be observed for the 27 kN peak load. The disbond growth behaviour of specimen with disbond from gap region was mainly governed by the shearing mode II as shown in Figure 5.19a. Whilst for specimen with disbond from the tapered end, Mode I was about 25% of the Mode II SERR as presented in Figure 5.19b. Considering that the critical strain energy release rate of Mode I was much lower than that of Mode II, Mode I’s effect was also significant.

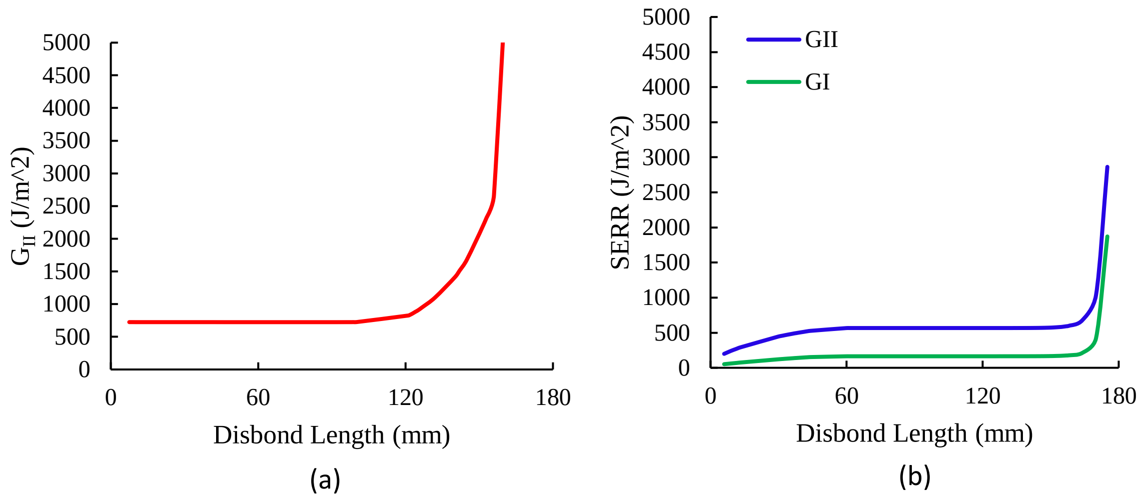

Figure 5.19: SERR plot. a) disbond initiated and propagated from the gap region; b) disbond initiated and propagated from the tapered end (Load = 33.3 kN).

5.5.2.2 Asymmetry Disbond Propagation

For specimens with disbond propagation dominated at one side, the full numerical model was used (Figure 4.1d, section 4.2). As the SERR of each disbond was also dependent on the other disbond length, both disbond lengths were needed when the SERR was calculated.

A case where one disbond length was fixed at 75 mm (D2) and the other propagated from 75 mm (D1) was shown in Figure 5.20a. In this case, SERR curves have a “fish shape” (Figure 5.20a) where the G_I and G_{II} values of growing disbond (D1) initially were higher than those of the fixed disbond (D2), which indicated faster disbond propagation of D1. The disbond growth would alternate between D1 and D2 at 120 mm and 140 mm for G_{II} and G_I, respectively, as indicated by the intersection of the SERR of D1 and D2. This phenomenon was also noted in [17].

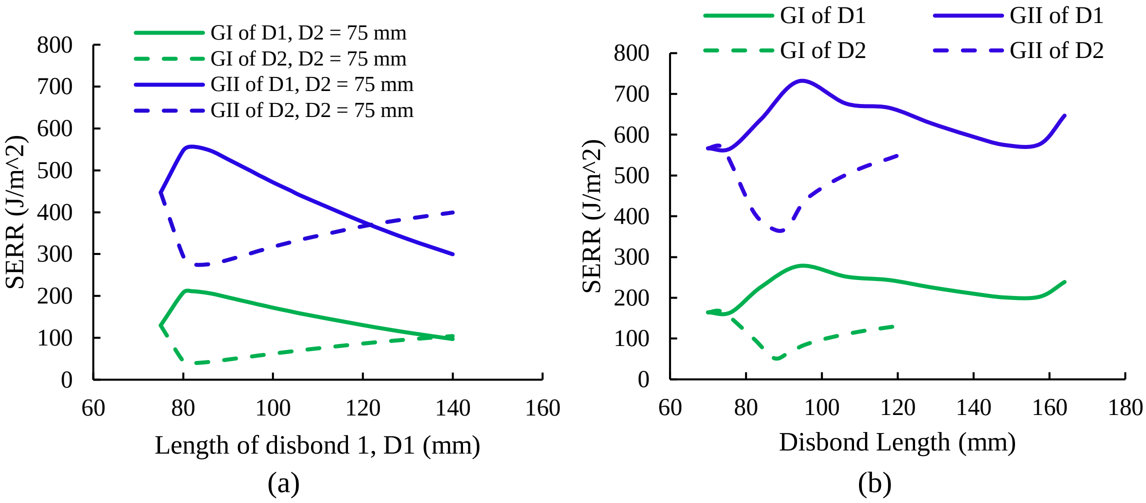

Figure 5.20: G_I and G_{II} of asymmetry disbond propagation (disbond initiated from the tapered end). a) SERR of D1 and D2 as a function of disbond 1 length, D1 (D2 = 75 mm); b) SERR of D1 and D2 as disbond 1 and disbond 2 propagate (Load 33.3 kN), from a test described in Section 5.7.

In this study, the SERR was calculated for two purposes. One was to correlate the experimentally measured growth rate and SERR value, and the other was to use the correlation established in the prediction of the joint fatigue life. These will be further discussed in Sections 5.6 and 5.7 below.

5.6 Correlation of Fatigue Disbond Crack Growth Rate Parameters

Crack propagation law developed by Paris and Endorgan [126] based on the power law relationship between the stress intensity factor (SIF) range (ΔK) and crack growth rate (da/dN) was used in this work.

$$\frac{da}{dN} = C\Delta K^m \tag{5.2}$$

Where C and m are material constants and ΔK refers to the SIF range caused by the cyclic fatigue loading ($K_{max} - K_{min}$). Various forms of modified Paris laws have been developed and reported in the literature [180, 181]. When applying the fracture mechanics approach to analyse the failure of structural adhesive and fibre reinforced composite, $\sqrt{G}$, which is directly correlated with K, or other forms of G are generally used rather than K as the variable [130, 131]. With a trial to fit the measured data, the disbond growth relationship shown in Equation 5.3 was considered in this study, where disbond growth contributions from Mode I and II are assumed to be additive:

$$\frac{\mathbf{da}}{\mathbf{dN}} = C_1(\frac{\Delta G_I}{G_{IC}})^{\mathbf{m_1}} + C_2(\frac{\Delta G_{II}}{G_{IIC}})^{\mathbf{m_2}} \tag{5.3}$$

Where C_1, m_1, C_2, and m_2 are experimentally determined constants. G_{IC} and G_{IIC} are the critical strain energy release rate that is defined in Table 3.4 and ΔG = G_{max} - G_{min}.

The SERR components, G_I and G_{II}, were examined using the VCCT approach defined in section 3.4.2.3. For the symmetrical model, the correlation between disbond length and SERR value as defined in Figure 5.19 was used. For the asymmetrical model, the SERR values were individually calculated using the measured uneven disbond lengths with the full FEM model. The disbond growth rate (da/dN) was measured from the experimental fatigue test.

Since G_I was negligible for specimens with disbond from the gap region, an attempt was made to determine the constants C_2 and m_2 by correlating only the Mode II component with the experimental measured disbond growth rate. The results are plotted in Figures 5.14 and 5.16 for specimens without and with hot-wet environmental pre-conditioning, which indicate a reasonable fitting with the measured data, even though there was some scatter particularly with the growth rate measurement from tests with the 27 kN peak load.

Since G_I and G_{II} were both present for specimens with disbond from the tapered end, all the four constants C_1, m_1, C_2, and m_2 were needed in correlation with experimental measured disbond growth rate from tests with these specimens. With C_2 and

m_2 pre-defined above, the constants C_1 and m_1 were further determined using all data from the experimentation and simulation including:

- Specimens with disbond from gap region and tapered end,
- Specimens with symmetry and asymmetry disbond propagation,
- Specimens tested with a fatigue peak load of 27 and 33.3 kN,
- Specimens with and without hot-wet environmental pre-conditioning, respectively.

A Parameter sensitivity study was followed in Excel to further tune the disbond growth correlation slightly. This was done by adjusting the constants C_1, m_1, C_2, and m_2. The resultant constants C_1, m_1, C_2, and $m_2$values are listed in Table 5.10, and the fittings are plotted in Figures 5.15 and 5.17.

Table 5.10: Values of C_1, m_1, C_2, and m_2 parameters.

Parameter	Without hot-wet conditioning	With hot-wet conditioning*
m_1	1.07	2.31
m_2	0.83	1.05
C_2	4E-6	7E-6
C_1	8.4E-6	3.3E-4

* Specimens conditioned at 71°C with 95% RH prior to fatigue testing

The reasonably high values of R^2 in Figures 5.14 – 5.17 indicated a good correlation between the experimental measured disbond growth and numerically calculated SERR. It was also worth considering that Figures 5.15 and 5.17 (with data from specimens with pre-disbond from gap region and tapered end) have almost equal correlation coefficient (R^2) than that with Figures 5.14 and 5.16 (containing only specimens with pre-disbond from gap region).

The results plotted in Figures 5.14 – 5.17 showed that lower fatigue peak load result in a lower SERR components value and thus lower disbond growth rate. For pre-conditioned specimens, a higher disbond growth rate was attained due to the degradation of the material properties.

5.7 Prediction of Specimen Disbond Growth and Fatigue Life

The approaches presented in Sections 5.5 and 5.6 above enabled prediction of disbond growth and joint life under constant amplitude fatigue loading. It was worth considering that this prediction only concerns adhesive bond strength of the joint. Although the life prediction of the joint limited by the aluminium adherend fatigue strength was also important, it was out of the scope of this study, and thus it required further research to this study.

For a joint with symmetrical disbond growth (bending constrained structure), once an initial disbond length was known, G_I and G_{II} SERR can be determined (Figure 5.19). Using the formulae shown in Figures 5.15 or 5.17 (with the constants in Table 5.10), the initial growth rate could also be calculated. With this rate and a small increment of number of cycles, the increment of disbond length could be determined (or alternatively with a small increment of disbond length, the increment of number of cycles could be determined). This step could be repeated, that is, with a numerical integration process the disbond length as a function of number of fatigue cycles, and joint fatigue life (when disbond length reached the critical values discussed in Section 5.5.1), could be predicted.

For a joint with asymmetrical disbond growth, with given initial uneven disbond lengths, G_I and G_{II} SERR values are needed to be determined for both disbonds. The uneven initial growth rates could be calculated for disbond using the formulae shown in:

i. Figure 5.15 with constants defined in Table 5.10 for specimens without pre-conditioning,

ii. Figure 5.17 with constants defined in Table 5.10 for specimens with pre-conditioning.

With a small increment of number of cycles, the uneven increment of disbond lengths could be determined. The remaining procedures were the same as those for the joint with symmetrical disbond growth. Figure 5.20b shows a typical example of how SERR values along both disbonds vary unevenly as disbonds propagate, which was determined incrementally using this numerical integration method.

The above approaches would result in a prediction for the maximum likelihood value of disbond growth and joint fatigue life. To predict with higher conservativeness, the statistics aspect should be considered. Based on the information provided in Figure 5.15, a dimensionless variable defined using the following formula may be considered.

$$z = \frac{\log(y_i) - \log(\hat{y}_i)}{\log(\hat{y}_i) - \log(1.0\mathrm{E}{-7})} \tag{5.4}$$

where y_i is the measured disbond growth rate, $\hat{y}_i$ is the predicted (maximum likelihood) disbond growth rate, and the value 1.0E-7 is the lower margin of the growth rate range considered. The part of $\log(y_i) - \log(\hat{y}_i)$ shows the scatter of the measured growth data. The variable *z* can be interpreted as the ratio between the data scatter and the predicted value in the range considered. The frequency distribution of the variable *z* with its 359 measured data, showing a normal distribution is plotted in Figure 5.21.

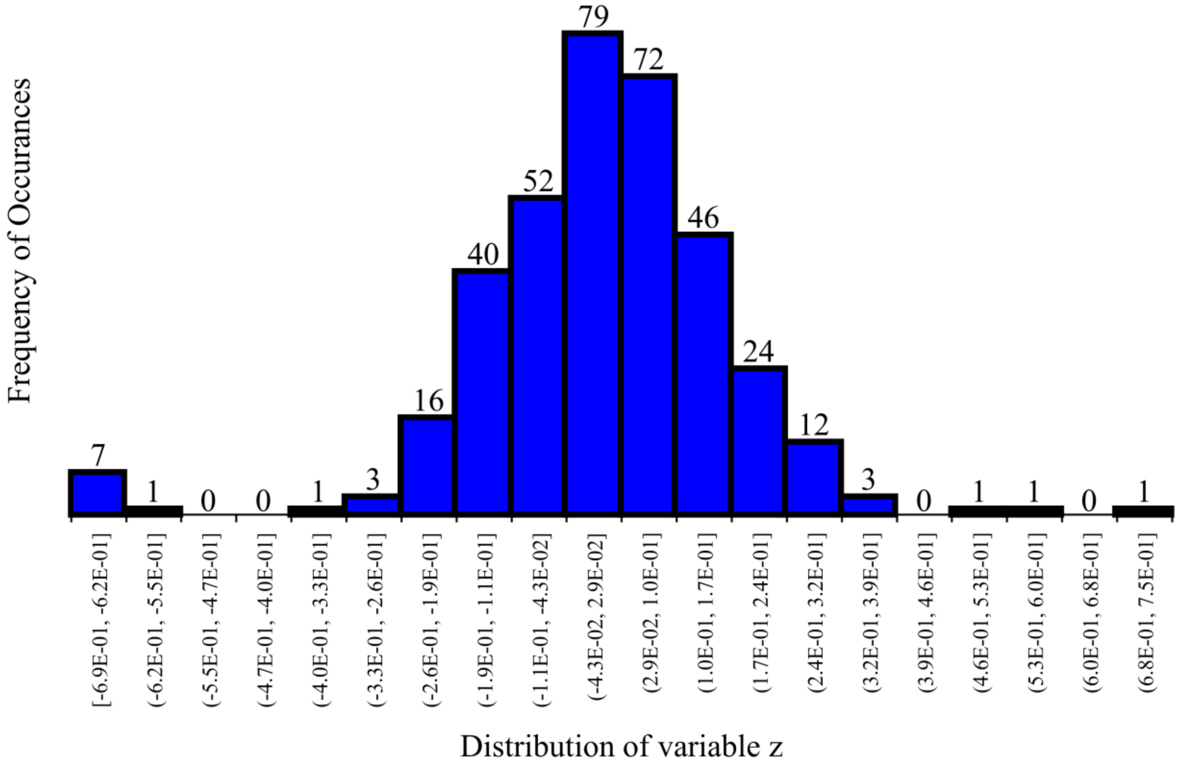

Figure 5.21: Normal distribution of the fatigue test results (the DOTES-LT specimen not pre-conditioned, fatigue peak load of 27 and 33.3 kN).

The mean (μ) was calculated using Equation 5.5 to be a negligible value as expected as the equation to calculate $\hat{y}_i$ was generated by regression. The standard deviation (σ) was calculated using Equation 5.6 to be 0.12.

$$\mu = \frac{\Sigma \frac{\log(y_i) - \log(\hat{y}_i)}{\log(\hat{y}_i) - \log(1.00\mathrm{E}{-7})}}{n} \tag{5.5}$$

$$\sigma = \sqrt{\frac{\Sigma(z_i - \mu)^2}{n}} \tag{5.6}$$

where n is the number of sample points, n = 359.

If a conservativeness level similar to that used for B-basis design allowable was considered, that is, a minimum threshold of 90% with a confidence level of 95%, the growth rate used for prediction could be scaled up from the maximum likelihood prediction by a factor $1 + k_B\, \sigma$, where k_B is one-sided (B-basis) tolerance limit factor for normal distribution [182, 183].

The value of k_B was obtained from the table provided in [184] that is, 1.405 with a calculated scale factor of 1.17 for 359 data points, presented in Figure 5.15. As shown in the figure, most of the measured data points were below the B-basis line which indicated that the growth rate estimation was indeed conservative.

An identical procedure was applied for the specimen that has been pre-conditioned, as described above. The calculated standard deviation and k_B values were 0.07 and 1.634, respectively.

The conservative predictions for the fatigue disbond growth and life of both specimen types (with and without pre-conditioning) are presented in Tables 5.6 – 5.9. In Table 5.6, the predicted disbond growth lengths and joint fatigue lives for all cases were conservative as compared to the measured tests data with a 27 kN peak load. Similarly, the predicted disbond growth lengths up to the last measurement conducted during the tests were conservative, as compared to the measured tests data with a 33.3 kN peak load, as shown in Tables 5.7 – 5.9.

As shown in Tables. 5.8 and 5.9, in the tests conducted with a 33.3 kN peak load using an anti-bending fixture, the predicted joint lives were conservative compared to the measured data in the cases where the failure mode was adhesive failure (not adherend failure).

Only in the tests with 33.3 kN peak load and without using the anti-bending fixture, the predicted joint lives were un-conservative compared with the measured data in the cases where the failure mode was adhesive failure. The B-basis line as shown in Figure 5.15 was not conservative for high G values, which was the case for specimens with asymmetric disbond growth. This would contribute to non-conservative life prediction. As noted earlier, adhesively bonded joints on aircraft structures were generally supported (bending constrained) and thus their fatigue performance would be more representative when the anti-bending fixture was used in the tests. Thus, no further efforts were made to develop a more comprehensive FEM model to accurately simulate the last stage fatigue tests where no anti-bending fixture was used.

5.8 Discussion

5.8.1 Disbond Initiated from the Tapered End and Gap Region

For disbond initiated from the tapered end, referring to Figure 5.18, Figure 5.19 b and Equation 5.3, as the disbond propagated within the taper region, the residual strength of the joint would decrease and the SERR/disbond growth rate would increase. Thus indeed as described in [11] when the disbond propagated into a region of increasing patch thickness through the taper, it would experience increasing stress and therefore anticipated more rapid disbond growth.

Using Equation 5.3, the disbond growth behaviour under constant amplitude fatigue loading could be estimated. The results with the fatigue peak load of 33.3 kN are listed in Table 5.11. On one hand, the results clearly indicated that the disbond growth rate would increase as the disbond length increased; and on the other hand, it showed that after the disbond propagated beyond the taper length, there was still a significant fatigue life remaining. If one considered a typical initial NDI detectable disbond of 10 mm length was assumed due to the damage tolerance requirement, then the ratio of the fatigue life (numbers of cycles) of the specimen with the disbond length beyond the taper region compared to that within the taper region would be 1.8. Note that for more commonly used taper length in bonded joint designs (1:10 slope and edge thickness = 0.5 doubler thickness), the tapered region would be shorter, and would show a higher ratio.

Table 5.11: Estimated disbond growth rates under the fatigue peak load of 33.3 kN, predicted using Equation 5.3 applied with B-basis conservativeness.

Disbond initiation	**Disbond propagation (mm)**	**Number of cycles**	**Average growth rates (mm/cycle)**
Tapered end	2-10	11,463	9.98E-4
	10-60	27,444	1.82E-3
	60-164	43,769	2.38E-3
Gap region	2-6	4,059	9.85E-4
	6-120	112,796	1.01E-3
	120-146	14,364	1.81E-3

The above discussion suggested that for disbond initiated from the tapered end, the application of the slow growth management approach was conditional, that is, the overlap length of the joint should be sufficiently long, and the fatigue peak load should be within the slow growth allowable region shown in Figure 4.13, Chapter 4.

In contrast, according to Figure 5.18, Figure 5.19a and Equation 53, for disbond initiated from the gap region, only within the first few millimetres, the residual strength of the joint would decrease and the SERR/disbond growth rate would increase as the disbond propagated. As shown in Table 5.11 and Figure 5.22, the growth rates only slightly increased as the disbond propagated up to 120 mm. Thus, in this significantly long range of disbond growth, the growth was slow and stable. Beyond that, the disbond propagated into the tapered region, and the growth rate increased rapidly owing to doubler thickness reduction, in addition to the reduction of the effective overlap length.

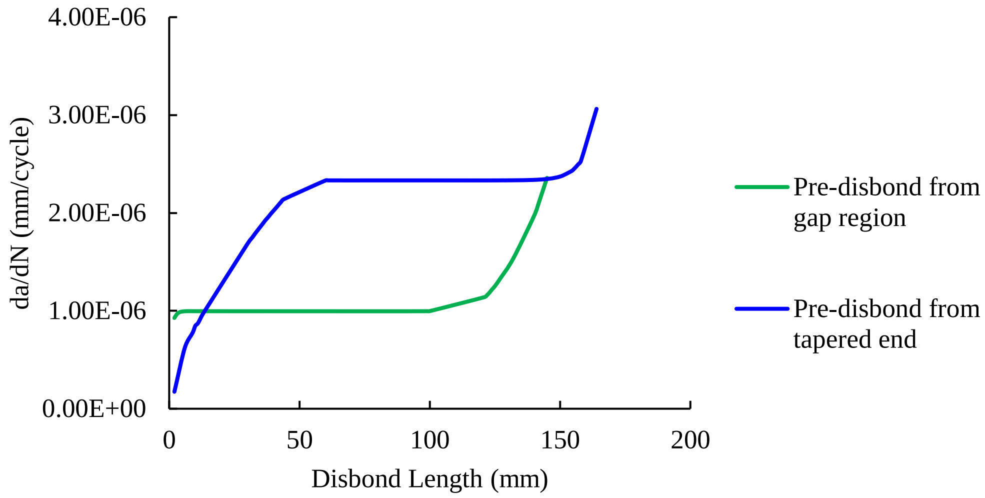

Figure 5.22: Disbond growth rate estimation based on B-basis with various disbond lengths, peak load of 33.3 kN.

Another factor to consider was the load bypass for a local or part width disbond initiated from the gap region. The SERRs assessment using displacement control defined in Section 4.4.2 indicated that as the disbond propagated, the compliance of the strip joint specimen would increase significantly. Thus, with the local compliance increase at the disbonded region, some load would be redistributed to the adjacent regions (load shedding effect). This was an additional factor contributing to the disbond slow growth. Note that this point merely suggested that a part width disbond would grow slower than a full-width disbond. How a local disbond grows and affects the bonded joint/repair effectiveness will be defined in Chapter 6.

5.8.2 Fatigue Life of Specimens with Humidity Conditioning

As reported in Section 5.4, the fatigue life of the specimens tested after the humidity environment conditioning was significantly shorter than that without the conditioning. In addition, the ultimate failure of all these specimens was adhesive bonding failure rather than adherend fatigue failure. These results indicated that for a relatively weaker adhesive, the adhesive fatigue strength was the dominant factor influencing the joint fatigue life.

It should also be noted that during specimen manufacture, corrosion-inhibiting primer was not applied. Accordingly, the results would apply only to the joints manufactured in such a way.

5.9 Summary

The disbond growth rate formulation based on modified Paris law was successfully determined through this computational and experimental study. From this study, it can be summarised that:

- The average moisture absorption of specimens pre-conditioning at 71℃ with 95% relative humidity for 33 days was around 3%.
- The residual static strength of the joint as a function of disbond length was established using the finite element method with the adhesive material failure criterion and progressive failure analysis.
- The upper limit fatigue peak load was determined by considering a static strength safety margin and manufacture defect tolerance, to be 33.3 kN.
- The residual strength analysis results indicated that under peak load of 33.3 kN, the joint would rapture at 146 mm and 167 mm disbond lengths for disbond initiated from the gap region and tapered end of the joint, respectively. For a lower peak load of 27 kN considered, these lengths increased to 155 mm and 169 mm.
- Constant amplitude fatigue tests ($R = 0.1$) were conducted using specimens with various initial disbond lengths. The entire disbond growth process up to joint failure was monitored. The fatigue test indicated that the life of specimen with artificial disbond length from gap region was longer than that from tapered end.
- High moisture content in the adhesive bond line would result in a significant reduction in fatigue life, as shown by the fatigue test results of specimens with humidity pre-conditioning.
- A virtual crack close technique approach was utilised to assess the strain energy release rates as a function of the disbond crack length. The results suggested that

for specimen with pre-disbond from the gap region, disbond growth was dominated by Mode II whilst for specimen with pre-disbond from the tapered end, Mode I contribute around 25% of the Mode II SERR.

- A modified Paris law was established by correlating the measured disbond growth rates with the strain energy release rates. Using the modified Paris law, the crack growth length as a function of the number of fatigue load cycles, and the fatigue life of each specimen were predicted by conducting numerical integration.
- The scatter factor in the prediction was handled by using the statistics approach and considering a conservativeness level similar to that used for the generation of B-basis design allowable. The predicted disbond growth agreed well with the measured values. For specimens with symmetric disbond growth and failed in the form of adhesive cohesive failure, the predicted fatigue life also showed a good correlation with the test results.
- The computational and fatigue test results indicated that for a joint having a sufficient static strength safety margin under a typical fatigue loading that would propagate disbond, the disbond growth would be stable in a particular length range.

From the analyses above, the slow growth approach was established for fatigue life prediction and inspection of interval determination, which is in accordance with the guidelines provided by FAA AC 20-107B [9]. In Chapter 6, the modified Paris law correlation established in this chapter is compared with the cohesive zone element (CZE) approach to assess the wide bonded metal joint specimen.

Chapter 6

Onset and Propagation of Disbonds in 3D Wide Bonded Metal Joint Under Cyclic Loading Using CZE Method

Preface

This chapter details the cohesive element formulations which is used to predict the onset and propagation of disbonds in a wide bonded metal joint specimen under cyclic loading. The element stress-strain based adhesive failure criteria defined in Chapter 3 was utilised to determine the residual strength of the wide bonded metal joint specimen. The CZE approach was used to determine the strain energy release rates (SERRs) as a function of disbond length and predict the disbond growth rate of wide bonded metal joint specimens. The material input properties of the cohesive zone element (CZE) approach were calibrated against the experimental results of the DOTES defined in Chapter 5. The performance of the cohesive element formulations to predict the disbond growth under fatigue loading was assessed using the DOTES specimen. The results were compared with those predicted using the VCCT approach incorporating the Modified Paris law established in Chapter 5. Using the developed cohesive element formulations, the effect of load shedding (load sharing or redistribution to the adjacent region) on the propagation behaviour of the disbond was investigated through the wide bonded metal joint specimen in this chapter.

The research works presented in this chapter are part of a paper entitled “Computational Assessment of Disbond Growth Behaviour in Adhesively Bonded Wide Joints/Patch Repairs of Aircraft Primary Structures”, which is submitted to “Theoretical and Applied Fracture Mechanics”.

6.1 Introduction

In previous chapters of this thesis, a correlation of disbond growth rates with the strain energy release rates (SERRs) calculation based on the modified Paris law was established. Using the modified Paris law formulation, the life of the joint could be predicted. In Chapters 4 and 5, the SERRs were determined using the virtual crack closure technique (VCCT) approach. This VCCT approach, however, still has some difficulties in propagating cracks within 3-D conditions [161]. Hence, the cohesive zone element (CZE) approach was used in this chapter to determine the SERR and to predict the disbond growth of 3-D wide bonded metal joint specimen.

Bazant and Chen [185] reported that the linear elastic fracture mechanics (LEFM) was not capable of predicting the crack nucleation as well as very short crack growth. Hence, the element stress-strain based adhesive failure criteria defined in Chapter 3 was used to assess the residual strength of wide bonded metal joint specimen. The upper limit of fatigue peak load of the wide bonded metal joint specimen was assumed to be equivalent to the upper limit fatigue peak load of the DOTES coupon specimen, which was 1.665 kN/mm. With this fatigue peak load, the fatigue life of the wide bonded metal joint specimen could be determined by considering the instant static failure of the joint, that is, when the disbond length reached the critical value in which the residual strength was equivalent to the fatigue peak load.

The investigation carried out in this chapter was based on a two-step approach: (1) 2-D strip specimen assessment (the DOTES); and (2) 3-D analysis of the wide bonded metal joint specimen. The 2-D strip specimen was used to calibrate the material input properties of the cohesive zone element (CZE) technique against the experimental results defined in Section 5.3. Also, the 2-D strip specimen was used to verify the cohesive fatigue model by comparing the predicted fatigue lives with that predicted using the VCCT approach incorporating the established modified Paris law defined in Chapter 5. Afterwards, the cohesive fatigue model was used to determine the SERRs and predict the disbond growth rate of the wide bonded metal joint specimen. The analysis of how a local disbond propagated and affected the bonded joint/repair effectiveness was performed in this chapter using the 3D analysis of the wide bonded metal joint specimen.

6.2 Cohesive Fatigue Damage Model

The S-N curves are widely used in many engineering applications to calculate the fatigue life under cyclic loads. Fatigue life prediction using the S-N diagrams did not require computational tools as the calculations were essentially dependent on the stress state. However, predicting the fatigue crack propagation was challenging. One of the key challenges was the implementation of fracture mechanics tools as a function of energy release rate (ERR).

The VCCT method was one of the methods used to calculate the ERR. However, this approach still has difficulty in propagating cracks using three-dimensional models, especially when the crack front was not aligned. CZE method has been widely accepted as a simulation tool for predicting the onset and propagation of debonding in bonded joints subjected to fatigue loading [103].

Recently, Davila [108] developed a damage model for cyclic loading that relied on the loading history and damage accumulation at the integration point. The bi-linear cohesive law implemented for the proposed cohesive fatigue damage model is presented in Figure 6.1. Similar to the static analysis, the cohesive law consisted of an elastic range, 0–E, followed by the "tearing" line, E-T as shown in Figure 6.1a. Any point outside the cohesive law corresponded to failure in the material state. The material experienced fatigue damage when $\sigma_{max} < \sigma_c$ as illustrated in Figure 6.1a. Furthermore, at point P in Figure 6.1b, the damage, d, accumulated with the number of cycles. As a result, the maximum displacement jump, λ increased from points A to F. At point F, unstable failure occurred as σ_{max} exceeded the load carrying capacity of the material defined by tearing region, E-T.

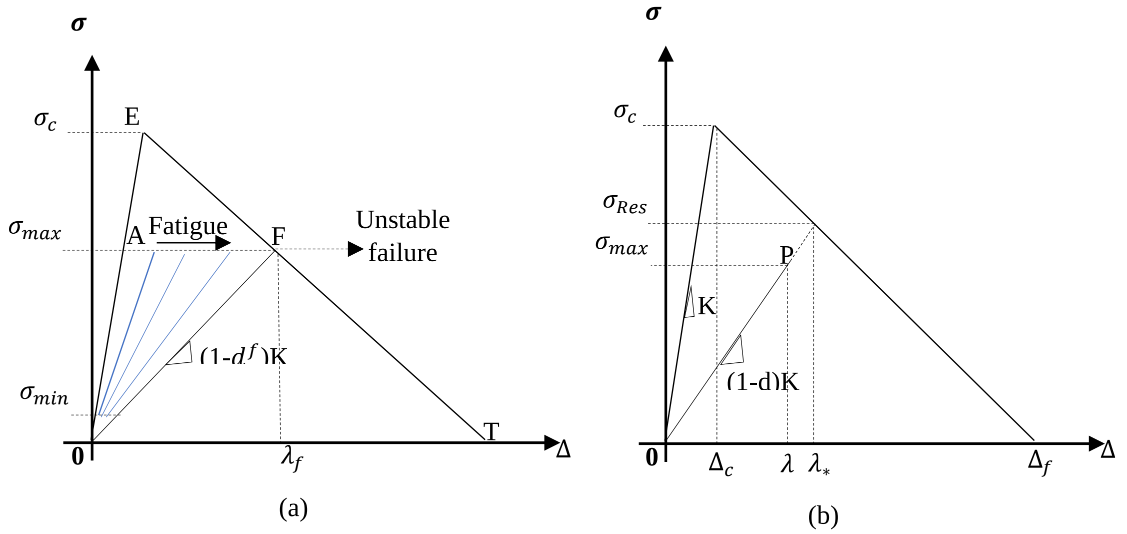

Figure 6.1: Bi-linear cohesive fatigue damage a) definition of fatigue under constant σ_{max} b) description of displacement jump in fatigue (Adapted from [108]).

The heuristic fatigue damage accumulation model of was expressed in terms of stress-amplification exponent β and γ:

$$\frac{dD}{dN} = (\mathrm{D} + \gamma)\left(\frac{\lambda}{\lambda_*}\right)^{\beta} \tag{6.1}$$

Where the coefficients β(R) and γ(R) are functions of the stress ratio (R) which are calculated by curves fitting from the integral equation to the S-N curve. The integral equation was:

$$N^f = \left(\frac{\sigma_{max}}{\sigma_c}\right)^{-\beta} \int_0^{D^F} \frac{(1-D)^{\beta}}{D+\gamma}\, \mathrm{dD} \tag{6.2}$$

Davila [108] determined the typical coefficients β and γ as a function of stress ratio (R) as presented in Table 6.1, based on Fleck's assessment result [186] that the endurance limit of a number of materials (including polymer) subjected to fully reversible loading approximately was equivalent to 1/3 of the yield strength, Goodman diagram and the assumed positions of low cycle limit and endurance limit anchor points of the S-N curve.

Table 6.1: β and γ coefficients for various typical stress ratio [108].

R	γ	β
-0.1	0.001911	13.611
0	0.002142	21.842
0.1	0.002194	23.649
0.5	0.002643	38.033

Davila [108] also demonstrated the link between Equation 6.1 and the Paris law. According to Vieira [187], several theoretical considerations were used to predict the linear relationship between β and m of the Paris law exponent (Equation 5.2). Furthermore, Allegri and Wisnom [188] calculated the correlation of m = $\beta/2$ by utilising the Mode II damage evolution model, which showed a good approximation for both Mode I and Mixed-mode analyses.

A modified Paris law relationship was established previously in Chapter 5 using extensive experimental data. Thus, the parameters β and γ in Equation 6.1 could alternatively be determined by using the link with this modified Paris law.

A similar approach used by Davila [108] was implemented in the current study, that is, the prediction was started using the coefficients β and γ as provided in Table 6.1. The fatigue life prediction for the DOTES specimen was benchmarked against the results from the prediction previously conducted using the VCCT approach and modified Paris law which will be discussed in Section 6.4.2.2.

It should be emphasized that generally to apply the cohesive fatigue damage model as developed by Davila, fatigue tests must be conducted to establish the S-N curve of the test specimens. Unless the S-N curve is fully consistent with that used by Davila, the parameters used in the model need to be determined using the S-N curve established and the procedures described by Davila [108].

The terms λ and λ_* in Equation 6.1 are the relative displacement jump at point P defined in Figure 6.1b and expressed as:

$$\frac{\lambda}{\lambda_*} = \frac{\sigma_{max}}{(1-D)\sigma_c} \tag{6.3}$$

Where the damage norm (D) is:

$$\mathrm{D} = \frac{\lambda_* - \Delta_c}{\Delta_f - \Delta_c} \tag{6.4}$$

This damage norm is a linear function of displacement jump in fatigue. The relation of damage norm (D) and loss of stiffness (1-d) can be interpreted as:

$$1\text{-d} = \frac{(1-\mathrm{D})\Delta_c}{D\Delta_f + (1-D)\Delta_c} \tag{6.5}$$

6.2.1 Mixed Mode

The mixed-mode cohesive model implemented was based on the mixed-mode model developed by Turon et al. [189]. The model was established with the correlation between Modes I and II parameters. The authors [189] showed that the ratio of Δ_c/Δ_f should be consistent for all mix modes to obtain thermodynamic consistency. The correlation is:

$$\frac{\Delta_c}{\Delta_f} = \frac{\sigma_c^2}{2K_{normal}G_{Ic}} = \frac{\tau_c^2}{2K_{shear}G_{IIc}} \tag{6.6}$$

Where σ_c and τ_c are the interlaminar peel and shear strengths; G_{Ic} and G_{IIc} are the critical ERR for Modes I and II; K_{normal} and K_{shear} are the penalty stiffness in Modes I and II, respectively. For the bilinear cohesive law, the effective mixed-mode displacement jump is defined as:

$$\lambda = \frac{K_{normal}\langle\lambda_I^2\rangle + K_{shear}(\lambda_{II}^2 + \lambda_{III}^2)}{\sqrt{K_{normal}^2\langle\lambda_I^2\rangle + K_{shear}^2(\lambda_{II}^2 + \lambda_{III}^2)}} \tag{6.7}$$

In which λ_I is the opening displacement jump, and λ_{II} and λ_{III} are the orthogonal in-plane displacement jumps. The mixed-mode ratio is:

$$\xi = \frac{K_{shear}(\lambda_{II}^2 + \lambda_{III}^2)}{K_{normal}\langle\lambda_I^2\rangle + K_{shear}(\lambda_{II}^2 + \lambda_{III}^2)} \tag{6.8}$$

And the mixed-mode penalty stiffness is defined as:

$$K_B = \frac{K_{normal}^2\langle\lambda_I^2\rangle + K_{shear}^2(\lambda_{II}^2 + \lambda_{III}^2)}{K_{normal}\langle\lambda_I^2\rangle + K_{shear}(\lambda_{II}^2 + \lambda_{III}^2)} \tag{6.9}$$

Finally, the critical (Δ_c) and maximum displacement (Δ_f) in mixed-mode are:

$$\Delta_c = \frac{\sqrt{\frac{\sigma_c^2}{K_{normal}} + \left(\frac{\tau_c^2}{K_{shear}} - \frac{\sigma_c^2}{K_{normal}}\right)\xi^{\eta}}}{\sqrt{K_B}} \text{ and } \Delta_f = \Delta_c \frac{2K_{normal}G_{Ic}}{\sigma_c^2} \tag{6.10}$$

Where η is the interpolation parameter of Benzeggagh and Kenane delamination propagation criterion [138].

6.2.2 Determination of Crack Propagation

The crack length of the CZE fatigue damage could be determined by adding the damage state variable of each cohesive element multiplied by the area of cohesive element. For elements in the process zone where d is a range from 0 to 1, the damage variable considered was the average of the damage from the integration points of each cohesive element. The illustration of the damage distribution in the process zone for 2D and 3D models is shown in Figure 6.2.

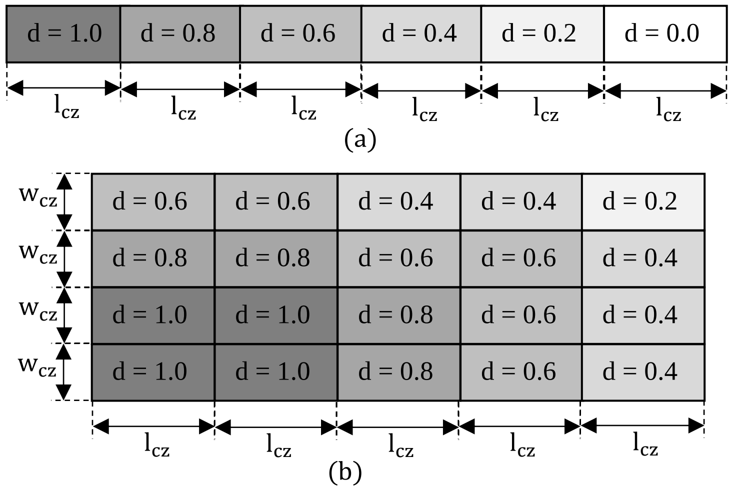

Figure 6.2: Illustration of damage in cohesive element a) 2D (side view) b) 3D (top view).

The crack extension (Δa) can be defined as:

$$\Delta a = \sum \frac{d}{n_{cz}} A_{cz} \tag{6.11}$$

Where:

A_{cz} = cohesive element length (l_{cz}) x n_{cz} for 2D model

A_{cz} = cohesive element length (l_{cz}) x cohesive element width (w_{cz}) x n_{cz} for 3D model

n_{cz} = number of cohesive elements in the process zone

d = $\frac{\sum d}{n_{ip}}$, n_{ip} is the number of integration points of the cohesive element.

6.2.3 Determination of Strain Energy Release Rate Using CZE

The energy release rate (G) can be determined using the constitutive law of the selected cohesive zone model:

$$G = \int_0^{\Delta} \sigma(\Delta)\, d\Delta \tag{6.12}$$

The maximum energy release rate (G_{max}) and change in the energy release rate ($\Delta G = G_{max} - G_{min}$) used in the Paris law formulation could be calculated based on the area of the cohesive law as illustrated in Figure 6.3.

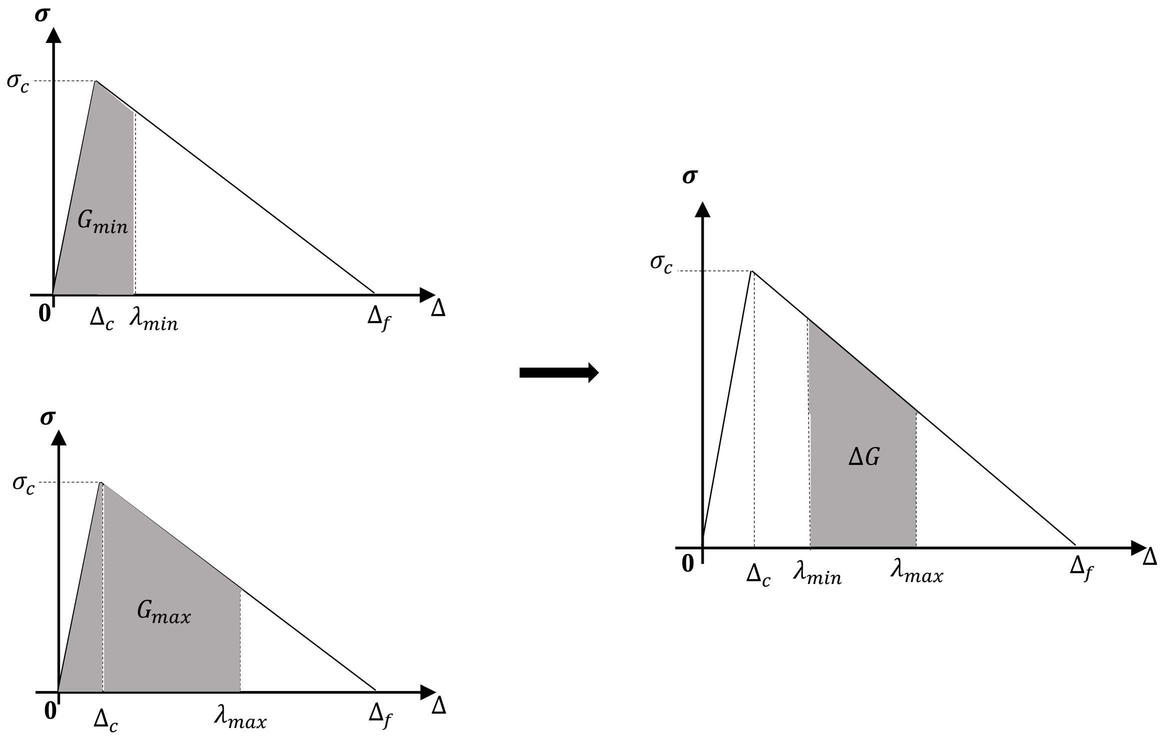

Figure 6.3: Definition of the strain energy release rate in bi-linear cohesive fatigue law (Adapted from [105]).

The equation of G_{max} can be defined as:

$$G_{max} = \frac{\sigma_{max}}{2}\,\lambda \qquad \text{for } \lambda <= \Delta_c \qquad (6.13)$$

$$G_{max} = \frac{\sigma_c}{2}\left[\left((\lambda - \Delta_c)\left(\frac{\Delta_f - \lambda}{\Delta_f - \Delta_c} + 1\right)\right) + \Delta_c\right] \qquad \text{for } \Delta_c < \lambda < \Delta_f \qquad (6.14)$$

$$G_{max} = G_c \qquad \text{for } \lambda = \Delta_f \qquad (6.15)$$

The correlation of G_{max} with load ratio (R) is:

$$R^2 = \frac{G_{min}}{G_{max}} \qquad (6.16)$$

Thus, the variation of energy release rate (ΔG) can be defined as:

$$\Delta G = \frac{\sigma_{max}}{2}\,\lambda\,(1\text{-}R^2) \qquad \text{for } \lambda <= \Delta_c \qquad (6.17)$$

$$\Delta G = \frac{\sigma_c}{2}\left[\left((\lambda - \Delta_c)\left(\frac{\Delta_f - \lambda}{\Delta_f - \Delta_c} + 1\right)\right) + \Delta_c\right](1\text{-}R^2) \qquad \text{for } \Delta_c < \lambda < \Delta_f \qquad (6.18)$$

$$\Delta G = G_c(1\text{-}R^2) \qquad \text{for } \lambda = \Delta_f \qquad (6.19)$$

When the variation of load ratio (R) was considered, a higher load ratio would decrease the variation in the energy release rate, as illustrated in Figure 6.4.

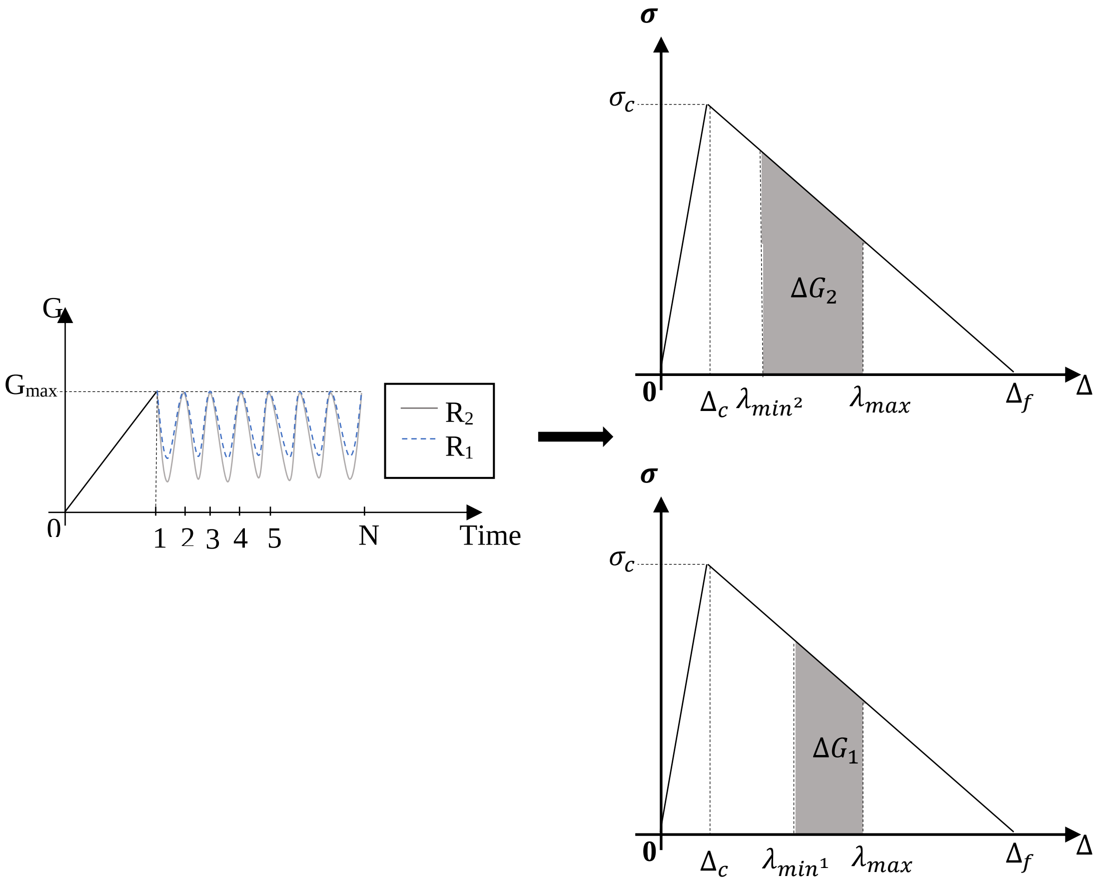

Figure 6.4: The effect of load ratio (R > 0) on strain energy release rate (Adapted from [105]).

6.3 User Subroutine

A user written Ucohesive subroutine was developed for MSC Marc cohesive element. The subroutine was called for every increment and integration point. Three modules were created for sharing data and/or procedures, namely: parameters, data, and calculations. One of the advantages of using a module is that it can be tested and updated separately from the main program. The parameter module contained all the parameters required for bi-linear cohesive law such as penalty stiffness (K), critical ERR (G), and maximum traction (σ_c). The data module was created to store all the data required for each increment (D, d, and G). The last module was used to define all the functions required. The Ucohesive subroutine was responsible for calling all the modules.

The Ubginc subroutine was used to initialise and modify the stored data, which was run at the beginning of each increment. In addition, the Uedinc subroutine was called at the end of the last increment to represent the total crack propagation and SERR calculation. The connections between the subroutines, Marc, and modules are illustrated in Figure 6.5.

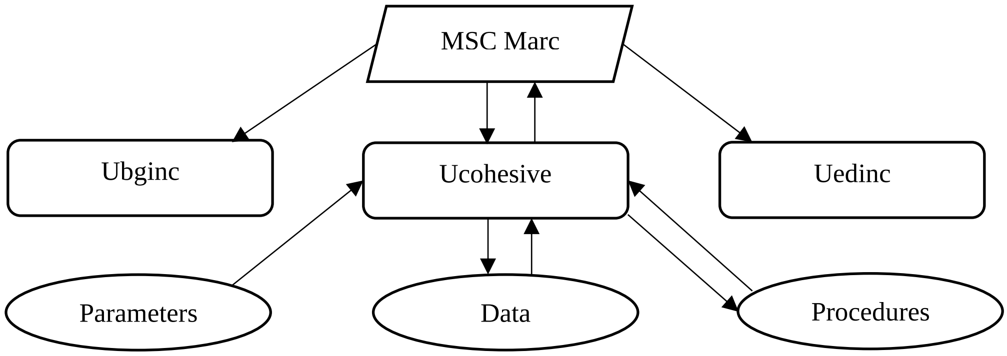

Figure 6.5: Interactions between MSC Marc, subroutines and modules.

The implementation of the cohesive fatigue damage under the quasi-static loading was achieved by adding the fatigue damage calculation into the Ucohesive which is illustrated in Figure 6.6.

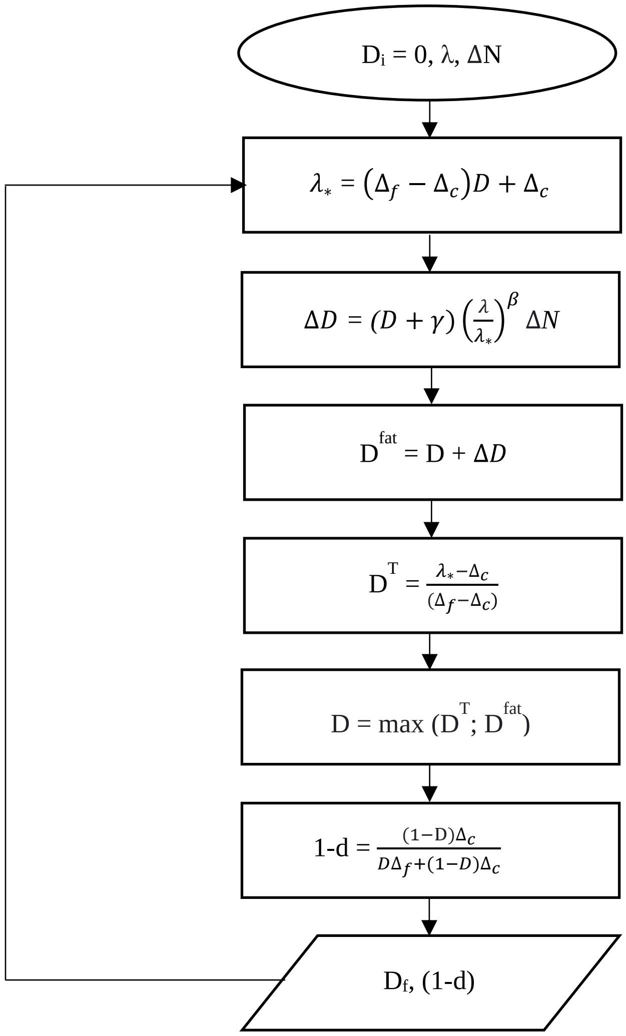

D^{fat}: Fatigue damage | λ: displacement jump | λ_*: reference displacement

D^{T}: Tearing damage | (1-d): loss of stiffness | Δ_f: maximum displacement

ΔD: Incremental fatigue damage | Δ_c: critical displacement | ΔN: step size for number of cycles

Figure 6.6: Calculation of fatigue damage cohesive law using SCL procedure (Adapted from [108]).

The damage calculation procedures defined in the subroutine that account for tearing, and fatigue damage are described in detail in Figure 6.7. The output of the subroutine is the damage state variable (d).

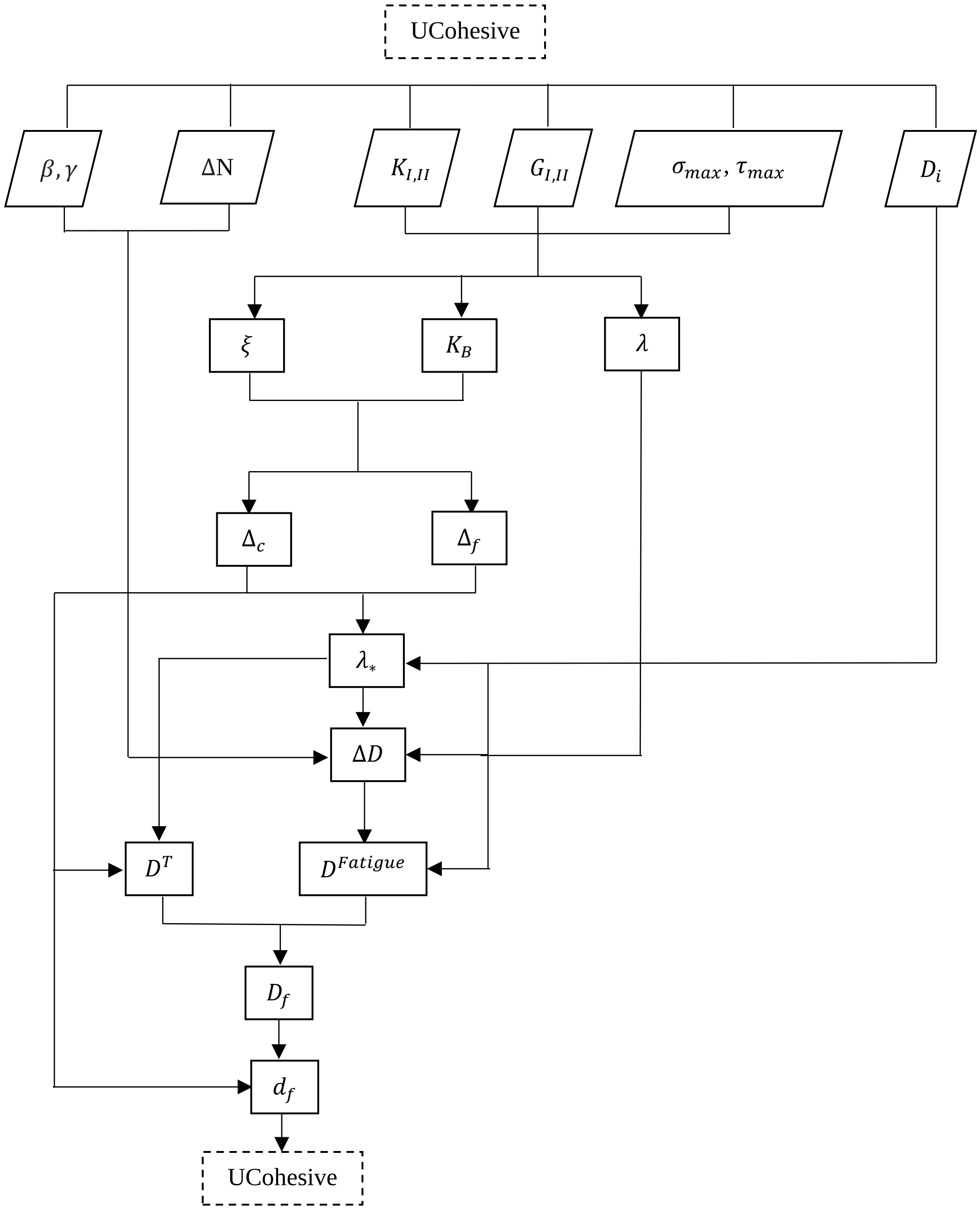

Notes:

Subroutine

Parameters

Function

Figure 6.7: UCohesive subroutine algorithm dependencies.

6.4 2D Finite Element Modelling

6.4.1 Static Loading

Interfacial failure that might arise from debonding of the adhesive was modelled using the Cohesive Zone Element (CZE) method with bi-linear and exponential traction-separation law. MSC Marc, a commercial finite element software was utilised in this study to predict the disbond growth initiation load (residual strength) of the DOTES with a pre-defined disbond. Cohesive failure was modelled through the insertion of a layer of cohesive elements at the adhesive interface. The irreversible response is characterised by increasing the damage ranging from 0 (onset delamination) to 1 (full delamination). Maximum effective traction (t_c) responses in pure Mode I and II along with the behaviour of the interface material under mixed-mode loading were calculated using the exponential and bi-linear function defined in Section 3.4.2.4.

Two-dimensional four-node linear plane-strain quadrilateral elements were used. The element size in the adhesive bond-line was set to 3.75E-2 mm in most areas. There were four elements through the adhesive bond-line thickness along with the interface element embedded in the middle of the adhesive bond-line.

According to Johnson et al. [190], the cohesive element was usually applied with a small thickness to reduce the convergence issue. For this reason, a cohesive thickness of 1E-2 mm was selected. Furthermore, meshing configuration was applied above and below the adhesive bond-line to reduce the computational cost. The mesh refinement strategy and boundary conditions applied are presented in Figure 6.8. Note that only specimens with adhesive cohesive failure mode (specimen with 150 mm pre-disbond) were modelled using the CZE technique.

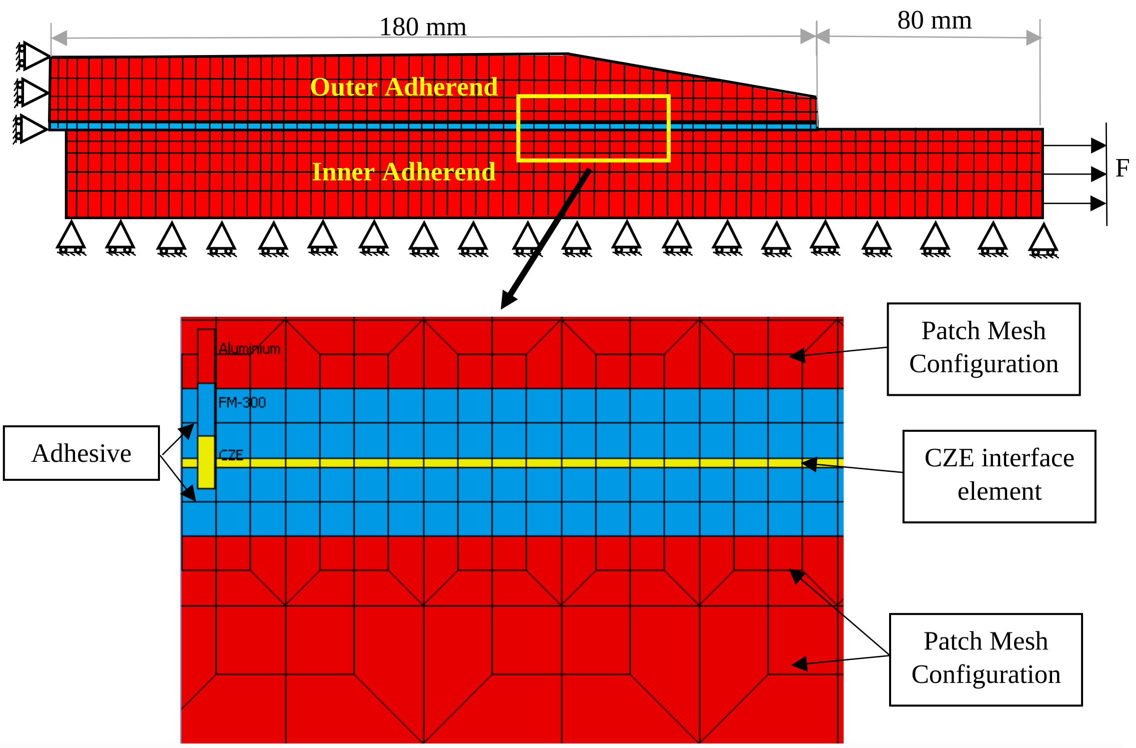

Figure 6.8: Boundary conditions and meshing strategy implemented for the DOTES specimen using the CZE approach.

6.4.1.1 DOTES-ST Specimen Configuration

The residual strength prediction using the CZE method of DOTES-ST un-balanced specimen with 150 mm pre-disbond length is plotted in Figure 6.9. The predicted results using exponential and bi-linear cohesive laws were correlated against the experimental results of the specimen with 150 mm pre-disbond length plotted in Figure 5.10, Section 5.3.1.2. As mentioned earlier in Section 3.4.2.4, the elastic stiffnesses of bi-linear cohesive law were calibrated against the static test results, which were K_n = 24,000 N/mm and K_s, K_t = 3,200 N/mm.

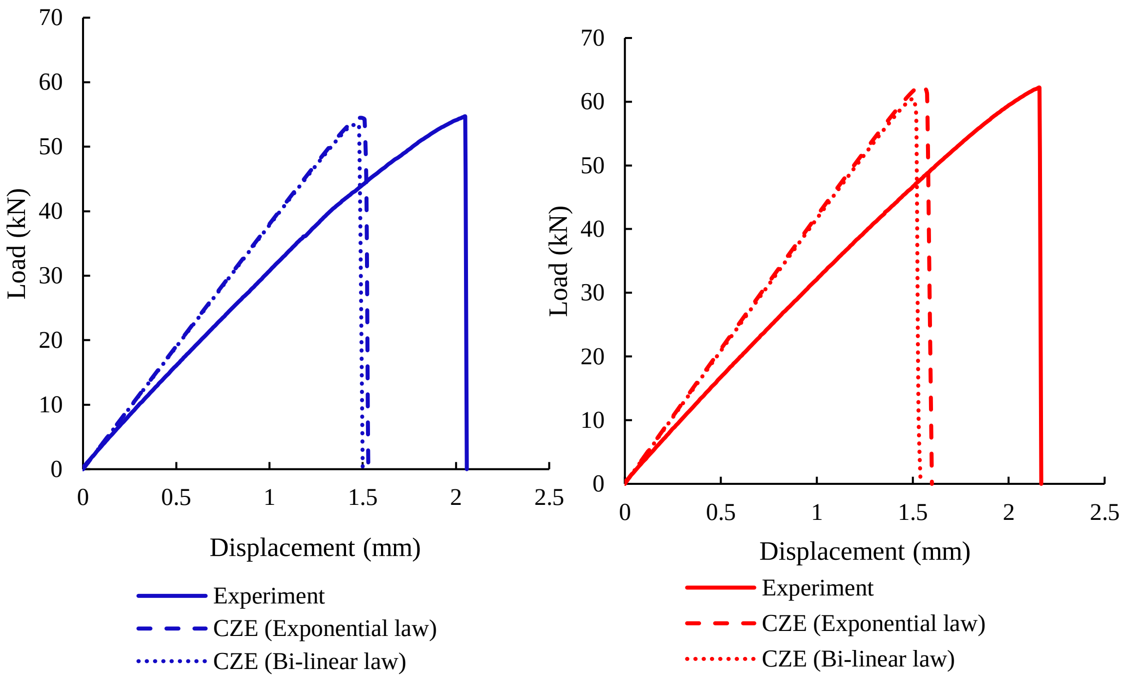

(a) (b)

Figure 6.9: Residual strength comparison of DOTES-ST specimen with 150 mm pre-disbond length at RD condition a) pre-disbond from the tapered end, Variation 1 – thicker outer adherend (TOA) b) pre-disbond from the gap region, Variation 2 – thicker inner adherend (TIA).

The residual strength prediction results showed that:

- For specimen with pre-disbond from the tapered end, Variation 1 – (TOA), the residual strength prediction using exponential law was under-predicted by 0.4%; whilst the prediction using bi-linear law under-predicted by 2.4% against the experimental failure load as presented in Figure 6.9a.
- For specimen with pre-disbond from the gap region, Variation 2 – (TIA), the residual strength prediction using exponential law was over-predicted by 0.62%; whereas the prediction using bi-linear law under-predicted by 2.86% against the experimental failure load as shown in Figure 6.9b.

From the numerical results, it was found that the predicted displacement was significantly lower than that measured from the experiments. This was caused by the compliance of the simulated section that was significantly lower than that of the system reflected by the measured crosshead displacement.

6.4.1.2 DOTES-LT Specimen Configuration

The predicted joint residual strength of the DOTES-LT un-balanced specimen is plotted in Figure 6.10. Since two specimens were tested for each configuration (Variation 1 - TOA and Variation 2 - TIA), the predicted residual strength using the CZE approach was correlated against the average experimental failure load of the two specimens tested defined in Section 5.3.2, which was 52.4 kN for specimen with 150 mm pre-disbond from the tapered end (Variation 1 - TOA) and 38 kN for specimen with 150 mm pre-disbond from gap end (Variation 2 - TIA).

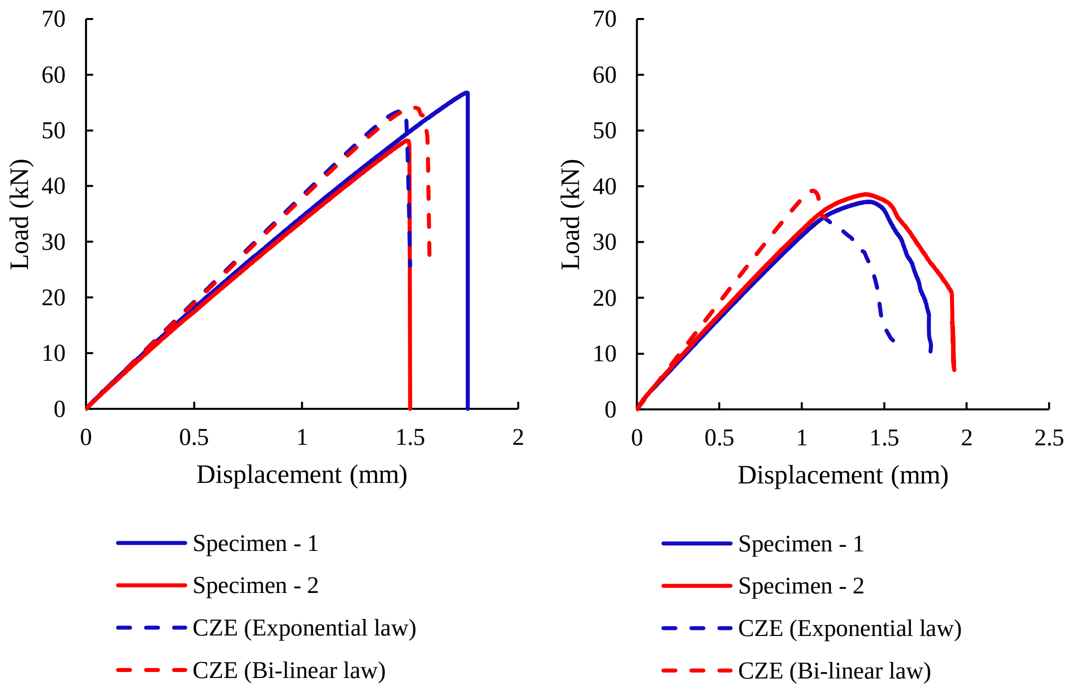

(a) (b)

Figure 6.10: Residual strength comparison of DOTES-LT specimen with 150 mm pre-disbond length at RD condition a) pre-disbond from the tapered end, Variation 1 - TOA b) pre-disbond from gap region, Variation 2 – TIA.

Similar to the description in Section 6.4.1.1, exponential and bi-linear cohesive laws were implemented to predict the joint residual strength at RD condition. The results showed that:

- For specimen with pre-disbond from the tapered end, Variation 1 - TOA (Figure 6.10b), the residual strength prediction using exponential law was over-predicted by 2%; whilst the prediction using bi-linear law was over-predicted by 3% against the average experimental failure load.
- For specimen with pre-disbond from the gap region, Variation 2 - TIA (Figure 6.10a), the residual strength prediction using exponential law was over-predicted by 2.58%; whereas the prediction using bi-linear law over-predicted by 3.1% against the average experimental failure load.

The residual strength predictions of the baseline specimen configuration at HW condition are shown in Figure 6.11. Compared to the failure load obtained from the experimental test using the specimen with a pre-disbond of 150 mm from the tapered end, plotted in Figure 5.11, the predicted results were over-predicted by 1.1% and 4.6% using the exponential and bi-linear cohesive laws, respectively.

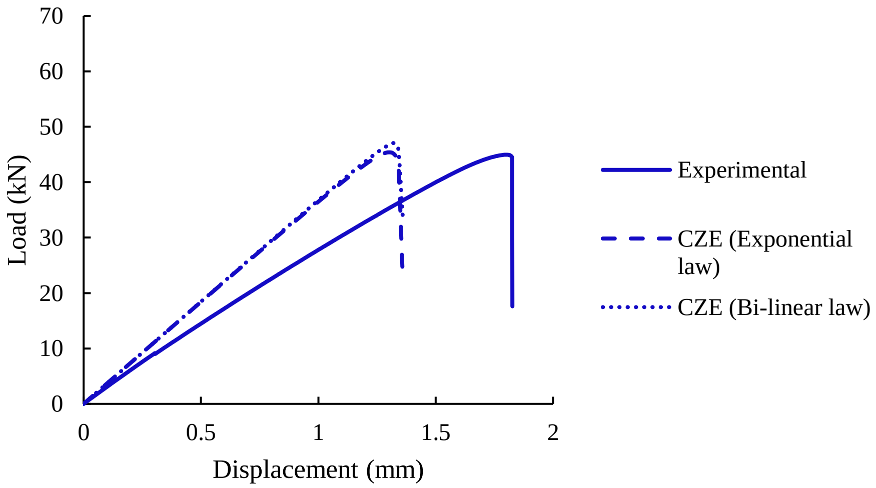

Figure 6.11: Residual strength comparison of DOTES-LT specimen (baseline configuration) with 150 mm pre-disbond length from the tapered end at HW condition.

All joint residual strength results predicted using both cohesive laws provided a good correlation with the results obtained from the experimental test. Thus, it was proven that both exponential and bi-linear cohesive laws could accurately be used to predict the residual strength of adhesively bonded joints. In the following section, the bi-linear cohesive law will be utilised to model the fatigue damage law.

6.4.2 Fatigue Loading

The cohesive fatigue model was applied using simplified cyclic loading (SCL) procedure as presented in Figure 6.12 to avoid high computational expenses. The analysis was performed in two steps. Firstly, the load was ramped up to the maximum load (steps 0 to 1). Then, it was held constant throughout the entire analysis. No fatigue damage was allowed during the first step. However, the solution was recalculated during the second step to account for the internal load redistribution (tearing and fatigue damage accumulation). The stress ratio (R) was introduced to account for the effect of cyclic on fatigue damage.

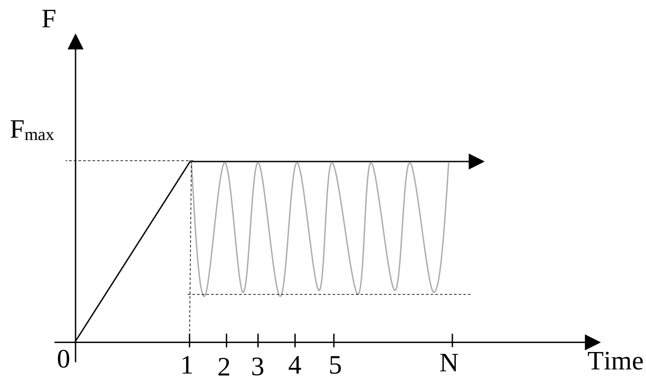

Figure 6.12: Simplified cyclic loading (SCL) procedure (Adapted from [108]).

6.4.2.1 Validation with Double Cantilever Beam (DCB) Specimen

The double cantilever beam (DCB) specimen has been widely used as a regular test method to determine the onset of delamination growth. As has been done by Davila [108], the developed Ucohesive subroutine was benchmarked against the DCB published results in [108] to validate its accuracy. The specimen configurations and material properties of using IM7/8852 graphite/epoxy unidirectional tape are summarised in Tables 6.2 and 6.3, respectively.

Table 6.2: Dimensions of DCB specimen.

a_o(mm)	w (mm)	h (mm)	L (mm)
50.8	25.4	2.25	178

Table 6.3: Material Properties of IM7/8852 [191].

E_{11} (avg T/C)	146,671 MPa
$E_{22} = E_{33}$	8703 MPa
$G_{12} = G_{13}$	5164 MPa
G_{23}	3001 MPa
G_{Ic}	0.24 N mm/mm^2
G_{IIc}	0.739 N mm/mm^2
σ_c	80.1 MPa
τ_c	97.6 MPa
$\nu_{12} = \nu_{13}$	0.32
ν_{23}	0.435

The parametric model was created in MSC Marc based on the model developed by Davila in Abaqus/std. The DCB model shown in Figure 6.13 was created in two-dimensional and three-dimensional. For the two-dimensional model, four-node linear plane-strain quadrilateral elements were used. The element size was set to 0.1 mm for the entire cohesive zone element with three layers through the arm thickness. For the three-dimensional model, eight-node hexahedral solid elements were used. The specimen was modelled with five elements across the width and three elements through the thickness.

Similar to the 2D model, the cohesive element at the propagation zone was sized to 0.1 mm. Also, the propagation zone length varied from 5 to 15 mm depending on the crack propagation length required.

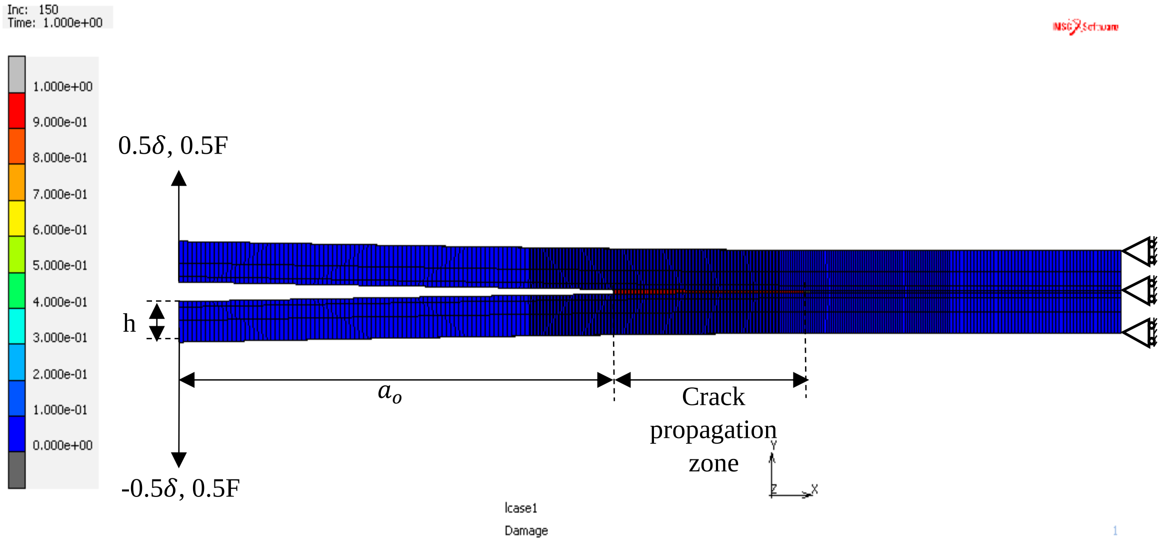

Figure 6.13: Two-dimensional FE model of DCB specimen with 25.4 mm geometric properties.

The crack propagation with a various number of cycles is presented in Figure 6.14. The red elements shown in Figure 6.14a were the completely damaged element, followed by the process zone and those to the right were intact. The points which correspond to the crack propagation length are reflected in Figure 6.14b. The results showed that both 2D and 3D analyses were well correlated to the FE analysis performed by Davila [108]. It was shown that the results converged with 1000 cycles/increment.

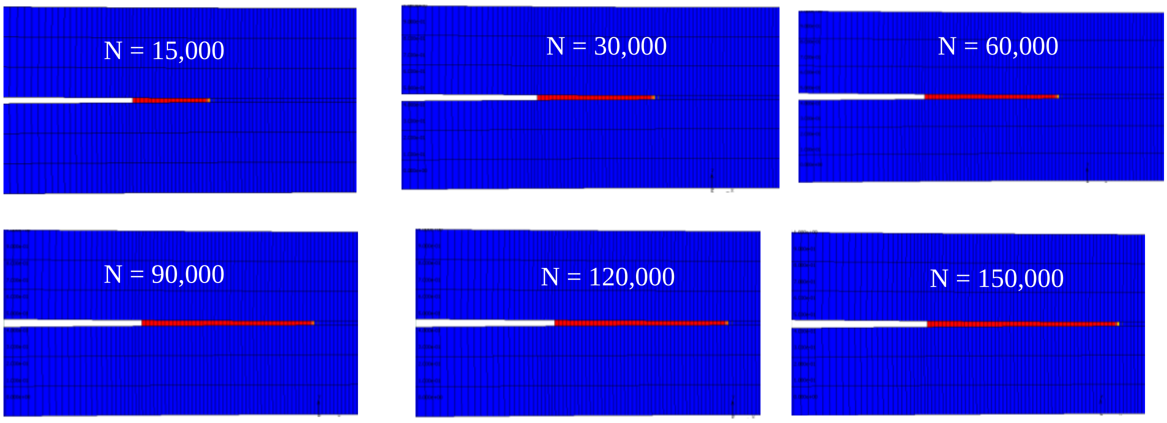

(a)

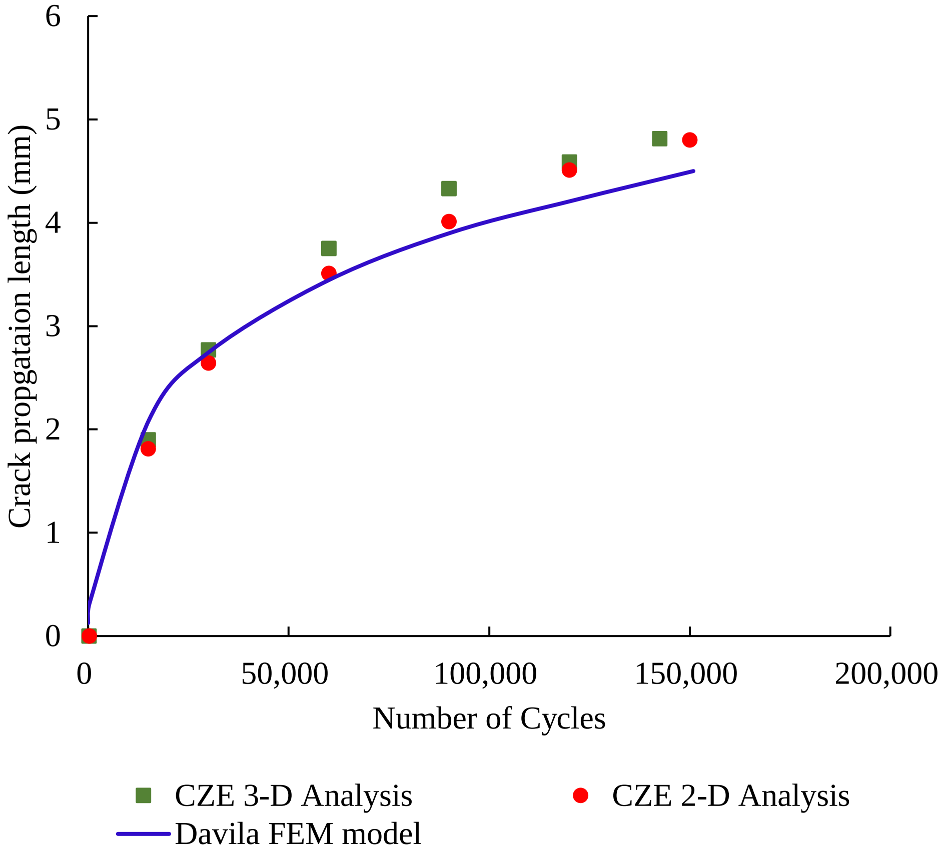

(b)

Figure 6.14: Implementation of cohesive fatigue damage law in DCB specimen with applied displacement (δ) of 1.92 mm a) detail of propagation zone (2D model) b) crack propagation as a function of number of cycles.

6.4.2.2 The DOTES Coupon Specimen

The SERR calculation using the cohesive fatigue model defined in Section 6.2.3 was compared with that determined using the VCCT approach. The meshing strategy and boundary conditions applied are presented in Figures 6.8. The material properties used are defined in Table 3.4 with normal elastic stiffness (K_n) of 24,000 N/mm, and shear elastic stiffness (K_s) of 3,200 N/mm as stated in Section 6.4.1.1.

The comparison of SERR results presented in Figure 6.15 for specimen with baseline configurations was determined using the VCCT method and cohesive fatigue model, with an applied load of 33.3 kN. A similar trend could also be observed with different applied loads. The results showed a good correlation using both techniques. As expected, Mode II was dominated for the case of disbond initiated from the gap region. Whilst for disbond initiated from the tapered end, Mode I contributed around 22% of the total SERR.

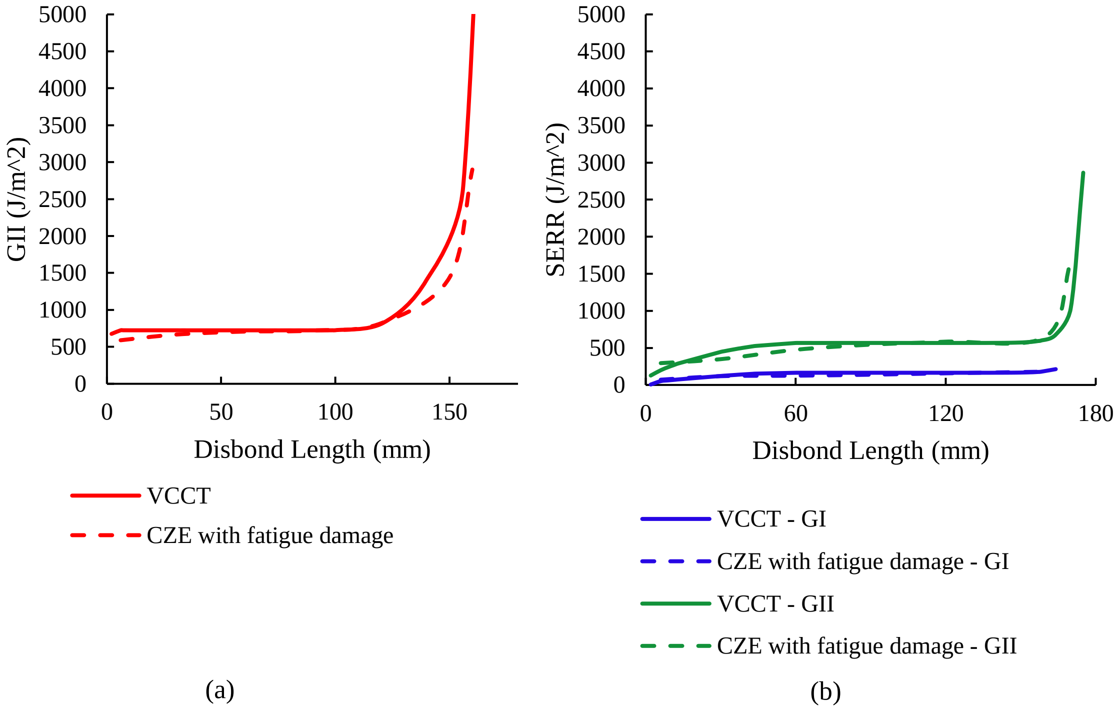

Figure 6.15: SERR curve a) disbond initiated and propagated from the gap end; b) disbond initiated and propagated from the tapered end (Load = 33.3 kN).

An attempt was made to verify the approach described in Section 6.2.2 (determination of the crack propagation). The disbond crack propagation was predicted using:

i. Specimen with pre-disbond length of 60 mm initiated from the gap region and tapered end, for the case of fatigue peak load equals to 33.3 kN, R = 0.1 (the 60 mm pre-disbond length was considered as it was within the steady-state range of the SERR value as presented in Figure 5.19); and

ii. Specimen with pre-disbond length of 30 mm initiated from the gap region and tapered end, for the case of fatigue peak load equals to 27 kN, R = 0.1.

The predicted results determined using the proposed method defined in Section 6.2 were compared with the life prediction determined using the VCCT approach incorporating the established modified Paris law and experimental test data defined in Section 5.6 (Equation 5.3 with the parameters defined in Table 5.10 for without hot-wet conditioning) and Section 5.4.1, respectively.

The comparison of predicted disbond growth results is plotted in Figure 6.16. It is shown that for the case of fatigue peak load equals to 33.3 kN, the CZE fatigue damage formulation underpredicts the disbond growth by 11% for specimen with disbond initiated from the tapered end, whilst it overpredicts the disbond growth by 8% for the specimen with disbond initiated from the gap region. Furthermore, the average difference between the CZE fatigue damage prediction with experimental data is about 33%. This difference is considered insignificant for the fatigue life prediction.

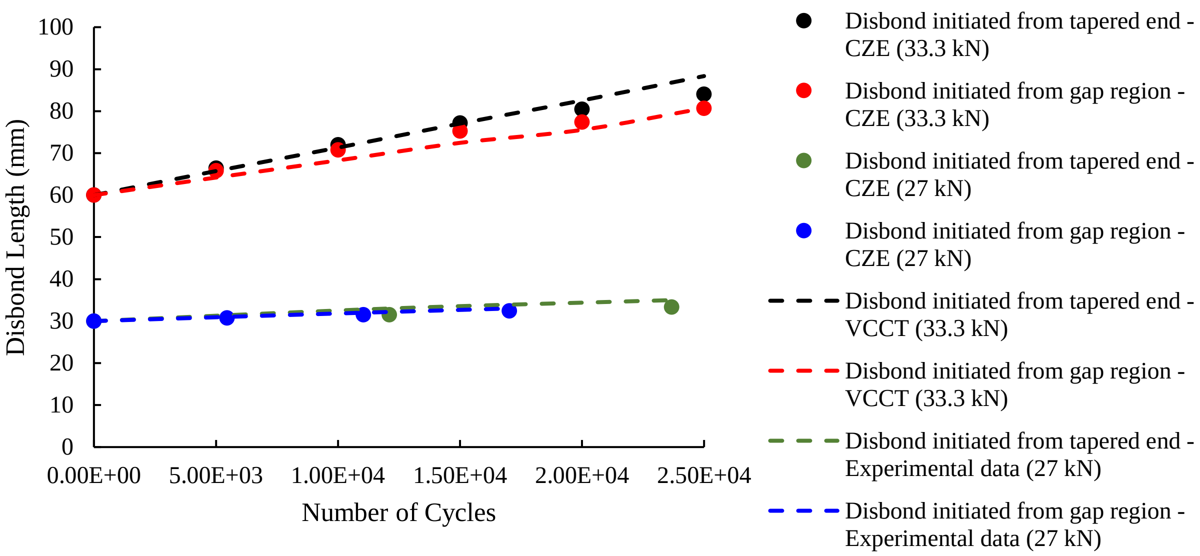

Figure 6.16: Comparison of the predicted disbond growth with fatigue peak load of 33.3 and 27 kN.

6.5 3D Finite Element Modelling

In this section, the effect of local or partial width disbond was investigated through an extended version of the DOTES coupon specimen. This specimen could be represented as: i) double lap joint, and ii) fully damaged panel reinforced with a bonded patch. Assessment of the joint residual strength was conducted by means of the CZE approach to determine the instant static failure of the joint. The SERRs value of the wide bonded metal joint specimen as a function of disbond length was determined using the CZE approach, as defined in Section 6.2.3. The Ucohesive subroutine defined in Section 6.3 was used to determine the SERRs value and predict the disbond growth rate based on the cohesive fatigue damage formulation.

6.5.1 Geometry and Boundary Conditions

The geometry of the fully damaged panel repaired with an adhesively bonded patch specimen is presented in Figure 6.17. It is worth noting that this specimen is similar to the extended version of the DOTES coupon specimen. Hence, it also consists of three different components, called the parent structure (thickness T_i), adhesive layer (thickness η) and patches (thickness T_o).

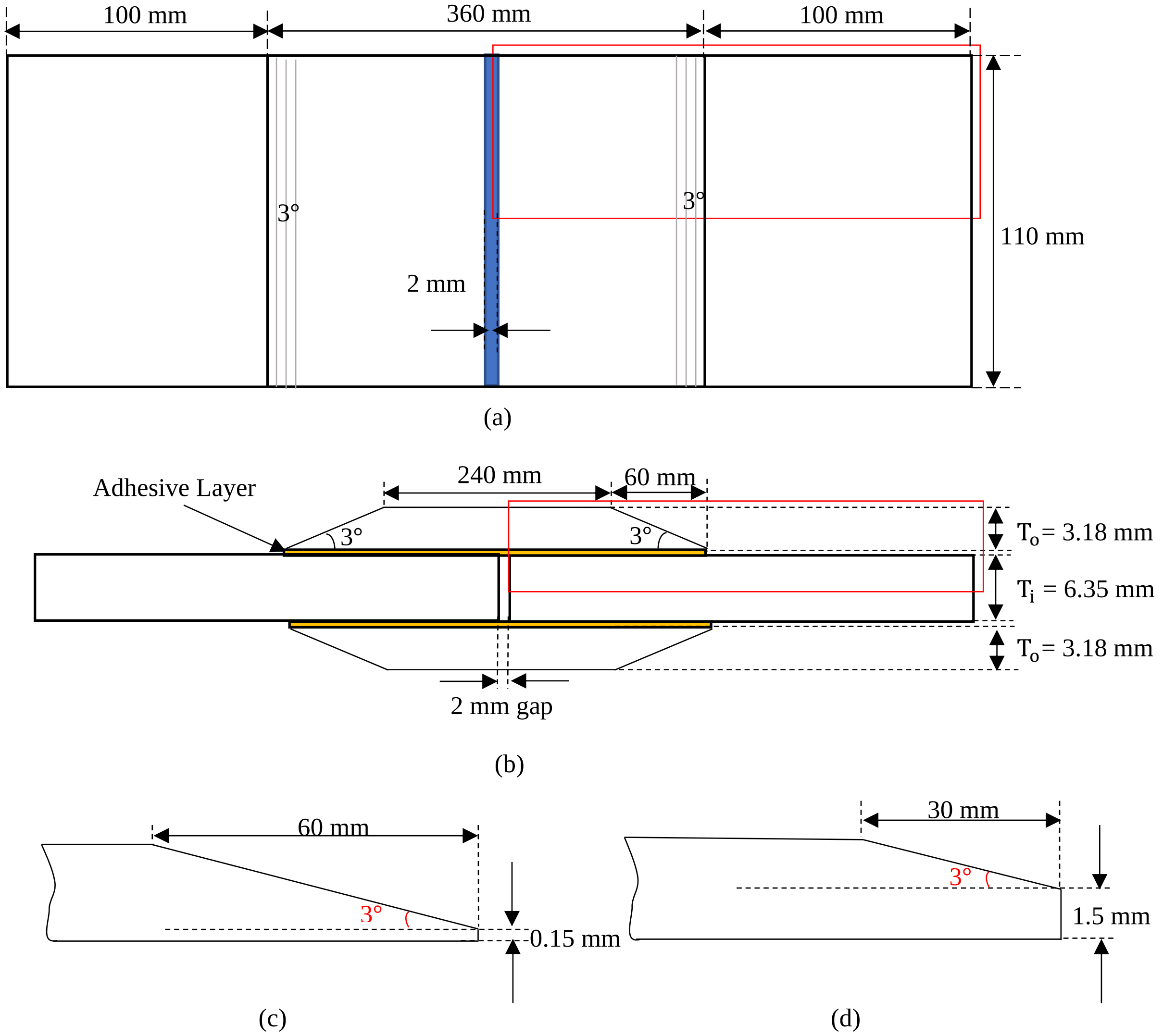

Figure 6.17: Wide bonded metal joint specimen configuration a) top view b) side view c) tapered side for disbond initiated from tapered end d) tapered side for disbond initiated from gap region.

A gap with dimensions of 110 x 2 mm (length x width) was created in the parent structure, which represents a fully damaged parent structure. For this wide bonded metal joint specimen configuration, balance joint configuration with a thickness ratio between inner adherend and outer adherend of 2:1 was considered. The commercial software MSC Marc was utilised to predict the disbond propagation behaviour in the wide bonded metal joint specimen. The twofold symmetry (red marked zone in Figures 6.17 a and b) was considered; and thus, only one-eighth of the specimen was modelled. It should be noted that two different tapered configurations were considered as shown in Figures 6.17 c and d. For the case of disbond initiated from the gap region, an edge thickness of 0.15 mm was applied to reduce the peel stress at the tapered section (similar to the DOTES-LT specimen design defined in Section 3.2.3). Whilst edge thickness of 1.5 mm was implemented for the case of disbond initiated from tapered end (DOTES-ST specimen design in Section 3.2.2).

The boundary conditions implemented are shown in Figure 6.18. To simulate the symmetry conditions, symmetry plane 1 of the specimen, symmetry plane 2 of the patch, and the bottom surface of the parent structure were constrained (displacement in the x-axis, z-axis and y-axis were set to zero respectively). In addition, the end edge of the parent structure was constrained in a manner to represent the test machine loading condition.

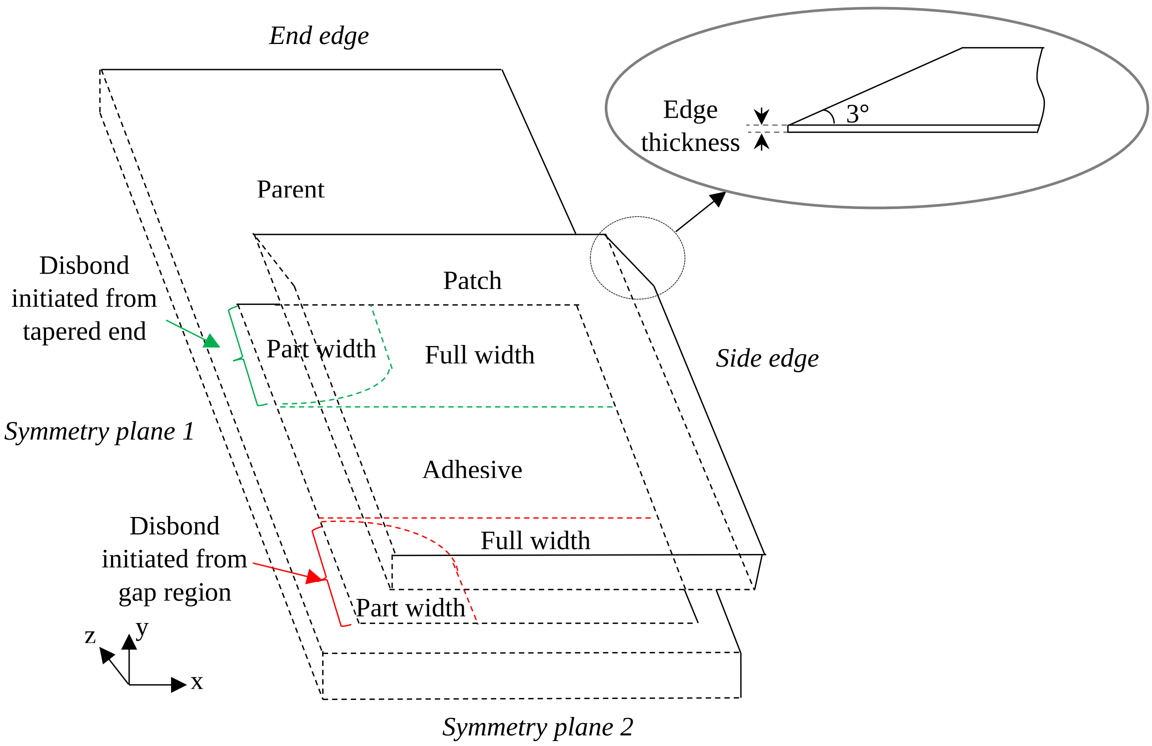

Figure 6.18: Three-layers finite element model (one-eighth portion).

According to a mesh sensitivity study performed by Anyfantis and Tsouvalis [192], the effect of 3D element sizes of (0.2 x 0.2) mm^2, (0.5 x 0.5) mm^2, and (1 x 1) mm^2 towards the single lap and double lap joints strength was less than 3%. Furthermore, Davila et al. [193] performed a numerical study on the effect of various element sizes (3-D, 8 nodes element) to predict the maximum load of double cantilever beam specimen (DCB). The results indicated that poor accuracy was observed when using element size greater than 1.25 mm. This was consistent with the results from Gonçalves [194], using a 1 mm element size, 18 node quadratic elements. Thus, this study uses a three-dimensional eight-node isoparametric solid elements along with a cohesive element size of 1 x 1 x 0.01 mm in most areas.

As stated in Section 6.4.1 and illustrated in Figure 6.8, the cohesive interface element was embedded in the adhesive bond-line. Two different shapes of pre-disbond initiated from both ends (gap region and tapered end) were considered, called full-width disbond and part width disbond as illustrated in Figure 6.18. The full-width pre-disbond shape has similar behaviour to the DOTES coupon specimen (2D analysis) whilst the part width pre-disbond shape was used to investigate the implication of local or part width disbond as discussed in Chapters 4 and 5.

6.5.2 Residual Static Strength Assessment

The residual strength of the wide bonded metal joint specimen was conducted using the element stress-strain based adhesive failure criteria. As mentioned in Section 3.4.2.2, the issue of mesh dependence was handled using the characteristic distance approach. The characteristic distance was so determined by calibrating the mesh size of 3D analysis with the static test result of the DOTES defined in Section 5.3.2, which was 0.1 mm. To reduce the computational cost, the symmetry model presented in Figure 6.18 was used along with mesh size refinement around the disbond crack tip by means of mesh biased technique.

The predicted residual strength as a function of disbond length for specimen with full and part width disbonds, initiated from both ends (gap region and tapered end) are presented in Figure 6.19, where the disbond front shape was kept unchanged. For the specimen with full-width disbond initiated from the gap region, the residual strength was steady up to 120 mm; it then gradually decreased when approaching the total overlap length of the specimen. On the other hand, for disbond initiated from the tapered end, the residual strength would reduce as disbond lengths increased up to 30 mm (where the outer adherend end taper terminates). The curve then became flat as the disbond length further increases, followed by a rapid decrease as the disbond length approached the total overlap length of the specimen. It is important to note that this analysis was done for specimen design with a tapered length of 30 mm as the result was sensitive to the tapered length.

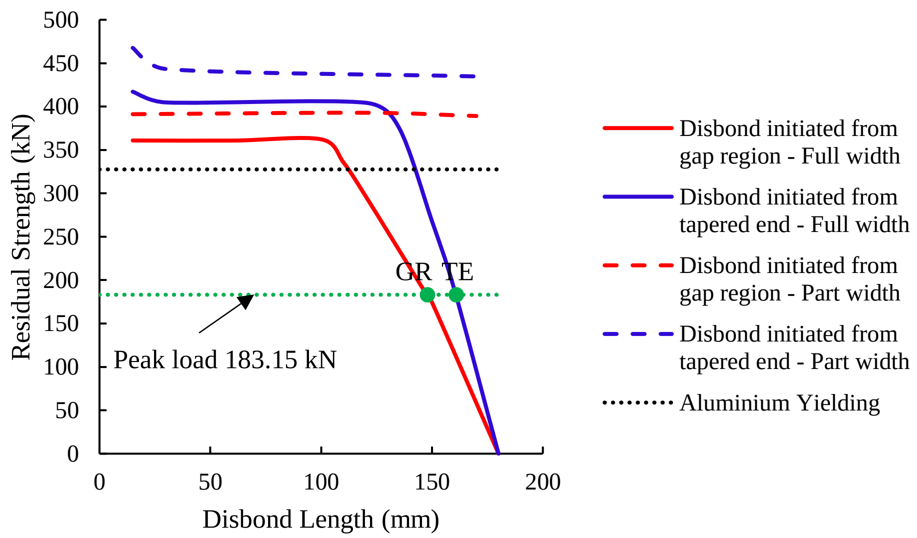

Figure 6.19: Residual strength prediction of wide bonded metal joint specimen for disbond initiated from the gap and tapered ends under HW condition.

The curve plotted in Figure 6.19 was limited by the adhesive strength under hot-wet condition. Considering the upper limit of the fatigue peak load for the DOTES coupon specimen was 33.3 kN (load/unit width = 1.665 kN/mm), the upper limit of fatigue peak load for wide bonded metal joint specimen was calculated to be 183.15 kN (1.665 kN/mm x 110 mm). The joint would rapture under static loading when the disbond reached its length, where the peak fatigue load was equivalent to the joint residual strength (points GR and TE for disbond from two ends) as presented in Figure 6.19. Thus, in the fatigue life prediction, the life of the wide bonded metal joint specimen should only be predicted up to points GR (148 mm) and TE (161 mm) for the case of full width disbond initiated from the gap region and tapered end, respectively.

For the case of part width disbond initiated from the gap region, the joint residual strength was steady throughout the entire disbond length. Whilst for the case of part width disbond initiated from the tapered end, the joint residual strength would slightly decrease as the disbond length increases up to 30 mm; followed by a flat curve as the disbond length increases.

The ultimate failure would occur when the static residual strength of the specimen was equivalent to the fatigue peak load, in which the disbond front shape was not pre-defined but from the disbond growth calculation. Further details will be provided in Section 6.5.4.

6.5.3 Determination of Strain Energy Release Rate

Using the approach described in Section 6.2.3 and the developed subroutine defined in Section 6.3, the SERR components as a function of the disbond length of the wide bonded metal joint specimen were determined.

A load of 183.15 kN (load/unit width = 1.665 kN/mm) was applied through the entire disbond length variations. As expected, the SERR results of disbond initiated from the gap region indicate that Mode I was insignificant compared to Mode II. This phenomenon was observed for both full width and part width disbond. Thus, only SERR of Mode II was considered as shown in Figure 6.20a.

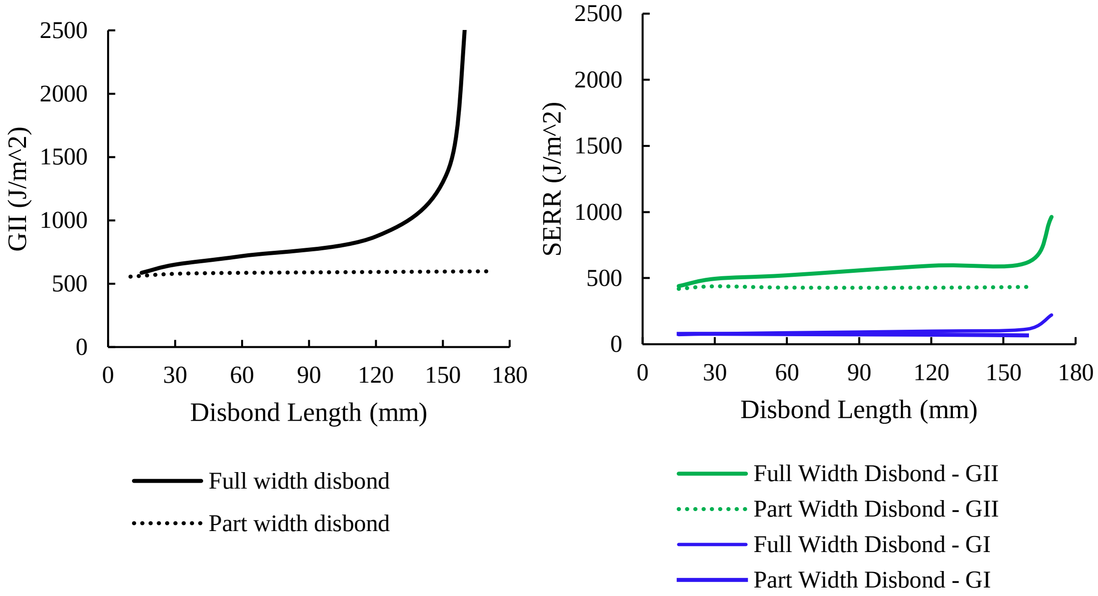

(a) (b)

Figure 6.20: SERR plot for a) disbond initiated and propagated from the gap region and b) disbond initiated and propagated from the tapered end (Load = 183.15 kN).

For the case of disbond initiated from the tapered end, Mode I contributed around 14% to the total SERR. This indicated that the contribution of Mode I in wide bonded metal joint specimen was slightly lower than that in the DOTES coupon specimen (Mode I contributes around 22% to the total SERR).

As shown in Figure 6.20, in the cases of full-width disbond, as the disbond lengths increase, the SERR values initially would increase slowly, then gradually faster, and then rapidly increasing when the disbond lengths approached 150 mm and 160 mm, in the cases of disbond from gap end and tapered end, respectively.

The impact of local or part width disbond to the SERR calculations was presented in Figures 6.20 a and b for the case of disbond initiated from the gap region and tapered end, respectively. Significant reduction of the SERR values was observed compared to the SERR results calculated from full-width disbond. This indicated that as the pre-existing disbond increased, the initial disbond growth rate in the part width disbond case would not increase significantly, due to the effect of load redistribution to the adjacent regions (load shedding effect).

6.5.4 Disbond Growth Prediction

The cohesive fatigue damage model defined in Section 6.2 was used to predict the disbond growth and fatigue life of a 3-D wide bonded metal joint specimen. The disbond growth behaviour of part and full-width disbonds of the wide bonded metal joint specimen are illustrated in Figures 6.21 – 6.23. A pre-disbond length of 30 mm was considered in this study.

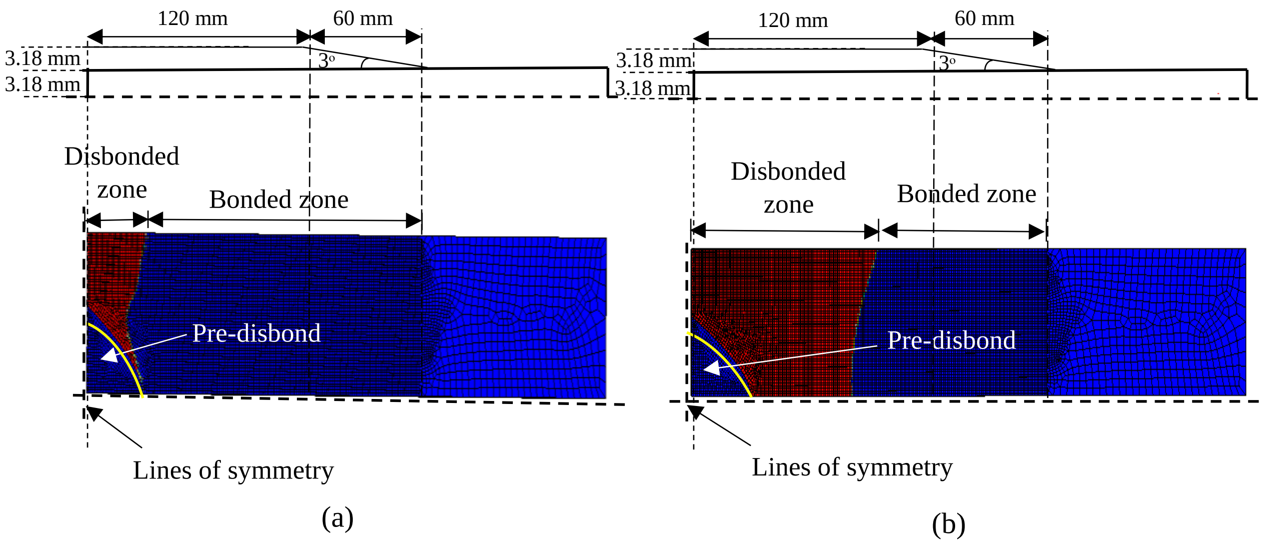

Figure 6.21: Details of propagation zone of a wide bonded metal joint specimen with part width disbond initiated from gap region a) 40,000 cycles b) 100,000 cycles (peak load of 183.15 kN and R = 0.1).

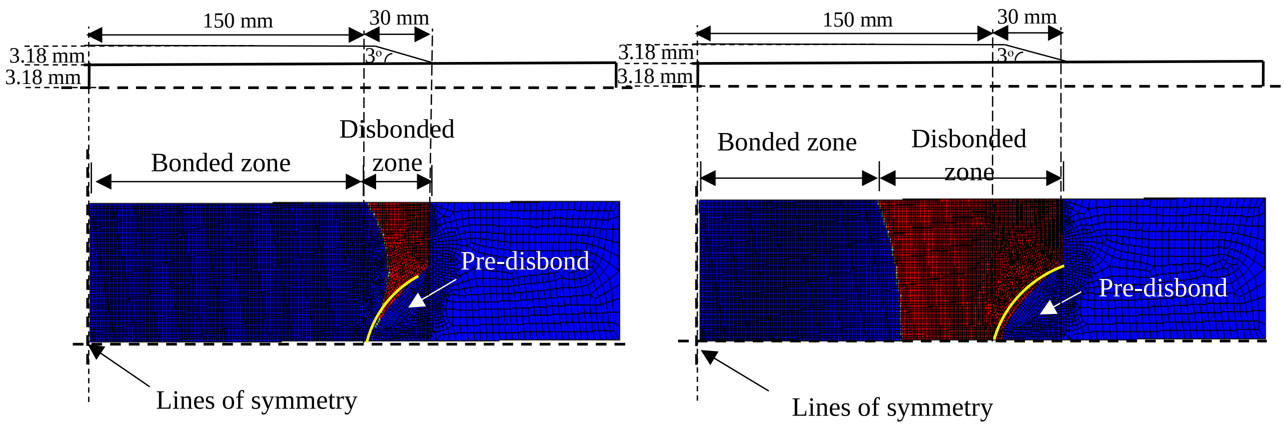

(a) (b)

Figure 6.22: Details of propagation zone of the wide bonded metal joint specimen with part width disbond initiated from tapered end a) 40,000 cycles b) 100,000 cycles (peak load of 183.15 kN and R = 0.1).

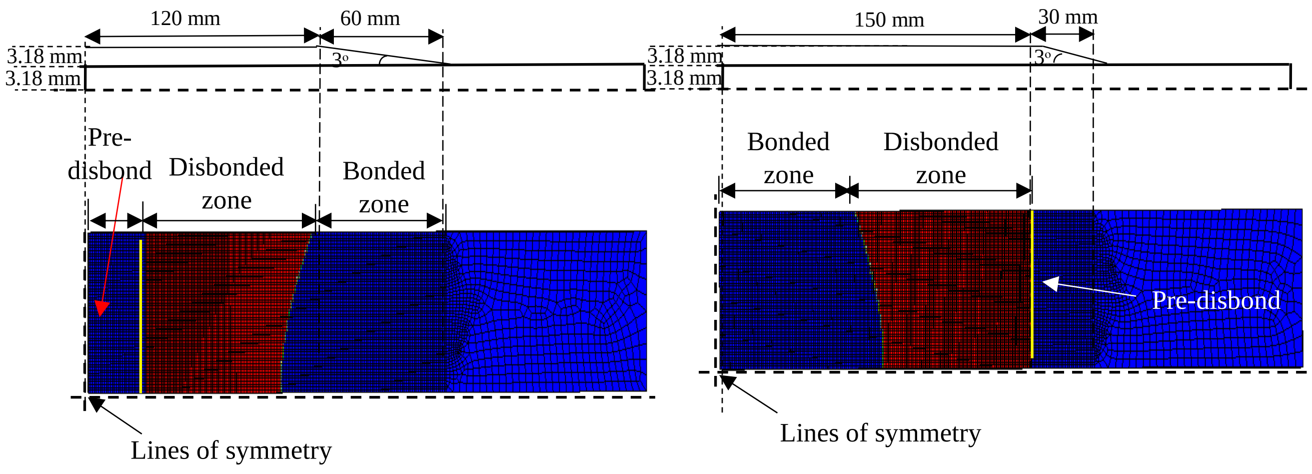

(a) (b)

Figure 6.23: Details of propagation zone-wide bonded metal joint specimen with full-width disbond within 100,000 cycles a) disbond initiated from gap region b) disbond initiated from tapered end (peak load of 183.15 kN and R = 0.1).

Numerical studies using various elements sizes indicated that the prediction's accuracy was notably lower if the size of the element was greater than a certain maximum value. The prediction of full-width disbond propagation within 20,000 cycles, initiated from the gap region was conducted with various element sizes. The results plotted in

Figure 6.24 indicate that the predicted disbond length tends to converge as the element size increases. Poor predictions were observed when the element area was greater than 1.25 mm^2. The analysis was conducted with 200 cycles per increment.

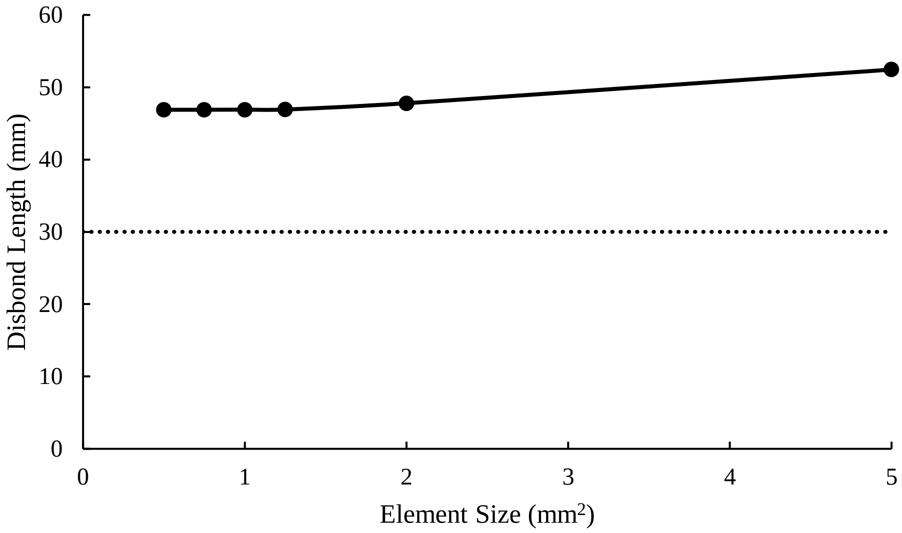

Figure 6.24: Disbond length as a function of the element size.

The disbond growth behaviour for specimens with part width disbond from the gap region is illustrated in Figure 6.21. As presented, disbond growth was initiated from the side edge of the pre-existing disbond crack region, and then propagated through the width of the specimen. This confirmed the indication made previously in Chapters 4 and 5 for the case of a local or part width disbond. Due to the compliance increase at the disbonded region, some load would be redistributed to the adjacent regions that delayed disbond growth at the initial disbonded region (load shedding effect).

The part-width disbond has similar behaviour with the full-width disbond when the disbond was propagated beyond the artificial disbond crack front shape and formed a full-width disbond as reflected in Figures 6.21b and 6.23a for the case of disbond initiated from the gap region. The disbond growth behaviour for disbond initiated from the tapered end (presented in Figures. 6.22 and 6.23b) was similar to that in the case of disbond initiated from the gap region.

The predicted average disbond growth rates of the specimen with full-width and part-width disbond initiated from both ends (gap region and tapered end) are summarised in Table 6.4. It was shown that the predicted average disbond growth rates of the specimen with pre-disbond from the tapered end were higher than that from the gap region. This was consistent with the results from the DOTES coupon specimen in Chapter 5.

Table 6.4: Wide bonded metal joint specimen disbond growth prediction (pre-disbond length of 30 mm).

Description	Initial part width disbond			Initial full-width disbond		
	Maximum Disbond Length (mm)	**Number of Cycles**	**Average disbond growth rate (mm/cycle)**	**Maximum Disbond Length (mm)**	**Number of Cycles**	**Average disbond growth rate (mm/cycle)**
Disbond initiated from tapered end (TE)	161	132,800	1.29×10^{-3}	161	118,200	1.38×10^{-3}
Disbond initiated from gap region (GR)	148	154,800	9.23×10^{-4}	148	124,400	1.02×10^{-3}

From the residual strength assessment conducted in Section 6.5.2, the wide bonded metal joint specimen would rapture rapidly under fatigue peak load of 183.15 kN when reached the disbond lengths of 148 and 161 mm from the gap region and tapered end, respectively. Therefore, the life of the joint should only be predicted to these disbond lengths as presented in Table 6.4. Note that the disbond length considered here was the average disbond growth of the fastest and slowest sides from the inverted arch as shown in Figures 6.21 – 6.23.

6.6 Summary

The applicability of the slow growth management strategy for disbond in a wide bonded metal joint specimen was evaluated computationally in this study using the CZE approach. The material input properties of the CZE approach were calibrated against the experimental results in Chapter 5 by using a 2-D strip specimen. The capability of the cohesive fatigue damage model was assessed by comparing the predicted fatigue lives with those predicted using the established modified Paris law and experimental data. A good correlation of the predicted fatigue lives was shown. Thus, the CZE approach was used to analyse disbond growth behaviour in a wide bonded metal joint specimen. From the analyses above, it can be summarised that:

- By considering an identical load/unit width of 1.665 kN/mm with the DOTES coupon specimen, the upper limit fatigue peak load of the wide bonded metal joint specimen was determined to be 183.15 kN
- The residual strength results indicated that under the peak load of 183.15 kN, the wide bonded metal joint specimen would rapture at 148 mm and 161 mm disbond lengths for disbond initiated from the gap region and tapered end of the joint, respectively.
- The strain energy release rates (SERRs) determined using the cohesive fatigue model showed a good correlation with the one calculated using the VCCT approach. Thus, the SERRs value as a function of disbond length of the wide bonded metal joint specimen with part and full-width disbond were assessed using the cohesive fatigue model.
- Significant reduction of the SERR values was observed for the case of part width or local disbond. This suggested that as the disbond propagated, some

load was redistributed to the adjacent regions (load shedding effect) that caused a slower disbond growth compared to the full-width disbond.

- The cohesive fatigue model implemented in the Ucohesive subroutine was also used to predict the disbond propagation of wide bonded metal joint specimens.
- A slower disbond growth rate was observed for specimens with part width disbond. This indicated that as the disbond propagates, some load was redistributed to the adjacent regions (load shedding effect) which caused a slower disbond growth compared to the full-width disbond.

Chapter 7

Conclusions and Future Work

7.1 Overview

The cost of airworthiness certification has been recognised as a significant concern in adhesively bonded joints, especially for damage repair in highly loaded regions [12]. The generic patch repair specimens are called the Double-Overlap Fatigue Specimen (DOFS), which represents the "disbond tolerant zone" and the Skin Doubler Specimen (SDS), which represents the "safe-life zone" have been established in aircraft industry to minimise the costs of the certification process. However, assessment of a long disbond up to ultimate failure of the joint could not be achieved just on the basis of these two specimens. Ideally, the entire process of disbond growth from disbond initiation up to the ultimate failure of the joint needs to be assessed in order to implement the damage slow growth management strategy. In this thesis, a generic patch repair specimen, called double overlap tapered end specimen (DOTES), contains both "disbond tolerant zone" and "safe-life zone" in the bonded patch repair was considered. Assessment of a joint with a long crack (either from the middle or ends of the overlap), up to the length corresponding to the ultimate failure of the specimens under any peak load could be conducted. The investigation was extended to identify the effect of local or part width disbond growth to bonded joint or repair effectiveness using wide bonded metal joint specimen. Numerical procedure to assess disbond growth in bonded joints or patch repairs used in primary aircraft structures was first carried out. Subsequently, static and fatigue testing at coupon specimen level were conducted to determine the allowable fatigue load range and established the modified Paris law relationships. Finally, numerical modelling of static and cyclic loaded of wide bonded metal joint specimen was investigated in this thesis.

7.2 Key Findings and Advancements

Based on the critical review of literature presented in Chapter 2, adhesively bonded joints were identified as a more effective joint technique in terms of structural cases than mechanically fastened joints. Among the various advantages of adhesively bonded joints, it was identified that a detail assessment on damage slow growth management strategy was required to help satisfy the certification requirement of bonded joints or patch repairs for primary aircraft structures.

The key contributions of this thesis are discussed in the following sub-sections.

7.2.1 Introducing The Modelling Approaches and Generic Patch Repair Design to Understand Disbond Growth Behaviour in Bonded Structure

The Hart-Smith analytical approach has been widely used to predict the joint strength of a pristine specimen. In finite element (FE) modelling, the joint residual strength with the existence of disbond was predicted using the adhesive element failure criteria. Initially, the characteristic distance was determined when the predicted joint strength of pristine specimen using FE analysis was equivalent to that predicted using the Hart-Smith analytical formula. The characteristic distance was determined by calibration with the experimental test results.

The strain energy release rate (SERR) of the joint as a function of disbond length was determined using the virtual crack closure technique (VCCT) for 2D analysis and cohesive zone element (CZE) approach for 3D analysis. The CZE approach was also utilised to assess the disbond growth behaviour in 3D FE modelling.

Two coupon specimen designs that represent the DOTES were used, called the DOTES-ST (short tapered) and the DOTES-LT (long tapered). Analysis on the shear and peel stresses distribution of each coupon specimen design was conducted. The numerical results showed that by reducing the edge thickness to 0.15 mm, the shear and peel stresses were also reduced by 51% and 47%, respectively.

The material properties and modelling approach used for all numerical studies carried out in this thesis were defined in Chapter 3. Single element simulations subjected to various loading conditions were conducted to ensure the FM300-2K material properties were correctly implemented. A good correlation was observed with the manufacturer data sheet.

7.2.2 Implementation of Slow growth Approach to Bonded Joints or Patch Repairs Used in Primary Aircraft Structures

With the analyses conducted in Chapter 4, the framework to implement the slow growth approach, predict allowable fatigue life and determine inspection interval, in accordance with the guidance provided in FAA AC 20-107B [9], was established. The entire process of a disbond crack growth from disbond initiation up to the ultimate failure of a typical double lap metallic joint was investigated using the DOTES-ST specimen. The residual static strength of the joint as function of disbond crack length was established using the finite element method with adhesive element failure criteria and a progressive failure analysis. The results indicated that under the static load the crack growth in both cases (disbond initiates from the gap region or from tapered end) was unstable. Particularly with a static load that was able to initiate the disbond or propagate a short disbond crack, the joint would rapture rapidly. However, when a fatigue loading with the peak load below the residual strength curves was considered, there would be no instant static failure. A fatigue failure would occur when the disbond crack propagated to the length with which the residual strength was equivalent to the fatigue peak stress.

The SERRs analysis indicated that for a joint having sufficient static strength safety margin under a typical fatigue loading that would propagate disbond crack, disbond growth would be stable in a particular length range. These include disbond initiated from either “disbond tolerant zone” or “safe-life zone”. The SERR results under constant amplitude end-displacement loading showed significant drop in SERR as the disbond crack length increases in a reasonable disbond crack length range. This result suggested for a local or part width disbond, the load shedding effect (load sharing or redistribution to the adjacent region) would further slow the damage growth. This might have a significant implication for application of the slow growth approach to the case of a local disbond in the “safe life zone”.

The effect of rigidity imbalance between inner adherend and outer adherend was observed. The numerical results showed that varying the adherend thickness could affect the adhesive bond strength and disbond growth rate. This information would be useful in design of validation experiment.

7.2.3 Establishment of Relationship Between Disbond Growth Rates and Disbond Strain Energy Release Rates

The applicability of the slow growth management strategy for disbond in bonded joints or patch repairs of primary aircraft structures was evaluated computationally and experimentally in Chapter 5 using the DOTES coupon specimen.

Boeing Wedge Test (BWT) was used to verify the quality of the bonding process. Part of the specimens were pre-conditioned at 71℃ with 95% relative humidity for 33 days. Static testing of DOTES-ST specimen under room temperature and dry (RD) condition was first carried out as a preliminary test. As followed, static testing of the DOTES-LT specimen was conducted in RD and hot wet (HW) conditions. The element size used in the FE method was determined through calibration against the static strength of the DOTES-LT specimens measured in (RD) and (HW) conditions. The upper limit fatigue peak load was determined by considering a static strength safety margin and manufacture defect tolerance, to be 33.3 kN.

Constant amplitude fatigue (R = 0.1) tests were conducted using the DOTES-LT specimens with various initial disbond lengths. The entire disbond growth process up to joint failure was monitored. Part of the specimens were tested with an anti-bending fixture applied to simulate the joints on aircraft where the bending was constrained. The disbond growth in these specimens was essentially sympatric. In other specimens tested without attaching the anti-bending fixture in the tests, significant asymmetrical disbond growth was observed. The VCCT method was used to assess the SERRs as a function of the disbond crack length. A half model and full model were used to simulate the specimens having symmetric and asymmetric disbond propagations, respectively. A modified Paris law was established by correlating the measured disbond growth rates with the SERRs. The specimens with humidity pre-conditioning showed faster disbond growth rate and shorter fatigue life. For these specimens, the modified Paris law was formed using different set of parameters.

Using the modified Paris law, the disbond growth length as a function of the number of fatigue load cycles, and the fatigue life of each specimen were predicted by conducting numerical integration. The scatter factor was handled by using the statistics approach and considering a conservativeness level similar to that used for generation of B-basis design allowable. The predicted disbond growth was agreed well with the measured values. For specimens with symmetric disbond growth and failed in the form of cohesive failure of the adhesive, the predicted fatigue life was also agreed with the test results reasonably well.

The computational and fatigue test results indicated that for a joint having a sufficient static strength safety margin under a typical fatigue loading that would propagate disbond, the disbond growth would be stable in a particular length range. Thus, the slow growth approach would be feasible for a bonded joint/patch repairs if the doubler/patch was designed to be sufficiently long to allow extended damage propagation, whilst in the case when patch size must be limited, the design for safe-life for the patch termination region in critical repairs must be considered. Should disbond growth occur in this case, the joint must be repaired or replaced.

7.2.4 Investigation on The Effect of Initial Disbond Size to Disbond Growth Behaviour

The effect of initial disbond size to disbond growth behaviour was investigated computationally using 3D analysis of wide bonded metal joint specimen in Chapter 6. Two pre-disbond shapes were considered called full width and part width disbonds.

The residual static strength of the specimen as a function of disbond length was established using the adhesive element failure criteria. The upper limit fatigue peak load of the wide bonded metal joint specimen was determined by considering static strength of the joint and static safety margin together with material knock down factors to be 183 kN (same as that for DOTES specimen considered in Chapter 5 in terms of load per specimen width).

Using the developed subroutine for the CZE approach, the SERR of the DOTES specimen as a function of disbond crack length was calculated and compared with that determined using the VCCT approach. A good correlation between the two approaches were established. Thus, the SERR value as a function of disbond length of the wide bonded metal joint specimen with part and full width disbond was assessed using the CZE approach. Significant reduction of the SERR values was observed in the case of part width or local disbond.

The cohesive fatigue model written in Ucohesive subroutine was used to predict the disbond propagation of the DOTES. The predicted results agreed well with that predicted previously using the VCCT approach and established modified Paris law. The cohesive fatigue model was then used to predict disbond propagation in the wide bonded metal joint specimen. It was found that for a specimen with the full width disbond, the disbond at the side edge would grow faster than that in the middle. For a specimen with a part width disbond, the disbond growth would initiate from the side edge of the disbond region instead of its front, resulting in the disbond growth in adjacent region to "catch up" and form a full width disbond. This load redistribution effect resulted in an overall significantly slower disbond growth and thus longer fatigue life of the joint with part width disbond than that with a full width disbond.

7.3 Future Work

This section outlines some key areas for the implementation of slow damage growth for management of bonded repairs where further research is still needed.

7.3.1 Fatigue Load Range

The number of fatigue tests based on coupon specimen level conducted in this study was limited. More tests are needed to fully define the slow growth allowable range, a significant task to be considered in future. Also, the effect of stress ratio on fatigue crack growth rate is important. As discussed in Chapter 5, only one stress ratio was considered

(R = 0.1) in this study. To fully understand the effect of stress ratio on fatigue crack growth rate, the work could be further expanded by considering cyclic load with various stress ratios. In addition, typical loading spectrum such as fighter aircraft lower wing skins (FALSTAFF) and transport aircraft lower wing skins (TWIST) should be considered to represent the actual stresses and strains experienced by the components during the service. For composite materials, environmental conditions including temperature and moisture effect were important. Hence, the environmental FALSTAFF (ENDSTAFF) loading spectrum was typically used to represent the stresses and environmental conditions encountered by composite structures in a modern fighter aircraft.

7.3.2 Manufacturing and Testing of Wide Bonded Metal Joint Specimen

A wide panel with equal width of patch and panel is required for the influence of part-width disbonds in a wide specimen. Chapter 6 provides a numerical model to address this issue; however, unfortunately, the manufacturing and testing of a wide panel specimen were not addressed in this thesis due to the time constraint. Further work should be performed including manufacturing and testing of wide bonded metal joint specimen for the purpose of calibration/validation of the numerical model. Thus, the effect of initial disbond size on disbond growth behaviour could be further expanded for implementation and assessment.

7.3.3 Non-Destructive Inspection (NDI) Method

It was shown in Chapter 5 that a microscope camera was capable for monitoring the disbond propagation in the DOTES coupon specimen. However, a more robust NDI method was required to capture the disbond crack front shape and its behaviour for the experimental test of wide bonded metal joint specimen. Promising NDI methods such as thermoelastic stress analysis (TSA) or C-scan could be more effective for imaging the disbond crack front shape and the disbond propagation behaviour with aluminium (outer adherend) thickness of 3.18 mm.

7.3.4 Large Panel with Patch Repair

Ideally, the implementation of damage slow growth approach should be expanded to a cracked large panel bonded with aluminium patch repair as presented in Figure 7.1. A numerical study investigating the driving force parameters of disbond growth, and crack growth in the parent structure as the disbond length increases should be carried out.

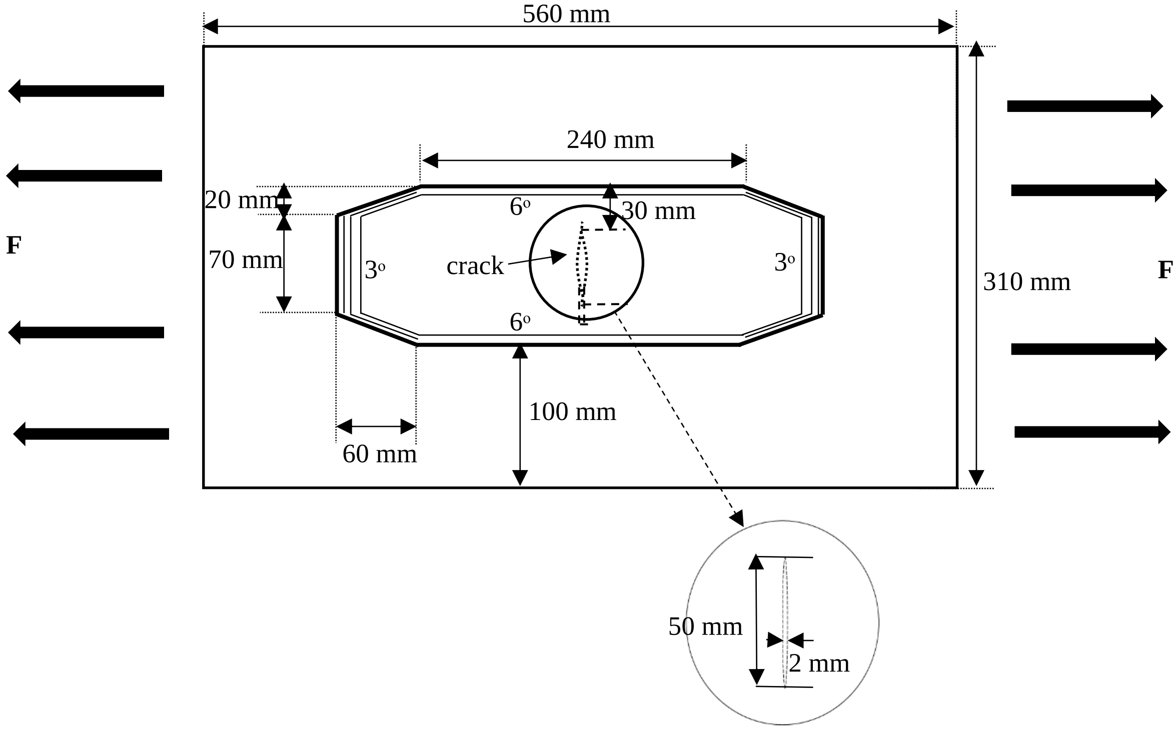

Figure 7.1: Large panel bonded with aluminium patch repair.

7.3.5 Adherend Material Consideration

The work conducted in this study was focused on aluminium patch material to simplify the interpretation compared with composite patch material, and thus, composite patches will be considered for the future research.

References

[1] R. L. Crane and G. Dillingham, "Composite bond inspection," *Journal of materials science,* vol. 43, no. 20, pp. 6682-6694, 2008.

[2] L. Hart-Smith, "Adhesive bonding of composite structures—progress to date and some remaining challenges," *Journal of Composites, Technology and Research,* vol. 24, no. 3, pp. 133-151, 2002.

[3] A. Vlot, S. Verhoeven, and P. Nijssen, *Bonded repairs for aircraft fuselages*. Delft University Press, 1998.

[4] K. Burke, "Qantas grounds third Boeing 737 over hairline cracking," in *Sunrise*, ed, 2019.

[5] D. Roach, "Development program to certify composite doubler repair technique for commercial aircraft," Sandia National Labs., Albuquerque, NM (United States)1997.

[6] D. Roach, "Damage tolerance assessment of bonded composite doubler repairs for commercial aircraft applications," 1998.

[7] K. Tserpes *et al.*, "A review on failure theories and simulation models for adhesive joints," *The Journal of Adhesion,* pp. 1-62, 2021.

[8] F. A. Administration, "Composite Aircraft Structure," *U.S. Department of Transportation,* vol. AC20-107A, 1984.

[9] F. A. Administration, "Composite Aircraft Structure," *U.S. Department of Transportation,* vol. AC20-107B, Change 1, 24 August 2010.

[10] A. Baker, A. J. Gunnion, and J. Wang, "On the certification of bonded repairs to primary composite aircraft components," *The Journal of Adhesion,* vol. 91, no. 1-2, pp. 4-38, 2015.

[11] P. Chalkley, C. Wang, and A. Baker, "Fatigue testing of generic bonded joints," in *Advances in the bonded composite repair of metallic aircraft structure*: Elsevier, 2002, pp. 103-126.

[12] P. Chalkley and A. Baker, "Development of a generic repair joint for certification of bonded composite repairs," *International journal of adhesion and adhesives*, vol. 19, no. 2-3, pp. 121-132, 1999.

[13] A. Baker, "Crack patching: experimental studies, practical applications," in *Bonded repair of aircraft structures*: Springer, 1988, pp. 107-173.

[14] A. Baker, "Repair of metallic airframe components using fibre-reinforced polymer (FRP) composites," in *Rehabilitation of Metallic Civil Infrastructure Using Fiber Reinforced Polymer (FRP) Composites*: Elsevier, 2014, pp. 11-59.

[15] P. Madelpech, S. Juaneda, and M. Pradels, "Bonded Composite Patch to Repair Metallic Structures: Disbond Propagation Testing and Modelling," in *ICAF 2009, Bridging the Gap between Theory and Operational Practice*: Springer, 2009, pp. 1019-1033.

[16] J. Wang, A. Rider, M. Heller, and R. Kaye, "Theoretical and experimental research into optimal edge taper of bonded repair patches subject to fatigue loadings," *International journal of adhesion and adhesives,* vol. 25, no. 5, pp. 410-426, 2005.

[17] P. Cheuk, L. Tong, A. Rider, and J. Wang, "Analysis of energy release rate for fatigue cracked metal-to-metal double-lap shear joints," *International Journal of Adhesion and Adhesives*, vol. 25, no. 2, pp. 181-191, 2005.

[18] J. Pascoe, C. Rans, R. Alderliesten, and R. Benedictus, "Fatigue disbonding of bonded repairs-an application of the strain energy approach," in *27th ICAF symposium, Jerusalem*, 2013, pp. 5-7.

[19] L. J. Hart-Smith, "Adhesive-Bonded Double Lap Joints," *NASA Langley Research Center Report NASA CR-112235,* 1973. https://ntrs.nasa.gov/archive/nasa/casi.ntrs.nasa.gov/19740005082.pdf.

[20] P. Cheuk, L. Tong, C. Wang, A. Baker, and P. Chalkley, "Fatigue crack growth in adhesively bonded composite-metal double-lap joints," *Composite Structures,* vol. 57, no. 1-4, pp. 109-115, 2002.

[21] M. J. Lee, T. M. Cho, W. S. Kim, B. C. Lee, and J. J. Lee, "Determination of cohesive parameters for a mixed-mode cohesive zone model," *International Journal of Adhesion and Adhesives,* vol. 30, no. 5, pp. 322-328, 2010.

[22] A. Baker, "Bonded composite repair of fatigue-cracked primary aircraft structure," *Composite Structures,* vol. 47, no. 1-4, pp. 431-443, 1999.

[23] C. Soutis, D. Duan, and P. Goutas, "Compressive behaviour of CFRP laminates repaired with adhesively bonded external patches," *Composite structures,* vol. 45, no. 4, pp. 289-301, 1999.

[24] R. D. Campilho, M. De Moura, and J. Domingues, "Modelling single and double-lap repairs on composite materials," *Composites Science and Technology,* vol. 65, no. 13, pp. 1948-1958, 2005.

[25] C. H. Wang and A. J. Gunnion, "Optimum shapes of scarf repairs," *Composites Part A: Applied Science and Manufacturing,* vol. 40, no. 9, pp. 1407-1418, 2009.

[26] M. Charalambides, R. Hardouin, A. Kinloch, and F. Matthews, "Adhesively-bonded repairs to fibre-composite materials I. Experimental," *Composites Part A: Applied Science and Manufacturing,* vol. 29, no. 11, pp. 1371-1381, 1998.

[27] A. J. Gunnion and I. Herszberg, "Parametric study of scarf joints in composite structures," *Composite structures,* vol. 75, no. 1-4, pp. 364-376, 2006.

[28] B. Whittingham, A. Baker, A. Harman, and D. Bitton, "Micrographic studies on adhesively bonded scarf repairs to thick composite aircraft structure," *Composites Part A: Applied Science and Manufacturing,* vol. 40, no. 9, pp. 1419-1432, 2009.

[29] K. B. Armstrong, L. G. Bevan, and W. F. Cole, *Care and repair of advanced composites*. SAE international Warrendale, PA, 2005.

[30] A. A. Baker, L. F. Rose, and R. Jones, *Advances in the bonded composite repair of metallic aircraft structure*. Elsevier, 2003.

[31] N. Chowdhury, J. Wang, W. Chiu, and P. Chang, "Experimental and Finite Element Studies of Thick Bolted, Bonded and Hybrid Carbon Fibre Step Lap Joints used in Aircraft Structures," *Journal of Composites Part B. v100,* pp. 68-77, 2016.

[32] N. M. Chowdhury, J. Wang, W. K. Chiu, and P. Chang, "Static and fatigue testing bolted, bonded and hybrid step lap joints of thick carbon fibre/epoxy laminates used on aircraft structures," *Composite Structures,* vol. 142, pp. 96-106, 2016.

[33] N. M. Chowdhury, J. Wang, W. K. Chiu, and P. Chang, "Experimental and finite element studies of thin bonded and hybrid carbon fibre double lap joints used in aircraft structures," *Composites Part B: Engineering,* vol. 85, pp. 233-242, 2016.

[34] A. A. B. Baker, *Composite materials for aircraft structures*. AIAA, 2004.

[35] S. Jeanne, "Bonded Patch repair for Composite Structure," (in English), Thesis 2010.

[36] A. A. Baker, "A proposed approach for certification of bonded composite repairs to flight-critical airframe structure," *Applied Composite Materials*, vol. 18, no. 4, pp. 337-369, 2011.

[37] N. Chowdhury, W. K. Chiu, J. Wang, and P. Chang, "Static and fatigue testing thin riveted, bonded and hybrid carbon fiber double lap joints used in aircraft structures," *Composite Structures*, vol. 121, pp. 315-323, 2015.

[38] A. A. Baker and J. Wang, A. A. B. Rhys Jones, Neil Matthews and V K Champagne, Ed. *Adhesively Bonded Repair/Reinforcement of Metallic Airframe Components: Materials, Processes, Design and Proposed Through-Life Management* (Aircraft Sustainment and Repair). Elsevier Publisher, 2017, p. 191.

[39] K. Zimmerman, "Mechanical fastening of composite materials," *Experimental Techniques*, vol. 16, no. 4, pp. 36-40, 1992.

[40] D.-C. Seo and J.-J. Lee, "Fatigue crack growth behavior of cracked aluminum plate repaired with composite patch," *Composite Structures*, vol. 57, no. 1-4, pp. 323-330, 2002.

[41] J.-H. Kweon, J.-W. Jung, T.-H. Kim, J.-H. Choi, and D.-H. Kim, "Failure of carbon composite-to-aluminum joints with combined mechanical fastening and adhesive bonding," *Composite structures*, vol. 75, no. 1-4, pp. 192-198, 2006.

[42] T. Ireman, T. Ranvik, and I. Eriksson, "On damage development in mechanically fastened composite laminates," *Composite Structures*, vol. 49, no. 2, pp. 151-171, 2000.

[43] A. A. Baker and J. Wang, "Adhesively Bonded Repair/Reinforcement of Metallic Airframe Components: Materials, Processes, Design and Proposed Through-Life Management," in *Aircraft Sustainment and Repair*, A. A. B. Editors: R. Jones, N. Matthews and V. K. Champagne, Ed.: Elsevier, 2018, pp. 191-252.

[44] A. B. Harman and C. H. Wang, "Improved design methods for scarf repairs to highly strained composite aircraft structure," *Composite structures,* vol. 75, no. 1-4, pp. 132-144, 2006.

[45] H. C. Li, T. Mitrevski, and I. Herszberg, "Impact on bonded repairs to CFRP laminates under load," in *Proc. 25th Congress of the International Council of the Aeronautical Sciences, Hamburg, Germany*, 2006, pp. 3-8.

[46] F. Matthews, P. Kilty, and E. Godwin, "A review of the strength of joints in fibre-reinforced plastics. Part 2. Adhesively bonded joints," *Composites,* vol. 13, no. 1, pp. 29-37, 1982.

[47] B. MEGANATHAN and E. E. RAJ, "Analysing The Composite Structure Of Riverted, Hybrid And Bonded Joints," *International Journal of Engineering Research and Applications,* vol. 5, no. 3, pp. 53-61, 2015.

[48] H. S. Kim and S. J. Lee, "Development of a strength model for the cocured stepped lap joints under tensile loading," *Composite Structures,* vol. 32, no. 1-4, pp. 593-600, 1995.

[49] C. C. Chamis and P. Murthy, "Simplified procedures for designing adhesively bonded composite joints," *Journal of Reinforced Plastics and Composites,* vol. 10, no. 1, pp. 29-41, 1991.

[50] M. Banea and L. F. da Silva, "Adhesively bonded joints in composite materials: an overview," *Proceedings of the Institution of Mechanical Engineers, Part L: Journal of Materials: Design and Applications,* vol. 223, no. 1, pp. 1-18, 2009.

[51] A. Riccio, G. Di Felice, F. Scaramuzzino, and A. Sellitto, "A practical tool for the preliminary design of bonded composite repairs," *Applied Composite Materials*, vol. 21, no. 3, pp. 495-509, 2014.

[52] A. Riccio, R. Ricchiuto, F. Di Caprio, A. Sellitto, and A. Raimondo, "Numerical investigation of constitutive material models on bonded joints in scarf repaired composite laminates," *Engineering Fracture Mechanics,* vol. 173, pp. 91-106, 2017.

[53] A. C. Okafor, N. Singh, U. Enemuoh, and S. Rao, "Design, analysis and performance of adhesively bonded composite patch repair of cracked aluminum aircraft panels," *Composite structures,* vol. 71, no. 2, pp. 258-270, 2005.

[54] G. Kelly, "Quasi-static strength and fatigue life of hybrid (bonded/bolted) composite single-lap joints," *Composite structures,* vol. 72, no. 1, pp. 119-129, 2006.

[55] J. Wang, A. Baker, and P. Chang, "Hybrid Repair Methods for Aircraft Primary Structure Repairs."

[56] L. Hart-Smith, "Bolted and bonded joints," *Materials Park, OH: ASM International, 2001.*, pp. 271-289, 2001.

[57] C. Sun, K. Bhawesh, P. Wang, and R. Sterkenburg, "Development of improved hybrid joints for composite structures," *Composite Structures,* vol. 35, pp. 1-20, 2005.

[58] L. J. HART-SMITH, "Bonded-bolted composite joints," *Journal of Aircraft,* vol. 22, no. 11, pp. 993-1000, 1985.

[59] G. Kelly, "Load transfer in hybrid (bonded/bolted) composite single-lap joints," *Composite structures,* vol. 69, no. 1, pp. 35-43, 2005.

[60] A. Barut and E. Madenci, "Analysis of bolted–bonded composite single-lap joints under combined in-plane and transverse loading," *Composite Structures,* vol. 88, no. 4, pp. 579-594, 2009.

[61] E. Paroissien, M. Sartor, J. Huet, and F. Lachaud, "Analytical two-dimensional model of a hybrid (bolted/bonded) single-lap joint," *Journal of aircraft,* vol. 44, no. 2, pp. 573-582, 2007.

[62] R. Matsuzaki, M. Shibata, and A. Todoroki, "Improving performance of GFRP/aluminum single lap joints using bolted/co-cured hybrid method," *Composites Part A: applied science and manufacturing,* vol. 39, no. 2, pp. 154-163, 2008.

[63] A. Baker, R. Jones, and R. Callinan, "Damage tolerance of graphite/epoxy composites," *Composite Structures,* vol. 4, no. 1, pp. 15-44, 1985.

[64] R. Alderliesten, "Damage tolerance of bonded aircraft structures," *International Journal of Fatigue,* vol. 31, no. 6, pp. 1024-1030, 2009.

[65] M. Dvorak, M. Ruzicka, V. Kulisek, J. Behal, and V. Kafka, "Damage detection of the adhesive layer of skin doubler specimens using SHM system based on fibre Bragg gratings," in *Proceedings of the Fifth European Workshop on Structural Health Monitoring*, 2010, pp. 70-75.

[66] F. Matta, V. M. Karbhari, and R. Vitaliani, "Tensile response of steel/CFRP adhesive bonds for the rehabilitation of civil structures," *Structural Engineering and Mechanics*, vol. 20, no. 5, p. 589, 2005.

[67] A. Baker, N. Rajic, and C. Davis, "Towards a practical structural health monitoring technology for patched cracks in aircraft structure," *Composites Part A: Applied Science and Manufacturing,* vol. 40, no. 9, pp. 1340-1352, 2009.

[68] H. Choi, S. Choi, and H. Cha, "Structural health monitoring system based on strain gauge enabled wireless sensor nodes," in *Networked Sensing Systems, 2008. INSS 2008. 5th International Conference on*, 2008, pp. 211-214: IEEE.

[69] V. Sabelkin, S. Mall, and J. Avram, "Fatigue crack growth analysis of stiffened cracked panel repaired with bonded composite patch," *Engineering Fracture Mechanics,* vol. 73, no. 11, pp. 1553-1567, 2006.

[70] D. Ouinas, B. B. Bouiadjra, S. Himouri, and N. Benderdouche, "Progressive edge cracked aluminium plate repaired with adhesively bonded composite patch under full width disbond," *Composites Part B: Engineering,* vol. 43, no. 2, pp. 805-811, 2012.

[71] A. Megueni, B. B. Bouiadjra, and M. Belhouari, "Disbond effect on the stress intensity factor for repairing cracks with bonded composite patch," *Computational materials science,* vol. 29, no. 4, pp. 407-413, 2004.

[72] L.-D. A. W. Group, "Modeling Guidelines Document Version 13-1," ed, 2013.

[73] L. F. M. Da Silva and A. Öchsner, *Modeling of adhesively bonded joints*. Springer, 2008.

[74] L. F. Da Silva and R. D. Campilho, "Advances in numerical modelling of adhesive joints," in *Advances in numerical modeling of adhesive joints*: Springer, 2012, pp. 1-93.

[75] G. Richardson, A. Crocombe, and P. Smith, "A comparison of two-and three-dimensional finite element analyses of adhesive joints," *International journal of adhesion and adhesives*, vol. 13, no. 3, pp. 193-200, 1993.

[76] J. García, A. Chiminelli, B. García, M. Lizaranzu, and M. Jiménez, "Characterization and material model definition of toughened adhesives for finite element analysis," *International Journal of Adhesion and Adhesives*, vol. 31, no. 4, pp. 182-192, 2011.

[77] D. Castagnetti and E. Dragoni, "Standard finite element techniques for efficient stress analysis of adhesive joints," *International Journal of Adhesion and Adhesives*, vol. 29, no. 2, pp. 125-135, 2009.

[78] I. Doghri, A. Muller, and R. L. Taylor, "A general three-dimensional contact procedure for implicit finite element codes," *Engineering Computations*, vol. 15, no. 2, pp. 233-259, 1998.

[79] L. Greve and F. Andrieux, "Deformation and failure modelling of high strength adhesives for crash simulation," *International Journal of Fracture*, vol. 143, no. 2, pp. 143-160, 2007.

[80] J. Van Hoof, "Modelling of impact induced delamination in composite materials," *Ottawa: Carleton University*, 1999.

[81] L. F. Trimiño and D. S. Cronin, "Evaluation of Numerical Methods to Model Structural Adhesive Response and Failure in Tension and Shear Loading," *Journal of Dynamic Behavior of Materials*, vol. 2, no. 1, pp. 122-137, 2016.

[82] M. Avalle, L. Peroni, M. Peroni, and A. Scattina, "Bi-material joining for car body structures: experimental and numerical analysis," *The Journal of Adhesion,* vol. 86, no. 5-6, pp. 539-560, 2010.

[83] L. Trimiño, "Analysis and performance of adhesively bonded crush tube structures," *University of Waterloo, Waterloo,* 2012.

[84] J. Pan and S.-H. Lin, "Fracture mechanics and fatigue crack propagation," *Fatigue Testing and Analysis,* p. 237, 2005.

[85] C. Wang and C. Duong, "Damage tolerance and fatigue durability of scarf joints," *Bonded Joints and Repairs to Composite Airframe Structures; Elsevier: Amsterdam, The Netherlands,* pp. 141-172, 2016.

[86] J. Huang, P. Fu, R. Settgast, J. Morris, and F. Ryerson, "Applicability of Virtual Crack Closure Technique for Simulating Hydraulic Fractures Breaking Through Stress and Stiffness Barriers," in *52nd US Rock Mechanics/Geomechanics Symposium*, 2018: OnePetro.

[87] E. F. Rybicki and M. F. Kanninen, "A finite element calculation of stress intensity factors by a modified crack closure integral," *Engineering fracture mechanics,* vol. 9, no. 4, pp. 931-938, 1977.

[88] I. Raju, "Calculation of strain-energy release rates with higher order and singular finite elements," *Engineering Fracture Mechanics,* vol. 28, no. 3, pp. 251-274, 1987.

[89] J. Jokinen, M. Wallin, and O. Saarela, "Applicability of VCCT in mode I loading of yielding adhesively bonded joints—a case study," *International Journal of Adhesion and Adhesives,* vol. 62, pp. 85-91, 2015.

[90] K. Senthil, A. Arockiarajan, and R. Palaninathan, "Numerical study on the onset of initiation of debond growth in adhesively bonded composite joints," *International Journal of Adhesion and Adhesives,* vol. 84, pp. 202-219, 2018.

[91] M. Quaresimin and M. Ricotta, "Life prediction of bonded joints in composite materials," *International Journal of Fatigue,* vol. 28, no. 10, pp. 1166-1176, 2006.

[92] P. Feraren and H. M. Jensen, "Cohesive zone modelling of interface fracture near flaws in adhesive joints," *Engineering Fracture Mechanics,* vol. 71, no. 15, pp. 2125-2142, 2004.

[93] R. D. Campilho, M. D. Banea, J. Neto, and L. F. da Silva, "Modelling adhesive joints with cohesive zone models: effect of the cohesive law shape of the adhesive layer," *International journal of adhesion and adhesives,* vol. 44, pp. 48-56, 2013.

[94] R. Campilho, M. d. Moura, D. A. Ramantani, J. Morais, A. Barreto, and J. Domingues, "Adhesively bonded repair proposal for wood members damaged by horizontal shear using carbon-epoxy patches," *The Journal of Adhesion,* vol. 86, no. 5-6, pp. 649-670, 2010.

[95] R. D. S. G. Campilho, M. De Moura, A. Pinto, J. Morais, and J. Domingues, "Modelling the tensile fracture behaviour of CFRP scarf repairs," *Composites Part B: Engineering,* vol. 40, no. 2, pp. 149-157, 2009.

[96] A. Needleman, "An analysis of tensile decohesion along an interface," *Journal of the Mechanics and Physics of Solids,* vol. 38, no. 3, pp. 289-324, 1990.

[97] Q. Yang, M. Thouless, and S. Ward, "Numerical simulations of adhesively-bonded beams failing with extensive plastic deformation," *Journal of the Mechanics and Physics of Solids,* vol. 47, no. 6, pp. 1337-1353, 1999.

[98] Y. Mi, M. Crisfield, G. Davies, and H. Hellweg, "Progressive delamination using interface elements," *Journal of composite materials,* vol. 32, no. 14, pp. 1246-1272, 1998.

[99] N. Choupani, "Mixed-mode cohesive fracture of adhesive joints: Experimental and numerical studies," *Engineering fracture mechanics,* vol. 75, no. 15, pp. 4363-4382, 2008.

[100] L. M. Fernández-Cañadas, I. Iváñez, and S. Sanchez-Saez, "Influence of the cohesive law shape on the composite adhesively-bonded patch repair behaviour," *Composites Part B: Engineering,* vol. 91, pp. 414-421, 2016.

[101] M. Ridha, V. Tan, and T. Tay, "Traction–separation laws for progressive failure of bonded scarf repair of composite panel," *Composite structures,* vol. 93, no. 4, pp. 1239-1245, 2011.

[102] S. Bayramoglu, S. Akpinar, and A. Çalık, "Numerical analysis of elasto-plastic adhesively single step lap joints with cohesive zone models and its experimental verification," *Journal of Mechanical Science and Technology,* vol. 35, no. 2, pp. 641-649, 2021.

[103] A. Pirondi and F. Moroni, "Improvement of a cohesive zone model for fatigue delamination rate simulation," *Materials,* vol. 12, no. 1, p. 181, 2019.

[104] B. Bak, A. Turon, E. Lindgaard, and E. Lund, "A benchmark study of simulation methods for high-cycle fatigue-driven delamination based on cohesive zone models," *Composite structures,* vol. 164, pp. 198-206, 2017.

[105] A. Turon, J. Costa, P. Camanho, and C. Dávila, "Simulation of delamination in composites under high-cycle fatigue," *Composites Part A: applied science and manufacturing,* vol. 38, no. 11, pp. 2270-2282, 2007.

[106] F. Moroni and A. Pirondi, "A procedure for the simulation of fatigue crack growth in adhesively bonded joints based on a cohesive zone model and various mixed-mode propagation criteria," *Engineering Fracture Mechanics,* vol. 89, pp. 129-138, 2012.

[107] F. Moroni, A. Pirondi, and G. Giuliese, "Simulation of fatigue debonding in adhesively bonded three-dimensional joint geometries using a cohesive zone model approach," *Gruppo Italiano Frattura. Convegno Nazionale IGF. Acta Fracturae,* vol. 22, p. 73, 2013.

[108] C. Dávila, "From SN to the Paris law with a new mixed-mode cohesive fatigue model for delamination in composites," *Theoretical and Applied Fracture Mechanics,* vol. 106, p. 102499, 2020.

[109] A. Needleman, "Some issues in cohesive surface modeling," *Procedia IUTAM,* vol. 10, pp. 221-246, 2014.

[110] G. Dean and L. Crocker, "The use of finite element methods for design with adhesives," *NPL Report ISSN,* vol. 1368, p. 6550, 2001.

[111] L. P. Djukic, "Effects of Thermal Residual Stresses on Static Strength and Fatigue Life of Welded Carbon-Fibre/Epoxy Composite Joints " Doctor of Philosophy, University of New South Wales, 2010.

[112] A. T. Sheppard, "The Failure Analysis of Adhesively Bonded Joints," Doctor of Philosophy, University of New South Wales, Australia, 1996.

[113] R. Raghava, R. M. Caddell, and G. S. Yeh, "The macroscopic yield behaviour of polymers," *Journal of Materials Science,* vol. 8, no. 2, pp. 225-232, 1973.

[114] A. Crocombe and A. Moult, "The effect of the adhesive thickness on the strength of a bonded joint," in *Adhesion 12*: Springer, 1988, pp. 174-192.

[115] A. Crocombe, G. Richardson, and P. Smith, "Measuring hydro-static dependent constitutive behaviour of adhesives using a bend specimen," *The Journal of Adhesion*, vol. 42, no. 3, pp. 209-223, 1993.

[116] R. Adams, J. Coppendale, and N. Peppiatt, "Failure analysis of aluminium-aluminium bonded joints," *Adhesion*, vol. 2, pp. 105-120, 1978.

[117] L. Hollaway, A. Romhi, and M. Gunn, "Optimisation of adhesive bonded composite tubular sections," *Composite Structures*, vol. 16, no. 1-3, pp. 125-170, 1990.

[118] R. Adams, R. Atkins, J. Harris, and A. Kinloch, "Stress analysis and failure properties of carbon-fibre-reinforced-plastic/steel double-lap joints," *The Journal of Adhesion*, vol. 20, no. 1, pp. 29-53, 1986.

[119] S. Gali, G. Dolev, and O. Ishai, "An effective stress/strain concept in the mechanical characterization of structural adhesive bonding," *International Journal of Adhesion and Adhesives*, vol. 1, no. 3, pp. 135-140, 1981.

[120] C.-C. Lee, "Determination of the Mechanical Properties of Adhesive for Design of Bonded Joints," Doctor of Philosophy, University of New South Wales, Australia, 1997.

[121] A. Bertarelli, "Beam-induced damage mechanisms and their calculation," *arXiv preprint arXiv:1608.03056*, 2016.

[122] G. R. Irwin, "Analysis of stresses and strains near the end of a crack traversing a plate," 1997.

[123] D. E. Martin, "Crack propagation under repeated loading," University of Illinois at Urbana-Champaign, 1956.

[124] H. Liu, "Crack propagation in thin metal sheet under repeated loading, Wright Air Development Center WADC TN 59-383, 1959. Also published as Liu HW. Crack propagation in thin metal sheet under repeated loading," Ph. D. Thesis, University of Illinois, 1959.

[125] M. P. G. P. C. Paris, and W. E. Anderson, "A rational analytic theory of fatigue," *Internal Report, Boeing Airplane Co.*, vol. 13, p. 9, 1959.

[126] P. Paris and F. Erdogan, "A critical analysis of crack propagation laws," 1963.

[127] A. Hartman and J. Schijve, "The effects of environment and load frequency on the crack propagation law for macro fatigue crack growth in aluminium alloys," *Engineering Fracture Mechanics,* vol. 1, no. 4, pp. 615-631, 1970.

[128] T. Lindley, I. Palmer, and C. Richards, "Acoustic emission monitoring of fatigue crack growth," *Materials Science and Engineering,* vol. 32, no. 1, pp. 1-15, 1978.

[129] S. Wang, J. Mandell, and F. McGarry, "An analysis of the crack tip stress field in DCB adhesive fracture specimens," *International Journal of Fracture,* vol. 14, no. 1, pp. 39-58, 1978.

[130] G. C. Sih, P. Paris, and G. Irwin, "On cracks in rectilinearly anisotropic bodies," *International Journal of Fracture Mechanics,* vol. 1, no. 3, pp. 189-203, 1965.

[131] R. Jones, S. Pitt, A. Bunner, and D. Hui, "Application of the Hartman–Schijve equation to represent Mode I and Mode II fatigue delamination growth in composites," *Composite Structures,* vol. 94, no. 4, pp. 1343-1351, 2012.

[132] S. Mall and W. S. Johnson, "Characterization of mode I and mixed-mode failure of adhesive bonds between composite adherends," in *Composite materials: testing and design (seventh conference)*, 1986: ASTM International.

[133] S. Mall, G. Ramamurthy, and M. Rezaizdeh, "Stress ratio effect on cyclic debonding in adhesively bonded composite joints," *Composite structures,* vol. 8, no. 1, pp. 31-45, 1987.

[134] C.-G. Gustafson and M. Hojo, "Delamination fatigue crack growth in unidirectional graphite/epoxy laminates," *Journal of Reinforced Plastics and Composites,* vol. 6, no. 1, pp. 36-52, 1987.

[135] M. Quaresimin and M. Ricotta, "Stress intensity factors and strain energy release rates in single lap bonded joints in composite materials," *Composites Science and Technology,* vol. 66, no. 5, pp. 647-656, 2006.

[136] T. Brussat and S. Chiu, "Fatigue crack growth of bondline cracks in structural bonded joints," 1978.

[137] C. Rans, R. Alderliesten, and R. Benedictus, "Misinterpreting the results: How similitude can improve our understanding of fatigue delamination growth," *Composites Science and Technology,* vol. 71, no. 2, pp. 230-238, 2011.

[138] M. L. Benzeggagh and M. Kenane, "Measurement of mixed-mode delamination fracture toughness of unidirectional glass/epoxy composites with mixed-mode bending apparatus," *Composites science and technology,* vol. 56, no. 4, pp. 439-449, 1996.

[139] A. Curley, H. Hadavinia, A. Kinloch, and A. Taylor, "Predicting the service-life of adhesively-bonded joints," *International journal of fracture,* vol. 103, no. 1, pp. 41-69, 2000.

[140] V. Tanulia, J. Wang, G. M. Pearce, A. Baker, M. David, and B. G. Prusty, "A Procedure to Assess Disbond Growth and Determine Fatigue Life of Bonded

Joints and Patch Repairs for Primary Airframe Structures," *International Journal of Fatigue*, p. 105664, 2020.

[141] R. Jones, D. Peng, J. G. Michopoulos, and A. J. Kinloch, "Requirements and Variability Affecting the Durability of Bonded Joints," *Materials*, vol. 13, no. 6, p. 1468, 2020.

[142] M. E. Hoffman and P. C. Hoffman, "Corrosion and fatigue research," 2001.

[143] C. G. Schmidt, J. E. Crocker, J. H. Giovanola, C. H. Kanazawa, D. A. Shockey, and T. H. Flournoy, "Corrosion-fatigue crack nucleation in Alclad 2024-T3 commercial aircraft skin," in *Effects of the Environment on the Initiation of Crack Growth*: ASTM International, 1997.

[144] D. Groner and D. Groner, "US Air Force aging aircraft corrosion," in *38th Structures, Structural Dynamics, and Materials Conference*, 1997, p. 1364.

[145] X. Wu, J. Newman, W. Zhao, M. Swain, C. Ding, and E. PHILLIP, "HIGH-STRENGTH ALUMINIUM ALLOYS: PARTI–EXPERIMENTAL," *Fatigue & fracture of engineering materials & structures*, vol. 21, pp. 1289-1306, 1998.

[146] D. Duquesnay, P. Underhill, and H. Britt, "Fatigue failure of adhesively patched 2024-T3 and 7075-T6 clad and bare aluminium alloys," *Fatigue & Fracture of Engineering Materials & Structures*, vol. 28, no. 4, pp. 381-389, 2005.

[147] A. ASTM, "D3762-03 (2010) Standard Test Method for Adhesive Bonded Surface Durability of Aluminium (Wedge Test)," *Adhesives, American Society for Testing and Materials*, 2010.

[148] R. D. Adams, R. D. Adams, J. Comyn, W. C. Wake, and W. Wake, *Structural adhesive joints in engineering*. Springer Science & Business Media, 1997.

[149] M. Davis and D. Bond, "Principles and practices of adhesive bonded structural joints and repairs," *International journal of adhesion and adhesives,* vol. 19, no. 2-3, pp. 91-105, 1999.

[150] J. Cognard, "Use of the wedge test to estimate the lifetime of an adhesive joint in an aggressive environment," *International Journal of Adhesion and Adhesives,* vol. 6, no. 4, pp. 215-220, 1986.

[151] J. Sargent, "Durability studies for aerospace applications using peel and wedge tests," *International Journal of Adhesion and Adhesives,* vol. 25, no. 3, pp. 247-256, 2005.

[152] A. I. H. Committee, *ASM Handbook: Properties and selection*. Asm International, 1990.

[153] J. Aakkula and O. Saarela, "CRACK GROWTH IN ALUMINIUM PLATES REPAI-RED WITH COMPOSITE REINFORCEMENTS," in *Proceedings of the 18th Symposium of the International Committee on Aeronautical Fatigue,* 1995, pp. 3-5.

[154] *FM300-2 modified epoxy resin film,* 2011.

[155] R. A. A. Force, "Composite materials and adhesive bonded repairs, engineering and design procedures " vol. (AAP 7021.016-1).

[156] J. M. Whitney and R. Nuismer, "Stress fracture criteria for laminated composites containing stress concentrations," *Journal of composite materials,* vol. 8, no. 3, pp. 253-265, 1974.

[157] A. Sheppard, D. Kelly, and L. Tong, "A damage zone model for the failure analysis of adhesively bonded joints," *International journal of adhesion and adhesives,* vol. 18, no. 6, pp. 385-400, 1998.

[158] R. Krueger, "Virtual crack closure technique: history, approach, and applications," *Applied Mechanics Reviews*, vol. 57, no. 2, pp. 109-143, 2004.

[159] D. Xie and S. B. Biggers Jr, "Progressive crack growth analysis using interface element based on the virtual crack closure technique," *Finite Elements in Analysis and Design*, vol. 42, no. 11, pp. 977-984, 2006.

[160] M. Marc and A. Volume, "Theory and user information," *MSC Corp*, vol. 8, 2018.

[161] A. Pirondi and F. Moroni, "A progressive damage model for the prediction of fatigue crack growth in bonded joints," *The Journal of Adhesion*, vol. 86, no. 5-6, pp. 501-521, 2010.

[162] M. De Moura, R. Campilho, and J. Gonçalves, "Mixed-mode cohesive damage model applied to the simulation of the mechanical behaviour of laminated composite adhesive joints," *Journal of Adhesion Science and Technology*, vol. 23, no. 10-11, pp. 1477-1491, 2009.

[163] M. Elices, G. Guinea, J. Gomez, and J. Planas, "The cohesive zone model: advantages, limitations and challenges," *Engineering fracture mechanics*, vol. 69, no. 2, pp. 137-163, 2002.

[164] P. W. Harper and S. R. Hallett, "Cohesive zone length in numerical simulations of composite delamination," *Engineering Fracture Mechanics*, vol. 75, no. 16, pp. 4774-4792, 2008.

[165] H. Khoramishad, A. Crocombe, K. Katnam, and I. Ashcroft, "Predicting fatigue damage in adhesively bonded joints using a cohesive zone model," *International Journal of fatigue*, vol. 32, no. 7, pp. 1146-1158, 2010.

[166] G. Alfano, "On the influence of the shape of the interface law on the application of cohesive-zone models," *Composites Science and Technology*, vol. 66, no. 6, pp. 723-730, 2006.

[167] M. A. Wahab, "Simulating mode I fatigue crack propagation in adhesively-bonded composite joints," in *Fatigue and fracture of adhesively-bonded composite joints*: Elsevier, 2015, pp. 323-344.

[168] S. Sugiman, A. Crocombe, and I. Aschroft, "Modelling the static response of unaged adhesively bonded structures," *Engineering Fracture Mechanics*, vol. 98, pp. 296-314, 2013.

[169] A. Chadegani, C. Yang, and E. Dan-Jumbo, "Strain-Energy Release Rate Analysis of Adhesive-Bonded Composite Joints with Prescribed Interlaminar Crack," *Journal of Aircraft*, vol. 46, no. 1, pp. 203-215, 2009.

[170] A. A. Baker and H. Y. Nezhad, "Adhesively bonded repairs to highly loaded structure," in *Adhesive Bonding*: Elsevier, 2021, pp. 437-497.

[171] N. Ung, "Surface Preparation and the Contamination Effects on Composite Adhesive," *The UNSW Canberra at ADFA Journal of Undergraduate Engineering Research*, vol. 11, no. 1, 2018.

[172] A. Rider, R. Vodicka, G. Mathys, and I. Stoyanovski, "Review of RAAF procedures for qualifying bonded repair technicians," DEFENCE SCIENCE AND TECHNOLOGY ORGANISATION VICTORIA (AUSTRALIA) AIR …2006.

[173] Cytec, "FM 300 Epoxy Film Adhesive," ed, 2013.

[174] P. Amin, "The Effect of Contamination on the Integrity and Durability of Composite Adhesive Bonds," *The UNSW Canberra at ADFA Journal of Undergraduate Engineering Research*, vol. 10, no. 2, 2018.

[175] S. International, "Composite Materials Handbook 17," *CMH-17-1G, SAE International*, 2012.

[176] J. Wang and D. Kelly, "Strength and failure mode of adhesively-bonded joints at different loading rates," *The Journal of Adhesion*, vol. 68, no. 1-2, pp. 1-19, 1998.

[177] W. J. a. H. A, "Mechanical Property Measurement," in *Composite Materials for Aircraft Structures*, B. A. a. S. M, Ed.: American Institute of Aeronautics and Astronautics, September, 2016.

[178] P. R. Ciriscioli, W. I. Lee, D. G. Peterson, G. S. Springer, and J.-M. Tang, "Accelerated environmental testing of composites," *Journal of composite materials*, vol. 21, no. 3, pp. 225-242, 1987.

[179] R. J. DeIasi and R. L. Schulte, "Experimental determination of the effects of moisture on composite-to-composite adhesive joints," 1981.

[180] J. A. Pascoe, R. C. Alderliesten, and R. Benedictus, "Methods for the prediction of fatigue delamination growth in composites and adhesive bonds–a critical review," *Engineering Fracture Mechanics*, vol. 112, pp. 72-96, 2013.

[181] A. Rocha *et al.*, "Paris law relations for an epoxy-based adhesive," *Proceedings of the Institution of Mechanical Engineers, Part L: Journal of Materials: Design and Applications*, vol. 234, no. 2, pp. 291-299, 2020.

[182] A. A. Baker and R. Jones, "Bonded repair of aircraft structures, 1988," ed: Martins Nijhoff Publishers, Dordrecht, 1990.

[183] A. Baker, *Bonded repair of aircraft structures*. Springer Science & Business Media, 2012.

[184] C. N. Chung, "Prediction of Design Allowables for Fatigue of Polymer Matrix Composites using Reliability Methods/eingereicht von Chi Nghia Chung," Universität Linz, 2018.

[185] Z. P. Bazant and E.-P. Chen, "Scaling of structural failure," 1997.

[186] N. Fleck, K. Kang, and M. Ashby, "The cyclic properties of engineering materials," 1993.

[187] A. P. Vieira, J. S. Andrade Jr, and H. J. Herrmann, "Subcritical crack growth: The microscopic origin of Paris' law," *Physical review letters,* vol. 100, no. 19, p. 195503, 2008.

[188] G. Allegri and M. Wisnom, "A non-linear damage evolution model for mode II fatigue delamination onset and growth," *International journal of fatigue,* vol. 43, pp. 226-234, 2012.

[189] A. Turon, E. González, C. Sarrado, G. Guillamet, and P. Maimí, "Accurate simulation of delamination under mixed-mode loading using a cohesive model with a mode-dependent penalty stiffness," *Composite Structures,* vol. 184, pp. 506-511, 2018.

[190] A. Johnson, N. Toso-Pentecôte, and D. Schueler, "Numerical modelling of impact and damage tolerance in aerospace composite structures," in *Numerical modelling of failure in advanced composite materials*: Elsevier, 2015, pp. 479-506.

[191] S. Wanthal, J. Schaefer, B. Justusson, I. Hyder, S. Engelstad, and C. Rose, "Verification and validation process for progressive damage and failure analysis methods in the NASA Advanced Composites Consortium," in *American Society for Composites (ASC) Technical Conference*, 2017.

[192] K. N. Anyfantis and N. G. Tsouvalis, "A 3D ductile constitutive mixed-mode model of cohesive elements for the finite element analysis of adhesive joints," *Journal of adhesion science and technology,* vol. 27, no. 10, pp. 1146-1178, 2013.

[193] C. Davila, P. Camanho, and M. de Moura, "Mixed-mode decohesion elements for analyses of progressive delamination," in *19th AIAA applied aerodynamics conference*, 2001, p. 1486.

[194] J. Gonçalves, M. De Moura, P. De Castro, and A. Marques, "Interface element including point-to-surface constraints for three-dimensional problems with damage propagation," *Engineering Computations,* 2000.

Appendices

ARC Training Centre for Automated Manufacture of Advanced Composites

Industrial Placement Report

Student name: Veldyanto Tanulia

Student email: veldyanto@yahoo.com

Company name: Defence Science and Technology Group (DSTG)

Industry supervisor: Dr. John Wang

Start date: 7/9/19 **End date:** 10/31/19 **Total no. of weeks:** 17

Brief description of placement:

- Specialised training on surface preparation through Boeing Wedge Test (BWT).
- Journal paper preparation.
- Analyse the loading capacity with various crack length using VCCT and Stress-based method.
- Analyse the Strain Energy Release Rate (SERR) using VCCT technique.
- Initial specimen design for experimental work.
- Refinement on the specimen design (grip length).
- Perform the static test along with support from DSTG.
- Perform the trial specimen of fatigue testing.

Industry supervisor comments:

Supervisor signature: John Wang **Student signature:** Digitally signed by Veldyanto Tanulia Date: 2020.09.29 17:06:12 +10'00'

ARC Training Centre for Automated Manufacture of Advanced Composites

Industrial Placement Report

Student name: Veldyanto Tanulia

Student email: veldyanto@yahoo.com

Company name: Defence Science and Technology Group (DSTG)

Industry supervisor: Dr. John Wang

Start date: 2/14/20 **End date:** 12/13/20 **Total no. of weeks:** 43

Brief description of placement:

- Refine the specimen design based on the first batch test (reduce the edge thickness and increase the tapered length).
- Prepare the drawing for the specimen manufacturing.
- Identify the shear and peel stresses distribution on the various tapered end thickness.
- Coupon specimen preparation for experimental work.
- Residual strength prediction using Cohesive Zone Element (CZE).
- Identify the effect of Clad layer on fatigue test as well as the Clad thickness

Industry supervisor comments:

Supervisor signature: John Wang **Student signature:** 18/12/20